MONASH UNIVERSITY
THESIS ACCEPTED IN SATISFACTION OF THE
REQUIREMENTS FOR THE DEGREE OF
DOCTOR OF PHILOSOPHY
ON..... 11 December 2001 .....
.....[redacted]
for Sec. Research Graduate School Committee

THE PRECIPITATION HARDENING RESPONSE IN Al-Mg(-Ag) ALLOYS

A thesis submitted in fulfilment of the requirement for the degree of Doctor of Philosophy

Masahiro KUBOTA

B.E., M.E., Dip.Ed. (Nihon University, Japan)

Department of Materials Engineering,
School of Physics and Materials Engineering,
Monash University

Clayton, Victoria 3168
Australia

August, 2001

Contents

Synopsis

The current investigation has involved a fundamental study of the age-hardening response, precipitate phases and evolution of microstructure during isothermal ageing heat treatments of Al-5Mg and Al-10Mg alloys, with and without microalloying additions of 0.5Ag (wt%). Specifically, the precipitation hardening response of these alloys has been monitored by measurements of their bulk Vickers hardness as a function of isothermal ageing time and temperature. The detailed characterisation of precipitate microstructures and precipitate phases in these experimental alloys has been carried out using analytical transmission electron microscopy (TEM), with a combination of electron diffraction and energy dispersive X-ray spectroscopy (EDXS). The principal aim of this investigation was to improve understanding of the effects of trace additions of Ag on the ageing response of binary Al-Mg alloys and the microstructural changes giving rise to this response.

Hardness measurements in the binary alloys indicated little or no age-hardening response in Al-5Mg alloy aged at 200°C, but an increase of solute Mg stimulated a modest precipitation hardening response in Al-10Mg alloy aged at 160°C, 200°C and 240°C. In contrast, trace additions of Ag to Al-5Mg alloy promoted a significant age-hardening response, and to Al-10Mg alloy accelerated significantly the age-hardening response and substantially increased the maximum hardness achievable. The effects of cold work on the age-hardening response in Al-10Mg-0.5Ag alloy were both to increase the maximum hardness and to moderately accelerate the age-hardening response.

Based on measurements of the dislocation density in the as-quenched microstructures of Al-10Mg alloys with and without 0.5Ag, the number density of dislocations in the as-quenched condition in the binary Al-10Mg alloy was slightly higher than that in ternary Al-10Mg-0.5Ag alloy. Defect analyses indicated that trace additions of Ag do not change the nature of the dislocations in binary Al-10Mg alloy, all line defects examined were perfect dislocations with a/2<110> type Burgers vectors.

Microstructural observations by TEM indicated that, in the early stages of decomposition of quenched Al-10Mg alloy at 240°C, a low density of plate- and lath-like precipitate β' particles (Al_3Mg_2, lattice parameters a = 1.002 nm, c = 1.636 nm) was formed. The maximum hardness was associated with a mixture of coarse-scale (~500 nm), blocky-shaped β particles (Al_3Mg_2, lattice parameter a = 2.824 nm), lath-like β' particles and a small fraction of irregularly-shaped

particles of an as yet unidentified phase. None of these precipitates appeared to share a simple, low index orientation relationship with the aluminium matrix.

In contrast, the aged microstructures in the binary Al-10Mg alloy were significantly modified by microalloying additions of 0.5Ag. A fine-scale, uniform dispersion of rhombohedral particles having quasicrystalline icosahedral structure were observed to have nucleated from supersaturated solid solution as a product of a solid-state reaction during isothermal ageing for just 0.5 h at 240°C. The orientation relationship between the icosahedral structure and the aluminium matrix phase was of the form i3 ∥ $<111>_\alpha$ and i5 ∥ $<011>_\alpha$. The quasicrystalline icosahedral precipitate phase contained all three principal elements in the alloy. Both TEM observations and intersection point group symmetry analyses confirmed that these particles were rhombohedral. These quasicrystalline particles were observed to contribute a significant increase in hardness, but they were metastable and replaced by a more stable phase by the time the alloy had reached maximum hardness at 240°C.

Fine-scale, uniformly distributed rod-like precipitate particles with rod axes parallel to $<110>_\alpha$ directions were the predominant dispersed phase in the ternary Al-10Mg-0.5Ag alloy aged 2 h at 240°C, which represented the maximum hardness condition. The $<110>_\alpha$ rod-like precipitates were identified as the b.c.c. T phase ($Mg_{32}(Al, Ag)_{49}$, lattice parameter a = 1.416 nm). The orientation relationship between T phase and the aluminium α matrix was of the form $(010)_T \| (1\bar{1}1)_\alpha$ and $[001]_T \| [1\bar{1}0]_\alpha$. According to this relationship and the observed precipitate forms, these particles of T phase have a long axis $[001]_T \| [1\bar{1}0]_\alpha$, and the intersection point group is 2/m with the common 2-fold axis parallel to the rod axis. Qualitative microanalysis by EDXS confirmed that the metastable crystalline T phase was a ternary compound that contained all three elements Al, Mg and Ag.

The rod-like particles of T phase were replaced by coarse-distribution, globular particles in over-aged samples of the Al-10Mg-0.5Ag alloy (e.g. aged 72 h at 240°C). These globular particles were identified as having the f.c.c. structure of β phase (Al_3Mg_2, lattice parameter a = 2.824 nm), which is the equilibrium phase in the equivalent binary Al-Mg alloy. The orientation relationship between the β phase and α -Al matrix was such that; $(100)\beta \| (100)\alpha$ and $[001]\beta \| [001]\alpha$. The coarse-scale, β particles were commonly observed to be multiply-twinned.

The precipitation sequences in supersaturated Al-10Mg(-0.5Ag) alloys aged at 240°C may thus be summarised as follows;

Al-10Mg alloy : Supersaturated α solid solution ------>
metastable α phase + metastable β' phases
------> metastable α phase + metastable β' + stable β + (minor unidentified phase)
------> equilibrium α phase + stable β phase.

Al-10Mg-0.5Ag alloy : Supersaturated α solid solution ------>
metastable α phase + metastable icosahedral quasicrystalline phase
------> metastable α phase + metastable T phase
------> equilibrium α phase + stable β phase.

Characterisation of the precipitate microstructures in Al-10Mg(-0.5Ag) alloys aged naturally at 20°C revealed uniformly-distributed, fine-scale spheroidal precipitate particles in the ternary alloy after a period of 16 months, while no such precipitation was observed in the binary alloy under the same ageing conditions. These spheroidal precipitate particles were identified as the β'' phase, which has an ordered $L1_2$ structure (lattice parameter a = 0.408 nm). The orientation relationship between the β'' phase and the aluminium matrix phase was of the form $(100)_{\beta''} \| (100)_\alpha$, $[001]_{\beta''} \| [001]_\alpha$. Such particles were unstable in the Ag-modified alloys when the specimens were subsequently aged at 90°C. No evidence of GP zones was detected in both binary and ternary alloys during natural ageing for periods of up to 16 months and 28 months, respectively.

In binary Al-10Mg alloy aged at 90°C, plate-like precipitate particles were initially nucleated (45 days) from supersaturated solid solution, and cuboidal precipitate particles were formed in later stages (60 days) of the decomposition process. These plate-like particles were formed on $\{100\}_\alpha$ planes and were identified have a structure consistent with the metastable β' phase (Al_3Mg_2, a = 1.002 nm, c = 1.636 nm), while the cuboidal particles were still remained unclear. In contrast, only the plate-like β' particles were observed in the Ag-containing alloy under the same ageing conditions.

In binary Al-10Mg alloy aged at 200°C, the predominant precipitate particles were of the $\{100\}_\alpha$ plate-shaped β' phase. However, in the Ag-modified alloy the major precipitate phase is to the form of fine-scale, uniformly-distributed quasicrystalline particles, together with a low volume fraction of the β' phase.

The principal effects of microalloying additions of 0.5Ag in Al-10Mg alloy may thus be summarised as:

(1) to accelerate the age-hardening response and increase the maximum hardness achievable by as much as 30VHN.

(2) to stabilise at least two metastable, intermediate phases in the ternary alloy that are not present in binary alloy (i.e. quasicrystalline i-phase and crystalline T phase).

It is noteworthy that the present study is one of the first in which a quasicrystalline phase of icosahedral symmetry (or a near approximant) has been observed to be the product of a conventional isothermal ageing heat treatment.

Statement of Originality

This thesis contains no material which has been accepted previously for the award of any other degree or diploma in any university or other institution and, to the best of my knowledge and belief, it contains no material previously published or written by any other person, except where due reference is made in the text of the thesis.

Masahiro KUBOTA

Melbourne, Australia, August, 2001.

Acknowledgments

First and foremost, I would like to express my sincere appreciation to my supervisor, Professor Barry C. Muddle for his supervision and encouragement throughout my scientific training period. Without his tireless criticism, enthusiasm and excellence of scientific inspiration including critical review of my thesis, I would not have completed this thesis. I'm a very lucky person to meet Professor Barry Muddle who is an honest, kind and dedicated scientist.

I acknowledge gratefully Emeritus Professor Ian J. Polmear who kindly provided some specimens as well as constant encouragement and advise. I also want to thank Dr. J. F. Nie (Logan Research Fellow) for helpful discussions regularly and for teaching me TEM techniques through the period of this course. I also should thank Dr. C.H.J. Davies for his help during Prof. Muddle's sabbatical leave.

All staff in the Department of Materials Engineering, Monash University, especially Mr. Irek Kozicki for laboratory work, Mr. Pan Renji for TEM work, Ms. Julie Fraser for assisting with photographic works and Ms. Layla Godfrey for helping lots of documentation during my writing up way periods, are greatly acknowledged.

I also acknowledge gratefully the financial support of an Overseas Postgraduate Research Scholarship (OPRS) from Department of Employment and Education and Training Youth Affair (DEETYA) and a Monash Graduate Scholarship (MGS) from Monash University. Without these financial supports, all possibilities happened to me in Australia would not have made.

As I am one of overseas students in the Department of Materials Engineering at Monash University, my special thanks go to all students and postdoctoral fellows who shared the same time with me that they were friendly and kindly to inform and give me enormous suggestions, not only research matters, but also what the life is. I would be never forgot such great experiences while I have been in Melbourne, Australia. Special thanks must go to my friends, members of Foo family and McNamee family who always gave me tremendous supports in many ways.

I would like to express special thank to Professors J. Kaneko and M. Sugamata in the Department of Mechanical Engineering, College of Industrial Technology at Nihon University, Japan, who provided me significant supports during periods of writing my Ph.D thesis.

Finally, I really appreciate that my parents, sister, grandmothers and relatives in my family gave me tremendous spiritual support while I was studying in Australia.

Chapter 1

Introduction

Improvements in the performance of automobiles and aircraft have been closely linked to progress in materials. Breakthroughs such as those associated with the research and development of aluminium alloys have made it possible to reduce significantly the weight of car components and of aircraft structures. This has enabled more efficient use of energy in cars and civil aircraft by allowing increased size for a given weight, and lowering fuel consumption. The requirements of high specific strength, stiffness, lower fatigue sensitivity, increased fatigue and creep resistance, weldability and excellent corrosion resistance, will continue to play a significant role in the research and development of aluminium alloys for applications in the automobile and aerospace industries. Those properties that make aluminium alloys particularly attractive, are generally determined by their microstructures which are in turn controlled by a combination of alloying, microalloying and appropriate thermal or thermomechanical treatment.

The conventional structural aluminium alloys are generally classified into two categories, such as non-heat treatable and heat treatable alloys. For instance, the alloy of Al-Mg systems possesses these two types, i.e. wrought (non-heat treatable) and cast (heat treatable) alloys. The mechanical properties of non-heat treatable aluminium alloys are generally determined by microstructures, in which contain higher concentrations of solute elements in the matrix. For heat treatable aluminium alloys, mechanical properties are significantly relied on aged microstructures which contain precipitate particles in the matrix.

Microstructural factors, which are the level of solute elements (non-heat treatable), the size and distributions of precipitate particles (heat treatable), and their crystal structures, are mainly controlled to strengthening mechanisms, such as the resistance of dispersed precipitate particles and/or solute atoms to pin dislocation motion. These strengthening mechanisms in the field of materials engineering are well-known as precipitation hardening and solid solution strengthening, respectively. For strengthening by precipitation hardening, the impedance to dislocation motion is controlled primarily by the scale and distribution of precipitate particles in the aluminium solid solution matrix, whilst solid solution strengthening is generally controlled by the concentrations of solute elements retained in matrix solid solution. The common principle adopted for

microstructural design of aluminium alloys for structural applications is that the microstructure should contain a significant volume fraction (typically 2-10%) of fine-scale, thermally stable precipitate particles distributed uniformly in the matrix (Nie et al. 1996).

Al-Mg alloys have been widely used commercially in wrought form (1-5 wt% Mg) and as casting alloys (5-10 wt% Mg) because they combine medium strength (~370 MPa tensile strength) with relatively low density, good ductility, excellent resistance to corrosion and good weldability. The commercial wrought and cast alloys achieve their strength primarily through solid solution strengthening and they are generally classified as non-heat treatable. Although further increases in strength, based on precipitation hardening, may be achieved by increasing the magnesium content, the strength increment is insufficient to compensate for the corresponding decrease in both stress corrosion resistance and hot workability. Recently, Al-Mg alloys relying on solid solution strengthening and work hardening have been the focus of attention in the automobile industry, because with appropriate microstructural control, Al-Mg alloy sheets can be produced to provide the properties required for particular automotive applications (Burger et al. 1995). These Al-Mg series alloy have relatively good formability, but relatively low strength. Therefore, their applications in structural components in the car industry remain limited.

It is well known that when trace amounts (~0.1 at%) of silver are added to conventional aluminium alloys containing Mg, especially heat treatable alloys such as the Al-Cu-Mg (2000 series) and Al-Zn-Mg (7000 series) alloys, the age-hardening response is enhanced and the resulting mechanical properties significantly improved. Two main reasons for this enhanced response have been proposed by Polmear (1968 and 1987). The first is that trace elements can alter the free energy relationships for the various phases involved, which may lead to an increase in the stability of the existing precipitates and/or to the introduction of new phase fields, i.e. new metastable precipitate phases. The second is that trace elements can influence the kinetics of nucleation by, for example, providing heterogeneous nucleation sites or perhaps by reducing the interfacial energy between selected precipitate phases and the matrix. The precipitation process is stimulated through phenomena such as these, which improves the mechanical properties of the resulting alloys.

Despite this demonstrated potential, very little attention has been paid to the effect of trace elements on Al-Mg (5000 series) alloys, because these alloys have traditionally shown a poor age-hardening response. Even where they age-harden, it is generally deemed insufficient to be useful in industrial applications in comparison with other age-hardening aluminium alloys, such as those of the 2000 and 7000 series. Because the principal hardening phase in aged binary Al-Mg alloys is the β' phase, which is nucleated heterogeneously and is thus relatively difficult to form in fine scale, uniform distributions, any strength increment is not appreciable. However, the automobile and aerospace industries have recognised the usefulness of the Al-Mg alloys

because of their attractive specific strength. Therefore, if Al-Mg based alloys could be induced to have a useful age-hardening response, an ideal alloy design combining high strength with relatively low density may be possible.

In the early 1960s, the effects of trace additions of Ag to Al-Mg alloys were first explored (Polmear and Sargant 1963, Polmear 1964), and the alloys exhibited some interesting phenomena. A significant age-hardening response was, for example, observed in an Al-5Mg-0.5Ag (wt%) alloy, where there was no such hardening response in corresponding Ag-free alloy. The age-hardening response was also substantially accelerated and enhanced in alloys of higher Mg content such as Al-10Mg-0.5Ag (wt%) alloy. However, there has been no systematic characterisation of the evolution of microstructure which occurs during ageing treatments, and there is still no detailed understanding of the precipitation hardening behaviour of these alloys and of the relationships between the microstructures and the mechanical properties. Since the 1960s, only limited microscopy work and a few preliminary X-ray diffraction experiments have been completed and these alloys, with and without microalloying additions of Ag, are not well-characterised in terms of microstructural analysis, such as the size, distribution and morphology of precipitate particles and the crystal structures of dispersed phases. In addition, the precise role of Ag in modifying the precipitation process of Al-Mg alloys is still unclear. Therefore, a systematic study of the age-hardening response of these alloys is required.

The main objectives of the present investigation were thus to provide an understanding of the effects on the precipitation hardening behaviour caused by trace additions of Ag to binary Al-Mg alloys, and to elucidate the strengthening mechanism(s) in terms of the identification of strengthening precipitate phases and characterisation of microstructures. The materials chosen for this study were nominally Al-5 wt% Mg alloys and Al-10 wt% Mg alloys with and without additions of 0.5 wt% Ag. The age-hardening response of these alloys has been examined using conventional bulk Vickers hardness measurements. Transmission electron microscopy has been employed in order to identify strengthening precipitate phases and to characterise microstructural changes during systematic isothermal ageing heat treatments. The principal experimental techniques used were analytical transmission electron microscopy with electron microdiffraction and energy dispersive X-ray spectroscopy (EDXS).

In this thesis, a literature review of previous studies which have investigated the characteristics of Al-Mg alloys and the effect of trace additions of minor alloying elements on the precipitation hardening behaviour of Al-Mg alloys is presented in Chapter 2. In Chapter 3, details of the specimen preparation and the experimental techniques employed are described. The results of measurements of the age-hardening response of the Al-5Mg(-0.5Ag) and Al-10Mg(-0.5Ag) (wt%) alloys and characterisation of the as-quenched microstructures are presented in Chapter 4, and identification of the precipitate phases in Al-Mg(-Ag) alloys aged isothermally at 240°C are

reported in Chapter 5. The results of microstructural changes in Al-Mg(-Ag) alloys during the isothermal ageing processes at different temperatures are presented in Chapter 6. The conclusions of this study are outlined in Chapter 7.

Chapter 2

Literature Review

2.1 Introduction

In recent years, significant attention has been paid to alloys of the Al-Mg system, because they exhibit high resistance to corrosion and achieve a relatively high specific strength, with good formability, through solid solution hardening (Burger et al. 1995). Alloys of Al-Mg have found commercial use in both wrought (1-5 wt% Mg) and cast (5-10 wt% Mg) forms. Commercial wrought and cast binary alloys are not hardenable by precipitation hardening, and thus find application where moderate strength and formability are priorities. The great advantage of alloys of this system is their light weight compared to other commercial aluminium alloys, arising from the low density of Mg. Therefore, Al-Mg alloys have potential for use in many applications in the automobile and aerospace industries where there is continuous emphasis on reduction in the weight of components to improve fuel efficiency and thus save energy.

Although Mg exhibits significant solid solubility in Al, and a declining solid solubility with decreasing temperature (Figure 2.1) (Murray 1988), binary alloys containing less than ~7 wt% Mg exhibit little or no precipitation hardening response when heat treated appropriately, and the ageing response of alloys of higher Mg content is only modest (Polmear 1964). If the alloys are to find wider application it is necessary that their strength be improved, and an approach to this might involve techniques to stimulate precipitation hardening. In other medium to high strength aluminium alloys, considerable success has been achieved in improving the age-hardening response by variations in thermal treatments, the additions of trace or microalloying elements, or by plastic deformation prior to the ageing treatment. This thesis is concerned primarily with attempts to stimulate precipitation hardening in Al-Mg alloys using microalloying additions of Ag and/or prior plastic deformation.

This chapter commences with a brief explanation of precipitation hardening to provide a basis for subsequent discussion. The characteristics of binary Al-Mg alloys, in terms of the decomposition processes from supersaturated solid solution, are described next because development of an understanding of the decomposition processes is significantly important. Subsequently, the effects of Ag on precipitation in Al alloys in general are described to provide useful general background. The effects of trace elements on precipitation hardening in Al-Mg alloys, and specifically the effects of Ag on precipitation in binary Al-Mg alloys are then summarised. The effects of cold work on precipitation in aluminium alloys are briefly discussed.

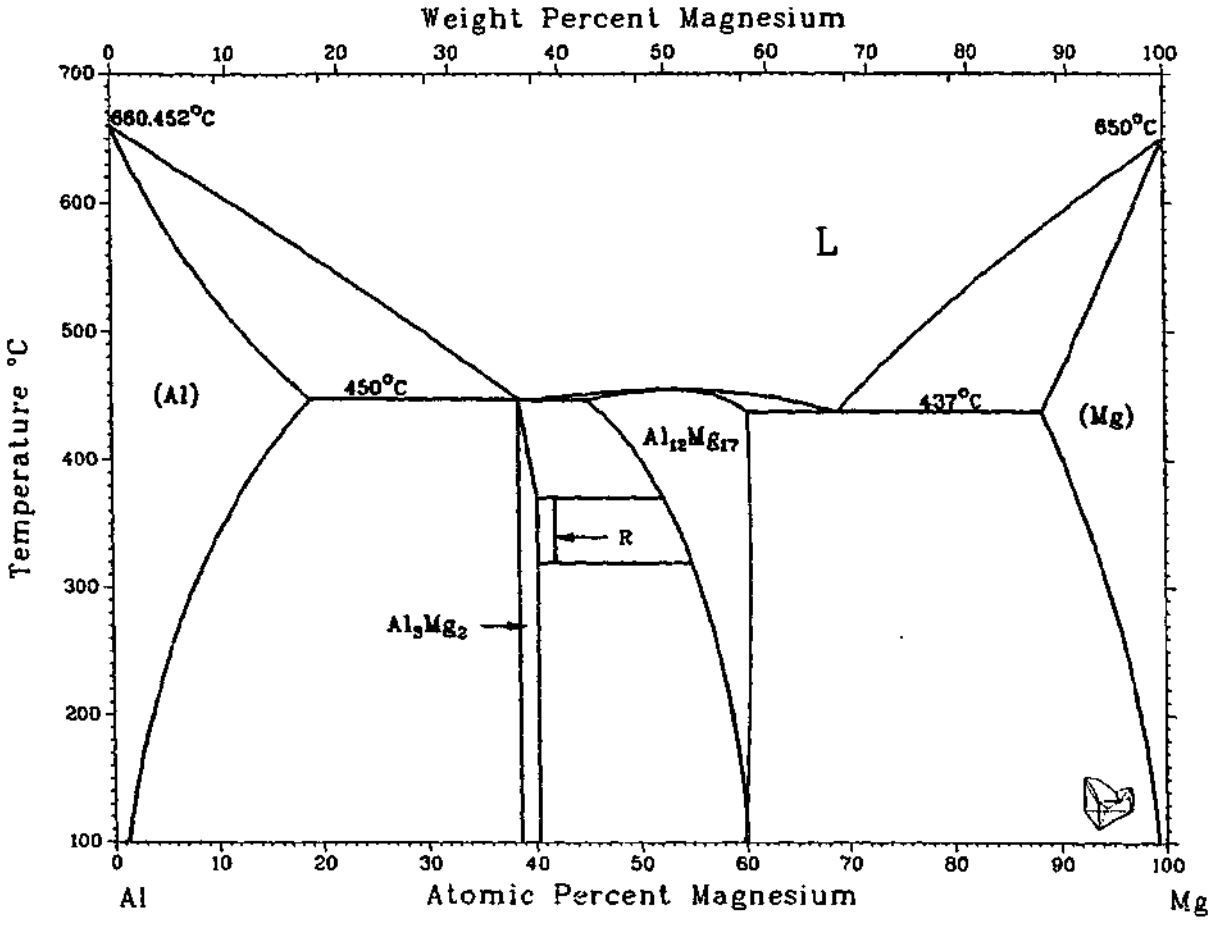

Figure 2.1 The equilibrium Al-Mg alloy phase diagram (Murray 1988).

2.2 Precipitation Hardening

The fundamental requirement for a precipitation hardening reaction in an aluminium alloy is that the alloy system exhibit a significant decrease in the solubility of the principal alloying element with decreasing temperature, as illustrated in Figure 2.2 (Porter and Easterling 1987). An alloy of original composition X_2^0 heated to a temperature in the range ΔT_1 will become a homogeneous solid solution of stable α phase. If the alloy is cooled slowly to temperature T_3 (i.e. in the vicinity of room temperature), the β phase will normally precipitate from the α solid solution according to the following reaction:

$$\alpha' \text{ --------> } \alpha + \beta$$

In this reaction, α' is a metastable supersaturated solid solution, α is a more stable solid solution with the same crystal structure as α', but with a composition closer to equilibrium, and β is the equilibrium precipitate. This is the equilibrium decomposition reaction and the remaining matrix will reduce its composition from X_2^0 to X_2 after the β phase is formed.

If, alternatively, the alloy is quenched rapidly to low temperature, there is no time for any significant decomposition to occur, so that the alloying element (solute atoms) are retained in supersaturated solid solution at the lower temperature. In this case, it is frequently found that a novel metastable precipitate phase (or phases) replaces the equilibrium β phase during any subsequent decomposition of this retained supersaturated solid solution.

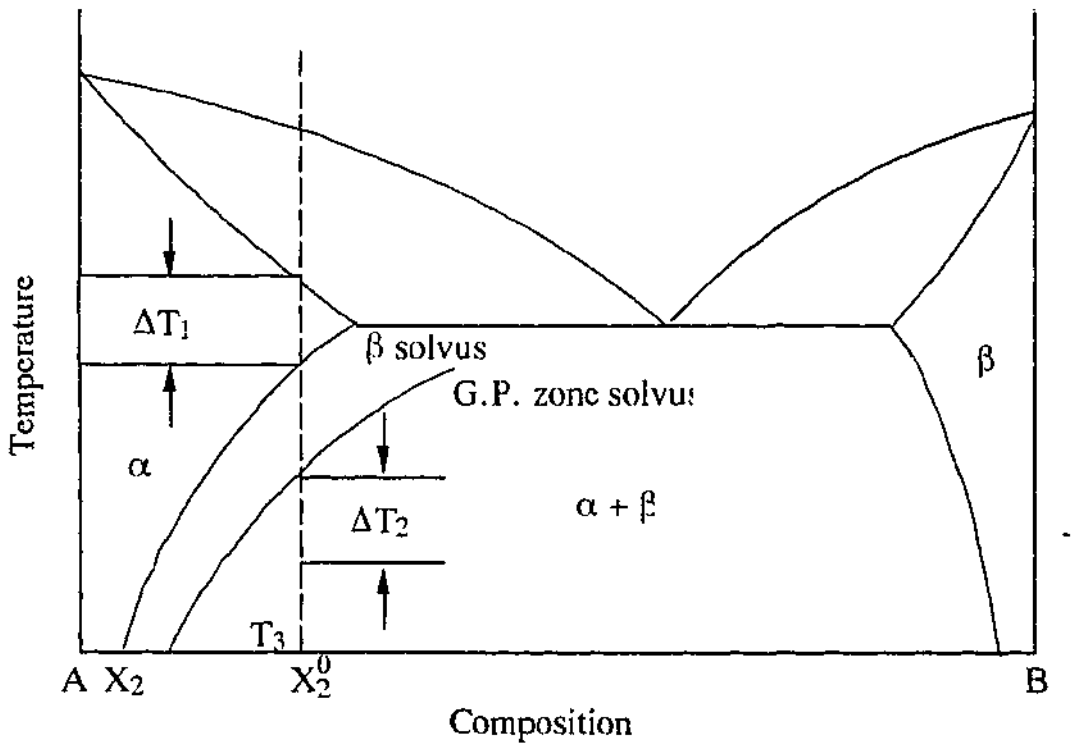

Figure 2.2 A schematic phase diagram illustrating the conditions required for the precipitation hardening process in a binary alloy system.

Because a supersaturated solid solution is thermodynamically unstable, there is a driving force for decomposition of the α' phase at all temperatures below the equilibrium solvus temperature, T_S. The magnitude of this driving force increases with increasing undercooling (i.e. decreasing temperature) and increasing solute supersaturation.

Precipitation within the supersaturated α' solid solution may be initiated by *ageing*, i.e. reheating and holding isothermally, typically within the temperature range designated ΔT_2. Isothermal decomposition of the supersaturated solid solution at such a large undercooling typically involves several stages. Commonly, initial decomposition will involve the formation of initially coherent solute atoms / clusters, which in Al-Cu based alloys are known as Guinier-Preston (GP) zones (Guinier 1938, Preston 1938) . These zones are replaced by one or more intermediate precipitates, which generally have a crystal structure distinguishable from that of the matrix and the equilibrium β phase. They are normally much larger than the GP zones in size, and they are typically only partly coherent (semi-coherent) with the lattice of the matrix. Formation of the final equilibrium precipitate (β) is commonly associated with complete loss of coherency with the lattice of the matrix (incoherent precipitate). The β phase forms only at higher ageing temperatures or after prolonged ageing at lower ageing temperatures, and the equilibrium precipitate particles normally form a coarse-scale dispersion. The decomposition of the supersaturated solid solution during isothermal ageing heat treatments is thus commonly a complex process involving several stages, with each stage represented by its own metastable equilibrium (i.e. metastable solvus curve). When the ageing temperature is below the GP zone (or coherent) solvus, then decomposition typically follows the general path:

Supersaturated solid solution (α') -----> α' + coherent clusters (GP zones)
-----> α' + intermediate precipitate(s) -----> α + equilibrium precipitate (β).

It is well known (Porter and Easterling 1987) that, while there is a higher driving force for precipitation of the equilibrium phase β than the metastable GP zones, the GP zones initially form more rapidly because they are coherent and thus have a significantly lower energy barrier to nucleation. Similarly, each subsequent metastable precipitate lowers the free energy, with each such precipitate enjoying a kinetic advantage over the equilibrium β phase because it faces a lower energy barrier to nucleation. The specific identity of the metastable precipitate and the rate of the decomposition process are generally controlled by whether ageing is carried out below or above a critical temperature defined by the appropriate metastable solvus curve on the equilibrium phase diagram. For example, if the alloy is aged at a temperature above the GP zone solvus, GP zones will not form because they are then thermodynamically unstable. The first precipitate to form will not have the form of GP zones, but an intermediate metastable phase may then be first in the precipitation sequence.

2.3 Precipitation Characteristics of Al-Mg Alloys

The equilibrium phase diagram for the Al-Mg system (Mondolfo 1976, Murray 1988) is shown in Figure 2.1. The maximum solid solubility of magnesium in aluminium is 17.4 wt% (hereafter wt% is used for all compositions unless otherwise specified) at 450°C, and the solubility decreases continuously to 1.9 % at 27°C. According to this binary phase diagram, it is suggested that it would be relatively easy to achieve a supersaturated solid solution with a high concentration of solute Mg atoms for alloys in the range of 2%-15% Mg. On this basis, alloys of the Al-Mg system would appear to have strong potential for precipitation hardening, as described in Section 2.2.

2.3.1 Precipitation Hardening Response

As described above, there is apparently great potential for an age-hardening response in Al-Mg alloys; however, when compared with other precipitation hardening aluminium alloys, such as those of the Al-Cu system, alloys with solute contents in the range 7%-10% Mg have been found to exhibit an abnormally low age-hardening response and no significant age-hardening response has been detected in those alloys with less than 5% Mg (Polmear 1964). As a typical example, Figure 2.3 represents the ageing curves (Vickers hardness as a function of ageing time) for Al-Mg alloys with different Mg contents aged at 200°C (Perryman and Brook 1950-51, Polmear 1964). These ageing curves clearly indicate the strong solid solution strengthening effect of Mg in solution in the as-quenched alloys. They also show that there is little or no hardening response during ageing for alloys below approximately 7% Mg. With increasing Mg content, the precipitation hardening increases but the increment in hardness is modest (< 20VHN), even at maximum hardness. It is also to be noted that the hardening reaction is sluggish; it takes tens of hours to reach maximum hardness in alloys containing 7-10% Mg.

In the case of typical heat-treatable aluminium alloys, such as the Al-Cu based alloys, the initial contribution to precipitation hardening is generally attributable to coherent GP zones (solute rich clusters) when an alloy is aged below the GP zone solvus (typically ~150°C) (Porter and Easterling 1987). Maximum hardness is commonly associated with a mixture of such zones and a metastable intermediate phase (θ'' in Al-Cu), or a mixture of two intermediate phases (θ'' and θ' in Al-Cu). Similar precipitation hardening effects from coherent GP zones (Mg-rich clusters) might initially be expected in the Al-Mg system. However, as shown in the age-hardening curves of Fig. 2.3, there is little or no age-hardening response observed during the early stages of ageing. This lack of response from the formation of GP zones is attributable to the fact that the GP zone solvus is depressed to the vicinity of room temperature in this composition range, according to the previous reports of Pollard 1964-65, Roth and Raynal 1974, Raynal and Roth 1975, and Lorimer 1978.

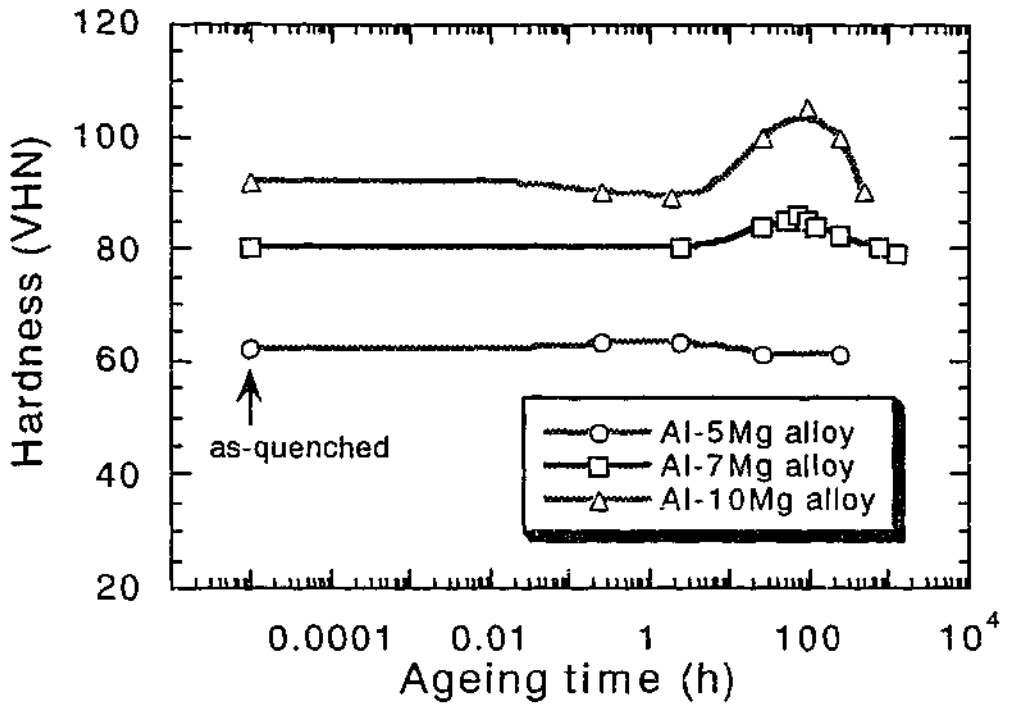

Figure 2.3 Age-hardening curves for Al-Mg alloys with different Mg concentrations (%) aged at 200°C (Al-7Mg and Al-10Mg alloys from Perryman and Brook 1950-51, Al-5Mg alloy from Polmear 1964).

The critical temperatures for the GP zone solvus in Al-Mg alloys have been determined experimentally using the small-angle neutron scattering technique (Roth and Raynal 1974, Raynal and Roth 1975). These results showed that no zones were formed in an Al-7% Mg alloy aged at room temperature, but that they were present in an Al-11.5% Mg alloy aged at both room temperature and 40°C. In addition, the GP zones detected in Al-11.5% Mg alloys aged at room temperature were observed to dissolve during annealing treatments at 100°C for just 15 min.. This would suggest that the GP zone solvus temperature for an Al-11.5% Mg alloy is somewhere between 40°C and 100°C. Similarly, the formation of GP zones was detected in Al-10% Mg alloys aged at room temperature based on monitoring changes in the ultimate tensile strength with elongation, but no such changes were observed at an ageing temperature of 50°C, suggesting that the zones are unstable and dissolve back into aluminium matrix above this temperature (Pollard 1964-65). As a representative example of GP zone solvus, the Al-Mg equilibrium phase diagram including the metastable GP zone solvus line is shown in Figure 2.4 (Lorimer 1978). These fundamental data on the position of the GP zone solvus curve are consistent with the results of the age-hardening curves shown in Fig. 2.3. That is, when Al-Mg alloys are aged at 200°C, those alloys with 5%, 7% and 10% Mg are not expected to acquire rapid hardening from GP zones, because the ageing temperature is well above the GP zone solvus temperature. Therefore, the initial rate and magnitude of the age-hardening response in these alloys are much lower than with heat-treatable aluminium alloys.

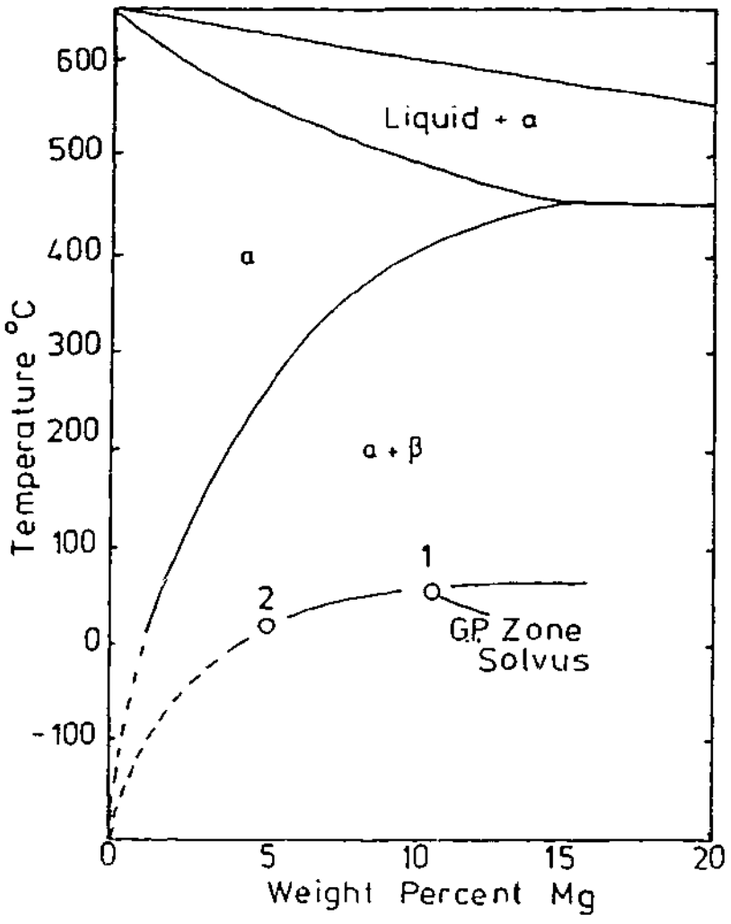

Figure 2.4 The equilibrium Al-Mg alloy phase diagram including metastable GP zone solvus line (Lorimer 1978). 1 from Pollard (1964-65) and 2 from Roth and Raynal (1974).

Since any hardening effects from GP zones are non-existent in Al-Mg alloys aged at typically 200°C, any precipitation hardening in such alloys will necessarily be the product of intermediate metastable phases or equilibrium β phase. However, the intermediate metastable β' phase has been observed to nucleate heterogeneously at dislocations in relatively coarse distribution in the matrix phase during isothermal ageing treatments (Matsuura and Koda 1965, Bernole 1974). Furthermore, when particles of equilibrium β phase (Al_3Mg_2) were formed, it was common for a large number of dislocations to be generated around the precipitates during growth. This has been interpreted to imply a relatively large misfit with the aluminium matrix, and thus a large energy barrier to initial nucleation (Matsuura and Koda 1965). This too results in a coarse distribution and a low number density of the equilibrium β precipitate particles within the matrix (Perryman and Brook 1950-51). Due to mainly these reasons, the overall age-hardening response in Al-Mg alloys is sluggish and the precipitation hardening effects, from both intermediate and equilibrium phases, are limited compared to other heat-treatable Al alloys.

2.3.2 Precipitation Sequence(s)

The precipitation sequence in binary Al-Mg alloy (≥ 7%) was initially examined (Cordier and Detert 1961) using a combination of X-ray diffraction and measurements of electrical resistivity. These early studies suggested that the decomposition process of a supersaturated solid solution in Al-Mg alloys containing more than 7% Mg aged below the GP zone solvus might be summarised as follows:

Supersaturated solid solution (α') -----> α' + GP zones

-----> α' + β' phase -----> α + β phase.

(Mondolfo 1976, Lorimer 1978).

The detailed structure and composition of each of the product precipitate phases will be presented in Section 2.3.3.

In later work (Nozato and Ishihara 1980), the decomposition process of the supersaturated solid solution in the Al-Mg alloys containing 6.9%-11.4% Mg was suggested to involve four stages in samples aged below 50°C, which is below the GP zone solvus temperature. These results were based on detailed measurements of specific heat using differential scanning calorimetry (DSC) by Nozato and Ishihara (1980), who proposed a precipitation sequence that can be described as follows:

Supersaturated solid solution (α')

-----> α' + δ'' (short-range ordered Al_3Mg or AlMg) phase

-----> α' + δ' (long-range ordered Al_3Mg or AlMg) phase

-----> α' + β' phase -----> α' + β phase.

In comparison with the precipitation sequence initially accepted, this work effectively distinguished two forms of GP zone (viz. two types of ordered Al_3Mg (or AlMg) phases). A similar precipitation sequence was subsequently proposed by Osamura and Ogura (1984), who reported that when Al-Mg alloys with 9.8% and 13.5% Mg were aged at near room temperature, nucleation of GP zones occurred during the early stages of the decomposition process, and that they were replaced by a β'' phase with an ordered $L1_2$ structure. It was suggested that the δ'' (short-range ordered Al_3Mg or AlMg) phase previously reported may in fact correspond to GP zones, while that designated δ' (long-range ordered Al_3Mg or AlMg) was an intermediate phase with ordered $L1_2$ structure. More recent studies (Nebti et al. 1995, Starink and Zahra 1997) using DSC have tended to confirm that the decomposition process of supersaturated solid solution in the Al-Mg alloys with 11%-16% Mg aged at 20°C is consistent with the results of Osamura and Ogura (1984), and is as shown below:

Supersaturated solid solution (α')

-----> α' + GP zones -----> α' + β'' (Al_3Mg) phase

-----> α' + β' (Al_3Mg_2) phase -----> α + β (Al_3Mg_2) phase.

The approximate formation and dissolution temperatures of the various phases within alloys in this composition range have also been determined to be as follows: formation of GP zones (0°C) and β'' phase (45°C); dissolution of GP zones and β'' (40°C-100°C); formation of β' phase (100°C) and β phase (250°C); and dissolution of β' and β phases (250°C-420°C).

In summary, to date the majority of experimental studies of the decomposition process in Al-Mg alloys (with typically more than 7% Mg) have been conducted using indirect (non-microscopic) techniques, such as DSC, and it has been recognised that the precipitation sequence in such alloys involves four stages, as briefly described above. However, detailed microstructural evidence to support the proposed precipitation sequence based on DSC results is limited. In order to confirm this precipitation sequence, the present work has thus involved detailed electron microscopy to characterise the age-hardening behaviour of Al-Mg alloys, aged in the temperature range 160°C to 240°C. This range of ageing temperatures for experimental alloys with 10% Mg, may not permit the formation of GP zones and β'' (Al_3Mg) phase. However, they were selected as a basis for comparison of the precipitation behaviour of similar alloys microalloyed with Ag.

The characteristics of each precipitation reaction product will now be reviewed and discussed briefly.

2.3.3 Precipitate Phases

GP Zones (Mg Rich Clusters) and Ordered β'' Phase

During ageing below the GP zone solvus in binary Al-Mg alloys, the first stage of precipitation involves formation of GP zones apparently homogeneously from the supersaturated solid solution. However, it has proven very difficult to obtain direct evidence experimentally for the formation of GP zones in Al-Mg alloys, using X-ray and electron diffraction techniques since the atomic numbers of Al and Mg are close, and it is difficult to distinguish the X-ray and electron diffraction patterns from Mg rich clusters and the aluminium matrix. The rate of decomposition is also extremely slow during isothermal ageing, which means that experiments are prolonged. As shown in Fig. 2.4 and described in Section 2.3.1, the solvus temperature for GP zone formation may be as low as 20°C (or below) depending upon the Mg concentration.

Despite such difficulties, a number of researchers have successfully obtained indirect evidence of the formation of GP zones using electrical resistivity measurements, examining alloys

with various Mg concentrations. Such measurements for a quenched Al-10% Mg alloy have revealed an increase in the electrical resistivity during isothermal ageing for 1000 h at temperatures ranging from -35°C to 50°C, and this phenomenon has been postulated to be associated with the formation of Mg-rich zones approximately 1.0 nm in diameter (Cordier and Detert 1961). Similarly, other electrical resistivity measurements carried out (Panseri et al. 1963) on alloys containing more than 1.5% Mg showed increasing resistivity during isothermal ageing in the range between -60°C and 30°C, and this was again considered to arise as a result of the formation of solute Mg clusters. However, alloys with less than 1.5% Mg exhibit decreased resistivity above 100°C due to the elimination of quenched-in vacancies. Using alternative experimental techniques, such as small-angle neutron scattering, evidence for the formation of clusters or GP zones has been obtained in a binary Al-Mg alloy with a solute concentration of 11.5% Mg aged 12 months at room temperature (Roth and Raynal 1974, Raynal and Roth 1975). These clusters or GP zones were unstable and dissolved back into solid solution when samples were annealed at 100°C. These experimental data thus suggest that the formation of GP zones certainly occurs during isothermal ageing heat treatments in the vicinity of room temperature in Al-Mg alloys with 1.5%-11.5% Mg. This range of ageing temperatures is significantly lower than those typical of commercial heat-treatable aluminium alloys.

Identification of the GP zone structure has been attempted using a combination of X-ray scattering, transmission electron microscopy (TEM) and electron diffraction. Initially, equiaxed zones with the Cu_3Au-type ordered structure were reported as a result of an electron diffraction study of an Al-12% Mg alloy aged at room temperature (Dauger et al. 1973). In contrast to this result, Bernole at al. (1973) observed directly using TEM coherent Mg-rich clusters with a tetragonal Al-Mg superlattice structure (lattice parameters a = 0.451 nm, c = 0.405 nm) in Al-10% Mg alloy aged 13 years at room temperature. However, applying a combination of TEM and X-ray small angle scattering techniques, Boudili et al. (1977) detected ordered GP zones with the $L1_2$ (Al_3Mg) superstructure in an alloy with 9.5% Mg, while an alloy with 14.8% Mg contained a structure modulated along $<100>_\alpha$ directions following isothermal ageing at 20°C. Gault et al. (1980), in addition, suggested that the existence of GP zones with the ordered $L1_2$ structure could be detected directly using TEM in an Al-11.9% Mg alloy aged 4000 h at 40°C. These existing results thus suggest that the GP zones have the ordered $L1_2$ structure, when formed during isothermal ageing at room temperature in Al-Mg alloys with typically 10% Mg.

In a series of studies of microstructural evolution during the very early stages of ageing in Al-10% Mg alloy aged 550 h at room temperature (Sato et al. 1982, Sato et al. 1984, Takahashi and Sato 1986, Sato and Kamio 1991), further detailed evidence was found of a modulated structure with Ashby-Brown contrast (Ashby and Brown 1963), which was aligned along the $<100>_\alpha$. This structure was observed to develop into spherical GP zones having the superlattice reflections of the $L1_2$ structure after a further 12 years ageing. In addition, the formation of the

$L1_2$ structure (Al_3Mg) was observed in Al-19.5% and 24.2% Mg alloys rapidly quenched from the melt and subsequently aged 20 min. and 40 min. at 100°C (Kumada et al. 1970). In contrast to these results, a recent study has suggested that GP zones are formed in Al-8% Mg alloys aged 12 years at room temperature and that these zones have the same crystal structure and lattice parameter as the matrix, and the cube-on-cube orientation relationship with the α-matrix (Bouchear et al. 1996).

In summary, based on these previously-reported results and the DSC results described in Section 2.3.2, it is widely accepted that the formation of GP zones with a modulated structure occurs in quenched Al-Mg alloys (with typically 10% Mg) naturally aged at room temperature. These GP zones are subsequently replaced by an ordered β'' (Al_3Mg) phase with the $L1_2$ structure during further prolonged ageing at room temperature. Some researchers (Sato et al. 1982, Sato et al. 1984, Kamio and Sato 1986, Sato and Kamio 1991) appear to consider GP zones and the ordered β'' (Al_3Mg) phase to be effectively the same constituent. However, the ordered β'' (Al_3Mg) phase has a distinguishable $L1_2$ crystal structure compared with the GP zones which have the same crystal structure as the aluminium matrix. It would thus seem appropriate for now to recognise that GP zones and the ordered β'' (Al_3Mg) phase are different transformation products. When these alloys are aged at typically 100°C, both the GP zones and the ordered β'' (Al_3Mg) phase are unstable and dissolve into the aluminium matrix.

β′ Phase

With increased ageing time, GP zones and/or the ordered β'' (Al_3Mg) phase decompose to be replaced by the metastable β' (Al_3Mg_2) phase. It is generally accepted that the intermediate β' phase in Al-Mg alloys has a hexagonal structure (lattice parameters, a = 1.002 nm, c = 1.636 nm) and is semi-coherent with the aluminium matrix (Bernole et al. 1969, Bernole 1974, Mondolfo 1976). Recently, apparently significant variations in the lattice dimensions of the precipitate β' phase have been reported. One such result describes a hexagonal structure with lattice parameters a = 1.03 nm, c = 1.68 nm in Al-2.46% Mg alloy, while a second reports lattice parameters a = 1.12 nm, c = 1.64 nm in Al-11.07% Mg alloy (Fei and Kang 1996). Although the latter defined the phase as β_2, it seems likely that it is in fact the phase more commonly referred to as β'. The source of the variation in lattice parameters has not been identified, but it may be related to solute content, defect structure or departures from stoichiometry in the intermetallic phase.

The maximum hardness of aged Al-Mg alloys is commonly associated with the presence of the β' phase. It has been claimed that the nucleation of the intermediate β' phase occurs heterogeneously on dislocation loops (Embury and Nicholson 1963, Bernole et al. 1969), but there have also been reports that the β' phase may form independently of defects (Eikum and Thomas 1964, Suzuki et al. 1978). The formation of irregular plates of the β' phase was first reported in an Al-12% Mg alloy aged at 120°C; they were formed on the $\{100\}_\alpha$ planes (Saulnier

and Mirand 1960). Following ageing for 20 h at 200°C or 5 h at 250°C, irregular plates up to 0.5 μm in thickness were observed on the $\{100\}_\alpha$ planes. The plates were normally oval-shaped and elongated along $<100>_\alpha$ directions. Typical morphologies of the intermediate β' phase were summarised as plate shapes on $\{100\}_\alpha$, $\{111\}_\alpha$, $\{210\}_\alpha$ and $\{310\}_\alpha$ planes when the specimens were aged at 150°C, and rod-like particles with long axes parallel to $<100>_\alpha$, $<110>_\alpha$, $<120>_\alpha$ and $<111>_\alpha$ when specimens were aged at 200°C (Matsuura and Koda 1965, Mondolfo 1976).

The orientation relationship between plate-like β' phase and the matrix has been reported to be of the form: $(0001)_{\beta'} \parallel (001)_\alpha$ and $[2\bar{1}\bar{3}0]_{\beta'} \parallel [110]_\alpha$ (Bernole et al. 1969). A second orientation relationship between plate-like β' phase and the matrix has been reported to have the form: $(0001)_{\beta'} \parallel (001)_\alpha$ and $[01\bar{1}0]_{\beta'} \parallel [110]_\alpha$ (Bernole 1974).

β Phase

Prolong ageing, at temperatures approaching the equilibrium solvus, may lead to the formation of the equilibrium β (Al_3Mg_2) phase. The existence of the equilibrium β phase (Al_3Mg_2) in the aged Al-Mg alloy was initially established on the basis of powder X-ray diffraction studies and the crystal structure was determined to be hexagonal with the lattice parameters of a = 1.12 nm, c = 1.60 nm (Riederer 1936, Laves and Moeller 1938). Supporting evidence for this crystal structure of the β phase was subsequently obtained using transmission electron microscopy of Al-8% and 10% Mg alloys aged at 150°C-300°C (Feller-Kniepmeier et al. 1964). However, in early work using the Laue X-ray diffraction method equilibrium β phase was described as having a f.c.c. structure with the lattice parameter a = 2.8285 nm (Perlitz 1944). Later, a phase with a similar f.c.c. crystal structure, but with a lattice parameter (a = 0.471 nm) equal to 1/6th of that reported by Perlitz (1944), was reported in aged Al-7-10% Mg alloys (Trehan 1969). More recently, precipitates of β phase (identified as β_1) have been reported with a f.c.c. structure and a lattice parameter of a = 1.20 nm in Al-2.46% and 11.07% Mg alloys (Fei and Kang 1996). There thus remains some uncertainty regarding the structure of the equilibrium β phase (Al_3Mg_2) in aged Al-Mg alloys, but it is perhaps most commonly assumed to be of face-centred cubic structure with a lattice parameter of 2.824 nm (Perlitz 1944, Samson 1965, Bernole et al. 1969).

The nucleation sites and morphologies of the β phase (Al_3Mg_2) have been studied by a number of researchers. It has been reported that the β phase is formed preferentially at grain boundaries and at the interphase boundaries of particles of β' phase formed within matrix grains, as well as on dislocations (Bernole et al. 1969, Bernole 1974, Bouchear et al. 1996). The choice of preferred nucleation sites is generally governed by the need to reduce the interfacial energy. Two morphologies of the equilibrium β phase have been observed in an Al-10% Mg alloy. One takes the form of blocky, faceted particles observed after typically 96 h at 200°C, and the other is globular particles (after typically 0.5 h at 300°C) (Bernole et al. 1969). Plate- and lath-shaped

particles have also been reported in Al-10% Mg alloy aged 2 h at 300°C (Bernole 1974). In more recent work, blocky particles of equilibrium β phase were reported in Al-9% Mg alloy aged 5 h at 250°C. These particles were formed preferentially at the interfaces between intermediate β' particles and the aluminium matrix. The observations were made using transmission electron microscopy, although no electron diffraction patterns were provided to support identification of the phases (Bouchear et al. 1996).

Two distinguishable orientation relationships between the precipitate β phase and the α-Al matrix have been proposed. Bernole et al. (1969) first reported a relationship of the form: $[001]_\beta \parallel [001]_\alpha$ and $[110]_\beta \parallel [100]_\alpha$ in Al-10% Mg alloy aged at 200°C and 300°C. However, in a later study, they reported a second orientation relationship of the form: $(111)_\beta \parallel (001)_\alpha$ and $[110]_\beta \parallel [010]_\alpha$ (Bernole 1974). Recently, new orientation relationships have been proposed by Fei and Kang (1996), who studied the precipitates in T4-treated Al-Mg alloys with 2.46% Mg and 11.07% Mg, which were heat treated 0.5 h at 150°C in air, then water quenched. The orientation relationship between what they defined as β_1 phase and the α-Al matrix was given by $\{133\}_{\beta 1} \parallel \{200\}_\alpha$ and $<011>_{\beta 1} \parallel <013>_\alpha$. The f.c.c. β_1 phase precipitates were also observed in an Al-11.07% Mg, and the orientation relationship between the two phases was of the form: $\{131\}_{\beta 1} \parallel \{131\}_\alpha$ and $<114>_{\beta 1} \parallel <310>_\alpha$.

In summary, descriptions of the form(s) and crystal structure of the equilibrium β phase, and the orientation relationships between the equilibrium β phase and the aluminium matrix, are as yet incomplete, partly because each existing study has used different alloy compositions, heat treatment schedules and characterisation techniques. Therefore, a systematic study remains necessary to establish the crystal structure of the equilibrium phase, the orientation relationship(s) with the matrix and the possible precipitate forms.

2.3.4 Summary

All of the above studies have focused on precipitation behaviour in alloy samples aged in the temperature range from sub-ambient (20°C) to approximately 150°C, because of the nature of this alloy system. Especially in those alloys aged naturally (20°C), there are practical disadvantages since it takes extremely long ageing times to obtain precipitation hardening and anything approaching useful mechanical properties. The rate of the decomposition process in supersaturated binary solid solution is extremely slow. Microstructural evolution during the relatively high temperature (160°C to 240°C) ageing treatments, which are potentially very important for industrial applications, has not been well studied. In addition, major experimental results previously reported, particularly with regarding to the precipitation sequence, have been obtained mainly from non-direct observations such as DSC, electrical resistivity measurements and neutron scattering experiments. In order to improve fundamental understanding of the ageing

behaviour in Al-Mg alloys, the main focus of the present work has thus been on ageing temperatures typically in the range 160°C-240°C, and on the use of a direct, high resolution characterisation technique in the form of transmission electron microscopy.

2.4 Effects of Microalloying Additions on Precipitation in Al Alloys

Trace additions (typically 0-0.5%) of a range of specific elements are known to modify the precipitation process, including the nucleation and growth characteristics of individual precipitate phases, in binary aluminium alloys during the isothermal ageing process. In general terms, the effects commonly observed to arise from microalloying additions can be summarised as follows:

(1) Trace additions of a third element may change the precipitation characteristics by promoting the formation of existing metastable or equilibrium precipitates. A typical example of this case is where trace additions of In, Cd or Sn stimulate the nucleation of the intermediate phase θ' in binary Al-Cu alloys, leading to refined precipitate distributions and improved resistance to plastic deformation (Kanno et al. 1979).

(2) Trace additions of a third element may alternatively stimulate nucleation of a new (metastable) phase. A typical example here involves microalloying additions of Ag to ternary Al-Cu-Mg alloys with higher Cu:Mg ratios (15:1). In Ag-modified alloys a metastable Ω phase is induced to form as thin, hexagonal plates on $\{111\}_\alpha$ planes of α-Al matrix in place of the intermediate θ' phase which forms on $\{100\}_\alpha$ planes in binary Al-Cu alloys and Al-Cu-Mg alloys of similar composition (Chester and Polmear 1983).

Previous studies (Polmear 1987) have indicated that most effects due to microalloying additions to aluminium alloys belong to the former category (1). It has been suggested that, in this case, the role of the microalloying element may either be: (i) to effectively raise the solvus temperature and thus, for a given ageing temperature, effectively increase the degree of undercooling achieved, or (ii) clustering to provide preferential nucleation sites for precipitate phases, or (iii) segregating to the precipitate-matrix interface to reduce the energy barrier to nucleation. In each case, the result is an increased nucleation rate and a refined, more uniform distribution of precipitate particles.

Rather than attempt a complete review of the roles of microalloying elements on precipitation in aluminium, the following sub-sections contain brief summaries of behaviour in two systems selected to be representative of examples of cases (1) and (2) above. These two examples provide useful background information for the present study of the effects of trace element Ag on precipitation in Al-Mg alloys.

2.4.1 Microalloying Additions of In, Cd and Sn to Al-Cu Alloys

Minor additions of In, Cd or Sn (0.05 - 0.1%) have been shown to have two distinct effects in modifying the precipitation hardening process in Al-Cu alloys (Hardy 1951-52). One is that the formation of GP zones is suppressed during room temperature or natural ageing. The other is that the nucleation of the θ' phase is accelerated at higher ageing temperatures.

For the former case, Hardy (1951-52, 1955-56) has suggested that the relatively large atom diameter of these trace elements means that they act as traps for smaller solute atoms to reduce the strain energy caused by the difference in the atomic volumes of the trace elements and the aluminium. Such interactions thus decrease significantly the number of Cu atoms which are freely available in solid solution for the formation of GP zones. However, Entwistle and Perry (1966) subsequently recognised that there is a strong binding energy between such elements and vacancies, and that such atoms will trap vacancies in solid solution and diminish the vacancy population available to accelerate the diffusion rate of Cu atoms required for GP zone formation at room temperature. These elements thus suppress the formation of GP zones at low ageing temperatures. Further confirmation of a strong binding energy between these trace elements and vacancies was subsequently obtained by Perry and Entwistle (1968).

For the latter case, it has been suggested that these elements promote the formation of dislocation loops during the initial stages of ageing and that these loops become preferential nucleation sites for the intermediate θ' phase during isothermal ageing (Van Nuyten 1967). However, there is no direct evidence to support this. A second proposal is that the trace elements may localised at the interfaces of nucleating θ' platelets, lowering the interfacial energy and thus the energy barrier to nucleation (Silcock et al. 1955-56). However, again modern microstructural characterisation has failed to provide evidence supporting this suggestion. More recently, microstructural observations by TEM have revealed that, in supersaturated Al-Cu-In alloys, very fine In particles are precipitated from solid solution during the initial stages of ageing (1 min. at 200°C), and that these elemental particles become sites for heterogeneous nucleation of the intermediate θ' phase (Kanno et al. 1980). Similarly, TEM combined with EDXS analyses have revealed formation of elemental Sn particles in Al-Cu-Sn alloys, with the uniform distribution of Sn precipitates providing sites for the development of a fine, uniform distribution of θ' phase (Kanno et al. 1979).

Using a combination of atom probe field ion microscopy (APFIM) and transmission electron microscopy (TEM), further detailed evidence for nucleation of independent clusters of Sn atoms (particles), that precede the formation of intermediate θ' phase, was observed in supersaturated solid solution of an Al-4% Cu-0.05% Sn alloy during very early stages of ageing (Ringer et al. 1995). It demonstrated clearly that the Sn particles act as nucleation sites for the θ'

phase, resulting in both a fine-scale, uniform distribution and an enhanced nucleation rate. Apart from these direct observations by TEM and/or APFIM, Nie et al. (1999) and Gao et al. (1999) have proposed a detailed mechanism(s) by which such elements, present as clusters or pre-existing precipitate particles, facilitate the nucleation of θ' phase, based primarily on the accommodation of shear strain energy associated with the formation of θ' phase. Rather than focus on the volumetric misfit or interfacial energy barriers to nucleation, this model suggests that clusters of Sn atoms combined with vacancies provide an environment in which the shear strain associated with formation of a critical nucleus of θ' may be accommodated.

2.4.2 Microalloying Additions of Ag to Al-Cu-Mg Alloys

It is well-established (Polmear 1964 and 1968) that additions of small amounts of Ag (0.5%) to Al alloys containing Mg have significant effects on the precipitation reactions in such alloys, especially in Al-Cu-Mg based alloys with higher Cu:Mg ratios (15:1). The precipitation hardening response is accelerated and significantly enhanced by trace additions of Ag to such alloys, and the precipitation sequence is changed significantly. In the ternary alloys with higher Cu:Mg ratios, the main contributions to the age-hardening response are from GP(B) zones and S phase. However, the formation of a new metastable phase, designated Ω (Chester and Polmear 1983, Knowles and Stobbs 1988, Muddle and Polmear 1989) has been observed to be the source of the age-hardening response in Al-Cu-Mg-Ag alloys of equivalent Cu:Mg ratio. The Ω phase forms as thin, hexagonal plates of large aspect ratio on $\{111\}_\alpha$ planes of α-Al matrix solid solution.

Recent studies using atom probe field ion microscopy (APFIM) have advanced understanding of the formation of this metastable phase in Al-4% Cu-0.3% Mg-0.4% Ag alloys. Hono et al. (1993) initially showed evidence of the segregation of Mg and Ag atoms to the planar, coherent precipitate Ω/matrix α interfaces of these thin $\{111\}_\alpha$ precipitate plates. Further detailed study using APFIM has suggested that Ag atoms effectively trap Mg atoms during the very early stages of solid solution decomposition, resulting in the formation of Ag-Mg co-clusters, which act as favourable nucleation sites, and thus accelerate nucleation rates for the thin, hexagonal plates of the Ω phase (Ringer et al. 1996). Clear inspection of the mechanism by which the Ω phase evolves from the Ω solute clusters, using three-dimensional atom probe field ion microscopy (3D-APFIM), has revealed (Murayama and Hono 1998) that the Ag and Mg atoms form co-clusters typically involving ~40-80 atoms during some 15 s of ageing at 180°C. These initially diffuse co-clusters assume a platelet configuration parallel to $\{111\}_\alpha$ planes as ageing progresses and Cu atoms begin to participate in the clustering process. With further ageing, platelets of the Ω phase emerge with Ag and Mg atoms segregated to the coherent planer interfaces that are parallel to $\{111\}_\alpha$.

In contrast, in ternary Al-Cu-Mg alloys with lower Cu:Mg ratios (1:4), the main contributions to age-hardening arise from the formation of GPB zones and T phase. The presence of trace concentrations of Ag in the alloys modifies the precipitation behaviour by retarding the formation of GPB zones and promoting the strengthening metastable T phase (Vietz and Polmear 1966). A recent study using TEM with electron diffraction has revealed that microalloying additions of Ag to such alloys can lead to formation of a new metastable phase, designated Z, (f.c.c., lattice parameter, a = 1.999 nm) (Chopra et al. 1996), and an APFIM study (Ringer et al. 1998) has revealed that the composition of this phase includes the four principal elements with 50-65at% Al, 20at% Cu and 20-25at% Mg, plus Ag. However, compared to ternary Al-Cu-Mg alloys with higher Cu:Mg ratios, the microstructural characterisation of such alloys has remained limited, due to the lower maximum hardness achievable in ternary Al-Cu-Mg alloys with lower Cu:Mg ratios.

2.4.3 Effects of Ag on Precipitation in Al Alloys

Alloys based on the Al-Zn-Mg system have been widely used as structural components in aerospace applications, because for a lengthy period such alloys exhibited the greatest age-hardening response of all age-hardenable aluminium alloys (Mondolfo 1976). It has been reported that microalloying additions of Ag to Al-Zn-Mg alloys are beneficial in both increasing tensile properties and decreasing susceptibility to stress corrosion cracking (SCC) (Polmear 1960). However, quench sensitivity is increased in the presence of Cr, Mn or Zr which are generally added to inhibit recrystallization in Al-Zn-Mg alloys (Polmear 1972).

Small additions of Ag were observed to enhance the age-hardening response in ternary Al-4% Zn-3% Mg alloy aged at 150°C, and following microstructural observations using TEM, this enhanced precipitation hardening response was attributed to the Ag stimulating the formation of the intermediate phase η' ($MgZn_2$, a = 0.496 nm, c = 0.868 nm), to produce a fine-scale, uniform precipitate distribution (Vietz et al 1963-64). In addition, the small concentrations of Ag were demonstrated to be effective in minimising or eliminating the precipitate-free zone (PFZ) at grain boundaries in samples aged at high ageing temperatures (Vietz et al. 1963-64). This treatment was effective in reducing the susceptibility to stress corrosion cracking.

Parker (1972) also studied the enhanced the precipitation hardening response in Al-4% Zn-3% Mg alloy during isothermal ageing, and his results showed that the presence of Ag also modified the formation of GP zones, with the position of the GP zone solvus being raised from the range of 120°C-140°C to ~200°C. These two effects arising from microalloying additions of Ag account for the finely-dispersed intermediate η' precipitate particles and the enhanced age-hardening response. However, the precise mechanism by which the range of stability of GP zones is increased by the presence of trace amounts of Ag is uncertain. There is a strong binding

energy between Ag atoms and vacancies and it is commonly speculated that Ag traps vacancies in solid solution to preserve a capability for solute transport.

There have been many studies of precipitation hardening behaviour in this alloy system with and without trace additions of Ag. However, the fine-scale of precipitate particles has long made it difficult to determine reliable crystallographic information. A recent study using TEM, including electron diffraction techniques, has confirmed that microalloying additions of Ag to an Al-4% Zn-3% Mg alloy produces an enhanced number density of refined precipitate particles of the intermediate η' phase, and not the formation of any new intermediate phases (Caraher et al. 1998). Further detailed observations using three dimensional atom field ion microscopy (3D-APFIM) have shown that the clustering of Ag atoms with Mg and Zn atoms occurs during the very early stages of ageing at 150°C, and that Ag atoms are partitioned into the intermediate η' phase in the Al-4% Zn-3% Mg alloy (Caraher et al. 1998).

2.5 Effects of Trace Elements on Precipitation in Al-Mg Alloys

Compared to the common heat-treatable aluminium alloys, particularly Al-Cu alloys containing Mg, little experimental work has been done on the effects of microalloying additions of third elements on the microstructure and properties of binary Al-Mg alloys, and the role of such microalloying elements is thus poorly understood. However, it is known that minor additions of Ag, Cd, Sn and In can greatly influence the ageing characteristics in aluminium alloys containing magnesium (Kelly and Nicholson 1963). The first attempt to characterise the effects of such trace additions in binary Al-Mg alloy was made by Polmear and his co-worker in the early 1960s (Polmear and Sargant 1963, Polmear 1964). Detailed review of these papers will be described in the following Section 2.6. Apart from Polmear's work, Kievits and Zuithoff (1964) examined the influence of Cd and Ag additions on the ageing characteristics of Al-10% Mg alloys aged at 150°C. Their results showed that the isothermal precipitation process was greatly accelerated by the addition of 0.2% Ag, but not by addition of 0.2% Cd alone. Interestingly, the combined addition of these two elements delivered the most significant boost to the age-hardening response. However, no detailed microscopic evidence was provided to support such promising results, and no detailed explanation was offered for the enhanced ageing response.

A second example of the effects of microalloying on the age-hardening response is the work of Baba (1972), who investigated the effects of small additions of elements, such as Cr, Zr, Fe, V, Ag, Be, Cd, In, Si, Ge, Sn and Cu, on the ageing characteristics of binary Al-Mg alloys with 1.5, 5 and 9at% Mg using measurements of electrical resistivity and hardness. The rate of the age-hardening response, attributed to precipitation of β' and β phases in the Al-9at% Mg alloy, quenched from 400°C and aged at 130°C, could be increased by the addition of 0.1at% of each of

the elements Cr, V, Fe, Zr, Ag, Cd, In or Be, but was decreased slightly in the presence of 0.1at% Cu. In addition, trace additions of 0.1at% Ag or Be not only accelerated the age-hardening response, but also enhanced the maximum hardness when the Al-9at% Mg alloy was aged at 200°C. The addition of 0.1 at% Si, Ge or Sn to Al-1.5, 5 and 9at% Mg alloys, quenched from 450°C and subjected to isochronal ageing, showed no significant effect in Al-Mg alloys containing more than 5at% Mg.

More recently, there has been a report of the effects of small additions of Cu and/or Zn on the age-hardening response in an Al-9% Mg alloy (Yukawa et al. 1995). It was found that the precipitation hardening response was enhanced by trace additions of 0.3% Cu and 0.3% Zn independently during isothermal ageing at 200°C. It was concluded that, in order to achieve the maximum hardness in such an alloy, small concentrations of Cu were more effective than small amounts of Zn. Ageing curves for Al-Mg-Cu, Al-Mg-Zn and Al-Mg-Cu-Zn alloys of similar compositions were quite similar, which implies that trace amounts of Cu and/or Zn increase the maximum hardness, but do not accelerate the time to reach maximum hardness. Limited microstructural observations have suggested that trace additions of Cu or Zn in Al-9% Mg alloys aged at 200°C produce as major modifications to the precipitate microstructures, compared to the binary alloy. However, no detailed characterisation of precipitate particles (using electron diffraction) and precipitation sequences in these alloys have been reported (Yukawa et al. 1995).

In recent studies, the effects of small additions of Cu (0.6-1.0%) to Al-Mg alloys have been explored, in pursuit of improved mechanical properties, including the inhibition of Lüder's bands and improved sheet formability for automotive applications (Ratchev et al. 1994 and 1998). The small additions of Cu in Al-4% Mg changed significantly their precipitation behaviour, with the precipitation sequences comparable to those in Al-Cu-Mg alloys with lower Cu:Mg ratios rather than those of Al-Mg alloys (see sub-Section 2.3.2) (Ratchev et al. 1994 and 1998). The precipitation sequence thus reported was as follows:

Supersaturated solid solution (α') -----> α' + GPB zones

-----> α' + S' phase -----> α + S phase.

It was reported that GP zone formation was not detectable, even after 15 months of natural ageing, in Cu-containing alloys, and this was attributed to the effect of the high concentrations of Mg in these alloys. When the ageing temperature was increased to 142°C, the formation of GP zones occurred during the early stages of ageing, and S' phase was formed at ageing temperatures in the range 177°C - 347°C.

2.6 Precipitation Characteristics of Al-Mg-Ag Alloys

As described in Section 2.4, it is well established that trace additions of Ag (0.4%) stimulate precipitation behaviour in all Al alloys containing Mg, with an acceleration in the kinetics of the age-hardening response and an increase in the maximum hardness achievable (Polmear 1964 and 1968). As demonstrated in Section 2.5, trace additions of Ag to non-heat treatable Al-Mg alloys represent perhaps the most promising prospect for introducing or enhancing an age-hardening response.

The aluminium-rich corner of the ternary Al-Mg-Ag phase diagram has been investigated, principally using X-ray diffraction techniques (Williams 1972), and the potential precipitate phases, when the alloys are aged at 200°C and 500°C, have been established, as shown in Figure 2.5. The phases detected and identified are as follows: the β phase (Al_3Mg_2), T phase ($Mg_{32}(Al,Ag)_{49}$), η phase (MgAgAl), β' phase (AgMg(Al)) and ζ phase (Ag_2Al). Crystal structures, lattice dimensions and compositions of these phases are listed in Table 2.1. Of these five intermetallic phases, only the ternary T phase would be expected to form as the equilibrium phase in those alloys with 5% - 10% Mg and 0.5% Ag when aged at 200°C, according to this ternary Al-Mg-Ag phase diagram (Williams 1972). These compositions represent the range relevant to the present research.

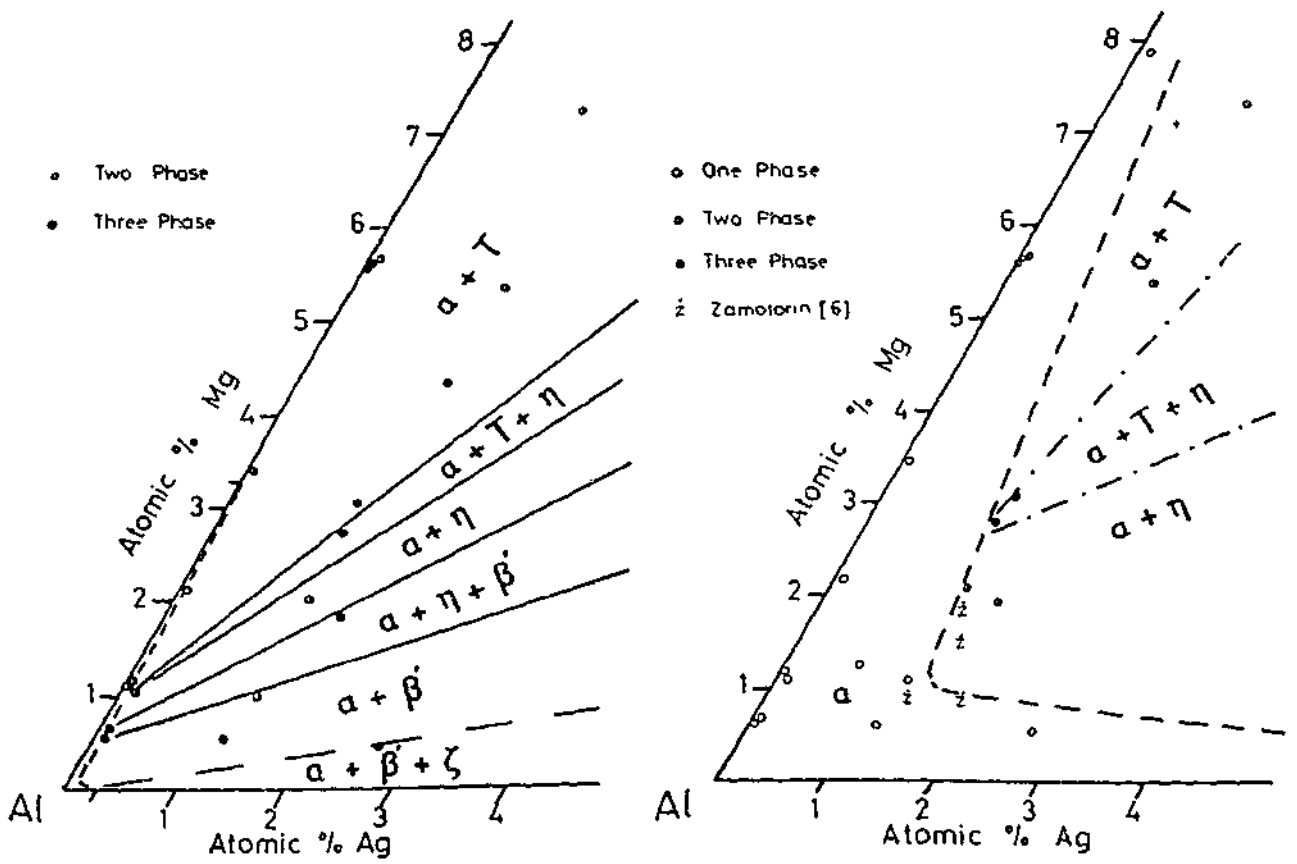

Figure 2.5 Isothermal sections of the Al-rich corner of the ternary Al-Mg-Ag alloy phase diagram at (a) 200°C and (b) 500°C.

Table 2.1 Summary of potential phases in Al-Mg-Ag alloys aged at 200°C and 500°C (Williams 1972).

Phase	Compositions	Crystal structure	Lattice parameter(s)
β phase	Mg_2Al_3	f.c.c.	a = 2.82 nm
T phase	$Mg_{32}(Al,Ag)_{49}$	b.c.c.	a = 1.45 nm
η phase	MgAgAl	h.c.p.	a = 0.538 nm
			c = 0.874 nm
β' phase	AgMg(Al)	orderd, CsCl-type	a = 0.323 nm
ζ phase	Ag_2Al	h.c.p.	a = 0.288 nm
			c = 0.458 nm

2.6.1 Precipitation Hardening Response

The first recorded experimental work on Ag-modified alloys (Polmear and Sargant 1963, Polmear 1964) was to explore the effects of microalloying additions of Ag to Al-5% Mg alloys in which it was commonly accepted (Section 2.3.1) that there was little or no age-hardening response. In broad terms, the effect of adding Ag was to induce a significant ageing response where none existed in the binary alloy. In the case of alloys of higher Mg content, e.g. 10% Mg, the very modest age-hardening response of the binary alloys was remarkably improved by microalloying additions of Ag. An example of these effects is shown in Figure 2.6, where typical age-hardening curves for Al-5% Mg and Al-10% Mg alloys (with and without 0.5% Ag) at 200°C are recorded. Polmear and Sargant (1963) observed that the remarkably enhanced precipitation hardening responses in the Ag-containing alloys were due to the very finely-distributed precipitate particles promoted by small concentrations of Ag.

The effect of different heat treatment schedules on the precipitation hardening response in Al-6% Mg-0.5% Ag alloy has been investigated (Ito et al. 1969a), and it has been suggested that the precipitation behaviour changes significantly at ageing temperatures above and below 200°C due to changes from heterogeneous to homogeneous nucleation of precipitates. When the alloy was aged below 200°C, the microstructure contained fine and homogeneous distributions of fine-scale precipitates. However, when the alloy was aged above 200°C, the microstructures exhibited coarser and inhomogeneous distributions of precipitates. In addition, when samples were direct-quenched to an ageing temperature above 200°C, the precipitates were mainly formed on dislocation lines during the early stage of ageing and only a coarse distribution of precipitate particles was observed after prolonged ageing. However, in direct-quenched samples aged below 200°C, the precipitate distributions were fine-scale and homogeneous and similar to those microstructures observed in those samples water-quenched and then aged isothermally. The identity of the precipitate phases nucleated homogeneously or heterogeneously was not

established, but it was speculated that hardening might be attributable to GP zones and/or the equilibrium T phase.

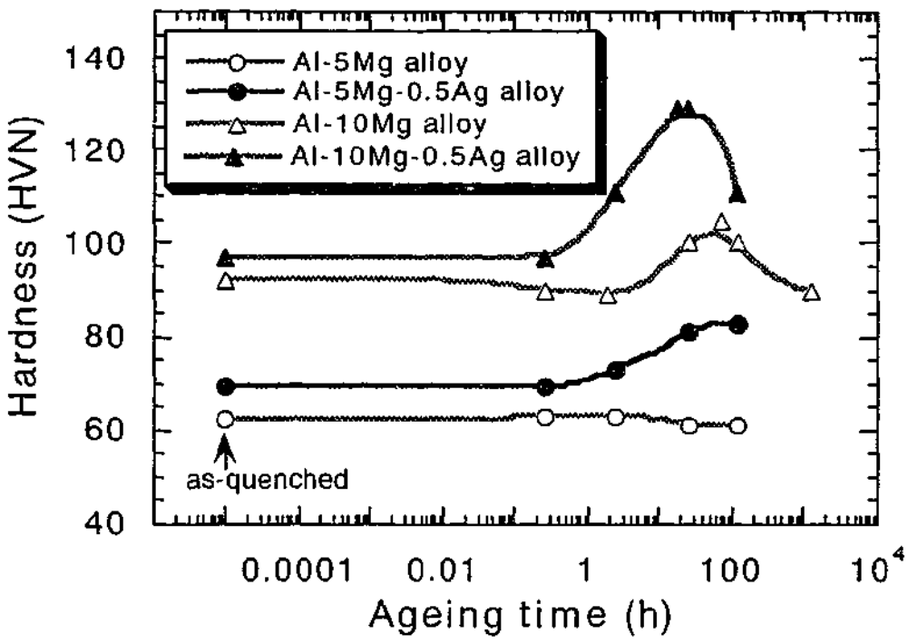

Figure 2.6 Age-hardening curves for Al-5% Mg and Al-10%Mg alloys, with and without trace additions of Ag, at 200°C (Polmear and Sargant 1963, Polmear 1995).

In a further study (Takahashi et al. 1978), a remarkable increase was observed in the hardness of a ternary Al-10% Mg-0.5% Ag alloy and attributed to the role of Ag in promoting formation of a fine-scale and homogeneous distribution of intermediate phases. However, once again no clear microstructural evidence was presented to identify the precipitate phase(s) and establish that they were indeed metastable.

A variety of explanations for the enhanced age-hardening response has emerged from studies on the effects of microalloying additions of Ag in Al-Mg alloys. It was first suggested that the effect of Ag was to accelerate the nucleation rate and refine significantly the distribution of the existing β' or β precipitates, and that this refinement of the precipitate distribution was the source of the increase in observed hardness (Polmear and Sargant 1963). However, it was subsequently proposed (Wheeler et al. 1965) that peak hardness in ternary Al-Mg-Ag alloy could be associated with fine-scale precipitates of a ternary T phase, $Mg_{32}(Al,Ag)_{49}$ (Bergman et al. 1957), rather than precipitation of the equilibrium β phase, Al_3Mg_2 (Perlitz 1944, Samson 1965). The Al-Mg alloys with trace additions of silver were thus to be regarded as ternary precipitation hardening alloys. Later work seemed to confirm the proposal that the age-hardening response in Al-Mg-Ag alloys was associated with the equilibrium T phase at maximum hardness, although maximum hardness was attributed to a metastable T' phase in some X-ray diffraction studies

(Auld and Cousland 1976, Cousland and Tate 1986), and the equilibrium T phase was suggested to form after longer term ageing (Cousland and Tate 1986).

Independently, it has been reported (Ito et al. 1969b and 1971) that the solubility of magnesium in aluminium is decreased significantly by the addition of 0.5% Ag, with the solvus curve in Al-rich alloys shifted to lower Mg contents and an appreciably higher temperature range when compared to the equilibrium curve for binary Al-Mg alloys, Figure 2.7. If such results are sustainable, they would suggest that the improvement in the age-hardening response by the trace additions of Ag could be partly associated with an effective increase in the degree of solute supersaturation during precipitation of the equilibrium T phase, and thus an increase in nucleation rate for a given ageing temperature. There is apparently good agreement between the initial work of Ito et al. (1969b and 1971) and that of Takahashi et al. (1978) with regard to the solvus temperatures for alloys containing 0.5% Ag. The increase in solvus temperature in Ag-containing alloys is typically 100°C for alloy compositions of interest (i.e. Al-(5-10wt%) Mg).

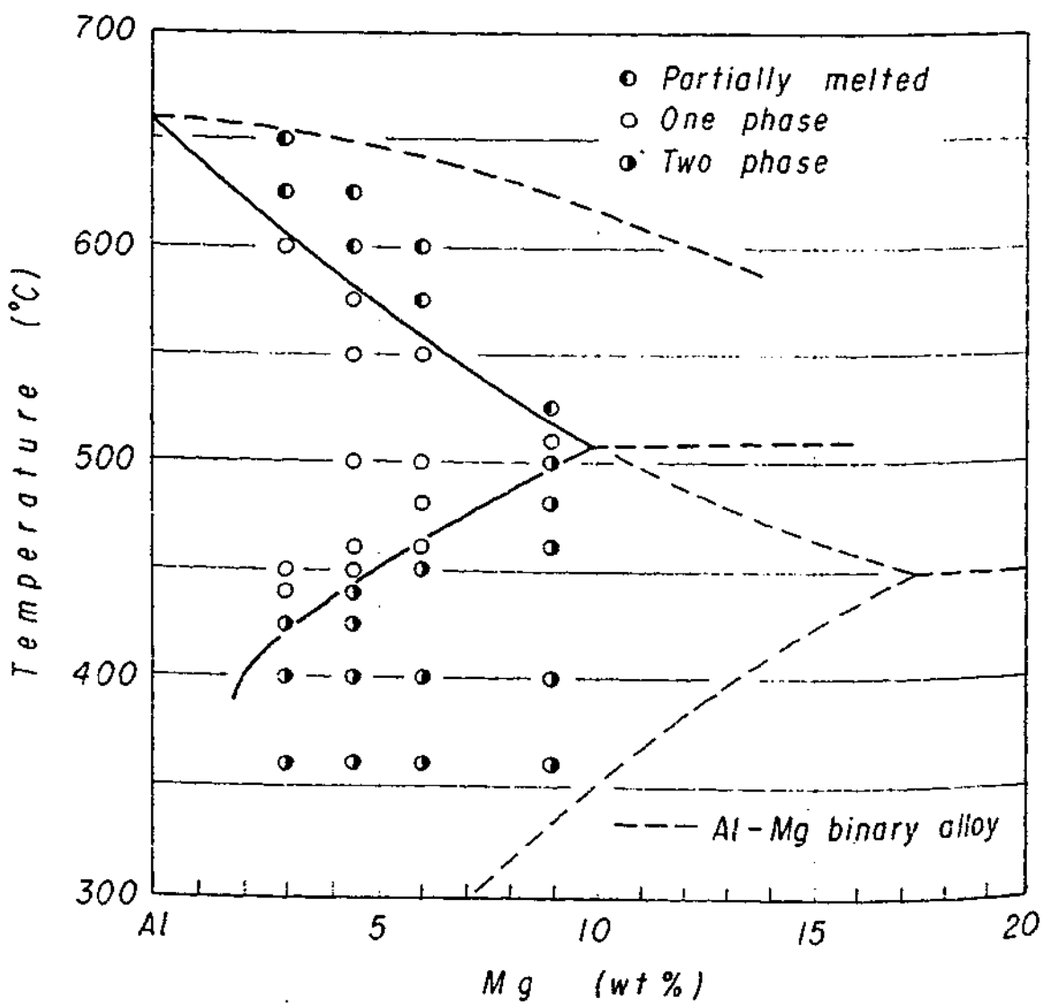

Figure 2.7 A section of the Al-rich corner of the ternary Al-Mg-Ag alloy phase diagram, together with the binary Al-Mg alloy phase diagram.

2.6.2 Precipitation Sequence and Precipitate Phases

The precipitation sequence during isothermal ageing of ternary Al-Mg-Ag alloys has only ever been investigated via X-ray diffraction studies (Auld 1968, Auld and Cousland 1976, Cousland and Tate 1986). Based on such studies, it has been suggested that the decomposition process for a supersaturated solid solution in Al - 4-5.7% Mg - 0.5-2.1% Ag alloys aged below the GP zone solvus can be expressed as follows:

Supersaturated solid solution (α') -----> α' + GP zones

-----> α' + T' phase -----> α + T phase.

The following discussion summarises briefly details of each of the transformation products formed during the isothermal ageing process.

GP Zones

That ternary Al-Mg-Ag alloys are age-hardenable by coherent spheroidal GP zones, was first established using the single crystal X-ray diffraction method (Auld 1968). Approximately spherical Mg-Ag zones, having the AuCu I type structure, were formed in Al-5% Mg alloys with 0.5% and 1% Ag during early stages of ageing at 120°C, 150°C and 175°C after quenching from 460°C. These zones were initially coherent with the matrix during early stages of ageing, but with further ageing, their tetragonality increased, mainly due to a decrease in spacing along the *c*-axis. The orientation relationship between the zones and α aluminium matrix was reported to be of the form $(101)_{zone} \parallel (110)_{\alpha}$ and $[010]_{zone} \parallel [001]_{\alpha}$ (Auld 1968). The lattice parameters of the zones were a = 0.442 nm, c = 0.348 nm, and an average diameter of these zones was at least 0.6 nm. In addition, no sign of the formation of GP zones was observed during early stages of ageing, when the Al-5% Mg-0.5% Ag alloy was aged isothermally at 200°C, suggesting that the GP zones are thermodynamically unstable at this temperature and that the GP zone solvus temperature is somewhere between 175°C and 200°C at 5% Mg. The formation of GP zones was studied using measurements of electrical resistivity in an Al-10% Mg-0.5% Ag alloy, and evidence of an electrical resistivity increase attributable to the formation of GP zones was detectable at ageing temperatures up to 100°C, indicating that GP zones are formed and stable at least up to this temperature range (Takahashi et al. 1978).

Two different types of GP zones have been reported in Al-Mg-Ag alloys with higher Ag:Mg ratios (Cousland and Tate 1986). Those GP zones described as type 1 were observed in an alloy of composition Al-4.0% Mg-2.1% Ag which lies in the (α+T) phase field, Fig. 2.5. Samples were aged 27.8 h to 11.5 days at 120°C, and 2.8 h to 27.8 h at 183°C. The crystal structure of GP1 zones was reported to be initially AuCu I type, and the lattice dimension parallel to the a-axis increased, while the parameter c decreased, with ageing up to 277.8 h at 120°C.

These results are consistent with those previously reported by Auld (1968). The second type of GP zones (GP 2 zones) were observed to form along with GP1 zones in Al-1.6% Mg-3.4% Ag and Al-0.9% Mg-5.0% Ag alloys aged 27.8 h - 11.5 days at 120°C and 2.8 h - 27.8 h at 183°C. These alloys have compositions that place them in the (α+η) and (α+β') phase fields respectively, Figure 2.5. The structure of type GP 2 zones was proposed to be body-centred tetragonal, with lattice parameters of a = 0.413 nm, c = 0.860 nm. It should be noted that these results were obtained using bulk X-ray diffraction techniques.

Only limited research work has been carried out to identify the form and structure of GP zones in aged Al-Mg-Ag alloys, and some researchers (Ito et al. 1969b and 1971, Takahashi et al. 1978) have used the early results obtained by Auld (1968) to explain observed age-hardening behaviour. It is to be emphasised that there have been little or no direct microstructural observations reported to date, and there remains a need for such observations using transmission electron microscopy and electron diffraction.

T' Phase

The existence of a metastable intermediate T' phase has been reported in alloys of the Al-Mg-Ag system in studies using the single crystal X-ray diffraction technique (Auld and Cousland 1976). The T' phase has, for example, been observed as a metastable phase in an Al-5.7% Mg-1.0% Ag alloy, aged 50 h at 197°C. The structure of the metastable T' phase was reported to be hexagonal with lattice parameters of a = 1.411 nm, c = 2.804 nm, and the orientation relationship between T' phase and the aluminium matrix was established to be of the form: $(0001)_{T'} \parallel (111)_{\alpha}$ and $(10\bar{1}0)_{T'} \parallel (11\bar{2})_{\alpha}$. A more recent study (Cousland and Tate 1986), using the X-ray diffraction technique and single crystal alloy specimens, has also indicated the presence of metastable T' phase in an alloy of composition Al-4.0% Mg-2.1% Ag, which lies in the (α+T) phase field of the equilibrium ternary phase diagram, Figure 2.5 (Williams 1972). Samples were aged 2.8 h - 11.5 days at 183°C, and 3.7 days at 235°C. However, again no direct microstructural observations by, for example, TEM were made.

T Phase

Prolonged ageing at temperatures approaching the equilibrium solvus, leads to the formation of the equilibrium T phase ($Mg_{32}(Al,Ag)_{49}$) in alloys of the appropriate composition, Figure 2.5. The existence of the equilibrium T phase ($Mg_{32}(Al,Ag)_{49}$) in aged Al-Mg-Ag alloys was initially proposed by Wheeler et al. (1965), and confirmed by Auld (1965) and Cousland and Tate (1986) using X-ray diffraction techniques. This phase has a body-centred cubic structure, lattice parameter a = 1.45 nm. In studies of the age-hardening behaviour in Al-Mg-Ag alloys, the orientation relationship between precipitates of the T phase and the aluminium matrix has been determined by X-ray diffraction techniques to be of the form: $(100)_T \parallel (112)_{\alpha}$, $[001]_T \parallel [1\bar{1}0]_{\alpha}$ (Auld 1968).

The equilibrium T phase was originally identified and thoroughly characterised in Al-Zn-Mg alloys. The T phase, $Mg_{32}(Al,Zn)_{49}$ (space group $Im\bar{3}$, body-centred cubic, a = 1.416 nm) is isomorphous with the compound $Mg_{32}(Al,Ag)_{49}$ in Al-Mg-Ag alloys. The crystal structure of the $Mg_{32}(Al,Zn)_{49}$ compound was shown (Bergman et al. 1957) to be based on a body-centred cubic lattice with 162 atoms. The reported stoichiometric compound $Mg_{32}(Al,Zn)_{49}$ is considered to provide a classic example of a close-packed structure dominated by icosahedral co-ordination shells (Frank and Kasper 1959), and it is thus a prototype of the so-call Frank-Kasper phases. It has been suggested (Ramachandrarao and Sastry 1985) that such equilibrium phases, having a high proportion of icosahedrally co-ordinated atoms, can be rapidly solidified from the melt into solid state quasicrystalline icosahedral phases.

Intensive investigations (Chandra and Suryanarayana 1988) of the $Mg_{32}(Al,Zn)_{49}$ phase, when produced by rapid solidification techniques, have indicated that it has a quasicrystalline icosahedral structure, confirmed by electron diffraction patterns exhibiting the required rotational symmetries. Compounds isomorphous with $Mg_{32}(Al,Zn)_{49}$ have been observed in a number of alloy systems, such as $Li_{32}(Al,Zn)_{49}$ in Al-Li-Zn alloys and $Mg_{32}(Al,Cu)_{49}$ in Al-Mg-Cu based alloys (Cassada et al. 1987). A stable ternary compound of Al_6CuLi_3, formerly designated as the T_2 phase by Hardy and Silcock (1955), in Al-Cu-Li alloys, has also been found to exhibit an icosahedral quasicrystalline structure (Ball and Lloyd 1985). Most of the icosahedral phases are observed to exist in composition ranges where equilibrium phases are of the Frank-Kasper type in which icosahedral coordination shells dominate in the structure.

Quasicrystalline icosahedral phases have been reported in rapidly solidified alloys of the Al-Mg-Ag system, such as Al-33.5% Mg-7.8% Ag and Al-42.7% Mg-7.9% Ag (Inoue et al. 1989). Although these alloys are significantly richer in Mg than those conventionally heat treatable, it is important to recognise the potential for production of such metastable phases, particularly in quenched alloys exposed to non-equilibrium processing.

2.6.3 Summary

In previous studies of the precipitation hardening behaviour of ternary Al-Mg-Ag alloys, described in detail in Section 2.6, the decomposition process of ternary Al-Mg-Ag alloys during isothermal ageing treatments has involve three principal precipitate phases, identified as GP zones, metastable T' and equilibrium T. The formation of these phases depends upon ageing conditions (temperatures and time). Nucleation of these phases in Al-Mg-Ag alloys is responsible for a significant stimulation in the ageing kinetics and enhancement of the age-hardening response, compared to those of Ag-free alloys, which have a different precipitation sequence (Sub-section 2.3.2). The essential differences are captured in Figure 2.6. However, all characterisation work, to establish the precipitation sequences in these alloys, has to date involved

mainly indirect experimental methods, such as X-ray diffraction techniques. It thus remains that precipitate microstructures and precipitate phases, particularly in the ternary alloys during isothermal ageing, are not thoroughly and convincingly understood.

Since microalloying additions of Ag to Al-Mg alloys promote significant improvement of the age-hardening response, as described in Sub-section 2.6.1, characterisation of the precipitate microstructures using transmission electron microscopy are required both to obtain direct evidence of the decomposition processes during isothermal ageing, and to better understand the mechanisms underpinning the enhanced age-hardening response.

The existence of a metastable intermediate T' phase has been reported in alloys of the Al-Mg-Ag system, arising from application of bulk X-ray diffraction techniques. Although this intermediate T' phase plays a potentially important role in determining their age-hardening behaviour, because it has been associated with maximum hardness in Al-Mg-Ag alloys during isothermal ageing, no direct microstructural observations of T' have been recorded and experimental correlation of the age hardening curves with corresponding aged microstructures has not been reported to date.

The equilibrium T phase, $Mg_{32}(Al,Ag)_{49}$, also plays an important role in strengthening of Al-Mg-Ag alloys during isothermal ageing. As mentioned earlier in Sub-section 2.6.2, this phase is isomorphous with the compound $Mg_{32}(Al,Zn)_{49}$ in Al-Mg-Zn alloys which has a structure dominated by icosahedral co-ordination shells. It is also interesting to point out that a quasicrystalline icosahedral form of the T phase has been produced by rapid solidification techniques.

2.7 Effects of Cold Work on Precipitation

The process of thermomechanical ageing involves the introduction of plastic deformation, in the form of uniaxial stretching or rolling, following solution heat treatment and water quenching and prior to isothermal ageing. This process is significantly important for industrial applications because of the improvements in mechanical properties, especially strength and hardness, that can be obtained during isothermal ageing in some age-hardenable aluminium alloys as a result of cold working supersaturated aluminium alloys. Other age-hardenable aluminium alloys show little or no significant improvement to strength, when the similar heat treatment schedules and deformation processes are applied. During the cold work that is imposed following solution treatment and water quenching, and prior to ageing heat treatment, excess dislocations are introduced to the supersaturated aluminium solid solution. The number density of dislocations is controlled by the degree and rate of the cold rolling or stretching processes. Those dislocations,

introduced by cold work post solution treatment and prior to ageing may provide preferred heterogeneous nucleate sites for certain intermediate precipitates, and thus often influence precipitation behaviour significantly (Kelly and Nicholson 1963).

In responsive alloys, the introduction of dislocations by plastic deformation both increases the level of maximum hardness achievable, and also typically reduces the ageing time to reach maximum hardness during isothermal ageing. The effects from such a treatment on the age-hardening response vary with alloy system and composition. The following two examples have been selected as representative of this behaviour.

As a first example, alloys of the Al-Cu system are particularly responsive to cold work after solution treatment and prior to ageing heat treatments. Plastic deformation is known to significantly enhance the age-hardening response in binary Al-Cu based alloys during isothermal ageing, with the additional strength increment arising from the introduction of dislocations, which provide effective nucleation sites for the principal strengthening phase θ'. These plate-shaped precipitates nucleate readily on dislocations, so that plastic deformation enhances the nucleation rate during ageing and promotes a fine-scale, uniformly refined distribution of precipitates (Silcock et al. 1955-56).

As a second example, it has been observed that introducing plastic deformation between solution treatment and isothermal ageing of water quenched Al-Zn alloys has little effect or may even decrease the age hardening response (Kelly and Nicholson 1963). This negative effect introduced by cold work is thought to be due to the dislocations that are introduced acting as additional sinks for migrating vacancies, and thus the rate of decay in the vacancy population will be greater than in an undeformed samples and diffusion rates will corresponding be decreased. In addition, dislocations introduced by plastic deformation have been observed to reduce the age-hardening response in Al-Cu alloys containing small concentrations of Cd, In or Sn (Hardy 1954-55). It has been suggested (Hardy 1954-55) that these trace elements are trapped at dislocations generated by the cold-working operation because they represent relatively the large atomic diameters (Cd: 0.298 nm, In: 0.325 nm and Sn: 0.302 nm).

The effect of cold-working on the ageing behaviour of an Al-Mg alloy was first explored by Pollard (1964-65). A 5% strain introduced to the Al-10% Mg alloy by stretching did not stimulate its age-hardening response significantly. In contrast, the effects of cold work on the ageing behaviour of an Al-8% Mg alloy was examined (Cottereau et al. 1989), and it was suggested that the hardness increased with increasing cold reduction. However, the number density of precipitate particles in the cold-worked samples was lower than that of undeformed samples. The effects of pre-ageing treatments prior to before cold-working were also studied, and observed to lead to a greater increase in hardness than normal ageing treatments. These

studies would suggest little encouragement for further attempts to stimulate an ageing response in binary Al-Mg alloys. However, no experimental work has been reported on the effect of cold work on the precipitation hardening response in Al-Mg-Ag alloys.

2.8 Summary

Aluminium-magnesium alloys containing less than 5% Mg exhibit little or no age-hardening response while, in order to obtain a useful age-hardening response in alloys with more than 7% Mg, the ageing temperatures must be kept as low as possible (preferably natural ageing). However, the time then required to achieve maximum hardness is extremely long, i.e. in excess of 10 years (Kojima et al. 1981). Clearly, it is practically impossible to apply such heat treatment schedules in industrial application. Alloys of the Al-Mg system have thus to date been regarded as non-heat treatable alloys. However, with the continuing demand to reduce the weight of structural components in both the automotive and aerospace industries, there are potential applications for lightweight alloys of the Al-Mg system if effective ways could be found to improve the strength and hardness of the alloys and generate formable materials of high specific strength.

Although they are of little practical value, the investigation of the precipitation processes in binary Al-Mg alloys is of considerable importance since it offers the potential to improve understanding of the reasons for the poor age-hardening response and identify strategies by which precipitation strengthening might be improved. Detailed microstructural characterisation is an important tool in improved microstructural design.

As reviewed in this Chapter, there has been considerable research into the decomposition processes in supersaturated Al-Mg alloys using mainly the indirect characterisation techniques of X-ray diffraction, DSC and electrical resistivity measurements. Work to date has mainly focused on precipitation behaviour in Al-Mg alloys aged in the temperature range from below room temperature to approximately 150°C because of the nature of this alloy system. However, experimental results for relatively high ageing temperatures ranging from 160°C to 240°C, which are very important for industrial applications, are very limited. Furthermore, almost all existing experimental results are the result of indirect observations, and there have been few detailed microstructural observations by transmission electron microscopy.

One approach to improving the hardening response that has proven effective in several different aluminium alloy systems involves the addition of microalloying elements in trace concentrations to modify precipitation behaviour. One of the most effective elements in this regard has proven to be Ag. Trace additions of Ag to Al-Mg alloys have already exhibited

potential to generate on age-hardening response in alloys of low Mg content and substantially improve the hardness in alloys of higher Mg content. Ternary Al-Mg-Ag alloy may thus have significant potential for realising the requirement for Al-Mg based alloys of high specific strength. Even if alloys containing Ag prove to be impractical commercially, an understanding of the role of Ag in promoting a useful age-hardening response may lead to the design of other ternary alloys with more cost effective alloying additions.

While the potential of Ag-modified Al-Mg alloys has been recognised, there has been no systematic microstructural characterisation of precipitation behaviour in Al-Mg-Ag alloys in order to correlate microstructure with mechanical behaviour and thus understand the source of the hardening response that the addition of Ag promotes. The primary goal of the present thesis is thus a detailed characterisation of precipitation behaviour in Al-Mg and Al-Mg-Ag alloys of appropriate composition using the direct characterisation techniques of TEM and electron diffraction.

A second approach to enhancing the precipitation hardening response that has proven effective in some aluminium-based alloys involves the introduction of significant plastic deformation to the supersaturated solid solution prior to the ageing heat treatment. This approach has shown little promise in some preliminary applications to binary Al-Mg alloys. However, it has not been applied to ternary Al-Mg-Ag alloys and thus a minor component of the present work has involved application of this approach to ternary alloys of interest.

Chapter 3

Experimental Procedures

This Chapter contains an outline of the preparation of the experimental alloy ingots and the specimen preparation techniques. The principal characterisation techniques, such as hardness measurements and microstructural observation by transmission electron microscopy (TEM) are described. The procedures for detailed dislocation analyses are also explained.

3.1 Preparation of Test Materials

Ternary alloy ingots of the nominal compositions used in this investigation are listed in Table 3.1. Ingots were prepared by induction melting in high purity alumina crucibles in a conventional muffle furnace under air using elemental components of high purity (i.e. 99.99% Al, 99.99% Mg and 99.9% Ag). The Mg was added just prior to pouring into a metal mould in order to prevent significant loss of Mg by oxidation during casting. The molten metals were stirred mechanically and then chill-cast into cast-iron moulds with dimensions of 110x60x15mm. After these ingots were homogenised for 52 h at 350°C, the surfaces on each side were scalped by milling. Binary Al-5.0Mg and Al-10.0Mg alloys were, in addition, supplied by Emeritus Professor I.J. Polmear from the Department of Materials Engineering at Monash University. The chemical composition (wt%) of these alloy ingots was analysed by the inductively coupled plasma-atomic emission spectroscopy (ICP-AES) method, and the detailed results of the chemical analyses are provided in Table 3.1. The levels of principal impurities in the alloy ingots prepared were: <0.01% Si and <0.01% Fe.

Table 3.1 Compositions of experimental alloys.

	Nominal Compositions (wt%)			Measured Compositions (wt%)		
	Mg	Ag	Al	Mg	Ag	Al
Alloy 1	5.0	---	Bal.	4.44	---	Bal.
Alloy 2	5.0	0.5	Bal.	4.17	0.40	Bal.
Alloy 3	10.0	---	Bal.	10.0	---	Bal.
Alloy 4	10.0	0.5	Bal.	10.0	0.48	Bal.

These ingots were then hot rolled to plate or sheet, approximately 50mm thick for hardness test specimens and approximately 0.3mm thick for TEM specimens. All specimens were solution treated 1 h at 500°C (±1°C) in a salt bath, water quenched and then aged isothermally at 160°C, 200°C and 240°C (±2°C) for various times up to 2400 h in oil baths or salt baths.

3.2 Hardness Testing

To assess the age-hardening response of these alloys, the bulk hardness of 50mm thick samples was measured as a function of thermal treatment using a Vickers hardness tester at a load of 5kg. Eight indents were made for each samples, and then the maximum and minimum hardness values derived from these were discarded. The remaining six measurements were used to calculate the average hardness to obtain the ageing curves. These measurements were carried out in air at room temperature as soon as possible after the ageing treatment (typically not more than 10 min. after heat treatment).

In the case of hardness testing of samples subjected to cold work post solution treatment and prior to ageing heat treatment, the alloys were solution treated in a salt bath for 1 h at 500°C (±1°C). Those specimens to be cold-worked after water quenching and prior to ageing were given a 7% reduction by rolling in a single pass immediately. To ensure uniform deformation, a small roll diameter (70mm) was selected and thin, flat specimens were used, so that the ratio of contact length to specimen thickness was approximately equal to or greater than unity, in the manner descried by Hirsch and Lücke (1988).

3.3 Transmission Electron Microscopy

All specimens for transmission electron microscopy (TEM) were punched mechanically as discs of 3mm diameter from the strips of 0.3mm thickness after appropriate heat treatment. They were then dry ground to a thickness of 0.1mm to 0.15mm. These disc samples were then thinned to perforation by a twin-jet electropolishing technique. The electrolyte used was either a solution of 33vol.% HNO_3 and 67vol.% C_2H_5OH or a solution of 33vol.% HNO_3 and 67vol.% CH_3OH. Polishing was carried out in the temperature range -15°C to 0°C, using a Struers Tenupol-3 twin-jet electropolisher operating at approximately 0.2A and 12V. After polishing, the thin foil specimens were washed and rinsed in a series of high purity ethanol baths before being dried on filter paper. The polished thin foils were stored in a vacuum desiccator to avoid the development of oxide films on the surface of specimens.

Microstructures were observed using either a Philips EM420 or a CM20 transmission electron microscope (TEM) operating at 120kV and 200kV, respectively. Both were equipped with the facility for energy dispersive x-ray spectroscopy (EDXS). The x-ray spectra for EDXS analyses were obtained from precipitate particles in which those areas of specimens having a thickness of typically 100nm or less, using a focused electron probe nominally 60nm or 55nm in diameter in the Philips EM420 or the CM20 TEMs. In general, x-ray spectra data were acquired for 100 s to 300 s. Electron microdiffraction patterns were recorded in conventional TEM mode

using a 30μm condenser lens aperture and an electron probe 55nm or 60nm in nominal diameter. The principal techniques employed for identification of precipitate phases were selected-area electron diffraction (SAED) and electron microdiffraction.

3.3.1 Dislocation Analysis

In order to investigate the nature of dislocations in the as-quenched microstructures, and to compare the distribution and densities of dislocations in alloys with and without trace additions of Ag, the as-quenched microstructures were observed using a combination of two-beam bright field (BF) and centred-dark field imaging (CDF) techniques with several different operating diffraction vectors **g**.

A method of estimating dislocation density described by Bailey and Hirsch (1960) has been adopted for the as-quenched microstructures in this work. In this method, dislocation density is deduced by determination of Burgers vectors, and measurements of the length of dislocation line and the local foil thickness. The procedures to obtain these parameters are described separately in the following sections.

The Determination of Burgers Vectors

The conventional method for the determination of the Burgers vector of perfect dislocations in f.c.c. metals is based on the well-known extinction rule (Edington 1976, Williams and Carter 1996). This rule is that the dot product **g•b** (where **g** is the diffraction vector for the beam used to image the dislocation, and **b** is the dislocation Burgers vector) is zero if the dislocation is invisible in BF and CDF images.

Considering the possibilities of various **g•b** values, it enables the determination of the most useful orientations needed for analyses, that is the range of reflections is required. In this study, therefore, the incident beam was chosen parallel to $[110]_\alpha$ directions because this orientation gives higher number of diffraction vector conditions.

The procedures used in this study to determine the direction of the Burgers vector for perfect dislocations are well established and described by some authors (Edington 1976, Williams and Carter 1996).

The Determination of Foil Thickness

The foil thickness must be known for several different types of quantitative measurements usir transmission electron microscope. Many different methods of determining the foil thickness transmission electron microscopy have been developed (Williams 1987). Most techniques are s accurate to better than 10%.

In this investigation, the local foil thickness of the TEM samples was estimated using the two-beam convergent beam electron diffraction (CBED) method which is straightforward and gives high accuracy (Kelly et al. 1975). This method is based on the two-beam dynamic theory which is related to the minima in intensity oscillations to the foil thickness t, using the following equation:

$$(S_i^2 + 1/\xi_g^2)t^2 = n_i^2 \quad \text{------ (1)}$$

where S_i is the deviation of the *i*-th minimum from the exact Bragg position, ξ_g is the extinction thickness, and n_i is a whole number.

In this investigation, two-beam CBED patterns were usually taken incorporating the (220) reflection. The largest condenser lens aperture (150μm) and small spot size (60nm in nominal diameter) of the electron incident beam were selected. A typical example of the schematic two-beam CBED pattern is illustrated in Figure 3.1.

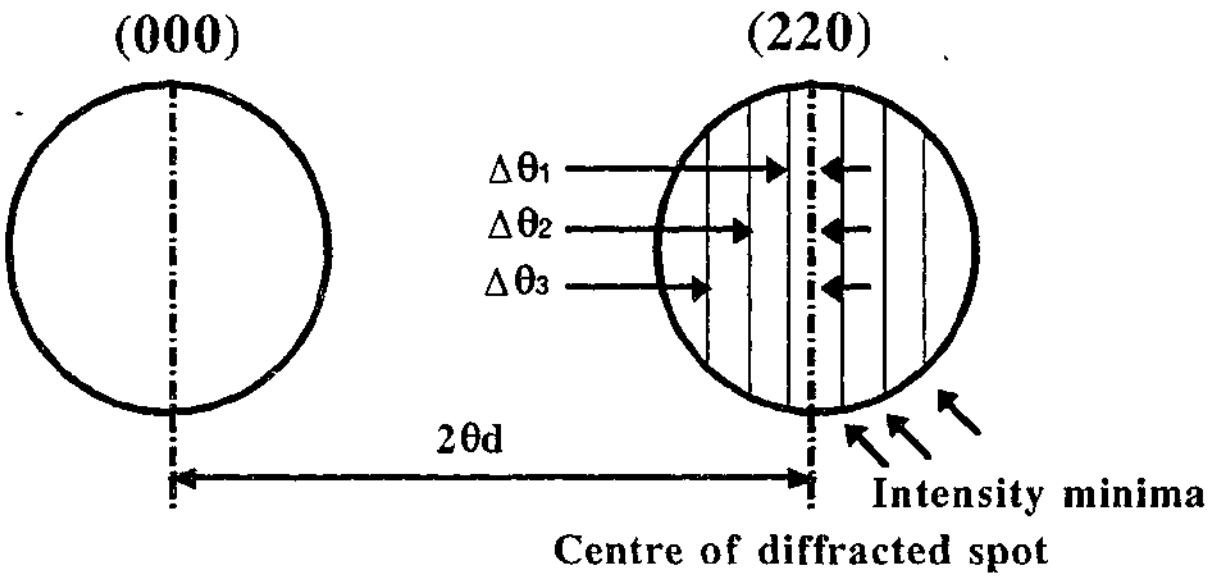

Figure 3.1 A two-beam CBED pattern showing the distance ($2\theta_d$) between the transmit (000) spot and diffracted (220) spot as well as the spacings $\Delta\theta_i$ from the centre of the diffracted (220) beam profile to each of the successive minima.

The values of S_i were determined by measuring the distance $\Delta\theta_i$ from the centre of the diffracted beam profile to each of the successive minima, together with the distance $2\theta_d$ between the centre spot and the diffracted spot as shown in the following equation:

$$S_i = \frac{\lambda}{d^2}\left(\frac{\Delta\theta}{2\theta_d}\right) \quad \text{------ (2)}$$

where λ is the wavelength and d is the spacing of the planes giving rise to the operating

reflection.

No calibration for camera length or magnification of the pattern was necessary since only the ratio of two distance $\Delta\theta_i$ and $2\theta_d$ is involved in (2).

With an operating accelerate voltage at 120kV, the values of the required parameters were as follow: $\lambda = 0.00335$nm, $a = 0.405$nm, $\mathbf{g} = 220$. From these parameters S_i can be obtained, and then equation (1) is expressed as follow:

$$\left(\frac{S_i}{n_i}\right)^2 + \left(\frac{1}{n_i}\right)^2\left(\frac{1}{\xi_g}\right)^2 = \frac{1}{t^2} \qquad \text{------ (1a)}$$

Then $(S_i/n_i)^2$ versus $(1/n_i)^2$ were plotted. Finally, foil thickness t was obtained from this plotting diagram. The calculation of the foil thickness described was carried out using the computer program called DIFFRACT. The brief sequences of this program used are described as follow: At first, to define initial parameters impute the necessary date such as g-vector, accelerating voltage and $2\theta_d$ through the SetUp Menu. Next, impute $\Delta\theta_i$ data into the diffracting beam which is appeared in the computer screen, then $(S_i/n_i)^2$ versus $(1/n_i)^2$ are plotted. Though this plot, foil thickness can be obtained. An example, which thickness is calculated using the parameters obtained from binary Al-10Mg alloy, of the plot is illustrated in Figure 3.2. The detailed results of parameters are presented in Chapter 4.

The Determination of Dislocation Density

Dislocation densities were estimated by measuring the total projected length R_p of dislocation lines in a given area A on a negative micrograph. Assuming that the dislocation segments are randomly oriented and define straight lines, the mean length of dislocation line R can be derived from the mean projected length R_p by using the relation.

$$R = 4R_p/\pi \qquad \text{------ (3)}$$

Then, the dislocation density is $\rho = R(AtM)$, where t is the local foil thickness, and M is magnification.

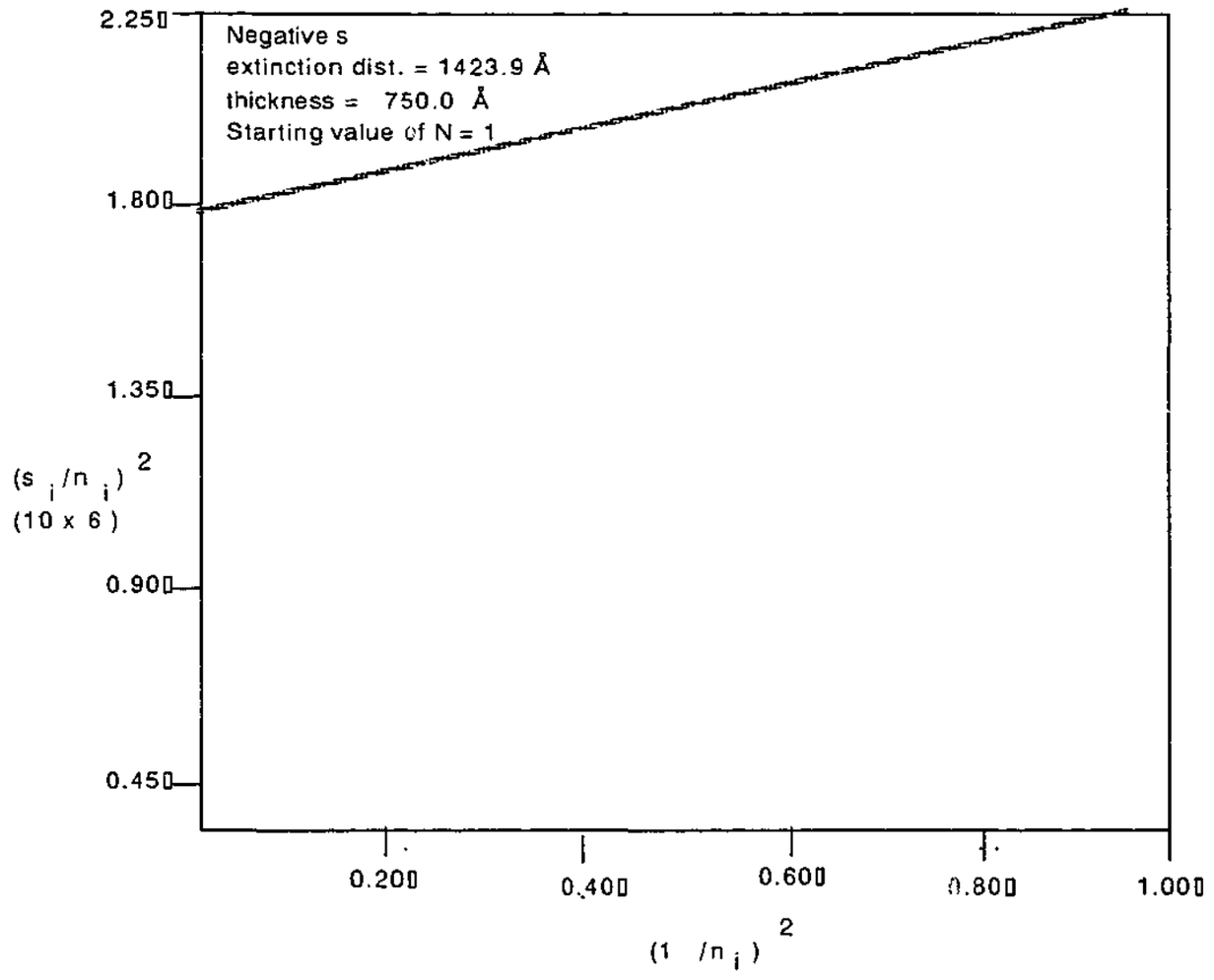

Figure 3.2 Graphical determination of foil thickness: $(S_i/n_i)^2$ versus $(1/n_i)^2$ plotted graph showing the relationship with the foil thickness t.

Chapter 4

Precipitation Hardening Response in Al-Mg(-Ag) Alloys

4.1 Introduction

It is well established (Polmear 1995) that Al-Mg alloys (5000 series) achieve a combination of good mechanical properties and formability through solid solution strengthening, and Al-Mg alloys have thus found commercial use in cast and wrought forms for a variety of applications. However, the recent consistent demand for a reduction in the weight of structural components, coupled with an increase in strength, has focused attention on the development of new structural aluminium alloys of high specific strength. As described in Chapter 2, section 2.2, ageing heat treatments of solution treated and quenched, supersaturated solid solutions may lead to increased strength in Al alloys through precipitation hardening. However, since the 5000 series Al alloys are commonly categorised as non-heat treatable, little interest has been paid to the precipitation hardening response of such alloys. As described in Chapter 2, Polmear and Sargant (1963) and Polmear (1964) investigated the effect of trace additions of Ag on the age-hardening response in Al-Mg alloys in the 1960's, but there is scope for further detailed investigation of the age-hardening behaviour of binary Al-Mg alloys and ternary Al-Mg-Ag alloys. It is important to explore whether or not a precipitation hardening response is found in a given alloy. Then, if found, to characterise the hardening behaviour, including the level of the peak hardness and the time to reach the peak hardness with different ageing temperatures and heat treatment conditions.

The present chapter thus includes the results from a systematic investigation of the age-hardening response in Al-Mg alloys, with and without trace additions of Ag, aged isothermally at 160°C, 200°C and 240°C. This chapter also contains the results of a study of the effect on ageing response of cold work introduced after solution treatment and water quenching of ternary Al-10Mg-0.5Ag alloy and prior to the ageing treatments.

During the early stages of the decomposition of a supersaturated Al-based solid solution produced by solution treatment and quenching, it has been suggested (Hardy 1951-52, Embury and Nicholson 1963) that the precipitation behaviour is influenced significantly by a range of factors, including the quenched-in defect population, solute-solute interactions and solute-defect interactions. In addition, trace additions of microalloying elements can influence the ageing behaviour through a range of effects on the nucleation and growth processes. For instance, Ag atoms are known to have a strong attractive interaction with vacancies, so that excess quenched-in vacancies are expected to be trapped by Ag atoms to form Ag-vacancy complexes in solid solution in the as-quenched microstructure and to effectively preserve an increased vacancy population during initial ageing (Ringer et al. 1996). It is also well known (Kelly and Nicholson 1963) that, in certain alloys, pre-existing dislocations provide preferred nucleation sites for metastable or equilibrium precipitates and that plastic deformation may thus be used to manipulate the dislocation distribution and hence the precipitate distribution. It is thus very important to characterise the as-quenched microstructures, particularly with regard to the form and identity of

pre-existing defects or defect clusters and their distribution. The present chapter also contains the results of analyses of the dislocation populations in the as-quenched microstructures of Al-10Mg alloys with and without 0.5Ag.

4.2 The Precipitation Hardening Response

It is well established that trace additions of Ag to Al-Cu-Mg alloys induce the formation of a thin plate-shaped precipitate, designated omega (Ω), which leads to a significant enhancement of maximum hardness in this alloy system (Chester and Polmear 1983, Muddle and Polmear 1989). However, much less work has been done on the effect of trace additions of Ag to simple binary Al-Mg alloys, despite the fact that alloys of this system would appear to have strong potential for precipitation hardening, as it is relatively easy to achieve a supersaturated solid solution with high concentrations of solute Mg. A description and an understanding of the age-hardening response of the Al-Mg(-Ag) alloys are thus essential aims of the present work.

Figure 4.1 shows the hardness curves (HV5) for the Al-5Mg(-0.5Ag) (wt%) alloys aged isothermally at 200°C and 240°C. There is little or no hardening detectable in the binary alloy aged at 200°C. However, the ageing response of the binary alloy is significantly enhanced by trace additions of Ag, with peak hardness values of ~85VHN and ~65VHN achieved after 5 h at 200°C and 50 min. (0.8 h) at 240°C respectively. These values are to be compared with an as-quenched hardness of ~56VHN, and with a maximum hardness of 56VHN in the binary alloy aged at 200°C. It is interesting to note that the ternary alloy, aged at both 200°C and 240°C, exhibits a broad hardness plateau at maximum hardness followed by a relatively rapid decline in hardness after ~100 h, suggesting that the precipitate particles present are relatively thermally stable or that there is perhaps a sequence of precipitation reactions sustaining a common maximum hardness. The measurements of the hardness in the as-quenched condition of the binary and ternary alloys were repeated several times to permit a consideration of errors (±3VHN) of measurement, and the hardness of the binary alloy in the as-quenched condition was observed to be consistently higher than that of the ternary alloy.

The ageing curves for binary Al-10Mg (wt%) alloy aged at temperatures of 160°C, 200°C and 240°C are presented in Figure 4.2. Samples of the Al-10Mg alloy have a hardness of ~90VHN (5kg load) in the as-quenched condition. At all three temperatures, there is an incubation period in excess of 1 h before the hardness increases gradually to maximum values of ~119VHN, ~112VHN and ~105VHN after ageing for 140 h, 16 h and 5 h at 160°C, 200°C and 240°C respectively. The behaviour is classical in form, for as the ageing temperature is decreased from 240°C to 160°C, the maximum hardness values increase, while the time required to achieve maximum hardness is increased. The precipitation response is accelerated by an increase in

ageing temperature. The as-quenched hardness of the Al-10Mg alloy (~90VHN) is significantly higher than that of the binary Al-5Mg alloy (~56VHN) (Fig. 4.1), reflecting the substantially higher concentration of solute retained in solid solution.

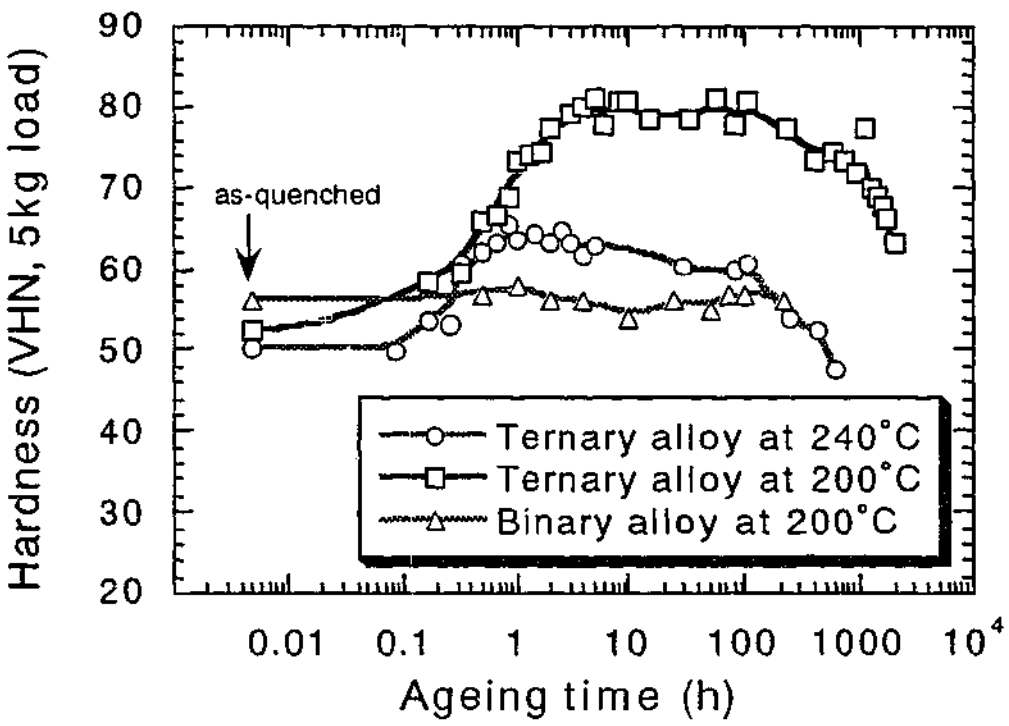

Figure 4.1 Isothermal age-hardening response of Al-5Mg alloys, with and without trace additions of 0.5Ag, at 200°C and 240°C.

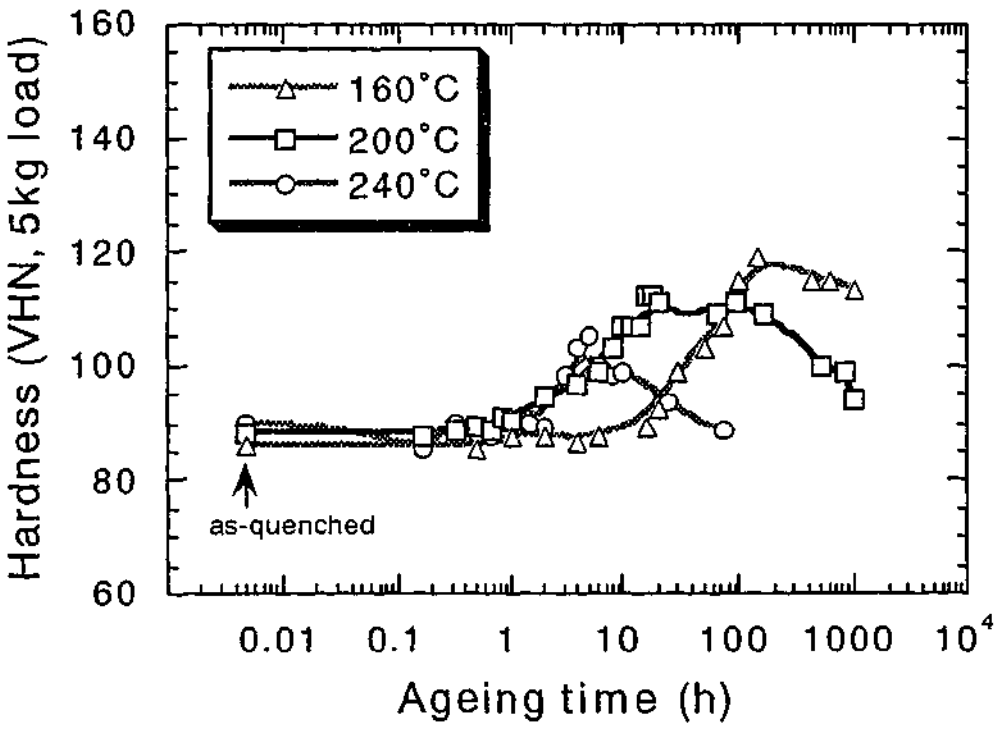

Figure 4.2 Ageing curves for binary Al-10Mg alloy aged at 160°C, 200°C and 240°C.

Figure 4.3 illustrates the age-hardening response of ternary Al-10Mg-0.5Ag alloys aged at 160°C, 200°C and 240°C as a function of ageing time. Although errors of measurement of typically (±3VHN) are associated with all measurements, the results indicate a Vickers hardness of ~85VHN (5kg load) in the as-quenched condition, which was consistently lower than that of binary Al-10Mg alloy (Fig. 4.2). The hardness reaches maximum values of ~150VHN, ~140VHN and ~120VHN (5kg load) after ageing for 65 h, 10 h and 2 h at 160°C, 200°C and 240°C respectively, and then decreases quite rapidly as over-ageing occurs. The time required to achieve maximum hardness is decreased significantly in these alloys as a result of the additions of trace amounts of Ag. It is noteworthy that there is evidence of two distinguishable stages in the hardening response and that this trend is more pronounced at the lower ageing temperatures. For the ageing curve at 160°C, the ageing response of the ternary alloy as initially relatively slow in the interval up to 10 h ageing, at which point the hardness is ~100VHN. Beyond this point the rate of a hardness increase accelerates to a maximum hardness. For the ageing curve at 200°C, there is again a suggestion of two distinguishable stages of the ageing response, involving an initial steady increase in hardness up to 1 h, before a relatively sharp acceleration in the rate of age-hardening to peak hardness. Although there is a perceptible acceleration in the rate of the age-hardening response after 0.5 h, this trend is not so clearly observed at the ageing temperature of 240°C. The ternary alloys exhibit an improved age-hardening response at all ageing temperatures compared to the equivalent binary alloy, but it is noteworthy that the ageing curves appear to have a relatively rapid decline after the peak hardness.

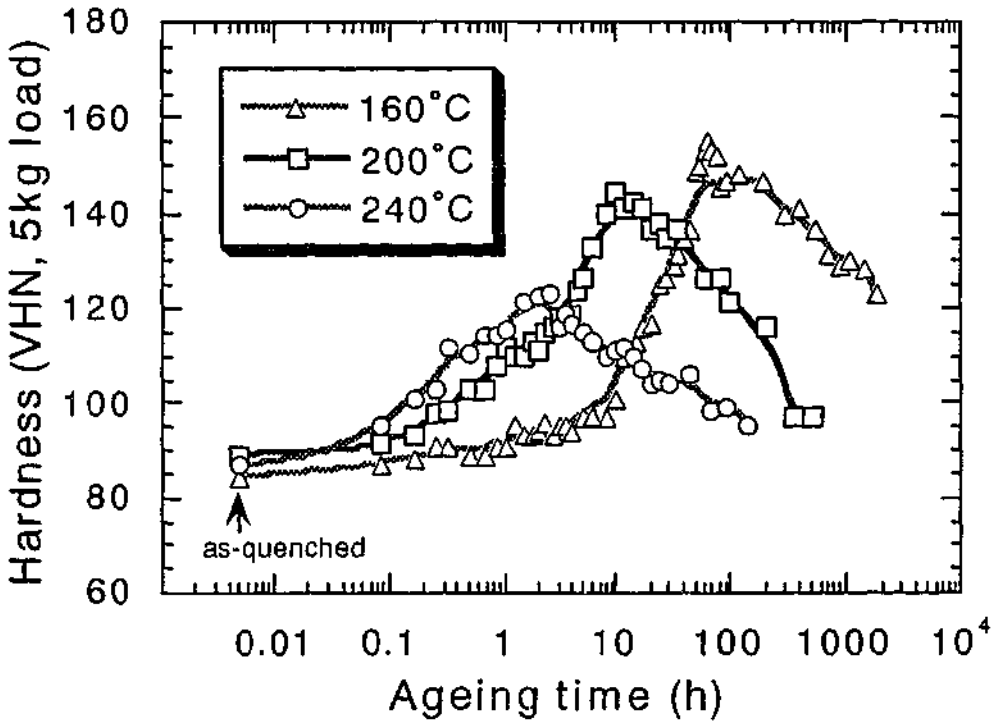

Figure 4.3 Ageing curves for ternary Al-10Mg-0.5Ag alloy at ageing temperatures of 160°C, 200°C and 240°C.

4.3 Effect of Cold Work on the Hardening Response

Cold work, post solution treatment and prior to ageing (T8 temper), is generally known to enhance precipitation behaviour in the most age-hardenable Al alloys, especially the Al-Cu and Al-Cu-Mg based alloys (Kelly and Nicholson 1963). This is because cold work introduces additional dislocations to the supersaturated solid solution and thus provides preferred heterogeneous nucleation sites for certain precipitate phases. The process has also significant commercial application in industrial processing as a tool in thermomechanical treatment. However, as, mentioned in Chapter 2, section 2.7, cold work has been shown to have little effect on the age-hardening response in binary Al-Mg alloys (Pollard 1964-65, Cottereau et al. 1989), and there is no experimental data available for the effect of cold work on the age-hardening response in ternary Al-Mg-Ag alloys. It is thus interesting to explore whether cold work might be used to stimulate further the age-hardening response in the ternary alloys.

In the present study, some 7% cold work was applied by a rolling process to the Al-10Mg-0.5Ag alloys post solution treatment and prior to ageing, and the resulting samples were then aged at 160°C and 200°C. Figure 4.4 (a) compares the ageing curves for the T8 treatment with that for general ageing (T6 treatment) in Al-10Mg-0.5Ag alloy aged at 160°C. In the cold worked sample, the hardness is increased significantly from ~89VHN in an as-quenched condition to ~124VHN after the 7% cold work, presumably due to the work hardening effect from the increasing dislocation density. There is an incubation period of approximately 0.5 h at 160°C before the hardness begins to gradually increase to reach a maximum value of ~167VHN after 8h. Comparing with the ageing curve for the T6 temper, the age-hardening response during the T8 temper is accelerated and the peak hardness is increased significantly in the cold worked sample. Time to reach maximum hardness (~10 h) in the T8 condition is reduced compared to that for the T6 treatment (~100 h), confirming that cold work stimulates precipitation, presumably through introducing a higher density of dislocations which provide preferred nucleation sites for precipitate particles.

The ageing curves for Al-10Mg-0.5Ag alloy aged at 200°C, with and without the 7% cold work, are presented in Figure 4.4 (b). The pattern is similar to that observed at the lower temperature. However, during ageing of the cold worked samples the hardness initially decreases to ~110VHN (0.1 h at 200°C) before a precipitation hardening response is detectable. This initial loss of hardness is presumably due to recovery of the cold-worked samples before precipitation produces detectable hardening. Maximum hardness of ~157VHN is achieved after ~3 h at 200°C (c.f. ~10 h in the T6 sample). During ageing, an approximately constant increment of ~15VHN is maintained between the curves for the T6 and T8 treatments for any given ageing time. Loss of hardness due to recovery of the cold worked samples is offset by increased precipitation hardening and the difference is sustained at maximum hardness.

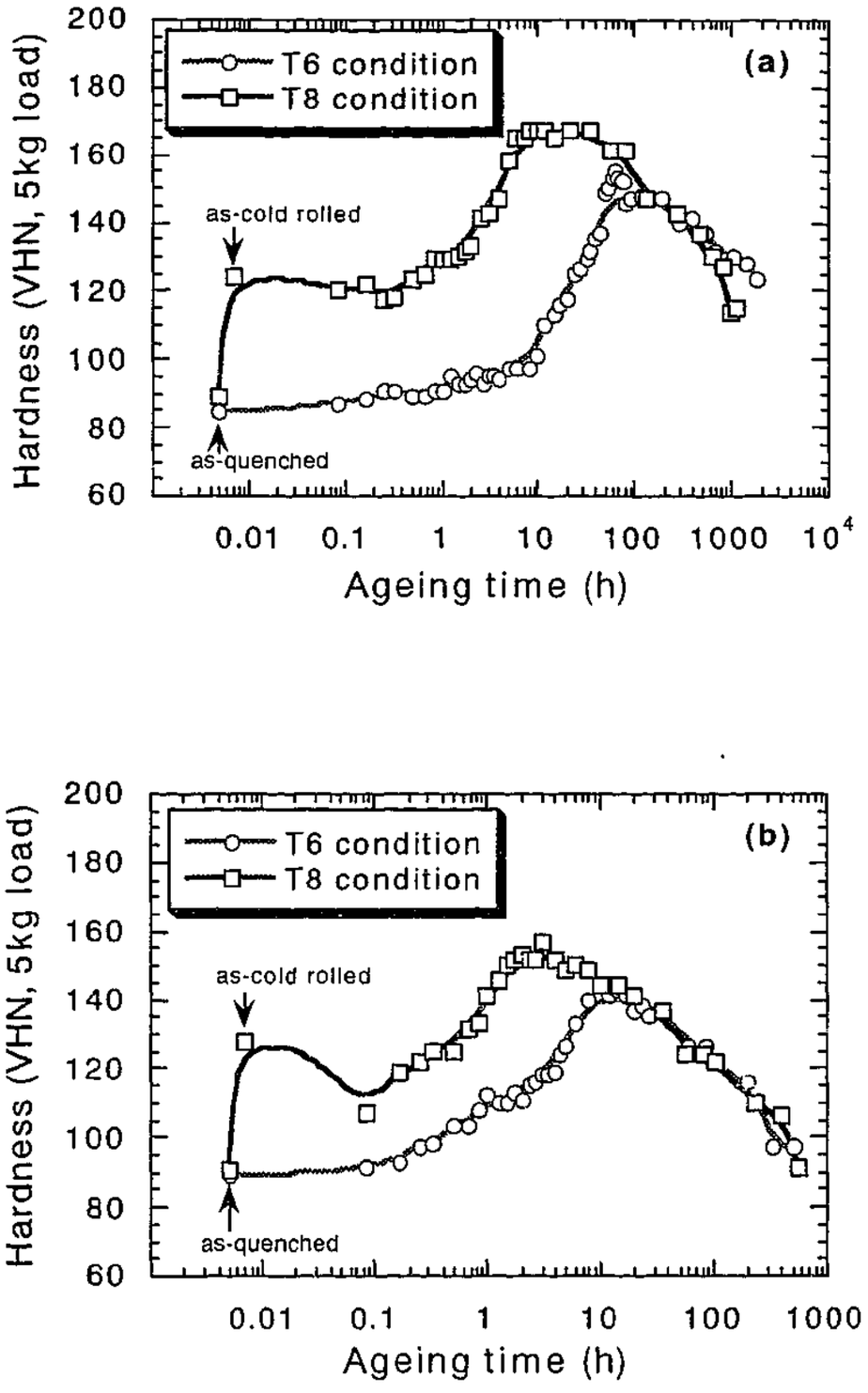

Figure 4.4 Ageing curves for Al-10Mg-0.5Ag alloy with and without 7% cold work, applied post solution treatment and prior to ageing at (a) 160°C and (b) 200°C.

It is noteworthy that the hardness arising from the T8 treatment at 200°C initially decreased significantly during the very early stages of ageing, but that this decrease in hardness was not detectable when T8 specimens were aged at 160°C. These results suggest that, as expected, the higher ageing temperature is more likely to promote recovery in the cold worked specimens.

The increments in hardness between the T6 and T8 samples at maximum hardness were modest, with values of ~13VHN and ~12VHN for specimens aged at 160°C and 200°C respectively, suggesting that this increment is effectively independent of the ageing temperature in this range.

As in the T6 treatment, there is some evidence of two distinguishable stages of ageing response in sample exposed to the T8 treatments. This suggests that the precipitation sequence may be similar during T8 and T6 treatments, with possibly only the density of precipitate particles in the T8 samples being higher than in the T6 specimens. Alternatively, the increased hardness achieved during the T8 treatment may be attributable to the precipitate particles in the cold work specimens being much more uniform by distributed than in the undeformed specimens.

4.4 The Relationship Between Hardness and Dislocation Density

Introduction

An interesting observation arising from the hardness measurements was that the hardness of the as-quenched samples of the Ag-modified alloys was consistently significantly lower than that of the Ag-free binary alloys. The effect was more pronounced in the Al-5Mg alloys, but also evident in the Al-10Mg alloys. In order to seek an explanation for this phenomenon, a brief study was conducted of the line defect structures in the as-quenched samples of the Al-10Mg based alloys.

Kuhlmann-Wilsdorf (1958) predicted that excess vacancies introduced by quenching a metal or an alloy from near its melting point should condense as small voids and subsequently collapse to form dislocation loops. It is now well established that when alloys are quenched rapidly from high temperatures to room temperature, quenched-in excess vacancies can be retained in metals and these retained vacancies can affect the precipitation characteristics significantly. Several factors have been proposed to account for the way in which the presence of excess vacancies affects the precipitation behaviour.

Previous investigations have indicated that the nucleation of precipitates may be influenced by trace additions of microalloying elements to age-hardenable alloys (Polmear 1968, and Polmear 1987). The effects are strongly related to vacancies; that is, the quenched-in vacancy population has a strong interaction with small additions of particular elements because of high solute-vacancy binding energies. For instance, elements such as Ag and In, which have low solid solubility and a strong affinity with vacancies in Al (Doyama 1966), suppress the vacancy condensation process during quenching. Therefore, trace additions of those elements tend to cluster and the clusters appear to provide preferential nucleation sites for the intermediate phases

during ageing treatment. On the other hand, third elements like Cd, which have relatively higher solid solubility and lower affinity for vacancies in Al, do not inhibit the condensation of vacancies and allow formation of dislocation loops during quenching (Nuyten 1967).

The evidence that Ag atoms bind with vacancies in Al alloys, such as Al-Cu and Al-Cu-Mg based alloys, has given rise to the proposal that these should be a lower dislocation density in as-quenched Ag-containing alloys compared to Ag-free alloys. With Ag atoms trapping vacancies, there are fewer excess vacancies to cluster and collapse to form dislocation loops or available to participate in climb processes that modify the shape of screw dislocations into spirals. Such modified dislocations act as preferential nucleation sites for precipitates. However, there have been few systematic microstructural studies to evaluate the form and density of dislocations in the as-quenched condition in Al alloys, particularly in the Al-Mg based systems. A significant step in identifying the role of Ag in Al-Mg based alloys therefore involves detailed analyses of the as-quenched microstructures in Ag-modified and Ag-free alloys, in order to characterise the defect structure that precedes ageing.

As described in Chapter 3, the nature of the dislocations in as-quenched alloys was initially analysed; the Burgers vectors were determined for each observed form of dislocation in both Al-10Mg and Al-10Mg-0.5Ag alloys. The foil thickness of selected TEM specimens was determined using the two-beam convergent beam electron diffraction (CBED) method (Kelly et al. 1975), and the number density of dislocations then estimated. Finally an attempt was made to correlate measured dislocation density with the hardness of the alloys in the as-quenched condition.

The Determination of Burgers Vectors

The method of determination of the dislocation Burgers vectors has been outlined in Chapter 3. It is based on the well-known extinction rule; that is, the dot product $\mathbf{g}.\mathbf{b}$ (where $\mathbf{g}$ is the diffraction vector used to image the dislocation and $\mathbf{b}$ is the Burgers vector) is zero when the dislocation is invisible.

Figure 4.5 presents TEM micrographs of typical dislocation structures in the as-quenched condition in the binary Al-10Mg alloy. Figures 4.5 (a) and (b) represent centred dark field (CDF) and bright field (BF) images respectively, with the electron beam approximately parallel to a $<101>_\alpha$ direction and the selected operating $\mathbf{g}$ vector corresponding to the $<0\bar{2}0>_\alpha$. Based on examination of the line directions of observed dislocations in these TEM micrographs, there are two distinguishable sets of dislocations which are visible. One set of dislocations has a projected trace parallel to $<\bar{1}31>_\alpha$ and the other set is parallel in projection to $<\bar{1}11>_\alpha$. Those sets of dislocations parallel to $<\bar{1}31>_\alpha$ and $<\bar{1}11>_\alpha$ are referred to as arrays A and B, respectively.

Figures 4.6 (a) and (b) present CDF and BF images respectively of the same field in the as-quenched microstructure in binary Al-10Mg alloy. The electron beam is again near $<101>_\alpha$ and the operating **g** vector now parallel to the $<11\bar{1}>_\alpha$ direction. As is evident, two distinguishable sets of dislocations are now visible. Those dislocations (set A) parallel to the trace of $<\bar{1}31>_\alpha$ remain visible, while there is a new set C of dislocations parallel to the trace of $<\bar{2}02>_\alpha$. It should be noted that the set of dislocations (type B), which were visible with $\mathbf{g} = <0\bar{2}0>_\alpha$ in Fig. 4.5, are now invisible. However, the array of dislocations (set C) with a projected line direction parallel to $<\bar{2}02>_\alpha$, which were invisible with $\mathbf{g} = <0\bar{2}0>_\alpha$ in Fig. 4.5, is now visible with $<\bar{1}11>_\alpha$.

Figure 4.7 presents further micrographs of line defects in the as-quenched condition in the binary Al-10Mg alloy. Figures 4.7 (a) and (b) represent CDF and BF images, respectively, with the electron beam again near $<101>_\alpha$ and the operating **g** vector is $<\bar{1}11>_\alpha$. The micrographs were recorded from almost the same area as that shown in Figures 4.5 and 4.6. As can be seen from these micrographs, two distinguishable sets of dislocations are now visible; these referred to as sets B and C. However, those with traces parallel to $<\bar{1}31>_\alpha$ (type A), which were visible with $\mathbf{g} = <0\bar{2}0>_\alpha$ and $\mathbf{g} = <11\bar{1}>_\alpha$ in Fig. 4.5 and Fig. 4.6 respectively, are now invisible.

Figures 4.8 (a) and (b) again show CDF and BF images respectively of the same region in the as-quenched microstructure in the binary Al-10Mg alloy. The electron beam is near $<101>_\alpha$ and the selected operating **g** vector is now $<\bar{2}02>_\alpha$. With this operating **g** vector, all three distinguishable sets of dislocations are now visible.

After careful tilting experiments including the micrographs presented above, it was confirmed that there are three distinguishable sets of dislocations, A, B and C within the as-quenched microstructure in the binary Al-10Mg alloy. The dislocation arrays shown in Figures 4.5 to 4.8 were found to be representative of the microstructure found at random locations within specimens in the as-quenched condition.

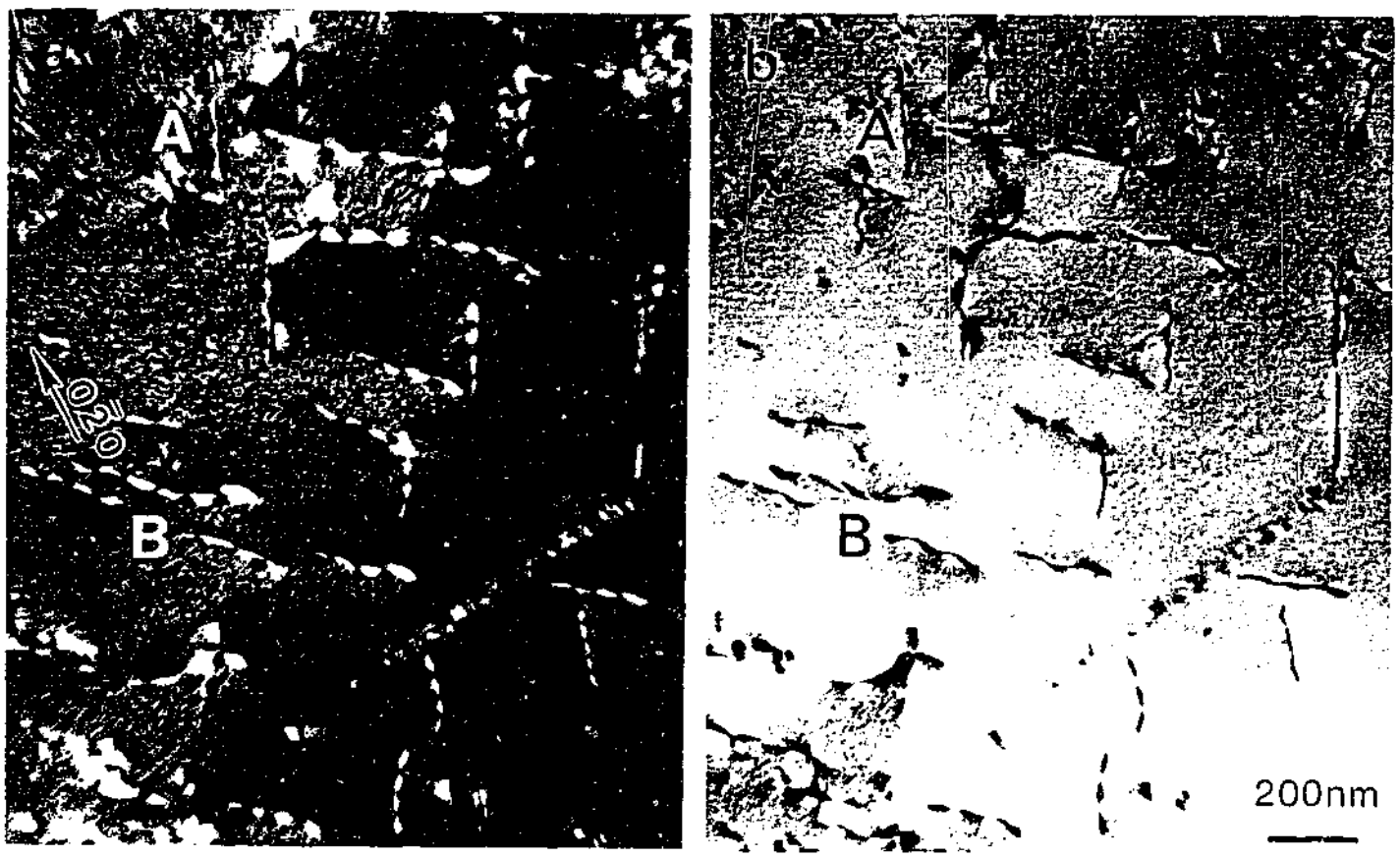

Figure 4.5 TEM micrographs showing (a) CDF and (b) BF images of the as-quenched microstructure in Al-10Mg alloy with **B** approximately parallel to $<101>_\alpha$ direction and the operating **g** vector parallel to $<0\bar{2}0>_\alpha$.

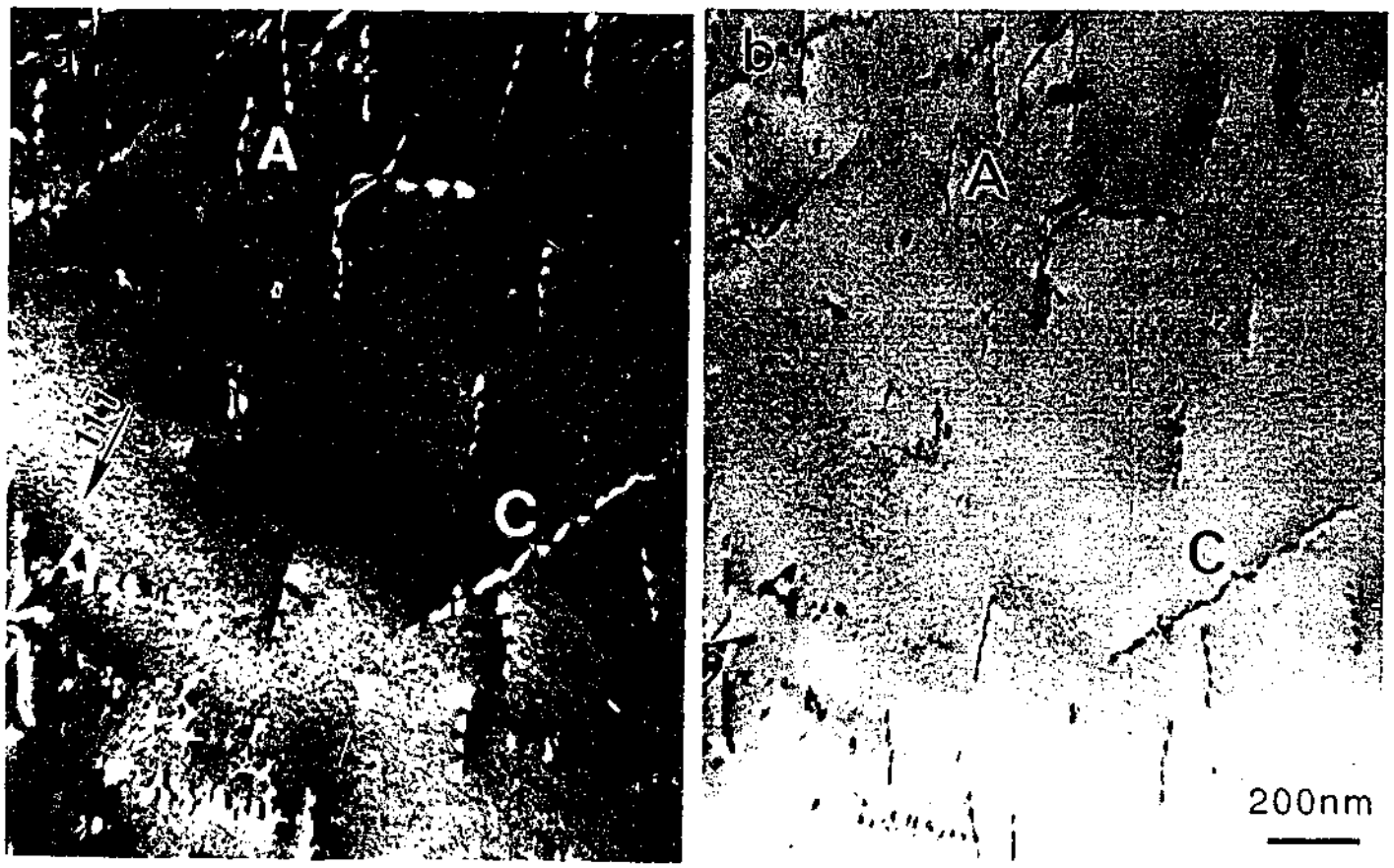

Figure 4.6 TEM micrographs showing (a) CDF and (b) BF images of the as-quenched microstructure in the binary Al-10Mg alloy. Electron beam is near a $<101>_\alpha$ direction and the operating **g** vector is $<11\bar{1}>_\alpha$.

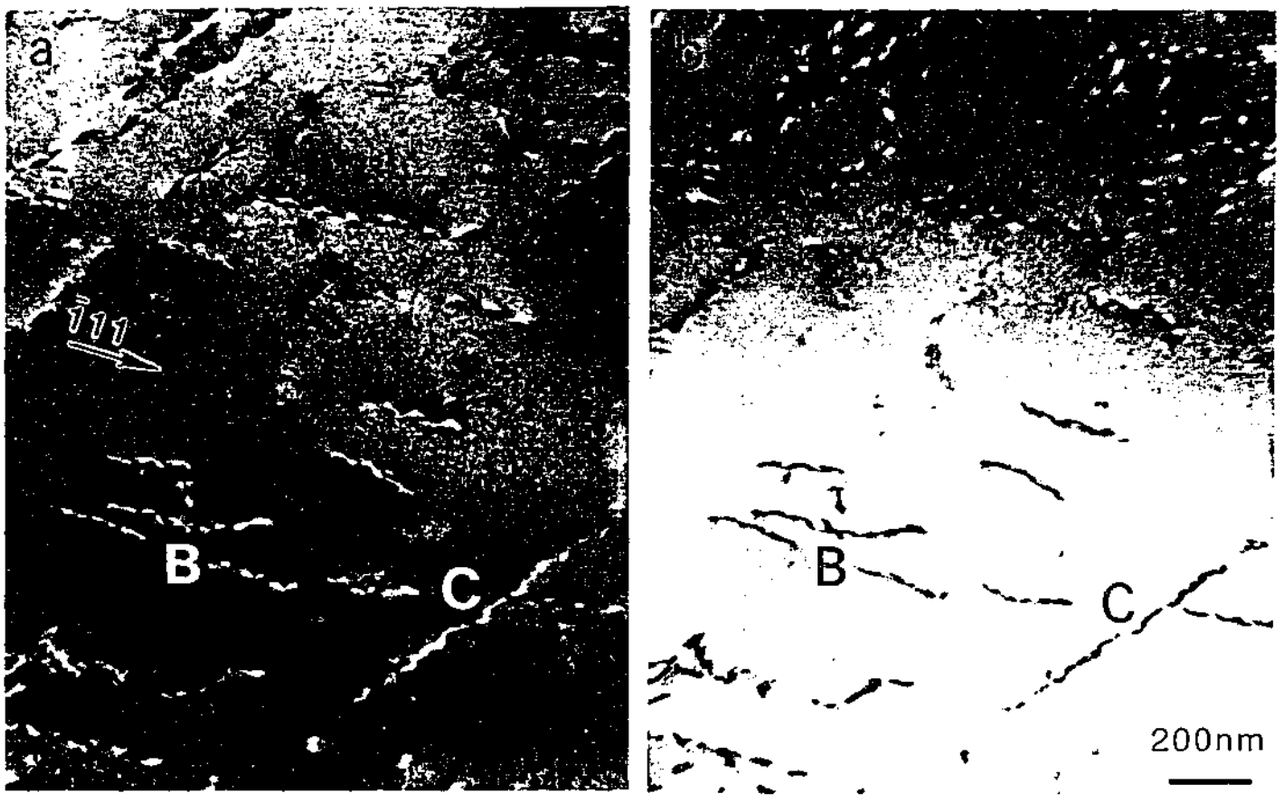

Figure 4.7 TEM micrographs showing (a) CDF and (b) BF images of dislocation structures in the binary Al-10Mg alloy. Electron beam is near $<101>_\alpha$ and the operating g vector is $<\bar{1}11>_\alpha$.

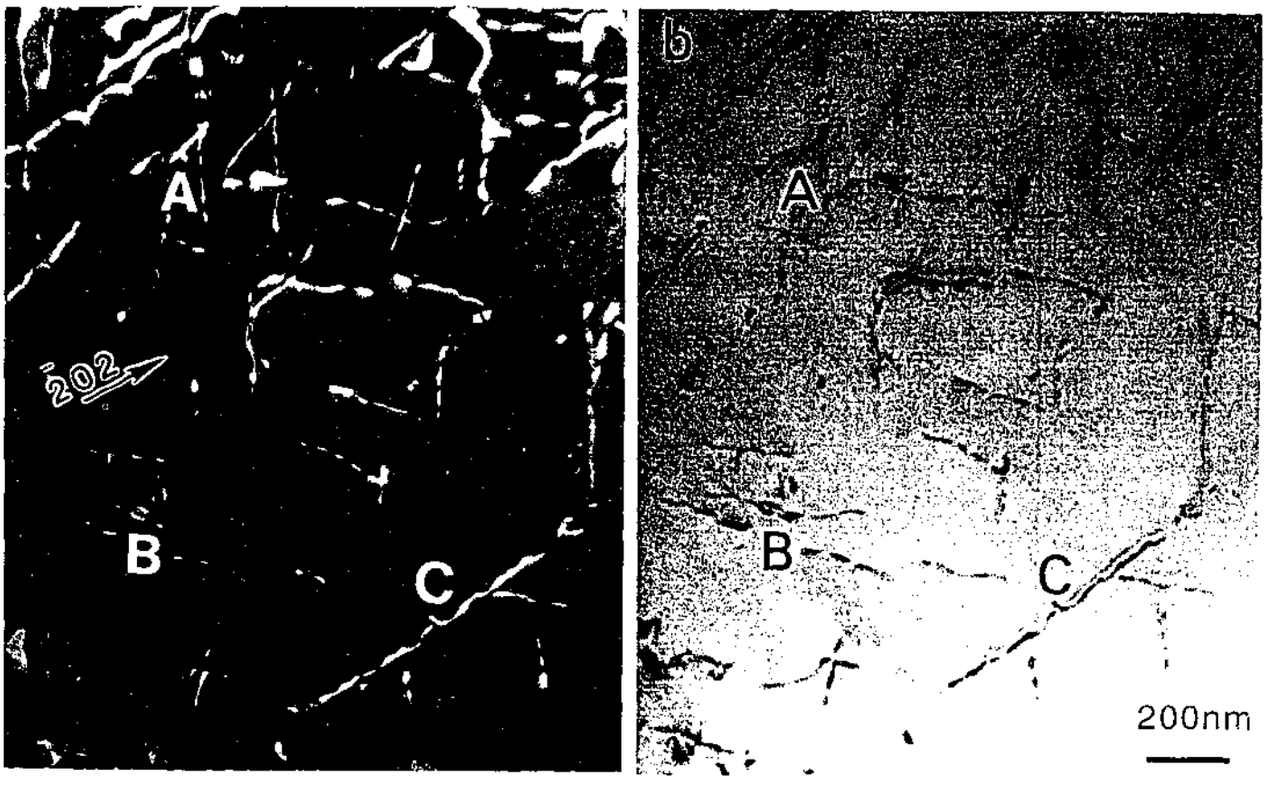

Figure 4.8 TEM micrographs showing (a) CDF and (b) BF images of the as-quenched microstructures in the binary alloy. Electron beam is near $<101>_\alpha$ and the selected operating g vector is $<\bar{2}02>_\alpha$.

Table 4.1 presents a summary of a crystallographic analysis of the dislocations observed in the as-quenched microstructure of the binary Al-10Mg alloy. Dislocations A were visible with any of the operating vectors **g** of <11$\bar{1}$>, <0$\bar{2}$0>, <$\bar{2}$02>, <131>, <220>, <20$\bar{2}$> and <022>, but invisible when the operating vectors **g** were parallel to <$\bar{1}$11> and <1$\bar{1}\bar{1}$>. Using the **g.b** = 0 invisibility criterion, the possible Burgers vectors are **b** = a/2[110], **b** = a/2[101] or **b** = a/2[01$\bar{1}$]. If the Burgers vector were **b** = a/2[101] for dislocations A, then these dislocations should be invisible with **g** =<0$\bar{2}$0>. However, the dislocations were visible in images with **g** = <0$\bar{2}$0>, eliminating this hypothesis. Similarly, if the Burgers vector were **b** = a/2[01$\bar{1}$] for dislocations A, then they should be invisible with **g** = <022>, but again this did act prove to be the case. Therefore, the only consistent solution for dislocations A was found to be **b** = a/2[110].

Dislocations B in as-quenched Al-10Mg alloy were visible when the operating **g** vectors were selected from <0$\bar{2}$0>, <$\bar{1}$11>, <$\bar{2}$02>, <131>, <1$\bar{1}\bar{1}$>, <20$\bar{2}$> and <022>, but invisible with both the <11$\bar{1}$> and <220> reflections. The possible Burgers vectors are thus initially defined as **b** = a/2[1$\bar{1}$0], **b** = a/2[101] and **b** = a/2[011], which have **g.b** = 0 for the <11$\bar{1}$>. However, only **b** = a/2[1$\bar{1}$0] satisfies the condition for the <220> reflection, for which dislocations B were invisible. Therefore, the only consistent solution for dislocations B was found to be **b** = a/2[1$\bar{1}$0].

Dislocations C in as-quenched Al-10Mg alloy were visible when the operating **g** vectors were selected from <11$\bar{1}$>, <$\bar{1}$11>, <$\bar{2}$02>, <220>, <1$\bar{1}\bar{1}$>, <20$\bar{2}$> and <022>, but invisible with the <0$\bar{2}$0> and <131> reflections. Applying the **g.b** = 0 invisibility criterion, the possible Burgers vectors are **b** = a/2[101] and **b** = a/2[10$\bar{1}$], which have **g.b** = 0 for the <0$\bar{2}$0> reflection, and **b** = a/2[10$\bar{1}$] for the <131> reflection. Therefore, for dislocations C the criterion is only consistently satisfied by the Burgers vector **b** = a/2[10$\bar{1}$].

Table 4.1 Conditions of visibility for dislocations in as-quenched Al-10Mg alloy.

Electron Beam **B**									
	<101>$_\alpha$ Vector **g**				<1$\bar{1}$2>$_\alpha$ Vector **g**			<1$\bar{1}$1>$_\alpha$ Vector **g**	
Dislocation	<11$\bar{1}$>	<0$\bar{2}$0>	<$\bar{1}$11>	<$\bar{2}$02>	<131>	<220>	<1$\bar{1}\bar{1}$>	<20$\bar{2}$>	<022>
A	X	X	O	X	X	X	O	X	X
B	O	X	X	X	X	O	X	X	X
C	X	O	X	X	O	X	X	X	X

X = loop visible **O = loop invisible**

A crystallographic analysis for dislocation structures in the as-quenched condition in the ternary Al-10Mg-0.5Ag alloy was conducted using a similar method to that for the binary Al-10Mg alloy that is presented in Figures 4.5 to 4.8, and for which the results are summarised in Table 4.1.

Figure 4.9 presents TEM micrographs of typical dislocation structures in the as-quenched condition in the ternary Al-10Mg-0.5Ag alloy. Figures 4.9 (a) and (b) show CDF and BF images, respectively. The electron beam is approximately parallel to a $<101>_\alpha$ direction and the selected operating **g** vector is $<0\bar{2}0>_\alpha$. There are two distinguishable sets of dislocations which are visible. One set of dislocations have a projected trace parallel to $<\bar{1}31>_\alpha$ and the other set is parallel in projection to $<\bar{1}\bar{1}1>_\alpha$. Those sets of dislocations parallel to $<\bar{1}31>_\alpha$ and $<\bar{1}\bar{1}1>_\alpha$ are referred to as arrays A and B, respectively.

Figures 4.10 (a) and (b) show CDF and BF images respectively of the same field in the as-quenched microstructure in ternary Al-10Mg-0.5Ag alloy. The electron beam is again near $<101>_\alpha$ and the operating **g** vector now parallel to the $<\bar{1}\bar{1}1>_\alpha$ direction. As is evident, only one set of dislocations (B) is now visible, but the array of dislocations (type A), which were visible with $\mathbf{g} = <0\bar{2}0>_\alpha$ in Figure. 4.9, are now invisible.

Figures 4.11 (a) and (b) again present CDF and BF images respectively of the same region in the as-quenched microstructure in the ternary Al-10Mg-0.5Ag alloy. The electron beam is near $<101>_\alpha$ and the operating **g** vector is now $<\bar{1}11>_\alpha$. With this operating **g** vector, only one set of dislocations (A) is now visible. However, the other set of dislocations (B), which were visible both with $\mathbf{g} = <0\bar{2}0>_\alpha$ and $\mathbf{g} = <\bar{1}\bar{1}1>_\alpha$, in Fig. 4.9 and Fig. 4.10 respectively, are now invisible.

After careful tilting experiments including the micrographs presented above, it was confirmed that there are typically two distinguishable sets of dislocations, A and B, within the as-quenched microstructure in ternary Al-10Mg-0.5Ag alloy. The dislocation arrays shown in Figures 4.9 to 4.11 were found to be representative of the microstructure found at random locations within specimens in the as-quenched condition.

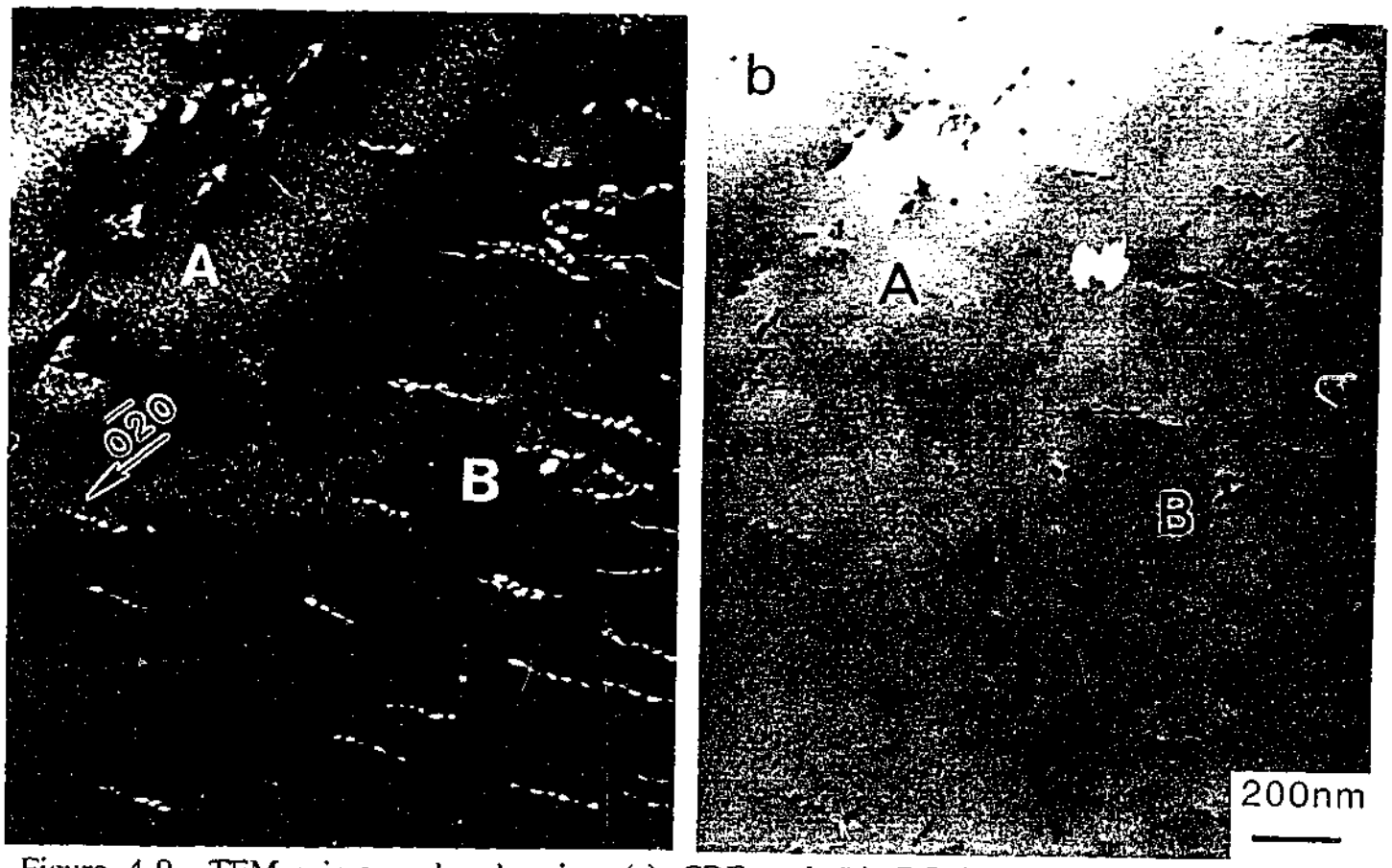

Figure 4.9 TEM micrographs showing (a) CDF and (b) BF images of the as-quenched microstructure in Al-10Mg-0.5Ag alloy with **B** approximately parallel to $<101>_\alpha$ and the operating **g** vector parallel to $<0\bar{2}0>_\alpha$.

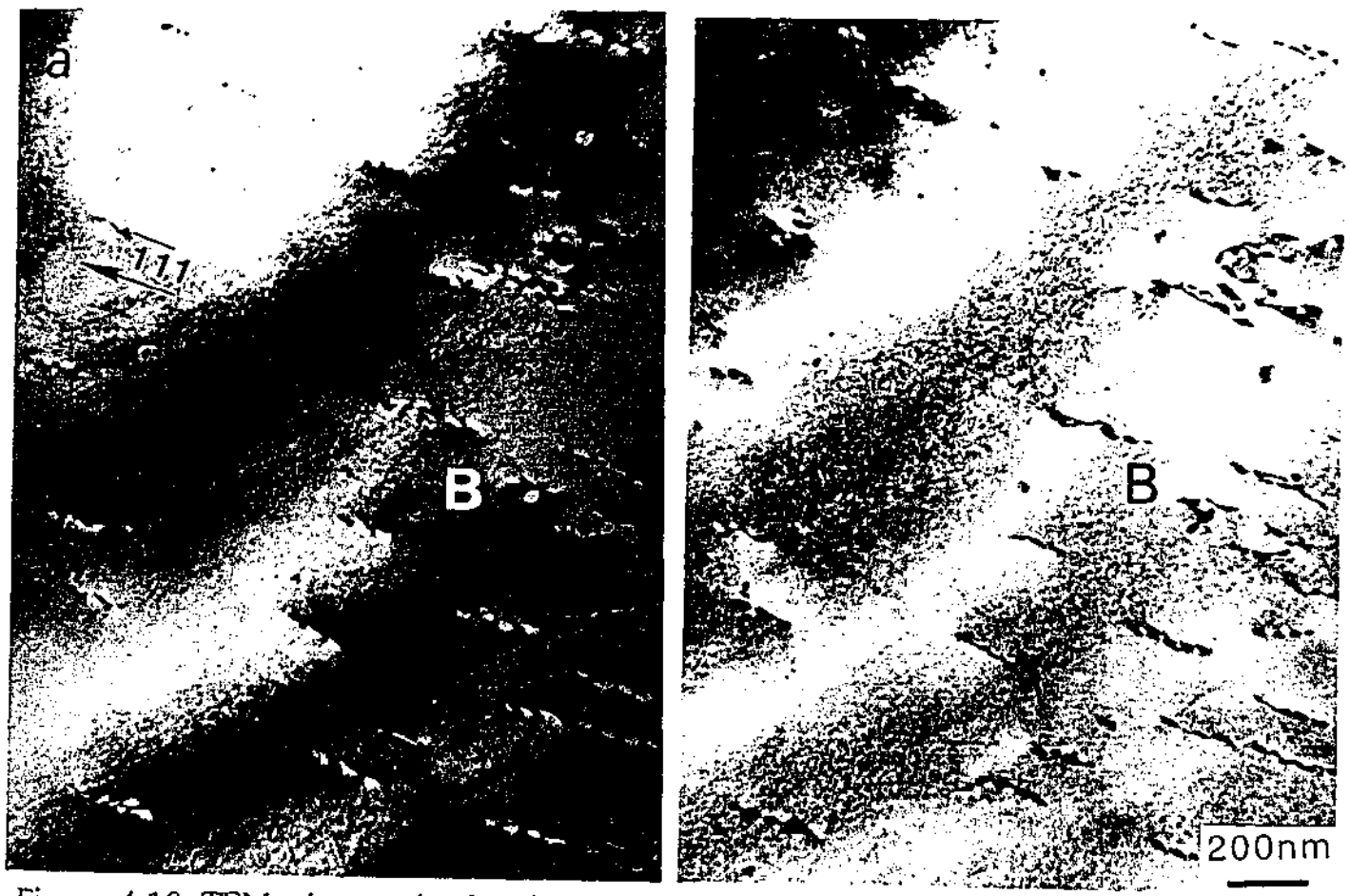

Figure 4.10 TEM micrographs showing (a) CDF and (b) BF images of dislocation structures in the ternary alloy. Electron beam is near $<101>_\alpha$ and the operating **g** vector is $<\bar{1}\bar{1}1>_\alpha$.

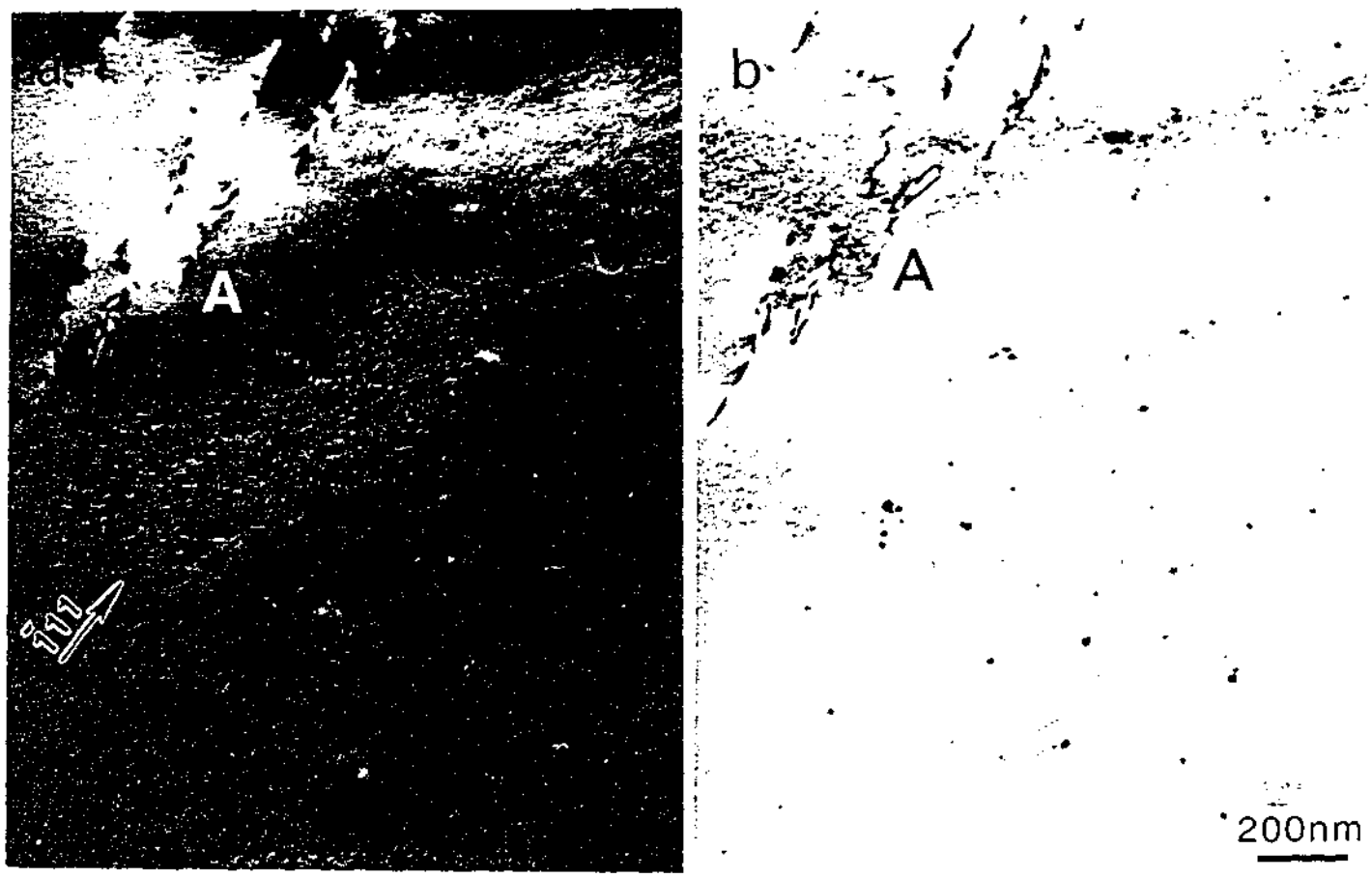

Figure 4.11 TEM micrographs showing (a) CDF and (b) BF images of dislocation structures in the as-quenched condition in the ternary Al-10Mg-05Ag alloy. Electron beam is near $<101>_\alpha$ and the operating **g** vector is $<\bar{1}11>_\alpha$.

Table 4.2 shows a summary of crystallographic analysis of the dislocations observed in the as-quenched microstructure of the ternary Al-10Mg-0.5Ag alloy. Dislocations A were visible with any of the operating vectors **g** of <020>, <0$\bar{2}$0>, <$\bar{1}$11>, <$\bar{2}$00> and <$\bar{2}$20>, but invisible when **g** was parallel to <$\bar{1}\bar{1}$1> and <11$\bar{1}$>. Using the **g.b** = 0 invisibility criterion, the possible Burgers vectors are **b** = a/2[1$\bar{1}$0], **b** = a/2[101] or **b** = a/2[011]. After detailed consideration, the only consistent solution for dislocations A was found to be **b** = a/2[1$\bar{1}$0].

Dislocations B in as-quenched Al-10Mg-0.5Ag alloy were visible when the operating **g** vectors were selected from <020>, <0$\bar{2}$0>, <$\bar{1}\bar{1}$1>, <11$\bar{1}$> and <$\bar{2}$20>, but invisible with both the <$\bar{1}$11> and <$\bar{2}$00> reflections. The possible Burgers vectors are thus initially **b** = a/2[110], **b** = a/2[101] and **b** = a/2[01$\bar{1}$], which have **g.b** = 0 for the <$\bar{1}$11> reflection, and **b** = a/2[01$\bar{1}$] for the only <$\bar{2}$00> reflection. Therefore, the only consistent solution for dislocations B was found to be **b** = a/2[01$\bar{1}$].

Table 4.2 Conditions of visibility for dislocations in as-quenched Al-10Mg-0.5Ag alloy.

	Electron Beam **B**						
	$<101>_\alpha$ Vectors g					$<001>_\alpha$ Vectors **g**	
Dislocation	<020>	$<0\bar{2}0>$	$<\bar{1}\bar{1}1>$	$<\bar{1}11>$	$<11\bar{1}>$	$<\bar{2}00>$	$<\bar{2}20>$
A	X	X	O	X	O	X	X
B	X	X	X	O	X	O	X

X = loop visible O = loop invisible

This series of dislocation analyses establishes that the identity of the dislocations in the as-quenched condition in both binary Al-10Mg and ternary Al-10Mg-0.5Ag alloys is the same. That is, both alloys contain exclusively unit perfect dislocations which have Burgers vectors of the classical form a/2<110>. This result suggests that trace additions of Ag to binary Al-10Mg alloys have no obvious effect on the identity of the predominant dislocations in the as-quenched microstructure. No evidence could be found for dissociation of these dislocations in the alloys in this condition. However, it was interesting to note that whilst it was common to observe all three sets of dislocations (A, B and C) in binary Al-10Mg alloys, there were often only two sets of dislocations in the images of the ternary Al-10Mg-0.5Ag microstructures. This result suggested that the density of dislocations in the as-quenched microstructure may be reduced by trace additions of Ag to Al-Mg alloys.

Measurements of Length of Dislocation Lines

A method for estimating the number density of dislocations, as initially described by Bailey and Hirsch (1960), was outlined in Chapter 3. The total projected length of observed dislocations in a thin foil sample, R_P, was measured from CDF and BF image negatives, with the selected operating **g** vectors being $<\bar{2}02>_\alpha$ and $<0\bar{2}0>_\alpha$ for the binary and ternary alloys, respectively. Both these g vectors allow that all possible existing dislocations are visible simultaneously as shown in the previous section. Assuming that the dislocation segments are randomly oriented, the mean length of dislocation line, R, can be derived from the projected length, R_P, using equation (4), Chapter 3.

Measured total projected length of dislocations, R_P, in the binary alloy was more than twice that measured in the ternary alloy, as presented in Table 4.3. The errors in R_P shown in Table 4.3 were calculated on the assumption that the length of each projected segment of dislocation line could be measured accurately to within ± 0.01 cm (0.1 mm). In the case of Al-10Mg alloy, for example, there were 61 separate segments of dislocation line and the total error was thus of the order of ± 0.61 cm.

Table 4.3 Measurements of dislocation line length in Al-10Mg and Al-10Mg-0.5Ag alloys.

Alloy	Al-10Mg	Al-10Mg-0.5Ag
R_P	64.92 ± 0.61 cm	29.83 ± 0.25 cm
R	82.66 ± 0.78 cm	37.98 ± 0.32 cm
A	9.75x8.10 = 78.975 cm^2	9.80x7.90 = 77.420 cm^2

Measurements of Foil Thickness

Foil thickness of the TEM samples was estimated using the two-beam convergent beam electron diffraction (CBED) method (Kelly et al. 1975), as described in Chapter 3. Figure 4.12 shows typical examples of CBED patterns recorded from (a) Al-10Mg and (b) Al-10Mg-0.5Ag alloys in the as-quenched condition. The two beam condition was selected with the electron beam parallel to $<110>_\alpha$ and an operating vector **g** = 220. The values of S_i are determined by measuring the distance $\Delta\theta_i$ from the centre of the diffracted beam profile to each of the successive minima, together with the distance $2\theta_d$ between the centre spot and the diffracted spot, Table 4.4. Then $(S_i/n_i)^2$ versus $(1/n_i)^2$ was plotted and the foil thickness calculated according to equation 1a, as shown in Chapter 3. Results of the thickness determinations are also shown in Table 4.4.

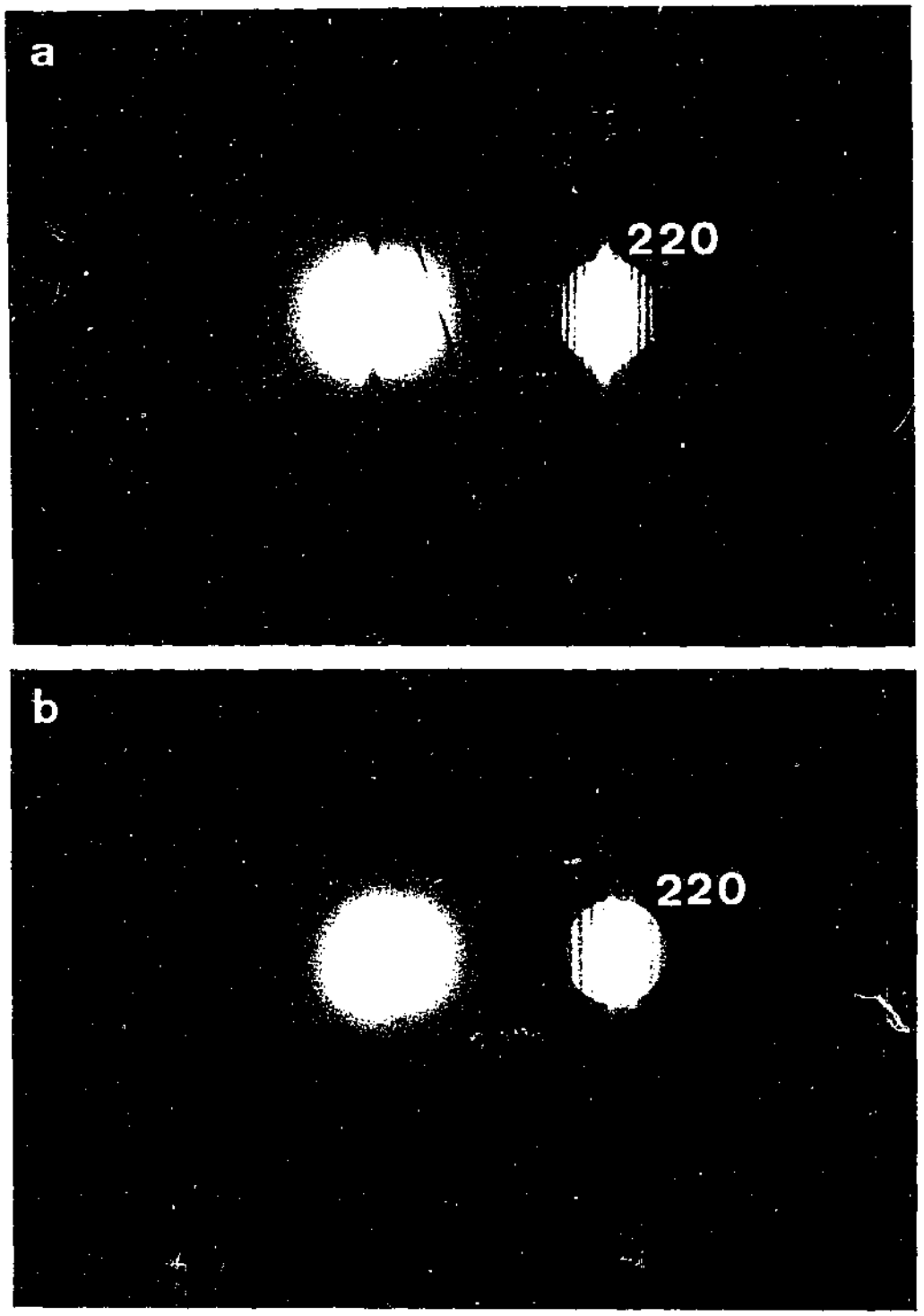

Figure 4.12 Two-beam CBED patterns recorded from (a) Al-10Mg and (b) Al-10Mg-0.5Ag alloys in the as-quenched condition for foil thickness determination. The two beam condition is such that g = 220 is the operating vector at 120kV.

Table 4.4 Measurements of pattern parameters and foil thickness in Al-10Mg and Al-10Mg-0.5Ag alloys.

No	$2\theta_d$ (mm)	$\Delta\theta_1$ (mm)	$\Delta\theta_2$ (mm)	$\Delta\theta_3$ (mm)	$\Delta\theta_4$ (mm)	R (mm)	Thickness (nm)
Al-10Mg	10.9	1.0	1.9	2.7	3.5	4.8	75.0
Al-10Mg-0.5Ag	10.9	1.8	2.3	3.8	-----	4.8	63.3

It is commonly recognised that dislocations may be lost from the thinner regions of thin foil samples, either during foil preparation due to the relaxation of matrix constraints or during handling or observation due to mechanical instability and/or local specimen heating. For this reason, an attempt was made to conduct these measurements in thicker regions of the thin foil samples and to choose regions of similar thickness in specimens of the two different alloys. In this way, an attempt was thus made to ensure that the values of dislocation density were at least comparatively accurate.

The errors in foil thickness were analysed by the repeated measurements of the fringes in the diffraction discs in the same negatives, and estimated to be approximately ± 2%. Therefore, foil thickness for the binary Al-10Mg alloy was 75.0 ± 1.5 nm, and for the ternary Al-10Mg-0.5Ag alloy was 63.3 ± 1.3 nm.

The Determination of Dislocation Density

The number density of dislocations was determined using equation (4), Chapter 3. It is defined as the measured total dislocation line length in a unit volume of crystal, giving a parameter with dimensions cm/cm^3 or cm^{-2}. Table 4.5 compares the dislocation densities calculated for the binary Al-10Mg and ternary Al-10Mg-0.5Ag alloys, and shows that density in the binary alloy is almost twice that in the ternary alloy. Bailey and Hirsch (1960) have suggested that this method of estimating the density of dislocations may involve errors of up to ± 25%. In addition, the foil thickness cannot be claimed to be accurate to better than ± 2% (Kelly et al. 1975).

Table 4.5 Comparisons of dislocation densities for Al-10Mg and Al-10Mg-0.5Ag alloys.

	Al-10Mg alloys	Al-10Mg-0.5Ag alloys
Foil Thickness, t (nm)	75.0 ± 1.5	63.3 ± 1.3
Magnification	36300 x	36300 x
Dislocation Density, ρ (cm^{-2})	5.08×10^9	2.81×10^9

However, even allowing for such errors, it is clear that the dislocation density in the ternary Ag-modified alloy is significantly lower than that in the binary alloy. This is consistent with the proposal that the addition of Ag will lead to a reduction in the as-quenched dislocation density. The precise role of Ag has not been verified directly, but it is commonly suggested that, because of the high binding energy between Ag atoms and vacancies (Huang and Zheng 1998), the Ag atoms present trap vacancies and reduce the number of vacancies that condense and collapse to form dislocation loops.

The Relationship Between Hardness and Dislocation Density

In order to examine the relationship between the hardness and the number density of dislocations in the as-quenched state, theoretical calculations of shear stress were carried out using an equation of the form (Dieter 1988):

$$\tau = \alpha \mu b \rho^{0.5} \qquad (4.1)$$

where **b** is the Burgers vector, ρ is the dislocation density, τ is shear strength, μ is the shear modulus and α is a geometric constant. Hansen (1977) obtained a value for α of 0.2 for aluminium alloys, while from TEM observations in the current research, the dislocation densities in the as-quenched condition were 5.1×10^9 cm^{-2} for the binary Al-10Mg alloy and 2.8×10^9 cm^{-2} for the ternary Al-10Mg-0.5Ag alloy. In the case of the aluminium alloy, **b** is 2.86×10^{-10} m and μ is 25GPa (a pure aluminium alloy) (Mondolfo 1976). Using these data, the values of shear yield strength were calculated to be 10.2MPa and 7.6MPa for the Al-10Mg and Al-10Mg-0.5Ag alloys respectively.

The relationship between tensile stress (σ) and shear stress (τ) is commonly assumed to be of the form $\sigma = A\tau$ (Dieter 1988), where A is the Taylor factor. The Taylor factor for f.c.c materials is approximately 3.067 (Hansen 1977), and the values of tensile yield stress derived from the above values of shear stress were thus 31.3MPa and 23.3MPa for the Al-10Mg and Al-10Mg-0.5Ag alloys respectively. Given that it is also commonly accepted that the relationship between tensile yield stress and Vickers hardness (VHN) is at least approximately of the form σ = 3xVHN, it is thus to be expected that on the basis of differences in dislocation density alone, the hardness values for the binary and ternary alloys would be expected to differ by a factors of $(5.1/2.8)^{0.5} = 1.35$. Allowing for errors of ± 25% on the measurements of ρ and taking the worst possible combination of errors, this ratio might be reduced to a value of 1.09.

From the measurements of bulk Vickers hardness (Figs 4.1 to 4.3), experimental values of the ratio of as-quenched hardness in the binary alloys to that in the ternary alloys were of the order of 1.12 and 1.06 for the Al-5Mg and Al-10Mg alloys respectively. Thus, even allowing for substantial experimental errors in the determination of dislocation densities (ρ), it is clear that the measured differences in ρ are sufficient to account for the measured differences in as-quenched hardness between the Ag-free and Ag-modified alloys.

4.5 Discussion

Precipitation Hardening Response

It has been well recognised (Polmear 1995) that alloys of the binary Al-Mg system are generally classified as non-heat treatable, so that an age-hardening response is not expected. However, to be accurate there is evidence that while binary Al-Mg alloys with <5% Mg exhibit little or no age-hardening response, those alloys with > 7% Mg do produce detectable precipitation hardening (Polmear 1964). The current hardness measurements in binary alloys, which are shown in Figures 4.1 and 4.2, are clearly quantitatively consistent with these earlier claims. No detectable age-hardening response was obtained in the alloy with lower Mg content (5%), but there was a small but significant age-hardening response at the higher magnesium level (10%). Increased levels of solute supersaturation will not only increase the volume fraction of precipitate particles, but may also promote an increased nucleation rate leading to a finer and more uniform precipitate distribution during the isothermal ageing process. The present results indicate that the measured age-hardening response is also very similar to that reported previously, as described in Chapter 2 (Polmear and Sargant 1963, Takahashi et al. 1978).

It is clearly seen from Figures 4.1 to 4.3 that the trace additions of Ag stimulate an age-hardening response for the Al-Mg alloy of lower Mg content where it did not exist in the binary alloy, and that the age-hardening response of an Al-10% Mg alloy is dramatically enhanced by trace additions of Ag. In the latter case, the addition of Ag both accelerates the hardening response and leads to a significant increase in maximum hardness at a given ageing temperature. One potential source of this stimulation of the age-hardening response and this improved hardening behaviour in both ternary alloys derives from observations (Ito et al. 1971) that as little as 0.5% Ag reduces substantially the solubility of magnesium in aluminium over the full range of temperatures below the eutectic temperature. It was suggested that the combination of increased supersaturation and the chemical affinity between Ag and Mg atoms would bring the formation of stable GP zones (approximately spherical Mg-Ag zones having the AuCu I type structure, a = 0.442 nm, c = 0.348 nm), which may act as nucleation sites for the stable T phase ($Mg_{32}(Al,Zn)_{49}$, space group $Im\bar{3}$, a = 1.416 nm) precipitates. However, these suggestions have yet to be supported by clear, direct evidence, such as direct observation of GP zones by transmission electron microscopy (TEM).

It has been suggested (Polmear 1987) that the effect of Ag on the age-hardening response is mainly two-fold. One is that Ag may facilitate the nucleation of an existing precipitate by the reduction of the interfacial energy between the precipitate and matrix. The other is that Ag may promote the formation of a different phase (e.g. omega (Ω) phase in an Al-4Cu-0.3Mg-0.5Ag alloy (wt%)). There is evidence (Wheeler et al. 1965) that trace additions of Ag may promote a change in precipitate identity in an Al-Mg-Ag alloy. In addition, modified intermediate phases

were observed in the ternary Al-10Mg-0.5Ag alloy (Takahashi et al. 1978). However, the experimental evidence was not sufficient to reveal the detailed crystal structures of precipitate particles in the ternary alloy. Detailed microstructural characterisation, including identification of the precipitate phases responsible for hardening will thus be presented the following Chapter 5, to provide a basis for understanding the origin of the enhanced age-hardening response in the Al-10Mg-0.5Ag alloy.

The hardness of the as-quenched condition in Al-10Mg alloys (~90VHN) is significantly higher than that of typical commercial age hardenable Al alloys, such as Al-4Cu-0.3Mg (2xxx series) alloys (~70VHN). This suggests that in Al-Mg alloys there is a substantial contribution to the as-quenched hardness from solid solution strengthening by solute Mg. This result is clearly supported by the observation that the binary Al-Mg alloy with higher Mg solute content has an as-quenched hardness (~90VHN) that is substantially higher than that of alloy of lower Mg content (~56VHN).

It has been reported that the age-hardening response in the ternary Al-4Cu-0.3Mg alloy is significantly enhanced by trace additions of Ag in sample aged at 150°C and 200°C (Polmear 1968; Lee, Muddle and Polmear 1995; Ringer, Polmear and Sakurai 1996). In the present research, similar enhancement of hardness was observed in the alloys of the Al-Mg system as a result of microalloying with Ag. The maximum hardness value of the experimental Al-10Mg-0.5Ag alloy is slightly higher than that of the quaternary Al-4Cu-0.3Mg-0.4Ag alloy when both alloys are aged at 200°C, but the time required to achieve maximum hardness in Al-10Mg-0.5Ag alloy is longer than that of the quaternary alloy. Although maximum hardness in the current experimental ternary alloys may be higher than that of the Al-Cu-Mg-Ag alloy, the age-hardening capability (i.e. the hardness increment between the as-quenched and maximum hardness) in the experimental ternary alloy is significantly lower than that of the Al-Cu-Mg-Ag alloy.

Effects of Cold Work

It has been demonstrated that 7% cold work post solution treatment and prior to ageing enhances the age-hardening response in ternary Ag-bearing alloys aged at both 160°C and 200°C. Although the increments in the maximum hardness of samples subjected T6 and T8 treatments were moderate (~12VHN), the time to achieve maximum hardness during the T8 treatment was significantly reduced compared to that for the T6 treatment. The effect of cold work on the age-hardening behaviour in binary Ag-free alloys has been investigated (Cottereau et al. 1989), as described in Chapter 2, and it has been shown that the maximum hardness does not increase significantly for up to 25% cold work. However, the current results suggest that the effect of microalloying additions of Ag may be further enhanced by cold-working prior to ageing, most notably via an acceleration in the kinetics of precipitation hardening. Such an observation is potentially significantly important if these alloys were to be considered for industrial applications

where the practicality of the thermomechanical processing route is a major issue.

A substantial decrease in hardness was observed in the ageing curve for the cold worked alloy aged at 200°C during the very early stages of ageing, but this was not as obvious during ageing at 160°C. It is suggested that this hardness decrease is controlled by the process of recovery during which those dislocations introduced during plastic deformation are rearranged and/or eliminated. The softening that accompanies such recovery is eventually balanced and outweighed by precipitation hardening, and the increase in maximum hardness observed in the cold-worked alloys suggests that the plastic deformation has ultimately been effective in promoting a precipitate distribution more effective in restraining dislocation motion. During ageing at 160°C the rate of recovery is slower and the softening due to recovery is less obvious during the early stages of ageing. It is also noteworthy that the difference in hardness sustained between the deformed and undeformed samples during ageing at 160°C in noticeably larger than during 200°C ageing.

As-Quenched Microstructures

The identity of the dislocations in the as-quenched microstructures of the binary Al-10Mg and ternary Al-10Mg-0.5Ag alloys was found to be the same; that is in both alloys all dislocations were unit perfect dislocations with Burgers vectors of the form a/2<110>. This result suggests that trace additions of Ag to binary Al-10Mg alloy have no effect on changing the identity of the dislocations. There was no evidence of dissociation of the a/2<110> dislocations in either alloy as-quenched. However, the present measurements did establish a significant difference in the dislocation densities within Ag-free and Ag-modified samples subjected to identical solution treatment and quenching. The dislocation density of the Al-10Mg-0.5Ag ternary alloy was only ~55% of that in the Al-10Mg binary alloy.

This significant reduction in the dislocation population is most likely attributable to the influence of Ag on the vacancy distribution following solution treatment and quenching. During solution treatment, an increased density of vacancies is created and, during a rapid water quench, a quenched-in excess of vacancies is retained in the solid solution. The binding energies between these quenched-in excess vacancies and distributed solute atoms are relatively high in those Al alloys containing Mg and Ag atoms, so that some fraction of those vacancies will effectively be trapped by the solute atoms.

Trace additions of particular elements in Al alloys, mainly in Al-Cu based alloys, such as Cd, In, Sn, Ag, Mg and Li can influence the age-hardening response at room and elevated temperatures significantly. The different influences can be interpreted in two ways; one involves the solute-solute interaction, and the second the interaction between solute quenched-in excess vacancies. The Mg and Ag atoms have a strong tendency to interact with each other because the

Ag-Mg pair has a negative excess enthalpy value, while the interaction between solute atoms and quenched-in vacancies is stronger for Mg atoms than for Ag atoms (Hung and Zheng 1998). This implies that a lower number density of dislocations is to be expected in Al-Mg-Ag ternary alloys compared Al-Mg binary alloys of similar composition. This is consistent with measurement of dislocation density recorded in Table 4.5.

4.6 Conclusions

Based on the measurements of hardness in binary and ternary alloys, and analyses of the as-quenched microstructures of Al-10% Mg alloys with and without 0.5% Ag, the principal results may be summarised as follows:

(1) There is no detectable age-hardening response in solution treated and quenched Al-5Mg alloy aged at 200°C. However, an increase in solute Mg content does lead to a modest precipitation hardening response in supersaturated Al-10Mg alloy aged at 160°C, 200°C and 240°C.

(2) Trace additions (0.5 wt%) of Ag to Al-Mg alloys with low solute Mg contents (< 5 wt%) promote an age-hardening response, while similar additions to Al-Mg alloys with higher solute Mg contents enhance significantly the age-hardening response. In the latter alloy, the addition of Ag leads to both an acceleration of the precipitation hardening process and an increase in maximum hardness. In Al-10Mg-0.5Ag alloy, maximum hardness value of ~150VHN, 140VHN and 120VHN can be achieved during ageing at 160°C, 200°C and 240°C respectively, compared to maximum hardness values of ~119VHN, ~112VHN and ~105VHN in binary Al-10Mg alloy aged at 160°C, 200°C and 240°C respectively.

(3) The age-hardening response in an Al-10Mg-0.5Ag alloy may be significantly enhanced by the introduction of 7% cold work, post solution treatment and prior to ageing at 160°C and 200°C. The ageing behaviour is further accelerated and a modest increase (~12VHN) in maximum hardness may be obtained.

(4) The identity of the dislocations in as-quenched Ag-free and Ag-modified Al-10Mg alloys has been confirmed as unit perfect a/2<110> type. The addition of Ag does not appear to modify the form of the dislocations and no dissociation of these dislocations was resolved in this condition.

(5) The density of dislocations in the solution treated and quenched condition in the Al-10Mg alloy was higher by a factor of ~2x compared to that in Al-10Mg-0.5Ag alloy subjected to similar treatment. This difference is more than sufficient to account for the higher hardness observed in the as-quenched binary alloy compared to that in the ternary alloy. The reduced density of

dislocations in the Ag-modified alloy is attributed to an interaction between Ag atoms and vacancies which reduces the vacancy population available to condense and collapse to form dislocation loops.

Chapter 5

Microstructural Characterisation of Al-10Mg(-0.5Ag) Alloys

5.1 Introduction

In the previous chapter, it was established that no significant age-hardening response was observed in Al-Mg alloys with lower solute contents (i.e. < 5wt%), and that Al-Mg alloys with higher solute contents (e.g. 10wt%) exhibited only a modest age-hardening response. Trace additions of Ag to binary alloys of lower Mg concentrations induced detectable precipitation hardening, while microalloying additions of Ag to Al-Mg alloys containing higher solute Mg significantly stimulated and enhanced their age-hardening response. The critically important questions, which arise from the results of these hardness measurements, are what are the characteristics of the precipitate particles formed during isothermal ageing heat treatments in the binary and ternary alloys, in terms of their crystal structures, orientation relationships with the aluminium matrix, morphologies and distributions, and how can these parameters be used to elucidate the hardening mechanisms of these experimental alloys during isothermal ageing. In addition, it is very important to clarify the effect of trace additions of Ag on the microstructural changes that occur in binary alloys, with a views to perhaps finding an alternative element to Ag to stimulate the hardening response.

As described in Chapter 2, there are existing reports on the precipitate phases in Al-Mg (Lorimer 1978, Nozato and Ishihara 1980) and Al-Mg-Ag alloys (Auld 1968, Williams 1972). Most previous studies seeking the identification of precipitate phases in Al-Mg alloys, with and without trace additions of Ag, have been carried out using DSC and the bulk X-ray diffraction techniques and there have been few detailed microstructural characterisations done using transmission electron microscopy (TEM). In particular, the constituent phases, phase distributions and morphologies of precipitate particles in aged Al-Mg(-Ag) alloys have attracted little attention and are poorly understood. Evidence on the precipitate phases in the ternary Al-Mg-Ag alloys is contradictory and it is unclear whether maximum hardness is associated with the metastable T' phase or not. Furthermore, the morphologies and distributions of this metastable T' and equilibrium T phases have not yet been clearly established.

The work to be presented in the present chapter represents the results of a detailed study of the effects of trace additions of Ag on the identities of the major precipitate phases in the Al-10Mg alloy, which exhibited attractive age-hardening behaviour. The chapter begins with the identification of precipitate phases in the binary Al-10Mg and ternary Al-10Mg-0.5Ag alloys aged at 240°C. The phases previously identified by the bulk X-ray diffraction technique and the current results from electron diffraction studies are compared. Finally, the precipitation hardening response and precipitation sequences are discussed.

In the current study, particular focus has been given to the microstructures in Al-10Mg(-0.5Ag) alloys aged at 240°C. The initial heat treatments at this temperature, which is slightly

above the normal range of ageing temperatures (130-200°C), were chosen deliberately to accelerate the ageing kinetics and promote relatively coarse precipitate particles to assist the identification of phases. A detailed and systematic characterisation of microstructural changes occurring during ageing at various temperatures (room temperature to 240°C) of Al-10Mg(-0.5Ag) alloys is presented in Chapter 6.

5.2 Experimental Results

5.2.1 Phase Identification in Binary Alloy (Al-10Mg)

Aged 0.5 h at 240°C

Bright-field (BF) transmission electron micrographs of the binary Al-10Mg alloy aged 0.5 h at 240°C are shown in Figures 5.1 (a), (b) and (c). The electron beam in these figures was approximately parallel to $<001>_\alpha$, $<110>_\alpha$ and $<112>_\alpha$ zone axes, respectively. The microstructure of this alloy contained coarse-scale (~1μm), sparsely-dispersed rod-like and/or plate-like precipitate particles. As indicated in Figs. 5.1 (a)-(c), the traces of these plate-like and rod-like particles were parallel to the traces of $\{100\}_\alpha$, $\{110\}_\alpha$, $\{311\}_\alpha$ planes and they were typically elongated parallel to a $<100>_\alpha$ direction.

A dense distribution of dislocations surrounds individual precipitate particles, especially in the $<110>_\alpha$ and $<112>_\alpha$ orientation (i.e. Figs. 5.1 (b) and (c)). These dislocations are clearly associated with the particles suggesting that significant plastic accommodation accompanies the processes of nucleation and/or growth as these particles form during the early stages of the isothermal ageing treatment. The other interesting feature of the microstructure of this binary alloy was that there was very little evidence of precipitation, i.e. there was a low volume fraction of coarse precipitate particles, compared, for example, with traditional age-hardenable Al-Cu based alloys. This is possibly due to the absence of coherent GP zones, which generally act as the nucleation sites for intermediate phases. The ageing temperature of 240°C in the present experiment is far higher than that of the GP zone solvus temperature for this composition (~0°C), so the formation of GP zones cannot be expected (Pollard 1965-65, Roth and Raynal 1974, Raynal and Roth 1975, and Lorimer 1978).

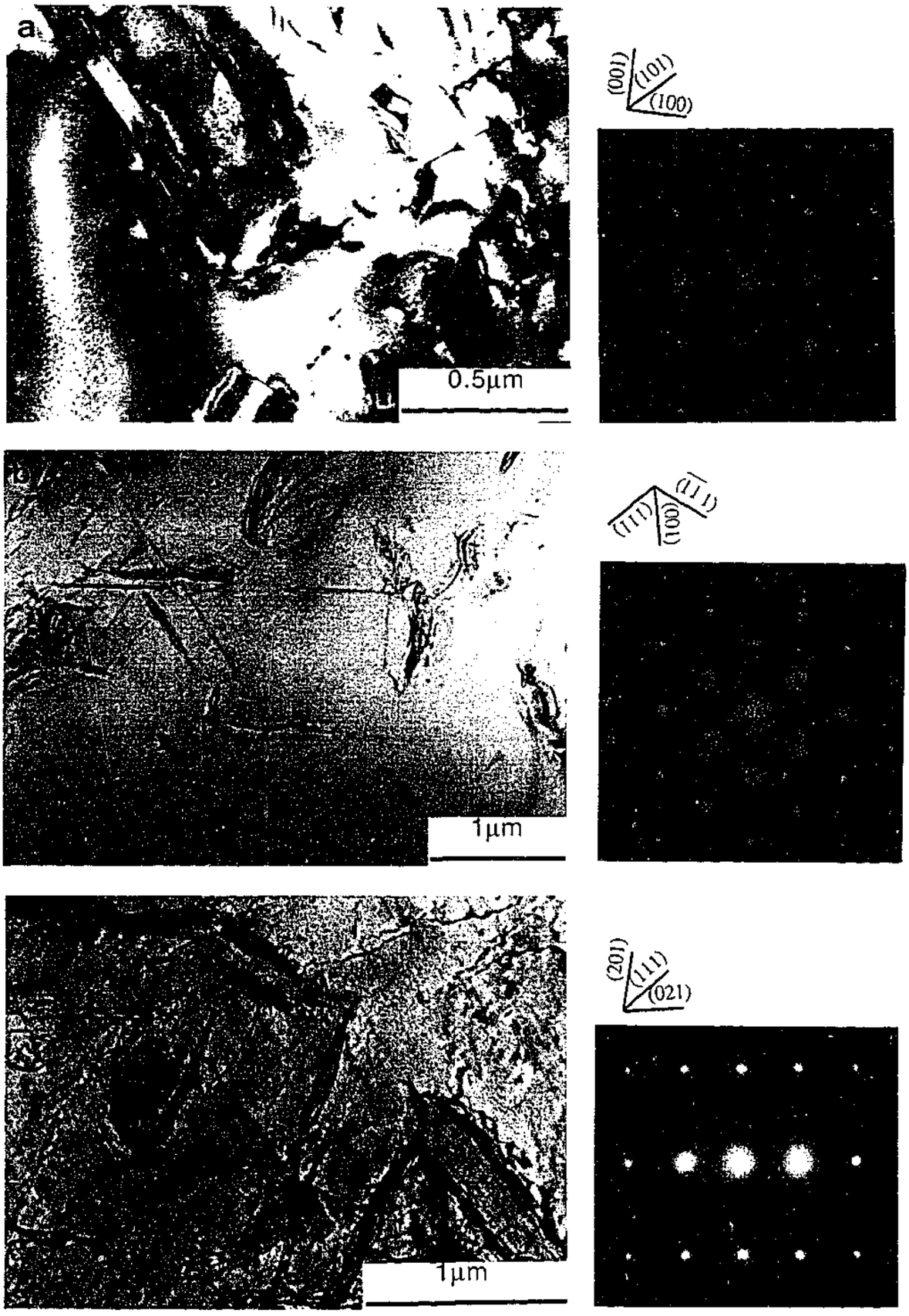

Figure 5.1 Transmission electron micrographs showing the typical aged microstructure of the Al-10Mg alloy aged 0.5 h at 240°C. Electron beam is parallel to (a) $<001>_\alpha$, (b) $<110>_\alpha$ and (c) $<112>_\alpha$ zone axes, respectively.

Identification of these rod-like or/and plate-shaped particles using electron diffraction techniques proved difficult due to rapid oxidation of these precipitate particles during the process of electropolishing. This rapid oxidation prevented to obtain diffracted reflections from these precipitate particles. However, limited evidence from low index zone axis SAED patterns recorded from regions containing these particles revealed that there were no obvious systematic zone axis patterns from the precipitate particles. This may imply that these precipitate particles do not share a simple rational orientation relationship with low index directions of the aluminium matrix phase. Alternatively, the lack of diffracted intensity from the precipitate particles may have been due to the low volume fraction of precipitate particles in the aluminium matrix, and/or to loss of precipitate particles through etching during the electropolishing process that proved to be unavoidable. The dislocation arrays surrounding the particles rule out any suggestion that these coarse particles may be coherent with the matrix phase.

Aged 2 h at 240°C

A BF transmission electron micrograph of the microstructure typical of the binary Al-10Mg alloy aged 2 h at 240°C is shown in Figure 5.2. The electron beam is approximately parallel to the $<112>_{\alpha}$ zone axis. Sparsely distributed, coarse-scale precipitate particles are observed, and these precipitate particles are larger and thicker than those in the specimen aged 0.5 h at 240°C, Fig. 5.1 (c). It is interesting to note that the number density of dislocations surrounding the precipitate particles appears to have increased as the ageing time was increased up to 2 h at 240°C. There is evidence that this coarse precipitate microstructure produces little or no precipitation hardening effect.

Although the identification of these precipitate particles proved impossible due to rapid oxidation of these precipitate particles during the process of electropolishing, the corresponding SAED pattern recorded from this region of the BF image contained evidence of diffraction spots from the precipitate particles.

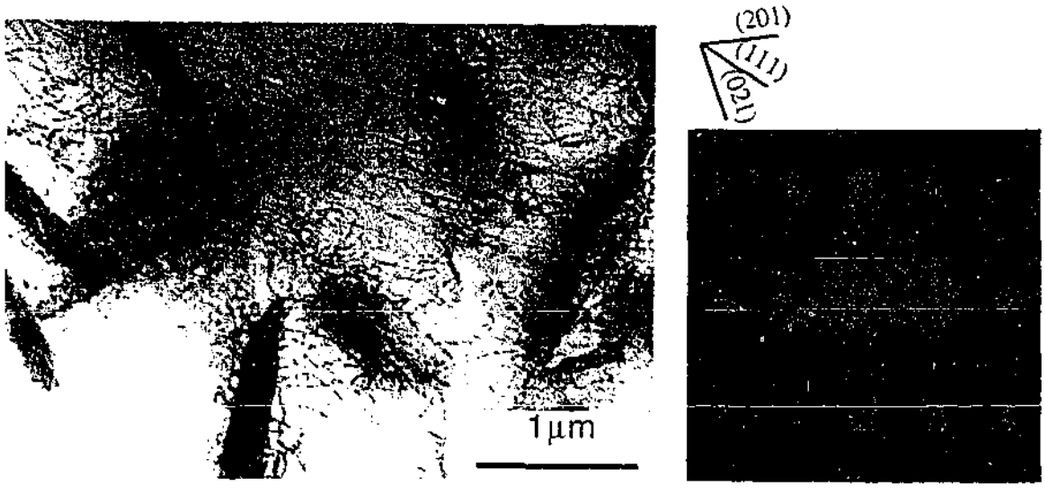

Figure 5.2 A transmission electron micrograph showing the microstructure typical of the binary alloy aged 2 h at 240°C. Electron beam is approximately parallel to the $<112>_{\alpha}$ direction.

Aged 5 h at 240°C

When the alloy was aged for 5 h at 240°C, the microstructure contained a coarse distribution of lath-like precipitate particles, together with an array of irregularly-shaped, randomly-oriented particles, as shown in Figures 5.3 (a) and (b). The electron beam is approximately parallel to the (a) $<001>_\alpha$ and (b) $<112>_\alpha$ directions. These precipitate particles are now much coarser than those observed in microstructures aged 2 h at 240°C. An interesting feature of these microstructures is that some of the irregularly-shaped particles contained an internal fault structure. The SAED patterns, Figs. 5.3 (c) and (d), recorded from the areas shown in the BF images, were complex because of the multiple orientations of particles present and it proved difficult to identify patterns from individual particles or systematic relationships between precipitate patterns and those from the matrix phase.

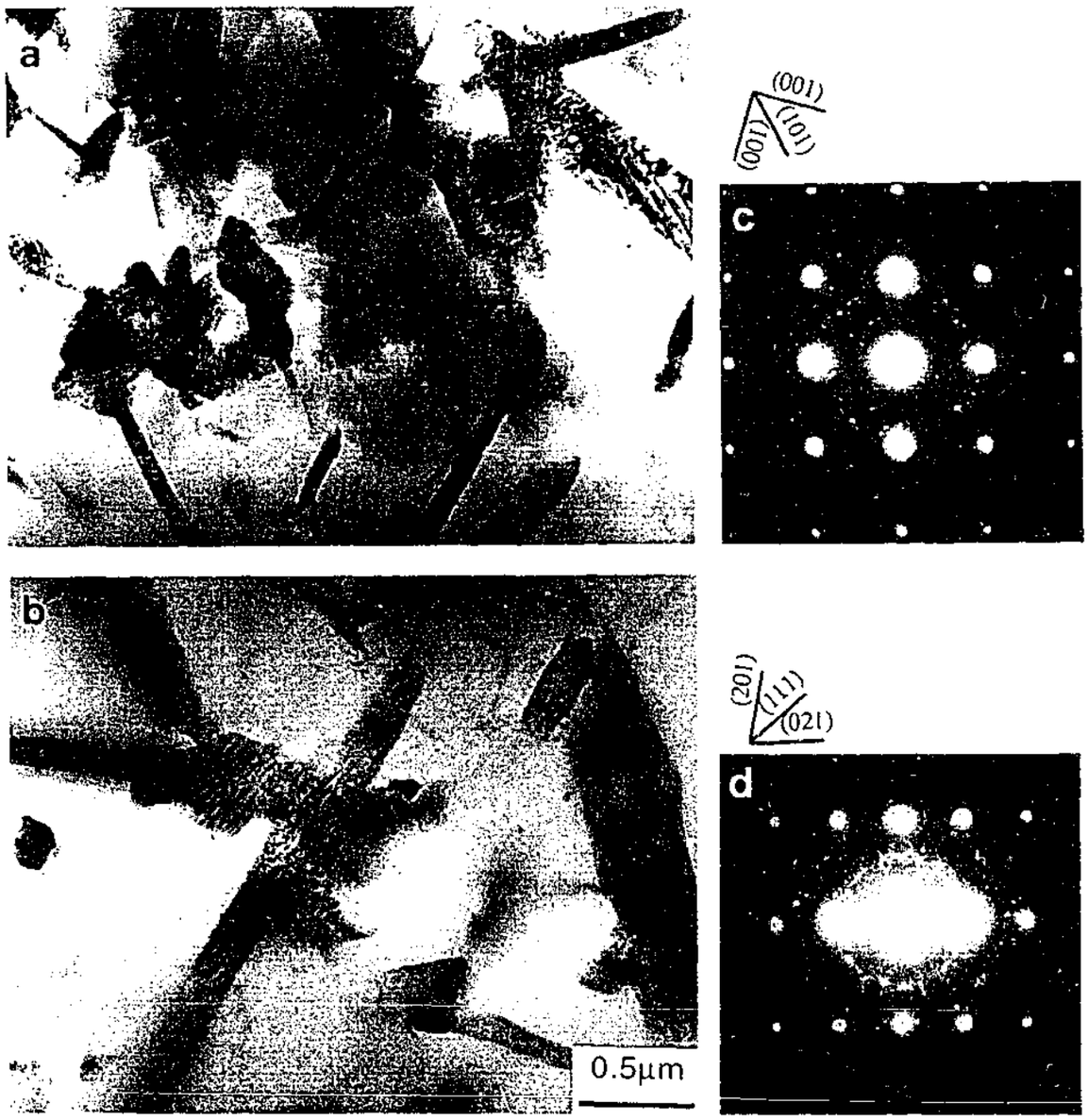

Figure 5.3 Transmission electron micrographs showing the microstructure typical of Al-10Mg alloy aged 5 h at 240°C. Electron beam is approximately parallel to (a) $<001>_\alpha$ and (b) $<112>_\alpha$ directions.

A more detailed BF image of precipitate particles in the Al-10Mg alloy aged 5 h at 240°C is shown in Figure 5.4 (a). This image was obtained after the specimen was tilted until several of the particles were strongly diffracting and the electron beam was approximately zone axes for at least some of these precipitate particles. Again in this orientation, there is little evidence that the precipitate particles maintain a single rotational orientation relationship with the aluminium matrix, as shown in the corresponding SAED pattern of Fig. 5.4 (b). This TEM micrograph also reveals that a precipitate cluster that consists of three distinguishable parts, that might be described as blocky, irregularly-shaped and lath-like (labelled A, B and C, respectively). A higher magnification image of an irregularly-shaped particle (labelled B) is shown in Fig. 5.4 (c), and this clearly exhibits that this coarse particle contains a faulted (and/or dislocated) substructure.

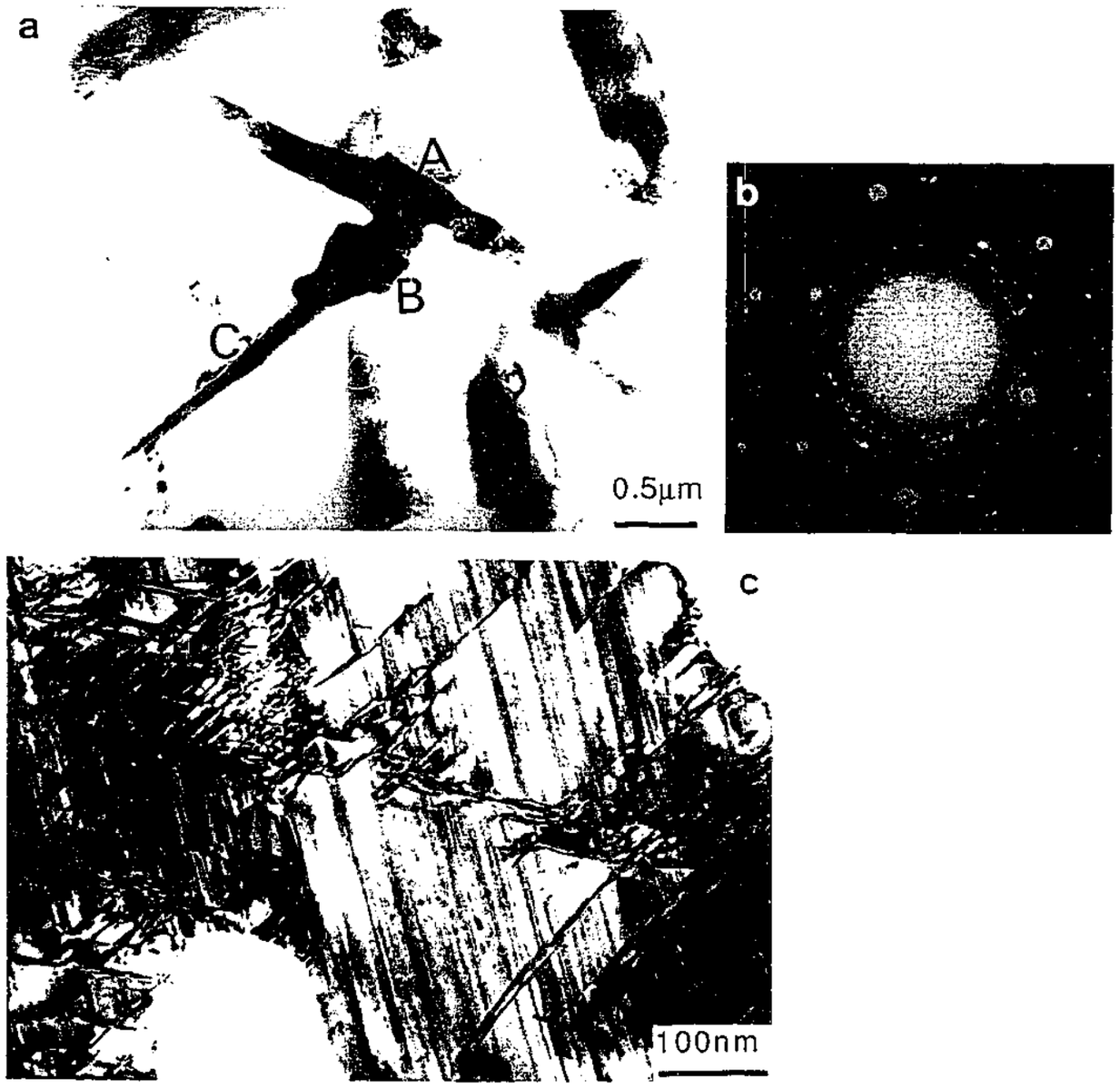

Figure 5.4 (a) Transmission electron micrograph showing a precipitate cluster comprising three different precipitate morphologies, (b) the corresponding SAED pattern, and (c) transmission electron micrograph showing a coarse particle with a faulted substructure, in the Al-10Mg alloy aged 5 h at 240°C.

In order to identify the crystal structures of the three different morphologies of precipitate particle, the electron microdiffraction technique was employed. Figures 5.5 (a) and (b) show the electron microdiffraction patterns recorded from the blocky precipitate particle (labelled A) in Fig. 5.4 (a) and corresponding schematic solutions. Figure 5.5 (a) was obtained with the tilting angles: x = 5.0° and y = 1.0°, whereas Fig. 5.5 (b) was recorded after the precipitate particle was tilted from the original position to x = 13.0° and y = -15.8°, to define a tilting angle of 19.1°. These patterns have been indexed successfully for a face-centred cubic structure, and the (a) $[001]_{cubic}$ and (b) $[114]_{cubic}$ zone axes. The total tilting angle (19.1°) between these two electron diffraction patterns compares well with the calculated angle (19.47°) between the $[001]_{cubic}$ and $[114]_{cubic}$ directions. The lattice parameter required to index these patterns was approximately a = 2.8 nm which corresponds well to that previously reported for the equilibrium β phase, a = 2.824 nm, in Al-Mg alloys (Samson 1965). Although only limited electron diffraction work has been completed, it seems likely that the blocky particle (A) may be identified as having the f.c.c. structure of the β phase, with a lattice constant of a = 2.824 nm.

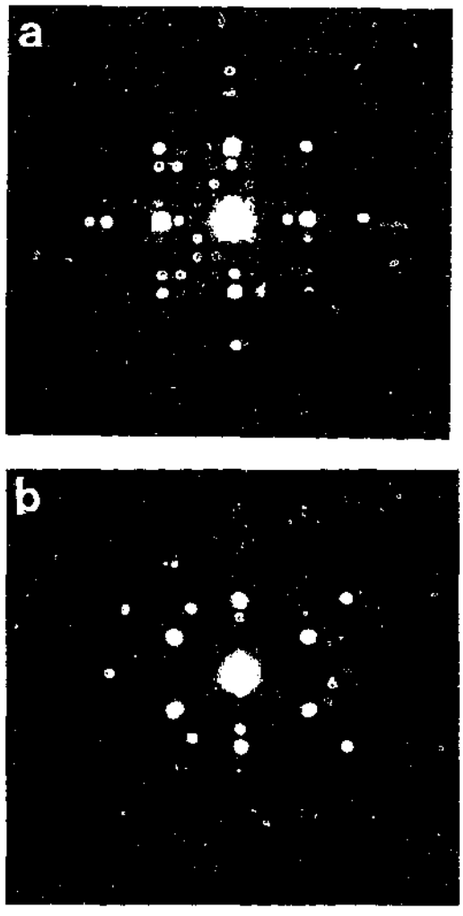

Figure 5.5 Electron microdiffraction patterns recorded from the blocky precipitate particle (labelled A in Fig. 5.4 (a)), indicating a f.c.c. structure with a lattice parameter of a = 2.8 nm. The electron beam is parallel to (a) [001] and (b) [114] axes of the precipitate phase.

Electron microdiffraction patterns recorded from the lath-like precipitate particle (labelled C) and the corresponding schematic solutions are presented in Figures 5.6 (a) and (b). These patterns have been indexed successfully for a hexagonal structure, with the two patterns representing $[11\bar{2}6]_{hexagonal}$ and $[1\bar{2}11]_{hexagonal}$ zone axes respectively. The lattice parameters of this phase are a = 1.0 nm, c = 1.6 nm, and are thus consistent with those of the metastable β' phase, a = 1.002 nm, c = 1.636 nm, reported in Al-Mg alloys (Bernole et al., Bernole 1974). The electron microdiffraction patters have been simulated using a close-packed hexagonal Bravais lattice with lattice parameters of a = 1.61 nm, c = 2.82 nm, and with atomic positions of (0, 0, 0) and (1/3, 2/3, 1/2) in the hexagonal unit cell. These atomic positions were chosen for simplicity because atomic positions for the intermediate β' phase in Al-Mg alloys have not yet been reported. The simulated electron microdiffraction patterns are in excellent agreement with those recorded experimentally. Apart from directly indexing these patterns for the metastable β' phase in Al-Mg alloys, a complete survey was made of any possible intermetallic compounds in alloys of the Al-Mg system from Pearson's Handbook (Villars and Calvert 1985). However, there was no evidence for hexagonal phases with lattice parameters close to those observed in this present experiment.

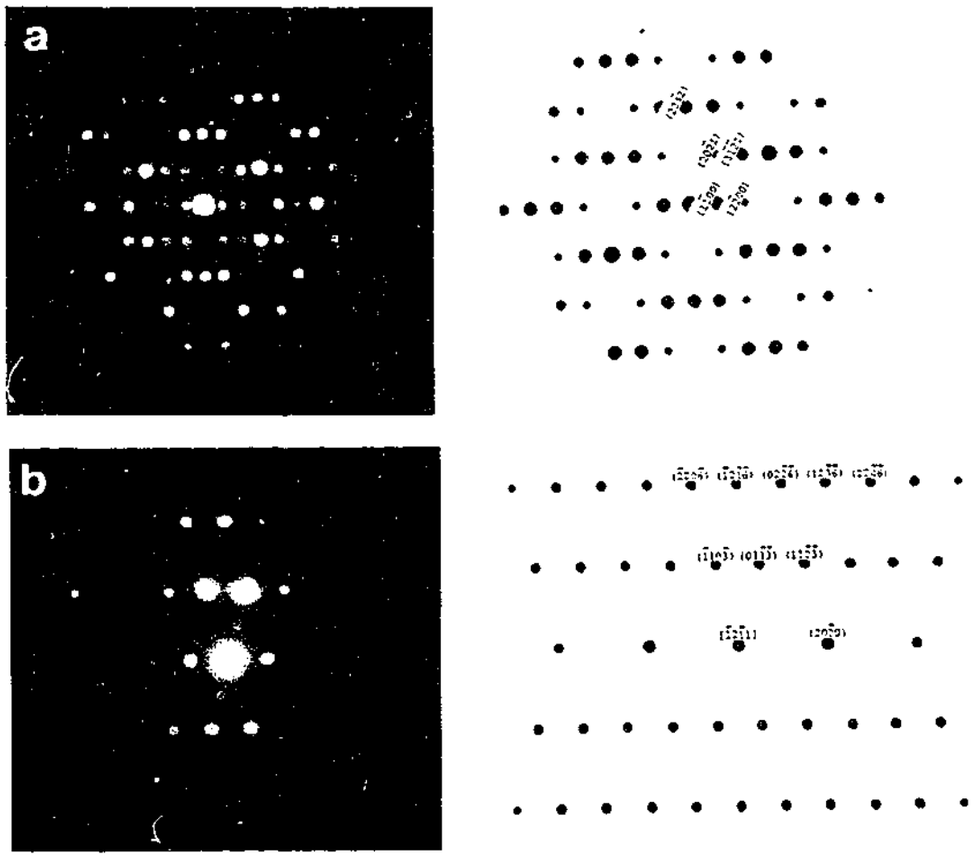

Figure 5.6 Electron microdiffraction patterns recorded from the lath-like particle (labelled C) in Fig. 5.4 (a), indicating a hexagonal structure with the lattice parameters of a = 1.6 nm, c = 2.8 nm. The electron beam is parallel to (a) $[11\bar{2}6]_{hexagonal}$ and (b) $[1\bar{2}11]_{hexagonal}$ zone axes.

Figure 5.7 shows the selected area electron diffraction (SAED) patterns recorded from the coarse-scale, irregularly-shaped precipitate particle (labelled B) in Fig. 5.14 (a). Indexing of these electron diffraction patterns was not completed. These patterns invariably exhibited a faulted or twinned substructure which gave rise to additional reflections and rendered the patterns quite complex.

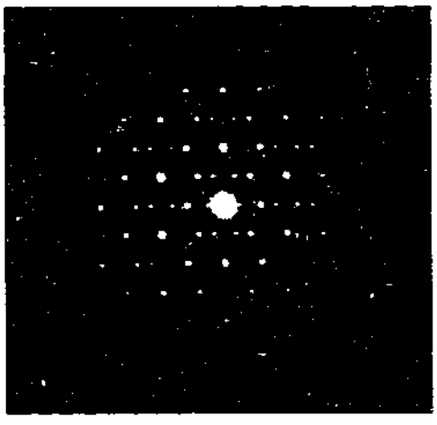

Figure 5.7 A selected area electron diffraction pattern recorded from the irregularly-shaped particle (labelled B) in Fig. 5.4 (a) indicating the complex reflection spots arising from faulted or twinned substructure.

Another example from the microstructure of the binary alloy, aged 5 h at 240°C, is shown in Figure 5.8 (a). This image shows two different types of precipitate morphology, lath-like (labelled D) and irregular (labelled E), with both forms being coarse-scale. Figures 5.8 (b)-(d) show SAED patterns recorded from the area of the microstructure shown in Fig. 5.8 (a). These patterns were recorded at orientations that were not parallel to any low index directions of the aluminium matrix. The SAED pattern (Fig. 5.8 (b)) from the lath-like particle (labelled D) shows complex reflections, and identification of this pattern was unsuccessful. It should be noted that this pattern is similar to that observed in the binary alloy aged 5 h at 240°C, and shown in Fig. 5.7. The SAED pattern, Fig. 5.8 (d), from the irregular particle (labelled E) could be indexed for the <110> zone of the equilibrium β phase in Al-Mg alloys (Samson 1965). The SAED pattern in Fig. 5.8 (c) was recorded from the boundary region between the two precipitate particles, D and E, and this pattern clearly exhibits a mixture of these two SAED patterns. These results from SAED patterns may imply that one type of precipitate particles is initially nucleated from the supersaturated solid solution during the isothermal ageing process, and then the other type of precipitate particles is nucleated heterogeneously on the precipitate particle formed initially.

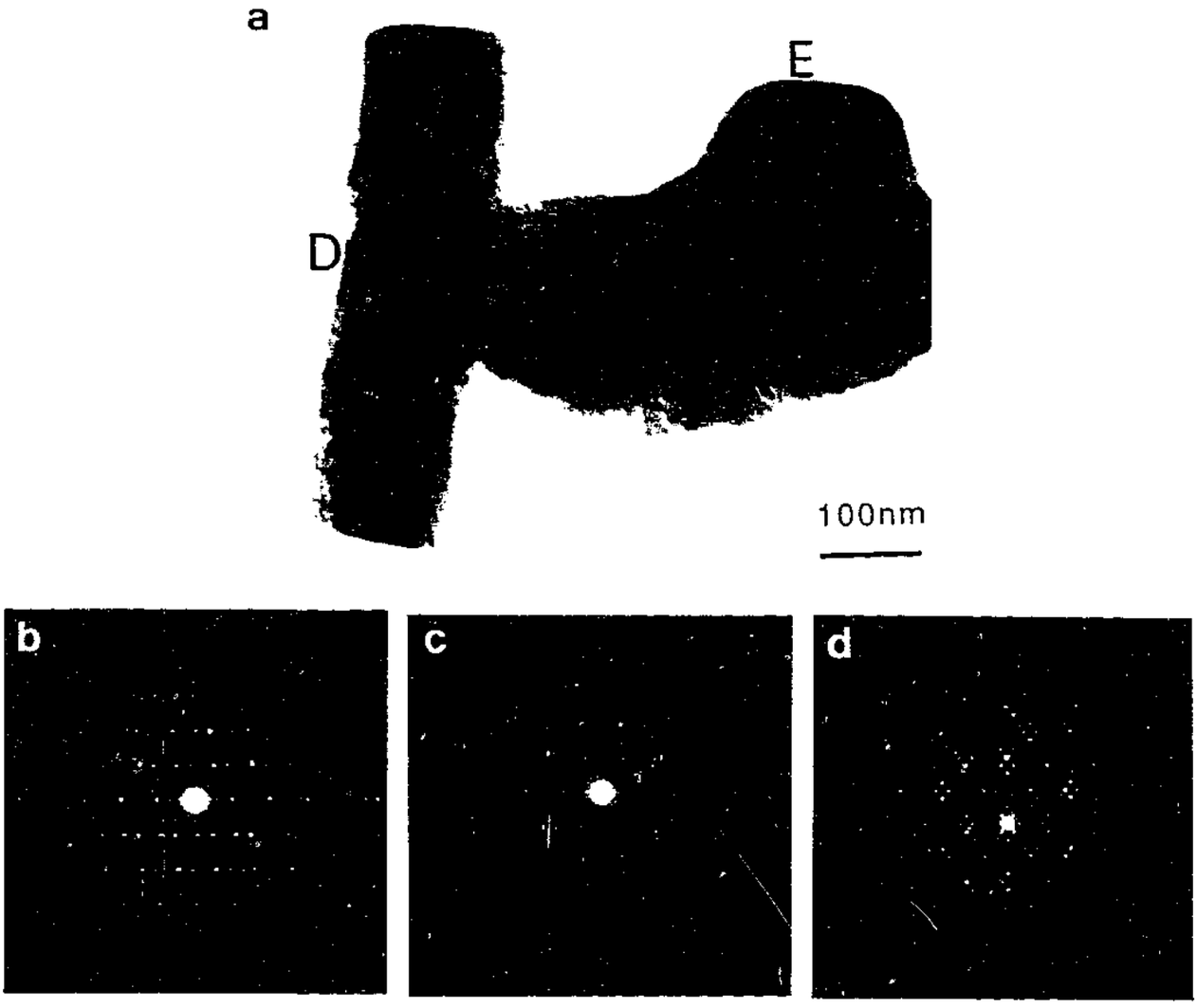

Figure 5.8 (a) BF image showing precipitate particles of two different morphologies, and (b)-(d) SAED patterns recorded from different regions of the image.

Figures 5.9 (a) and (b) show additional BF images of the binary Al-Mg alloy aged 5 h at 240°C, with the electron beam approximately parallel to $<110>_\alpha$ and $<112>_\alpha$ zone axes, respectively. These are as of the microstructure contain coarse-scale, sparsely distributed blocky and lath-like particles. An SAED pattern, Fig. 5.9 (c), recorded from the blocky particle (labelled F) in Fig. 5.9 (a) could be indexed for the equilibrium β phase, and implies parallelism of $<110>_\beta$ and $<110>_\alpha$ zone axes. In contrast, the SAED pattern, Fig. 5.9 (d), recorded from the second blocky particle (labelled G) in Fig. 5.9 (b) could be indexed for the metastable β' phase, and implies approximate parallelism of the $<11\bar{2}6>_{\beta'}$ and $<112>_\alpha$ zone axes. The SAED pattern, Fig. 5.9 (e) recorded from the lath-like particle (labelled H) in Fig. 5.9 (b) contains a pattern from the precipitate that corresponds to the $<110>_\beta$ zone, while the pattern from the aluminium matrix corresponds to a $<112>_\alpha$ zone axis. These two zone axes are not exactly parallel, but have few degrees of misorientation.

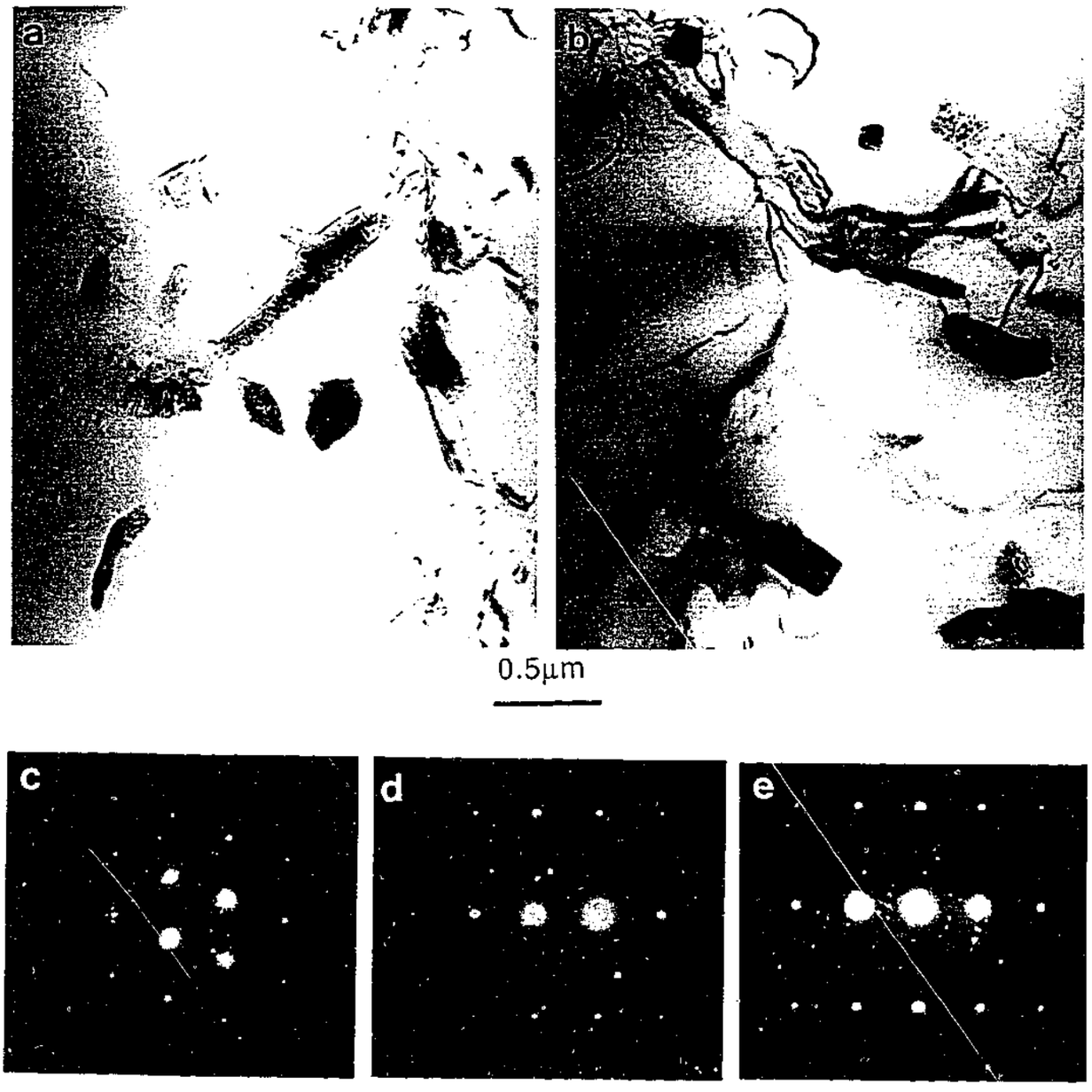

Figure 5.9 (a), (b) BF images showing microstructure typical of the binary Al-10Mg alloy aged 5h at 240°C. The electron beam is approximately parallel to $<110>_{\alpha}$ and $<112>_{\alpha}$ zone axes, respectively. (c)-(e) SAED patterns comprising overlapping patterns from precipitate particle and surrounding matrix phase.

Aged 72 h at 240°C

When the ageing time was further increased to 72 h at 240°C, the microstructure was changed significantly, as shown in Figure 5.10. The morphology of the precipitate particles was consistently irregular, and the scale of these precipitate particles was well in excess of 1 μm. Although detailed identification of these coarse particles failed due to the relative thickness of the precipitate particles, it is to be expected that the equilibrium β phase would be the predominant phase to observed in the later stages of the ageing process in binary Al-Mg alloys (Mondolfo 1976, Lorimer 1978).

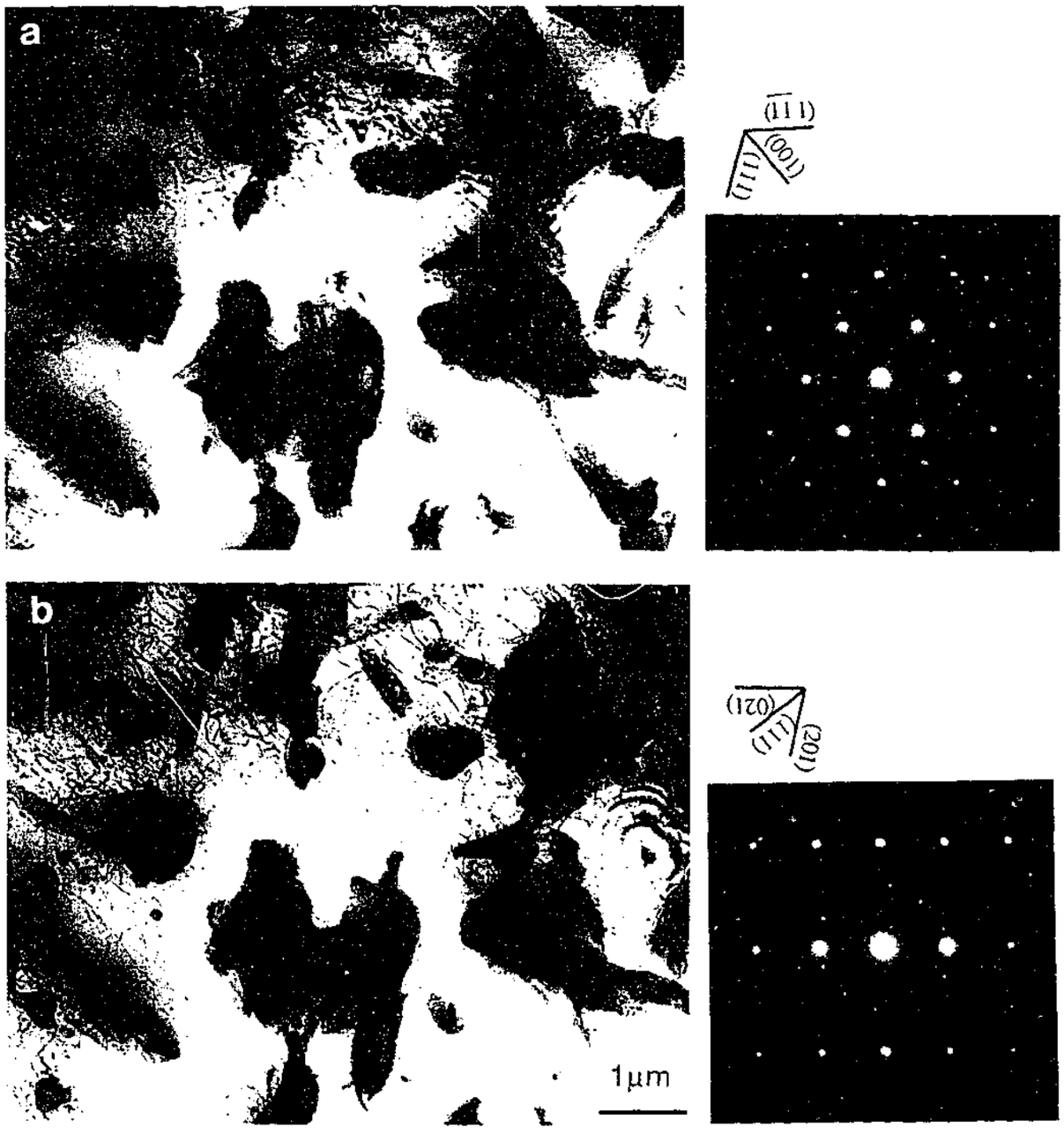

Figure 5.10 (a), (b) BF images showing the microstructure typical of over-aged specimens of the binary alloy aged 72 h at 240°C. The electron beam is parallel to $<110>_\alpha$ and $<112>_\alpha$ directions, respectively.

5.2.2 Phase Identification in Ternary Alloy (Al-10Mg-0.5Ag)

Aged 0.5 h at 240°C

Bright-field (BF) images of the microstructure typical of the Al-10Mg-0.5Ag alloy aged 0.5h at 240°C, together with the corresponding SAED patterns, are shown in Figure 5.11. The electron beam is approximately parallel to (a), (d) $<110>_\alpha$, (b), (e) $<112>_\alpha$ and (c), (f) $<111>_\alpha$ directions, respectively. Those transmission electron micrographs in Figs. 5.11 (a)-(c) were taken from an area close to a grain boundary, while the micrographs in Figs. 5.11 (d)-(f) were recorded from a region within the centre of a matrix grain. The regions close to the grain boundaries, Figs. 5.11 (a)-(c), contained evidence of a precipitate-free zone (PFZ) and coarse-scale, faceted precipitate particles adjacent to that zone. The particles became coarser (60-80 nm) approaching the grain boundary precipitate-free zones. The coarser distribution adjacent to the PFZ presumably reflects a lower nucleation rate in these regions, perhaps arising from a combination of a depleted solute and a reduced vacancy concentration.

A uniform distribution of much finer-scale (typically 20 nm), faceted precipitate particles was observed within the core of the grains, Figs. 5.11 (d)-(f), suggesting that such precipitate particles were nucleated homogeneously from the supersaturated solid solution of the aluminium matrix during the isothermal ageing treatment. The refined scale of these precipitate particles implies a high nucleation rate.

In order to first assess whether the crystal structure of these precipitate particles of different scale within these different regions were the same or not, selected area electron diffraction (SAED) patterns were taken from representative regions containing precipitate particles corresponding to each of the BF images. As can be seen clearly from these SAED patterns, the two distinguishable sizes of uniformly distributed, faceted precipitate particles in different regions of the same grain appear to have a similar crystal structure. The precipitate diffraction patterns from those particles in regions close to the grain boundary PFZ were identical to those from particle arrays at the core of the grain.

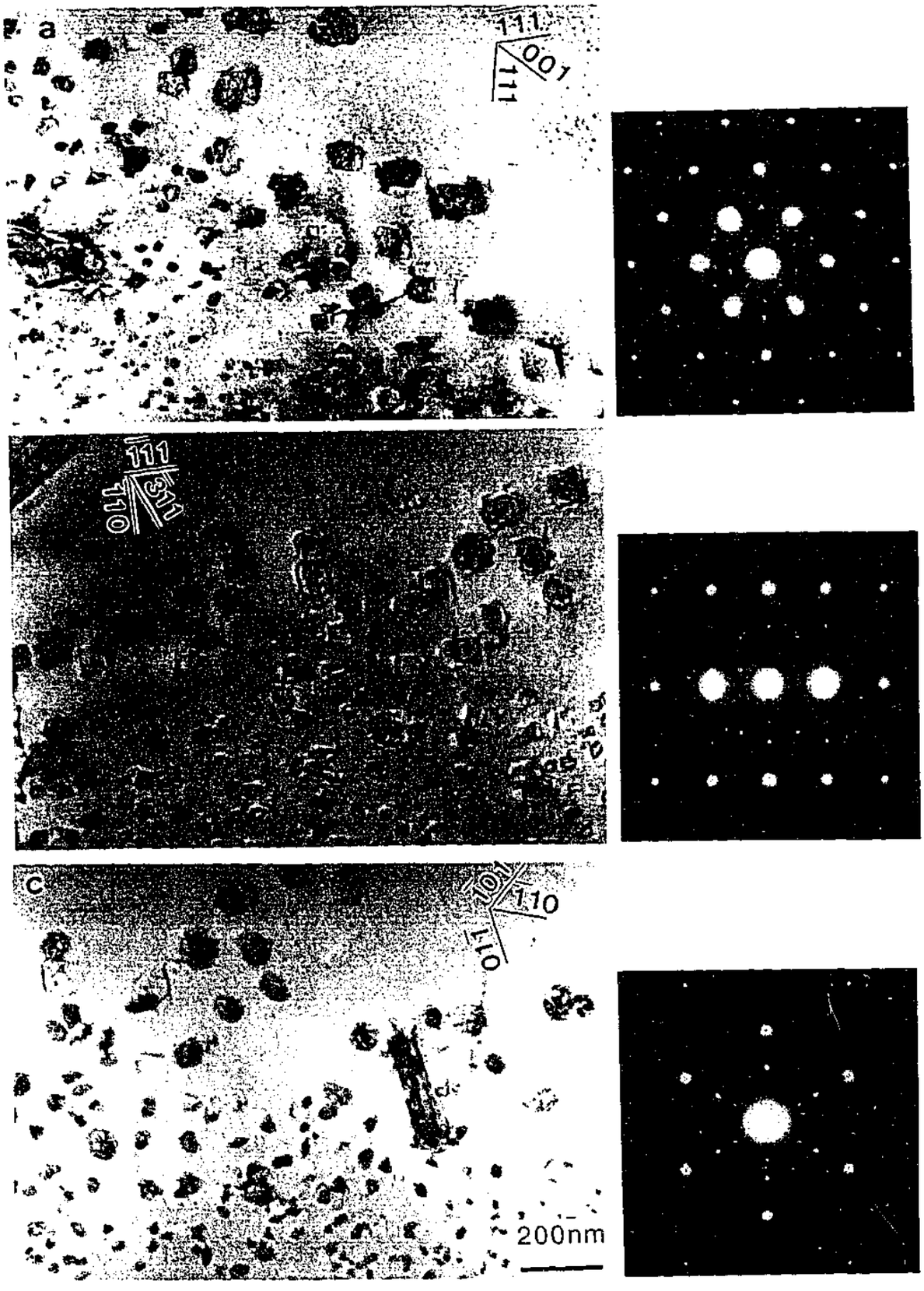

Figure 5.11 Transmission electron micrographs showing the morphologies of faceted precipitate particles with different distributions in the Al-10Mg-0.5Ag alloy aged 0.5 h at 240°C. The electron beam is the approximately parallel to the (a), (d) $<110>_{\alpha}$, (b), (c) $<112>_{\alpha}$ and (c), (f) $<111>_{\alpha}$ directions. Figures 5.11 (a)-(c) recorded from regions adjacent to grain boundary, and Figures 5.11 (d)-(f) from region at core of grain.

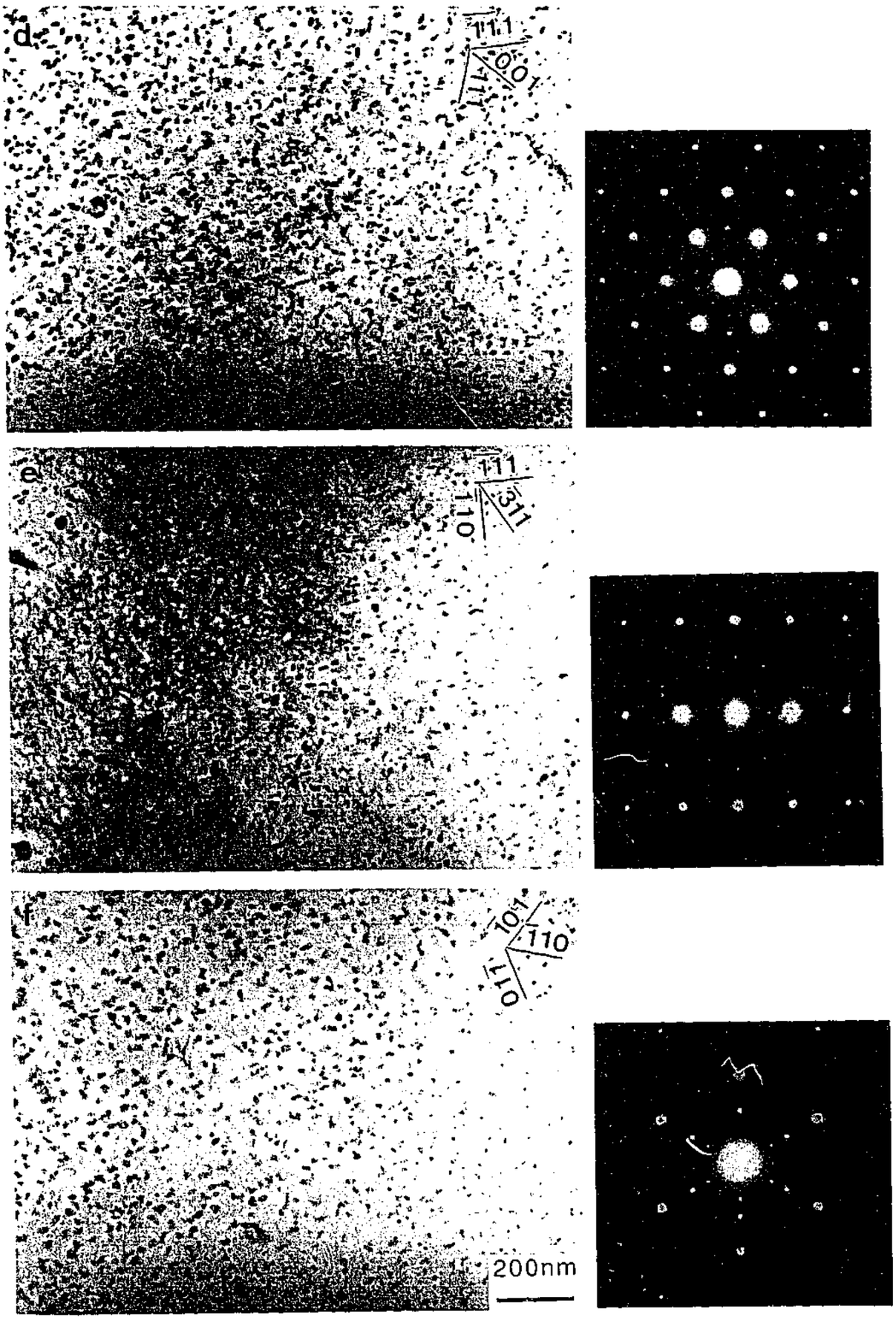

Figure 5.11 Continued.

In an attempt to determine the precise morphology of the precipitate particles in Al-10Mg-0.5Ag alloys aged 0.5 h at 240°C, BF images were first recorded in the $<001>_\alpha$ orientation. Figure 5.12 (a) shows the microstructure which was observed with the electron beam parallel to the $<001>_\alpha$ zone axis, while Figure 5.12 (b) shows the same region tilted a few degrees away from the zone axis. When the specimen was tilted from the $<110>_\alpha$ orientation, Fig. 5.11 (a), to the $<001>_\alpha$ orientation, Fig. 5.12 (a), (b), the form of the precipitate particles was observed to change from a regular diamond shape to one of square outline. Many of the precipitate particles of square outline in the $<001>_\alpha$ orientation exhibited modulations in contrast parallel to the particle edges with the particles, as shown in Fig. 5.12 (c)-(d). The traces of the projected edges of the precipitate particles in the $<001>_\alpha$ orientation are parallel to the traces of $\{110\}_\alpha$ planes of the aluminium matrix.

Detailed higher magnification BF images of the precipitate particles are presented in Figure 5.13. The micrographs of Figs. 5.13 (a) and (b) were taken exactly parallel to the zone axes in order to obtain the exact traces of the shape of the precipitate particles, while the micrograph of Fig. 5.13 (c) was taken slightly off the zone axis in order to observe the projected image. Careful examinations of these microstructures in the $<110>_\alpha$ orientation revealed that there were, in fact, two distinguishable shapes within the particle array. In this $<110>_\alpha$ orientation, Fig. 5.13 (a), the diamond-shaped profiles of the particles define two different angles of approximately 70° and 80°. The bright field image at higher magnification in Fig. 5.13 (b) provides examples of these two forms of precipitate particles with distinguishable different angles defined by the edge traces. Particle labelled A has a regular well-faceted diamond shape with angles of 80° between edge traces, while particle labelled B is irregular and has angles of ~70° between edge traces.

When these particles were observed in the $<001>_\alpha$ orientation, Figs. 5.12 (a)-(d), there were also two apparent forms; One shape is almost rectangular or square in section and the other is not well-faceted square-shaped particle. From these and other observations of precipitate particles over a range of orientations, it is deduced that they have the form of rhombohedra.

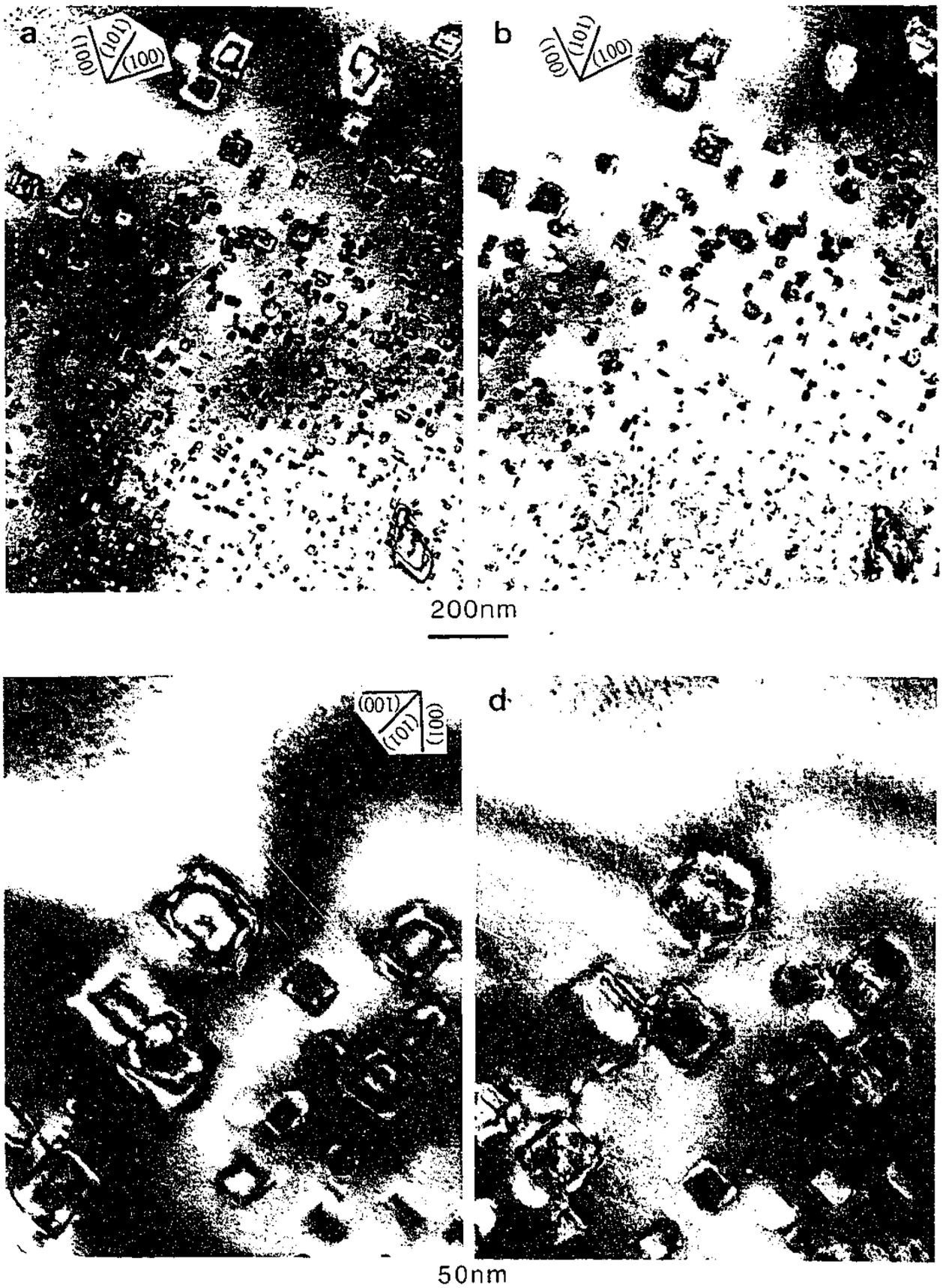

Figure 5.12 Bright-field images of the precipitate particles in the Al-10Mg-0.5Ag alloy aged 0.5h at 240°C showing the distribution and morphology of the precipitate particles. The electron beam is the approximately parallel to an $<001>_{\alpha}$ zone axis.

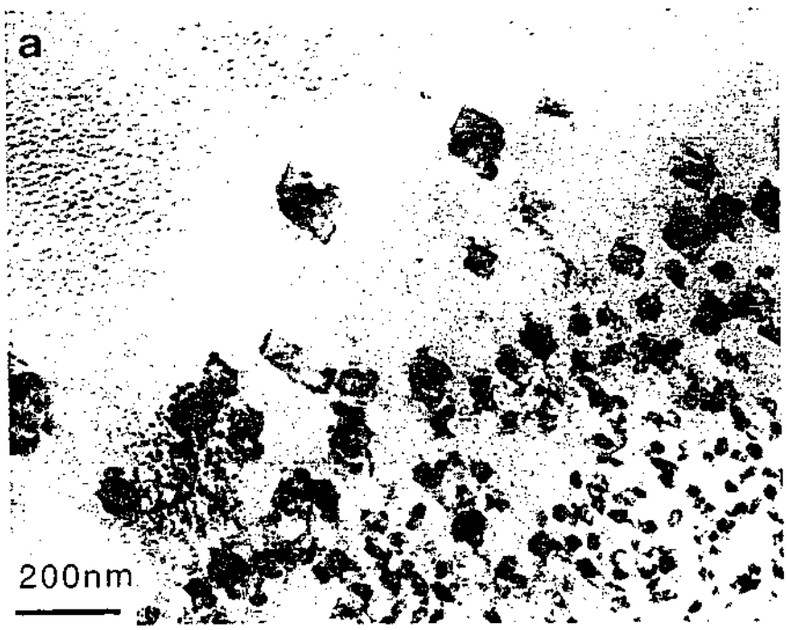

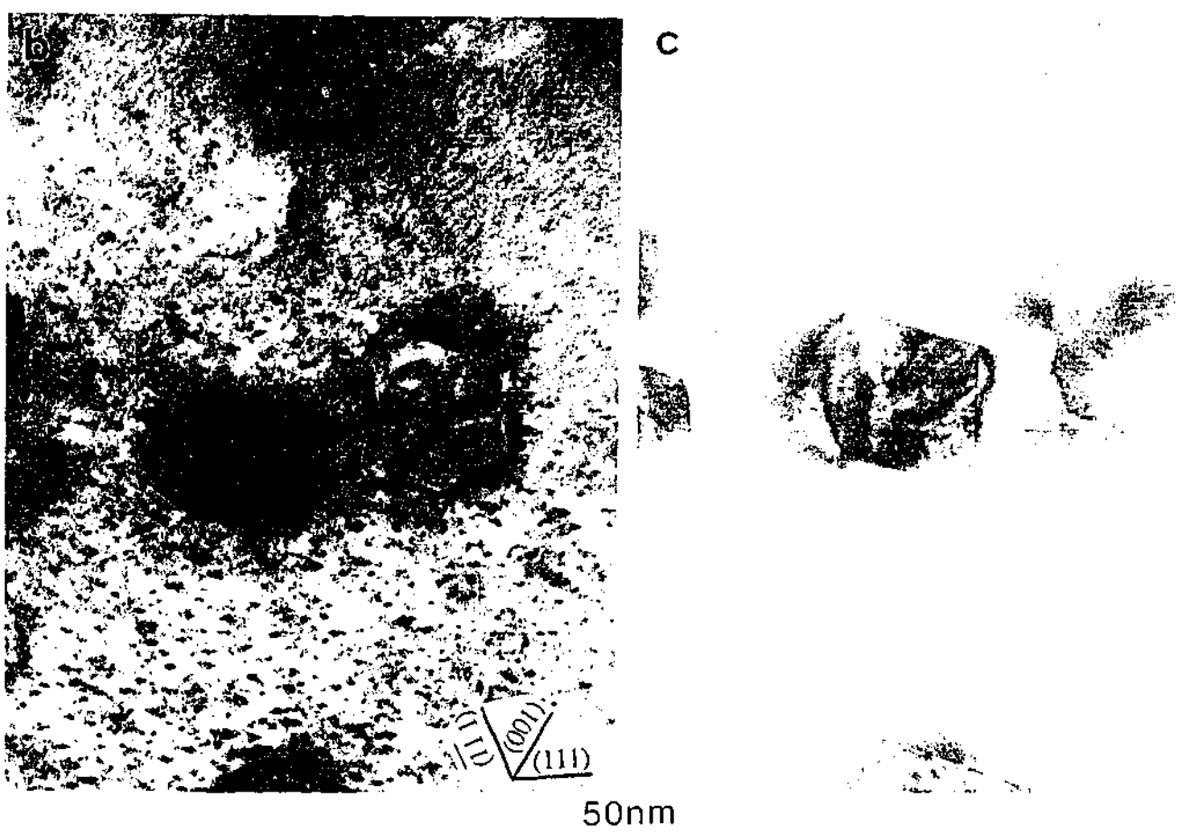

Figures 5.13 TEM micrographs (a)-(c) showing two distinguishable profiles of diamond-shaped precipitate particles. Micrographs (a) and (b) were taken exactly parallel to the $<110>_{\alpha}$ zone axis, while micrograph (c) was taken after tilting off the on zone axis.

If strain fields are associated with precipitate particles in a matrix, or are produced by nucleation and growth of precipitate particles during isothermal ageing processes, then the strain fields could be significantly influenced on hardness or strength in materials. Thus in order to observe any strain fields associated with the precipitate particles, bright field images were taken under different two-beam diffraction conditions, and these are shown in Figure 5.14. The operating vectors **g** were (a) $[1\bar{1}1]_\alpha$, (b) $[\bar{1}1\bar{1}]_\alpha$, (c) $[200]_\alpha$ and (d) $[220]_\alpha$ in the $[110]_\alpha$ zone axis pattern. Precipitate particles with both diamond-shaped profiles and rectangular projected images were observed. It is noteworthy that these particles were generally associated with a little strain field (coherent elastic strains), which is clearly indicated (arrows) in Fig. 5.14 (a)-(d). The strain fields associated with those precipitate particles formed during isothermal ageing processes may provide an increase of the hardness in the ternary Al-10Mg-0.5Ag alloy.

As confirmed earlier in the separate SAED patterns recorded from arrays of coarser and finer scale precipitate particles in the different regions of a grain, the crystal structure of these different forms of precipitate particle appeared to be the same. The detailed crystal structure of these particles was established using the microbeam electron diffraction technique, but it was extremely difficult to obtain useful information from the microbeam electron diffraction patterns from the finer scale precipitate particles. Thus work on identification of the crystal structure was thus focused on those relatively coarse-scale precipitate particles located near to the grain boundaries.

Figures 5.15 (a)-(f) show a series of microbeam electron diffraction patterns recorded from a series of relatively large scale, diamond-shaped particles in the Al-10Mg-0.5Ag alloy aged 0.5 h at 240°C. A regular array of diffraction spots from the precipitate particle is observed in a $<110>_\alpha$ direction (Fig. 5. 15 (a)). Most notably, the precipitate pattern in Fig. 5.15 (b), recorded near to a second $<110>_\alpha$ orientation, exhibits five-fold rotational symmetry. The misorientation between the precipitate five-fold axis and the matrix $<110>_\alpha$ axis was experimentally obtained during a large angle tilting experiment, and was approximately 2°-4° tilted away from the $<110>_\alpha$ matrix zone axis towards to the matrix $<002>_\alpha$ direction. Fig. 5.15 (c) exhibits three-fold rotational symmetry in the precipitate pattern in this $<111>_\alpha$ orientation. The angle of tilt required to move from the axis of five-fold symmetry to that of three-fold symmetry was approximately 37°. Two-fold rotational symmetry is detectable in the precipitate diffraction pattern in the $<112>_\alpha$ orientation, when the specimen is tilted ~ 21° from the $<111>_\alpha$ to ~ $<112>_\alpha$ zone axis, as shown in Fig. 5.15 (d). Figure 5.15 (e) shows a regular array of diffraction pattern from the precipitate particle which is observed in the $<001>_\alpha$ orientation when the sample is tilted from the $<112>_\alpha$ axis of (d) to the nearest $<001>_\alpha$ matrix orientation, while Fig. 5.15 (f) shows a second variant of the five-fold rotation symmetry which is observed in an $<011>_\alpha$ orientation that is 60° from that shown in Fig. 5.15 (b).

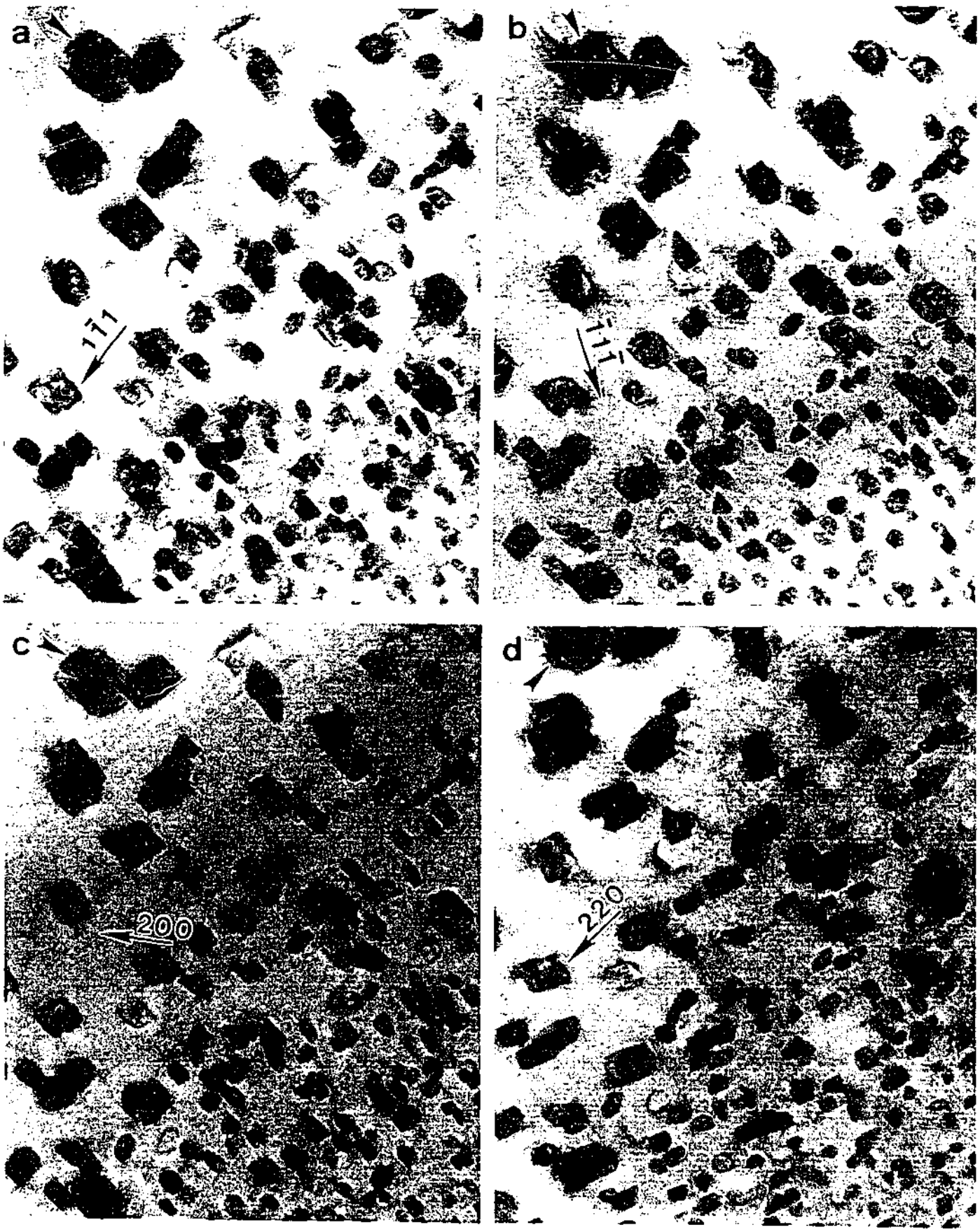

Figures 5.14 BF images recorded in different two-beam diffraction conditions. The operating vectors g are (a) $[1\bar{1}1]_\alpha$, (b) $[\bar{1}1\bar{1}]_\alpha$, (c) $[200]_\alpha$ and (d) $[220]_\alpha$, with the electron beam parallel to $[110]_\alpha$.

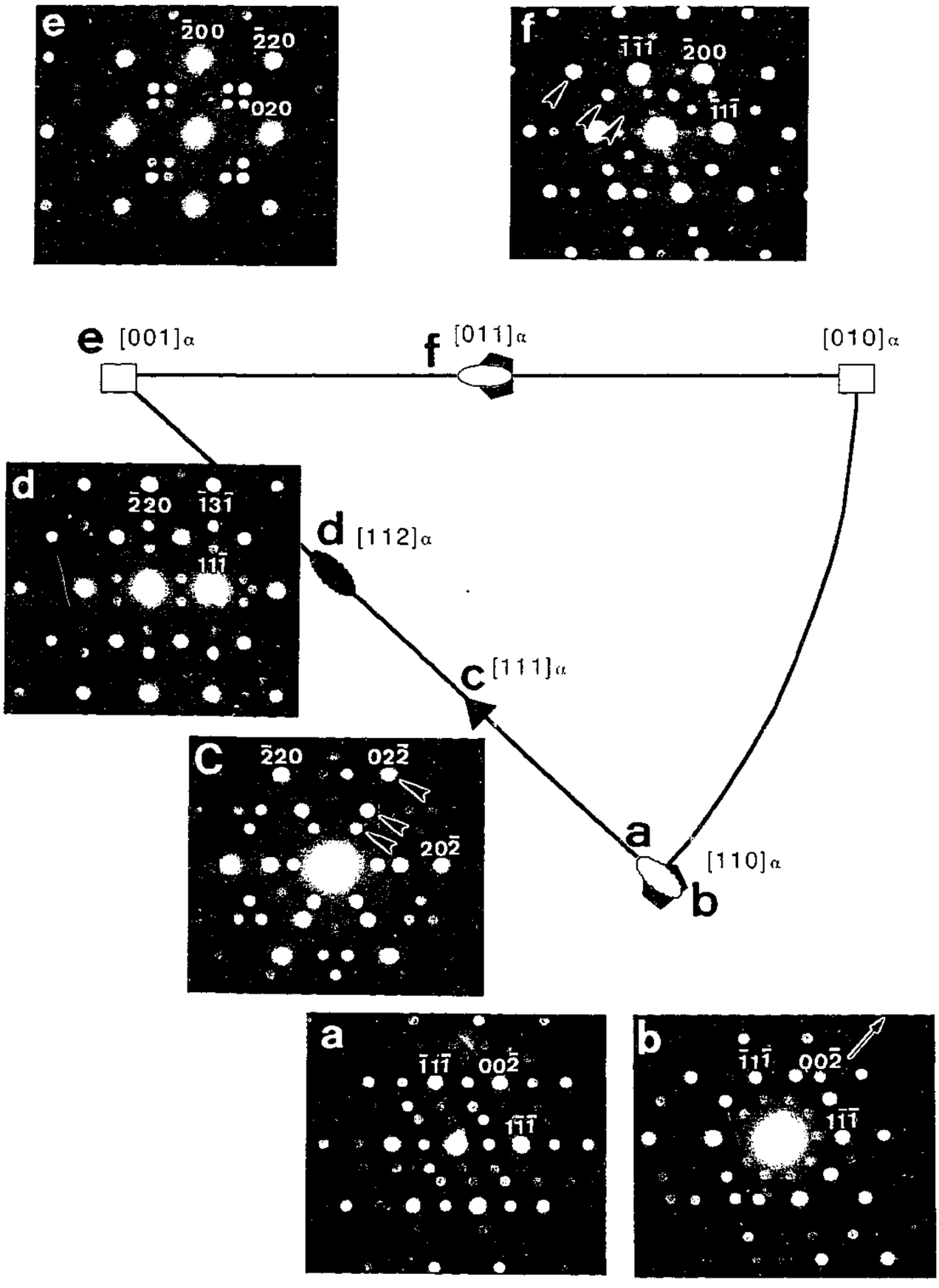

Figure 5.15 A series of microbeam electron diffraction patterns ((a)-(f)) recorded from a single large scale (~50 nm) diamond-shaped particle in the Al-10Mg-0.5Ag alloy aged 0.5 h at 240°C.

Careful measurements of d-spacings in the observed microbeam electron diffraction patterns exhibiting five-fold, three-fold and two-fold axes reveal that they are equivalent to those reported for a phase of icosahedral symmetry by Shechtman et al. (1984). In addition, the experimental tilt angles recorded between the major symmetry axes of the precipitate phase were also consistent with those previously reported for icosahedral phase in rapidly solidified Al-Mn alloys (Shechtman et al. 1984). These tilt angles, along with those previously reported, are compared in Table 5.1. These systematic large angle tilting experiments suggest that the homogeneously distributed, fine scale of precipitate particles produced by the isothermal ageing heat treatment process have the icosahedral structure of a quasicrystalline phase.

Table 5.1 Comparison of experimental and theoretical tilt angles between major zone axes in matrix and icosahedral precipitate phase.

α-matrix	**$[011]_\alpha$**	**$[110]_\alpha$**	**$[111]_\alpha$**	**$[112]_\alpha$**
i-phase	**5-fold**	**near 5-fold**	**3-fold**	**near 2-fold**
α-Al matrix	60°	35.16°	19.28°	
i-phase (present research)	63°	37°	21°	
i-phase (Shechtman et al. 1984).	63.43°	37.38°	20.91°	

The precise form of the crystallographic relationship between the precipitate phase, tentatively identified as having icosahedral structure, and the matrix proved difficult to define. For example, Figs. 5.15 (c) and (d) suggest that there are three-fold and two-fold rotational axes of the icosahedral precipitate parallel to $<111>_\alpha$ and $<112>_\alpha$ directions respectively. However, the angle between the $<111>_\alpha$ and $<112>_\alpha$ axes is 19.28°, while that between the relevant axes of the icosahedral structure is 20.91°. This indicates that the two icosahedral axes cannot simultaneously be exactly parallel to the appropriate axes of the matrix structure, and raises the question whether either is an exact parallelism.

In order to address this question and to seek confirmation of the icosahedral structure, further large angle tilting experiments were carefully carried out. Aside from attempting to establish parallelism between precipitate and matrix axes, efforts were made to tilt a specimen from the $[111]_\alpha$ zone axis through $[112]_\alpha$ (i.e. about $[110]_\alpha$) and a further 20.91°. For an icosahedral structure this would be expected to bring the electron beam at least approximately parallel to a second axis of three-fold rotational symmetry. Figure 5.16 (a) shows a precipitate pattern of three-fold rotational symmetry superimposed on the $[111]_\alpha$ zone axis pattern. When the specimen was tilted systematically 1° and 2° away from the exact $[111]_\alpha$ zone axis about

$[110]_\alpha$, then the precipitate pattern immediately lost three-fold symmetry in the diffracted intensity (Figs. 5.16 (b) and (c), respectively), suggesting that within permitted accuracy, the three-fold axis of the precipitate phase is parallel to the corresponding three-fold axis of the matrix. The microbeam electron diffraction pattern, in Figure 5.16 (d) was recorded in the $[112]_\alpha$ matrix orientation when the specimen was tilted from the $[111]_\alpha$ orientation. The two-fold rotational symmetry of the precipitate pattern is approximately superimposed on the $[112]_\alpha$ zone axis pattern. When the specimen was tilted ~2° away from the $[112]_\alpha$ zone axis of the matrix about the $<001>_\alpha$ direction, a symmetric pattern with two-fold rotational symmetry was observed from the precipitate phase, as shown in Fig. 5.16 (e). This confirms that the two-fold axis of the precipitate structure is not exactly parallel to the $[112]_\alpha$ axis. When the specimen was tilted a further ~22° away from the $[112]_\alpha$ zone axis about $<001>_\alpha$, a second precipitate pattern with three-fold rotational symmetry was detected, Fig. 5.16 (f), once again approximately parallel to a $<117>_\alpha$ direction. This series of microbeam electron diffraction patterns during the careful large angle tilting experiment agrees well with the tilt angles among major rotational symmetry axes in the result previously reported (Shechtman et al. 1984)

The distances between diffraction spots from the precipitate phase along systematic rows of the diffraction patterns were such as to suggests a quasiperiodicity. For example, the row from the transmit spot to the $(220)_\alpha$ matrix spot in five-fold and three-fold rotational symmetry patterns (Figs. 5.15 (f) and (c), respectively) contained a sequence comprising two segments that might be designated S (short) and L (long). These segments were arranged to be consistent with Fibonacci sequence, i.e. LSLLSLSL, where the ratio (L+S)/L was equal to approximately 1.7. This is entirely consistent with the golden mean $\tau = (1+\sqrt{5})/2 = 1.618$ (Jaric 1988), and implies a quasiperiodic order in this direction.

Results of the systematic large angle tilting experiments, reproduced in Figs. 5.15 and 5.16, suggest an orientation relationship between the icosahedral quasicrystalline and matrix phases, that is of the form:

$$i5 \parallel [011]_\alpha$$
$$i3 \parallel [111]_\alpha$$

The approximate orientation relationship between the icosahedral and matrix phases was deduced, and that is of the form:

$$i5\sim \parallel [110]_\alpha$$
$$i3\sim \parallel [117]_\alpha$$
$$i2\sim \parallel [112]_\alpha$$

It is thus similar in form to that reported for the precipitate icosahedral phase formed during isothermal decomposition of strip-cast Al-Mn-Fe-Si alloys (Hansen, Gjønnes and Andersson 1989).

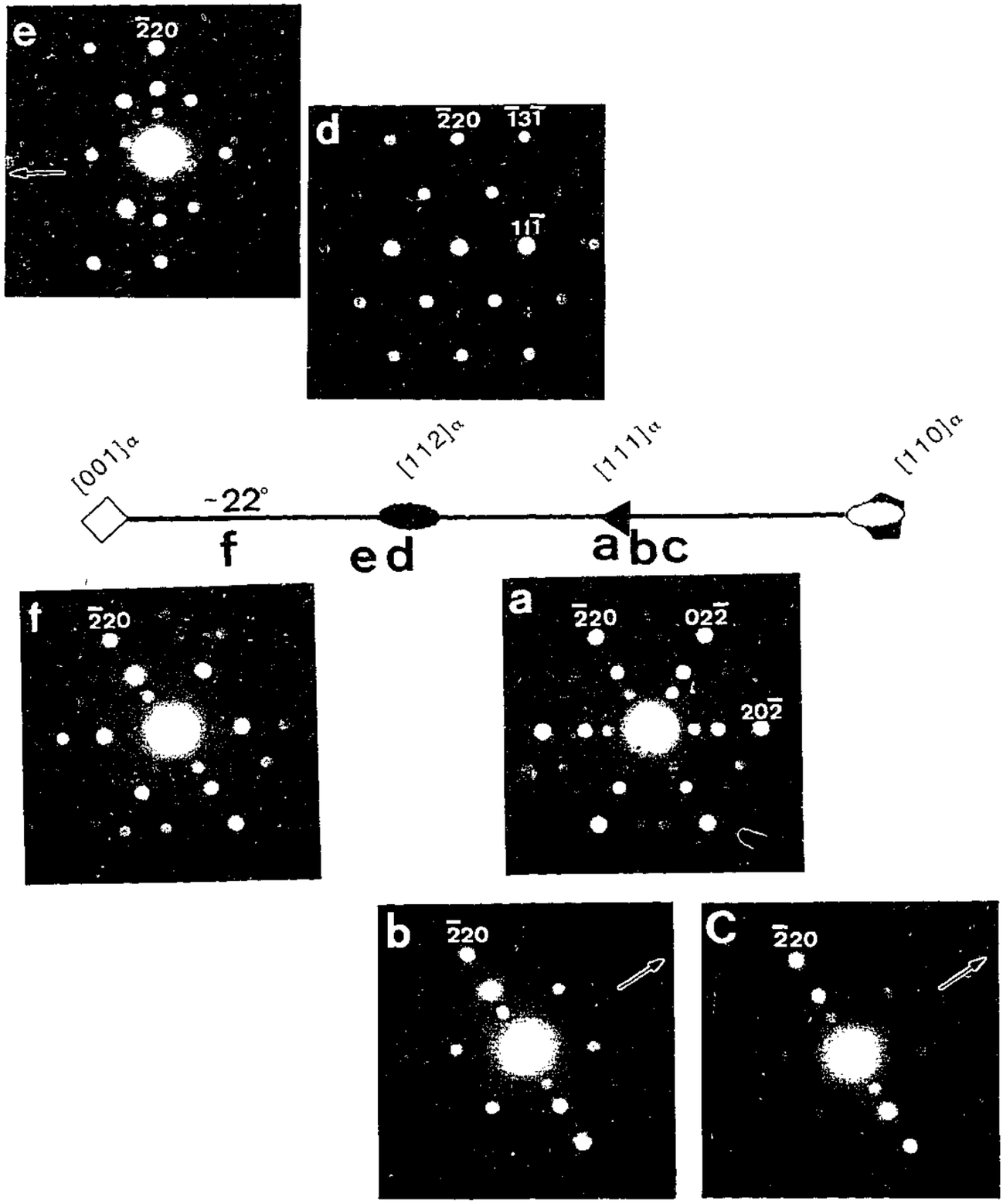

Figure 5.16 A series of electron microdiffraction patterns recorded from a single large scale diamond-shaped particle in the Al-10Mg-0.5Ag alloy aged 0.5 h at 240°C. (a) three-fold rotational symmetry recorded in the $[111]_\alpha$ zone axis, (b) tilted 1° and (c) 2° away from the exact $[111]_\alpha$ zone axis about $[110]_\alpha$, (d) near two-fold rotational symmetry recorded in the $[112]_\alpha$ zone axis (e) tilted ~2° away from the $[112]_\alpha$ zone axis about the $<001>_\alpha$ direction, (f) the other variant of the three-fold rotational symmetry.

Further confirmation of the identification of the icosahedral structure of the quasicrystalline particles was gained by testing the tilting angles between major rotational axes using further this large angle tilting experiments. The aim was to test whether measured angles were consistent with those previously reported (Shechtman et al. 1984). According to these results, for example, there should be another five-fold rotational symmetry parallel to the $[11\bar{3}]_\alpha$ axis. In addition, a further two-fold axis of rotational symmetry is expected to be approximately parallel to the $[11\bar{1}]_\alpha$ direction. In order to confirm these two points, large angle tilting experiments were carried out from the $[00\bar{1}]_\alpha$ direction to $[11\bar{1}]_\alpha$, and further to the $[10\bar{1}]_\alpha$ direction through the $[11\bar{2}]_\alpha$ orientation. These systematic tilt directions are obtained from the established orientation relationship between the quasicrystalline and matrix phases, as mentioned above.

The resultant microbeam electron diffraction patterns are presented in Figures 5.17 (a)-(f). Figure 5.17 (a) shows a precipitate pattern with some systematic symmetry superimposed on the $[00\bar{1}]_\alpha$ zone axis pattern. When the specimen was tilted ~1.5° away from the $[00\bar{1}]_\alpha$ orientation, the systematic reflections from the precipitate phase remained, as shown in Fig. 5.17 (b). Fig. 5.17 (c) shows that a precipitate pattern with five-fold rotational symmetry about the electron beam was observed approximately parallel to the $[11\bar{3}]_\alpha$ orientation when the specimen was tilted approximately 22° away from the $[00\bar{1}]_\alpha$ orientation. The misorientation between the five-fold rotational axis and the $[11\bar{3}]_\alpha$ orientation was obtained experimentally, and was approximately 3°. With further tilting, from close to the $[11\bar{3}]_\alpha$ orientation towards the $[11\bar{1}]_\alpha$ orientation, a precipitate pattern with two-fold rotational symmetry was observed approximately parallel to the $[11\bar{1}]_\alpha$ orientation, Fig. 5.17 (d). The regular array of reflection spots from the precipitate particle is observed in the $[10\bar{1}]_\alpha$ direction, shown in Fig. 5.17 (e). A further axis of two-fold rotational symmetry in the precipitate was observed approximately parallel to the $[10\bar{1}]_\alpha$ orientation, as shown in Fig. 5.17 (f). Figure 5.17 (g) shows an axis of three-fold rotational symmetry for the precipitate that is approximately parallel to the $[31\bar{2}]_\alpha$ orientation; the tilting angle from the axis of two-fold symmetry to that of three-fold symmetry was approximately 19.4°. A regular array of diffracted spots from the precipitate particle was observed in the $[11\bar{2}]_\alpha$ orientation, when the specimen was tilted about 60° from close to the $[10\bar{1}]_\alpha$ to the $[11\bar{2}]_\alpha$ matrix directions, Fig. 5.17 (h). A five-fold rotational symmetry of the precipitate pattern which is observed in near the $[11\bar{3}]_\alpha$ orientation when the sample is also tilted 11.5° from the $[11\bar{2}]_\alpha$ to the $[11\bar{3}]_\alpha$ matrix orientations. The two-fold rotation symmetry which is observed near the $[11\bar{1}]_\alpha$ orientation. This pattern is obtained when the specimen is also tilted form the five-fold axis in close to the $[11\bar{3}]_\alpha$ to the $[11\bar{1}]_\alpha$ orientation by approximately 28.6°. These results obtained using microbeam electron diffraction and systematic tilting of the specimen are thus entirely consistent with an icosahedral structure for the precipitate phase (Shechtman et al. 1984), and the orientation relationship between the precipitate phase and the matrix that is shown in Figure 5. 17.

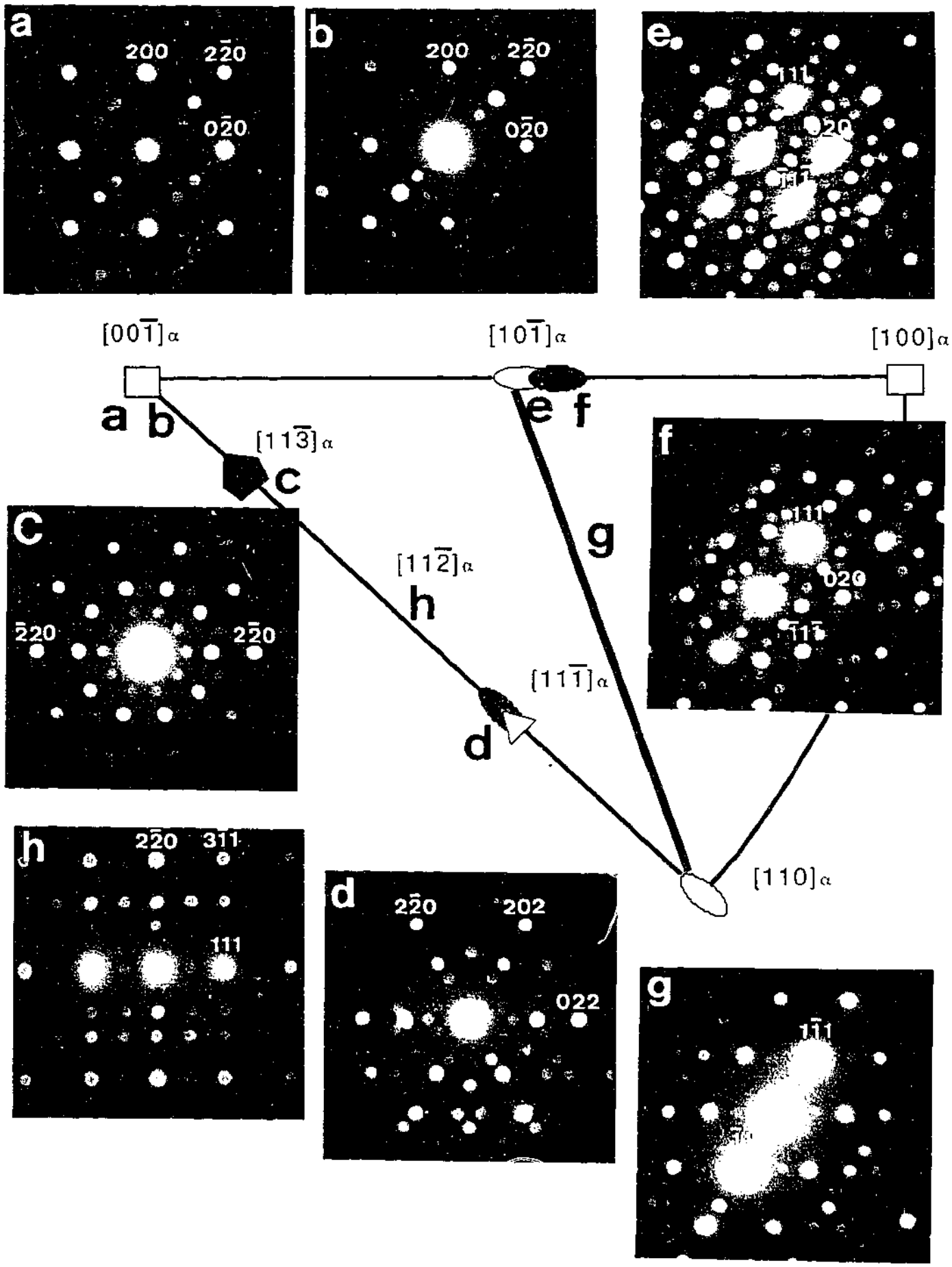

Figure 5.17 A systematic series of electron microdiffraction patterns ((a)-(h)) recorded from a relatively large scale, diamond-shaped particle in the Al-10Mg-0.5Ag alloy aged 0.5 h at 240°C. The patterns confirm the icosahedral structure of the precipitate phase and the orientation relationship.

The electron microdiffraction patterns confirm the icosahedral structure of the precipitate phase and the orientation relationship between the icosahedral structure of the precipitate phase and the aluminium matrix is shown in Figure 5.18.

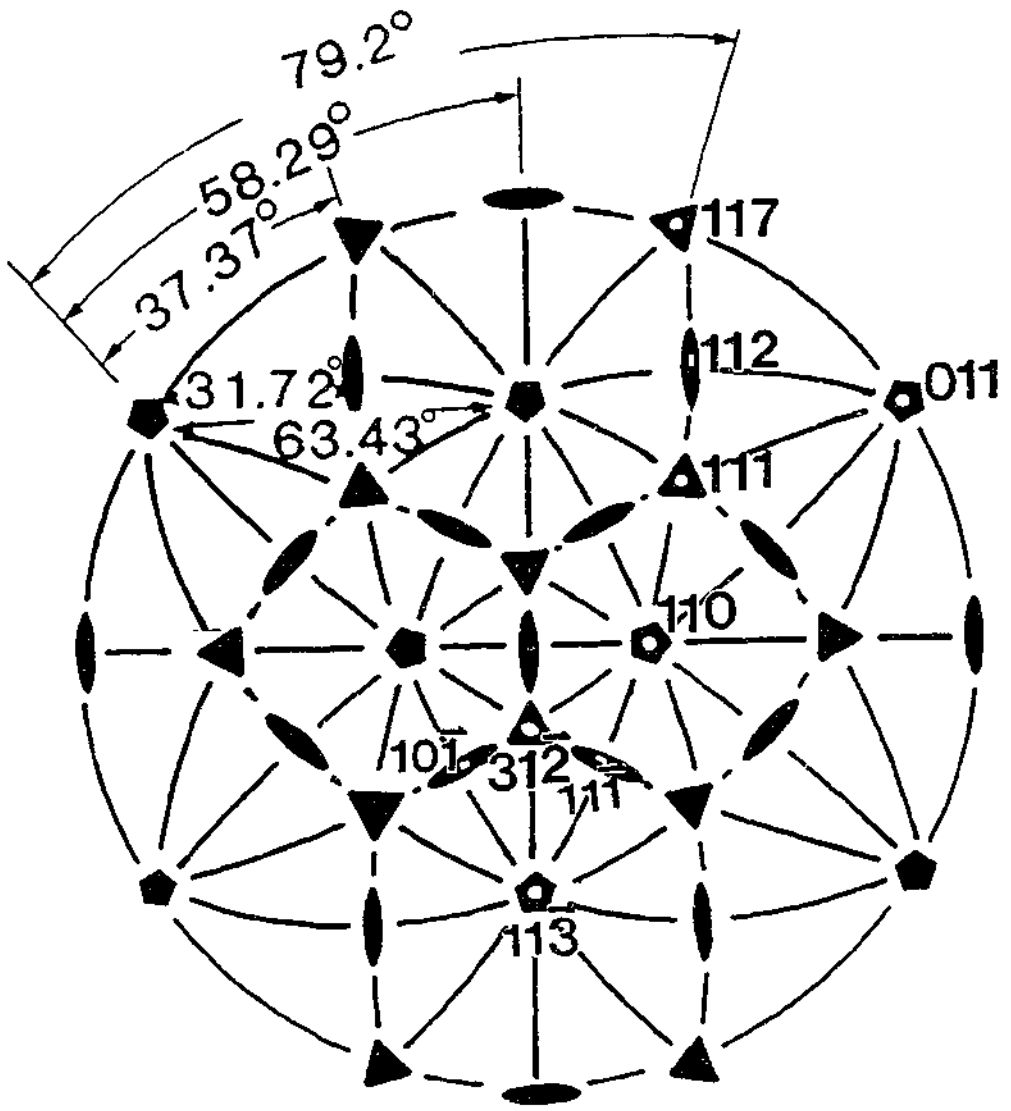

Figure 5.18 A stereographic projection showing the orientation relationship between the icosahedral structure of the precipitate phase and α-Al matrix. The symmetry elements and zones of indices representing the superimposed zone axes for the icosahedral phase and Al matrix, respectively.

Energy dispersive X-ray spectroscopy (EDXS) was carried in an attempt to assess the composition of the quasicrystalline precipitate phase. Typical energy dispersive X-ray spectra recorded from the diamond-shaped particles of precipitate phase and the aluminium matrix phase are compared in Figure 5.19. The comparison revealed that a significant concentration of Mg, with a small but still detectable concentration of Ag, were associated with the icosahedral particles, as shown in Fig. 5.19 (a). However, similar analysis of the matrix phase, Fig. 5.19 (b), revealed a relatively lower concentration of Mg, and no evidence of enhanced Ag concentration. Qualitative microanalysis thus suggested that the quasicrystalline phase was a

ternary compound that contained all three elements Al, Mg and Ag. Since the nominal diameter of the electron probe (~15 nm) was slightly larger than the typical cross section of the precipitate particles, it was difficult to avoid some overlap of the electron beam to the aluminium matrix phase. Accurate quantitative chemical analysis of the particles thus proved impossible due to the difficulty of isolating individual particles from the matrix phase.

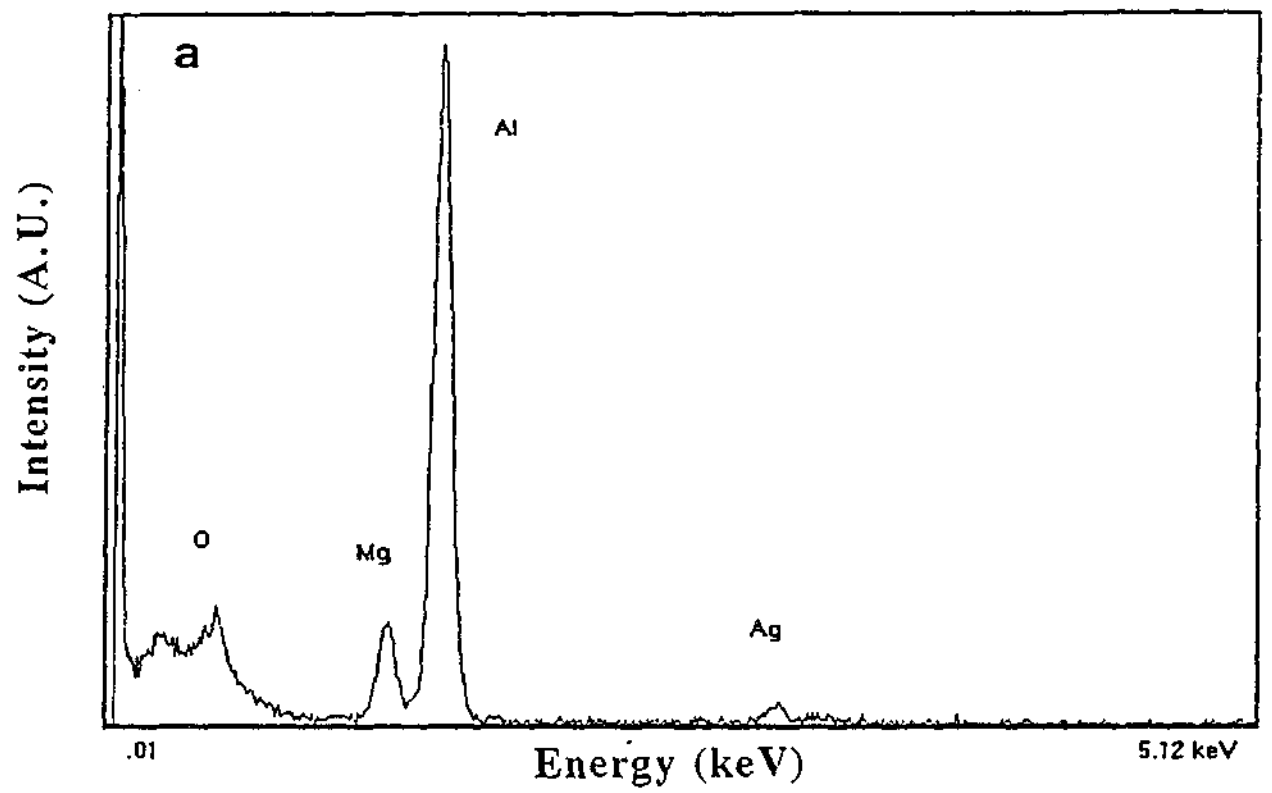

Figure 5.19 Energy dispersive X-ray spectra (EDXS) comparing compositions of (a) a quasicrystalline precipitate particle and (b) the α matrix phase adjacent to the particle. Fig. 5.19 (a) reveals small concentrations of Mg and Ag partitioning to the icosahedral phase.

Aged 2 h at 240°C

In specimens that had been aged for 2 h at 240°C, the microstructure also contained a uniform, fine-scale dispersion of precipitate particles, but the form and crystallography of the particles had changed significantly. General bright field TEM micrographs of the ternary alloy aged 2 h at 240°C are shown in Figure 5.20. The electron beam was approximately parallel to the (a) $<001>_\alpha$, (b) $<110>_\alpha$ and (c) $<112>_\alpha$ zone axes. The majority of precipitate particles now had a rod-like form (typical ~200 nm) with typical directions of the $<110>_\alpha$ and were uniformly distributed throughout the aluminium matrix. Those were two distinguishable orthogonal sets of these elongated rod-like precipitate particles, as can be seen in Fig. 5.20 (a). One set had traces parallel to the $<110>_\alpha$ directions, and the other set had the particles elongated parallel to the $<100>_\alpha$ directions. Such a distribution is consistent with a single array of rod-like forms with rod axes parallel to the $<110>_\alpha$ direction. Those particles with $<110>_\alpha$ traces are normal to the electron beam (**B** = $<001>_\alpha$), while those generally shorter particles with $<100>_\alpha$ traces are inclined at 45° to the beam direction. A small number of square-shaped precipitate particles was also observed, and these could be identified as either end-on particles of rod-like form or the faceted quasicrystalline particles which were observed in the early stages of the decomposition process during the isothermal ageing heat treatment. Higher magnification images, such as shown in Fig. 5.20 (d), and the BF images of Fig. 5.20 (a)-(c) revealed that these precipitate particles had formed and developed as near-continuous networks.

Selected area electron diffraction (SAED) patterns (Fig. 5.20) from regions containing these particles exhibited a systematic array of diffraction spots, in similar patterns to those from the quasicrystalline phase, Fig. 5.11. This implies that the SAED patterns may arise from the combination of at least two types of precipitate phases, such as rod-like and the icosahedral structures.

Figures 5.21 (a)-(c) present the microbeam electron diffraction patterns recorded from the single rod-like precipitate particles, along with the corresponding computer simulated patterns, for specimens of the ternary Al-10Mg-0.5Ag alloy aged 2 h at 240°C. The electron beam is parallel to the $[1\bar{1}0]_\alpha$, $[112]_\alpha$ and $[11\bar{1}]_\alpha$ orientations, respectively. As illustrated schematically, these patterns could be indexed consistently for the crystalline b.c.c. structure of the T phase with the lattice parameter of a = 1.41 nm, $Mg_{32}(Al,Ag)_{49}$ (Bergman et al. 1957). The atomic positions for the T phase to generate the computer simulated patterns were obtained from Pearson's Handbook (1985).

These electron diffraction patterns imply a single discrete orientation relationship between the T phase and the α - aluminium matrix, which is of the form: $(010)_T \parallel (11\bar{1})_\alpha$ and $[001]_T \parallel [1\bar{1}0]_\alpha$. Figure 5.22 shows the orientation relationship represented in stereographic projection.

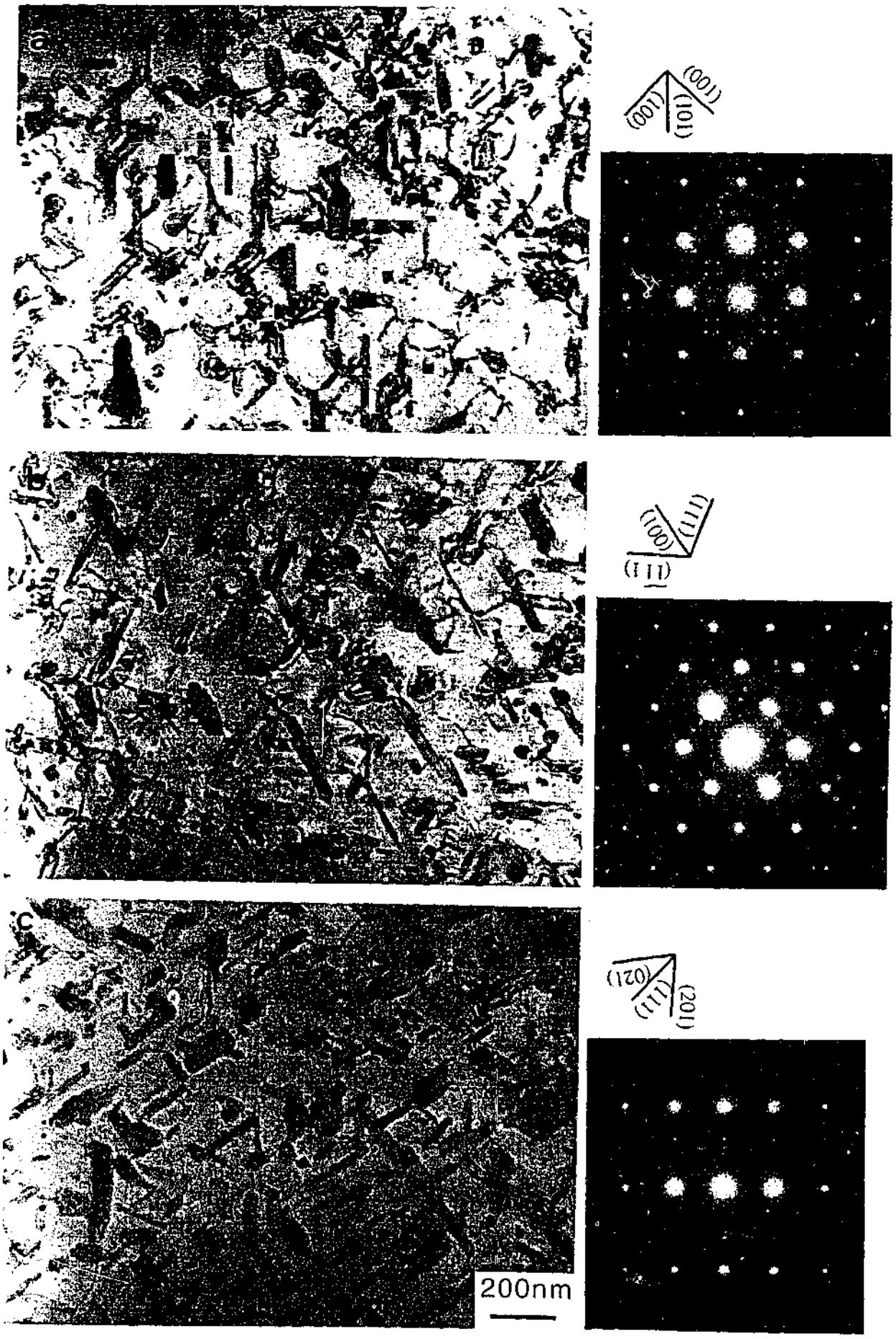

Figure 5.20 General bright field TEM images (a)-(c) and a higher magnification image (d) of the Al-10Mg-0.5Ag alloy aged 2 h at 240°C showing fine-scale, uniformly distribute rod-like precipitate particles. The electron beam is approximately parallel to the (a), (d) $<001>_{\alpha}$, (b) $<110>_{\alpha}$ and (c) $<112>_{\alpha}$ zone axes.

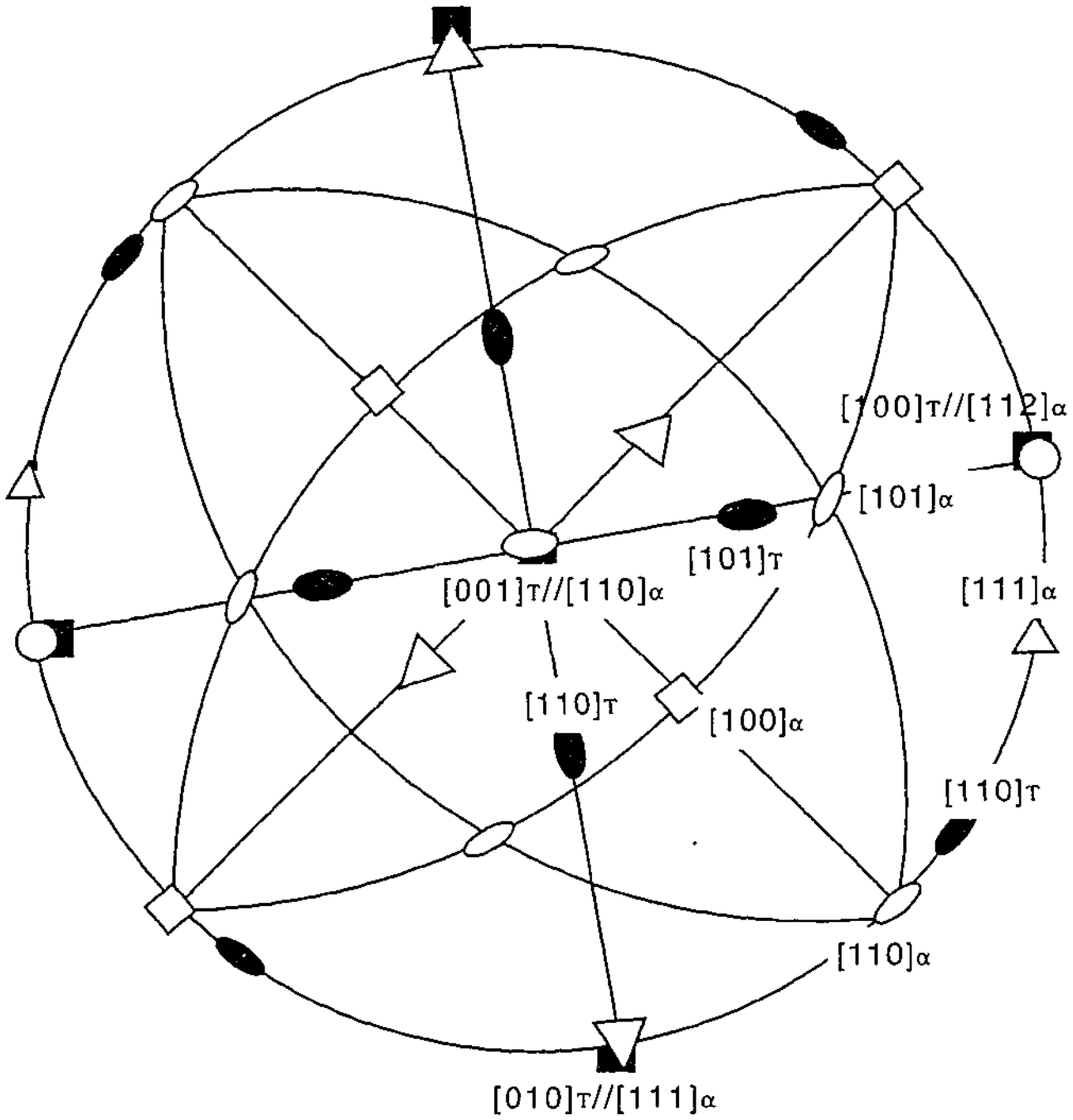

Figure 5.22 Stereographic projection showing the experimental orientation relationship between T phase and matrix, i.e. $(010)_T \parallel (11\bar{1})_\alpha$ and $[001]_T \parallel [1\bar{1}0]_\alpha$.

While the dominant phase in this microstructure has been confirmed to be the T phase by electron diffraction, the microstructure also contained a relatively small volume fraction of faceted equiaxed precipitate particles, as shown in Fig. 5.20. The microbeam electron diffraction patterns recorded from these precipitate particles have been identified as arising from the quasicrystalline phase, as shown, for example, in Figure 5.23 (a). This pattern from the quasicrystalline particle is compared with the electron microdiffraction pattern recorded from a rod-like particle of T phase, Fig. 5.23 (b). In both Figures 5.23 (a) and (b), the electron beam is approximately parallel to the $[112]_\alpha$ orientation. Although these two electron microdiffraction patterns are clearly distinguishable from each other in this orientation, they share some common diffracted

beams, suggesting the possibility of a structural relationships between the quasicrystalline phase and the crystalline T phase.

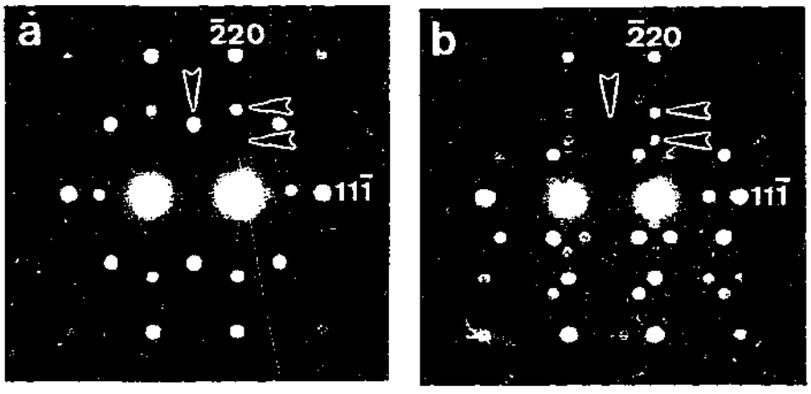

Figure 5.23 Electron microdiffraction patterns comparing distinguishable patterns from (a) a faceted, equiaxed particle and (b) a rod-like particle, in the specimen aged 2 h at 240°C. The electron beam is parallel to $[112]_\alpha$ in both cases.

Microanalysis using energy dispersive X-ray spectroscopy (EDXS) was performed in an attempt to assess the composition of the crystalline T phase. A typical energy dispersive X-ray spectrum recorded from a single rod-like particle is presented in Figure 5.24. The spectrum reveals a substantial Mg concentration with a small, but still readily detectable, concentration of Ag associated with the T phase precipitate. Qualitative microanalysis thus suggests that the crystalline T phase is a ternary compound that contains all three elements Al, Mg and Ag.

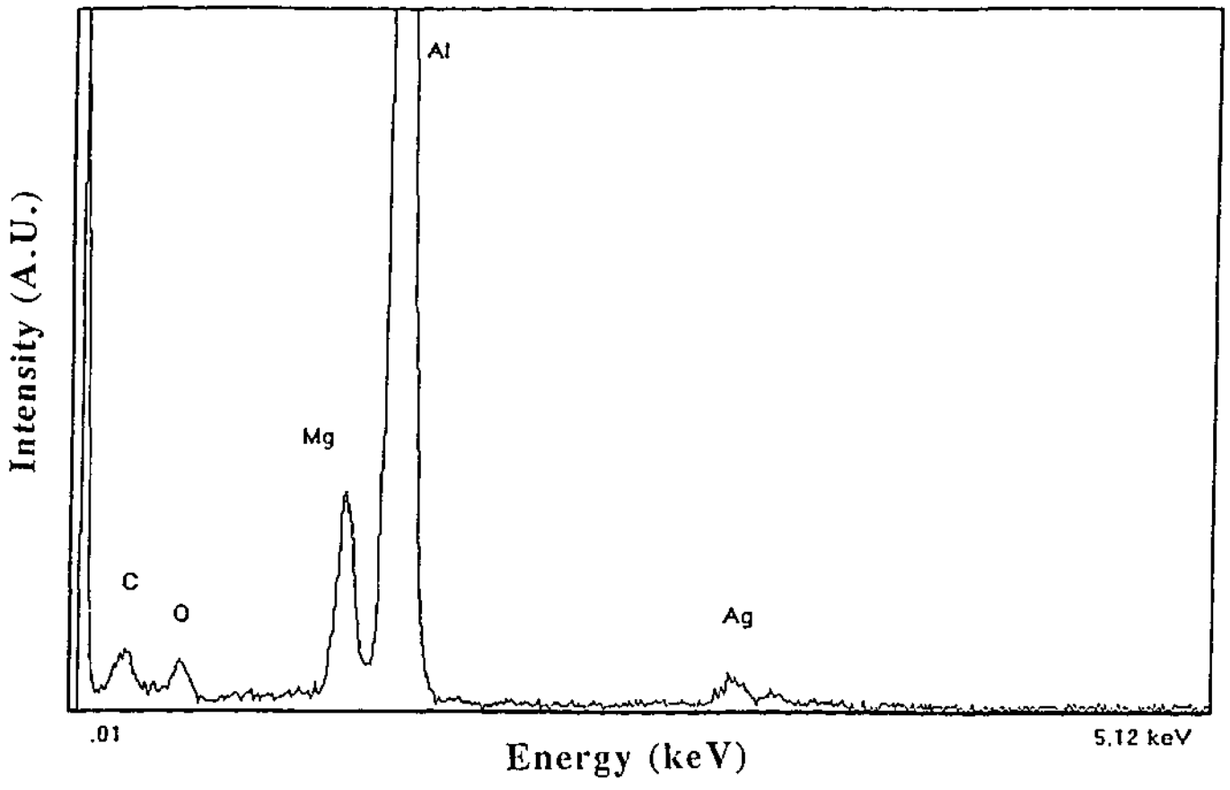

Figure 5.24 An EDXS spectrum showing that both Mg and Ag are components of the crystalline T phase observed in a sample aged 2 h at 240°C.

In addition to the above forms of particle, a small number density of elongated particles with a rectangular profile were observed in the Al-10Mg-0.5Ag alloy aged 2 h at 240°C. Figure 5.25 (a) presents a bright-field TEM micrograph which was recorded with the electron beam approximately parallel to the $<001>_\alpha$ direction. The main precipitate has dimensions of ~150 x 100 nm, which is relatively small compared to the $<110>_\alpha$ rod-like precipitates. The traces of the faces of this particle in this orientation are parallel to those of the $\{110\}_\alpha$ and $\{1\bar{1}0\}_\alpha$ planes. Microbeam electron diffraction patterns were recorded from a single particle of this form with the incident beam exactly parallel to low index zone axes of the aluminium matrix and these patterns are shown in Figure 5.25 (b)-(d). As indicated in the schematic solutions, it was possible to index the superimposed precipitate patterns as representing (a) [001], (b) [110] and (c) [111] zone axis patterns from a body-centred cubic structure. The lattice parameter of the b.c.c. phase, which was measured from the electron microdiffraction patterns shown in Fig. 5.25, was a = 1.41 nm, which again corresponds to the b.c.c. structure of the crystalline T phase, $Mg_{32}(Al,Ag)_{49}$ (Bergman et al. 1957). These patterns imply a cube on cube orientation relationship between the rectangular plate-shaped particles of precipitate T phase and the α - matrix, i.e. a relationship of the form: $(100)_T \| (100)_\alpha$ and $[001]_T \| [001]_\alpha$.

Aged 72 h at 240°C

When the ageing time was increased to 72 h at 240°C, the microstructure was dramatically changed, as shown in Figure 5.26. The electron beam is approximately parallel to the (a) $<001>_\alpha$ and (b) $<110>_\alpha$ directions. As can be seen from these TEM micrographs, no rod-like $<110>_\alpha$ particles were observed, and they were replaced by coarse-scale precipitate particles, with two distinguishable morphologies. The dominant morphology was that of coarse-scale, irregularly globular particles, while there was a small volume fraction of finer-scale, spherical precipitates. Detailed microstructural examination revealed that a majority of the coarse globular particles contained an internal faulted structure. It was interesting to note that these precipitate particles were also surrounded by a high density of dislocations within the aluminium matrix, suggesting that nucleation (and growth) of these globular particles may generate such defects.

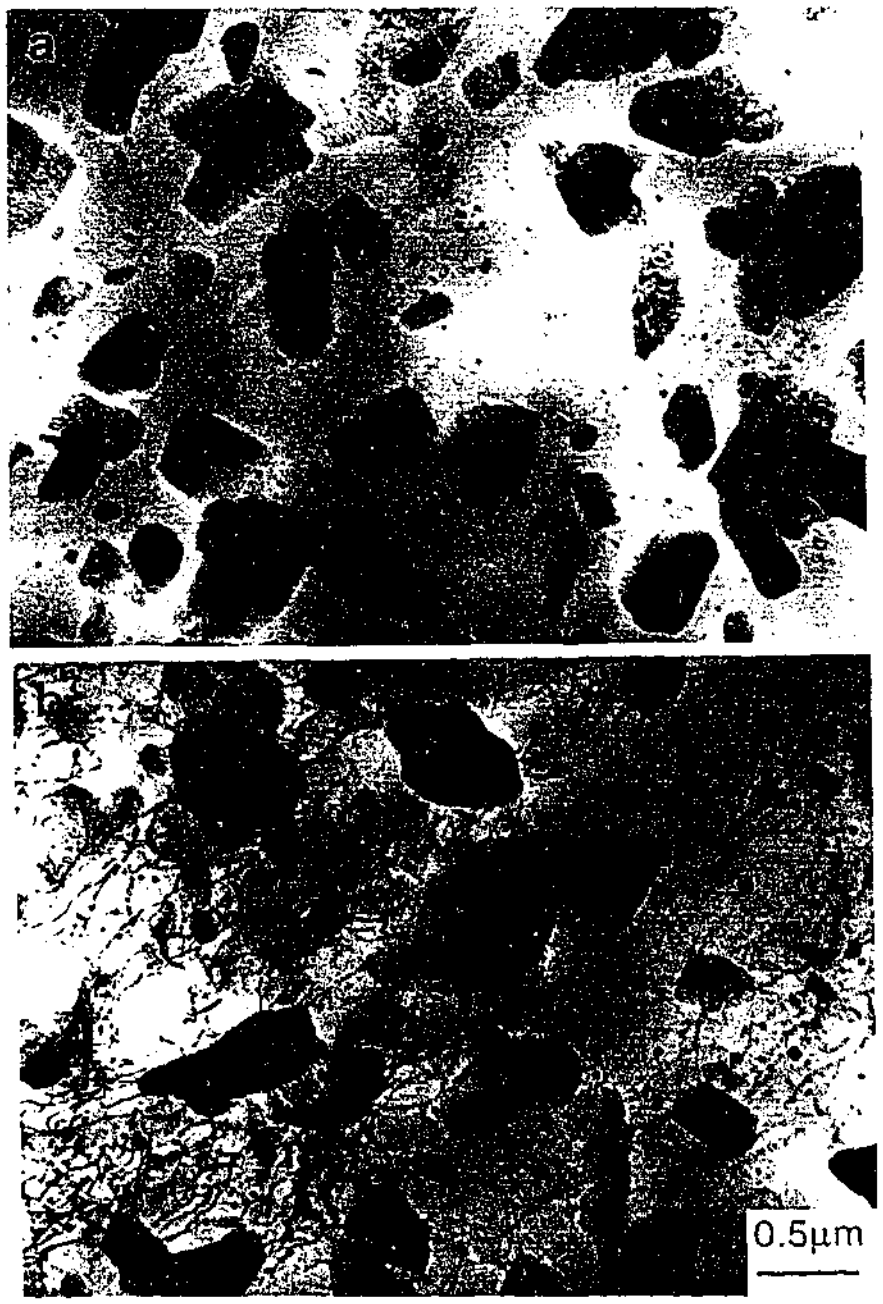

Figure 5.26 The microstructure typical of the Al-10Mg-0.5Ag alloy aged 72 h at 240°C showing two different morphologies of precipitate particle. The electron beam was approximately parallel to the (a) $<001>_\alpha$ and (b) $<110>_\alpha$ directions.

X-ray microanalysis (EDXS) was performed in an attempt to assess the composition of the coarse globular precipitate phase. A typical energy dispersive X-ray spectrum recorded from a single globular particle is presented in Figure 5.27. The spectrum reveals a substantial concentration of Mg, but no detectable concentration of Ag associated with the particle. Qualitative microanalysis thus suggested that the globular precipitate phase was a binary compound of Al and Mg.

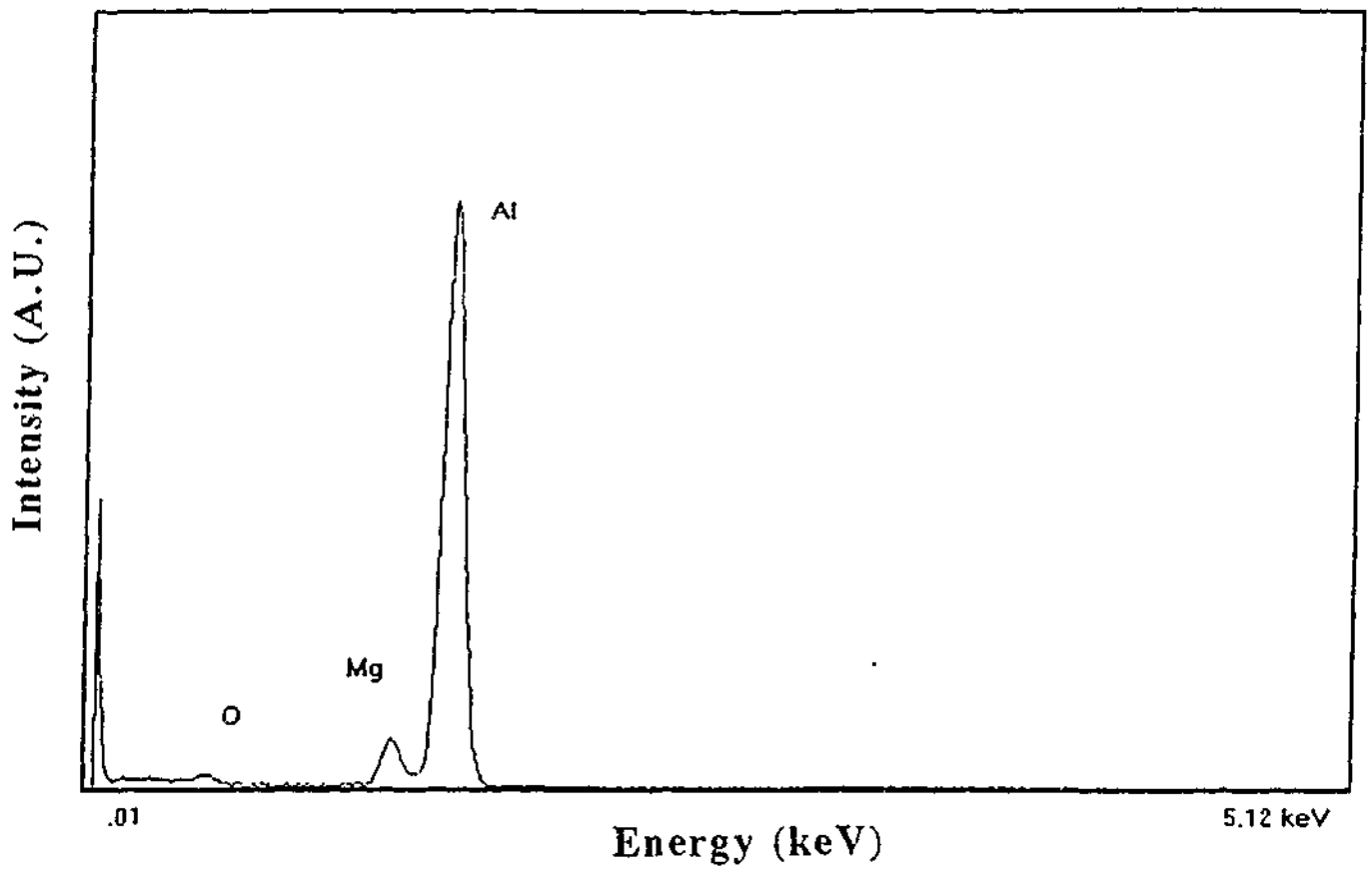

Figure 5.27 X-ray microanalysis (EDXS) spectrum showing that only the elements Mg and Al were detectable in association with globular particles such as those shown in Fig. 5.26.

Figures 5.28 (a) and (b) show TEM micrographs of regions containing the smaller spheroidal particles in the specimen aged 72 h at 240°C; the electron beam was approximately parallel to the (a) $<110>_\alpha$ and (b) $<112>_\alpha$ directions. As can be seen from these BF images, the scale of such particles was less than 100 nm, and a dislocation array was invariably observed surrounding each precipitate particle. Electron microdiffraction patterns recorded from such small spheroidal precipitate particles, together with the schematic solutions, are shown in Fig. 5.28 (c)-(e). These diffraction patterns could be indexed consistently for the f.c.c. structure of the equilibrium β phase, with the lattice parameter of a = 2.82 nm (Samson 1965). It is to be noted that the lattice parameter of the β phase is almost exactly seven times that of the aluminium matrix phase, and the precipitates share an identity orientation relationship with the aluminium matrix, i.e. a relationship of the form $(100)_\beta \parallel (100)_\alpha$ and $[001]_\beta \parallel [001]_\alpha$. Such particles and this form of orientation relationship have not been reported previously for the equilibrium β phase.

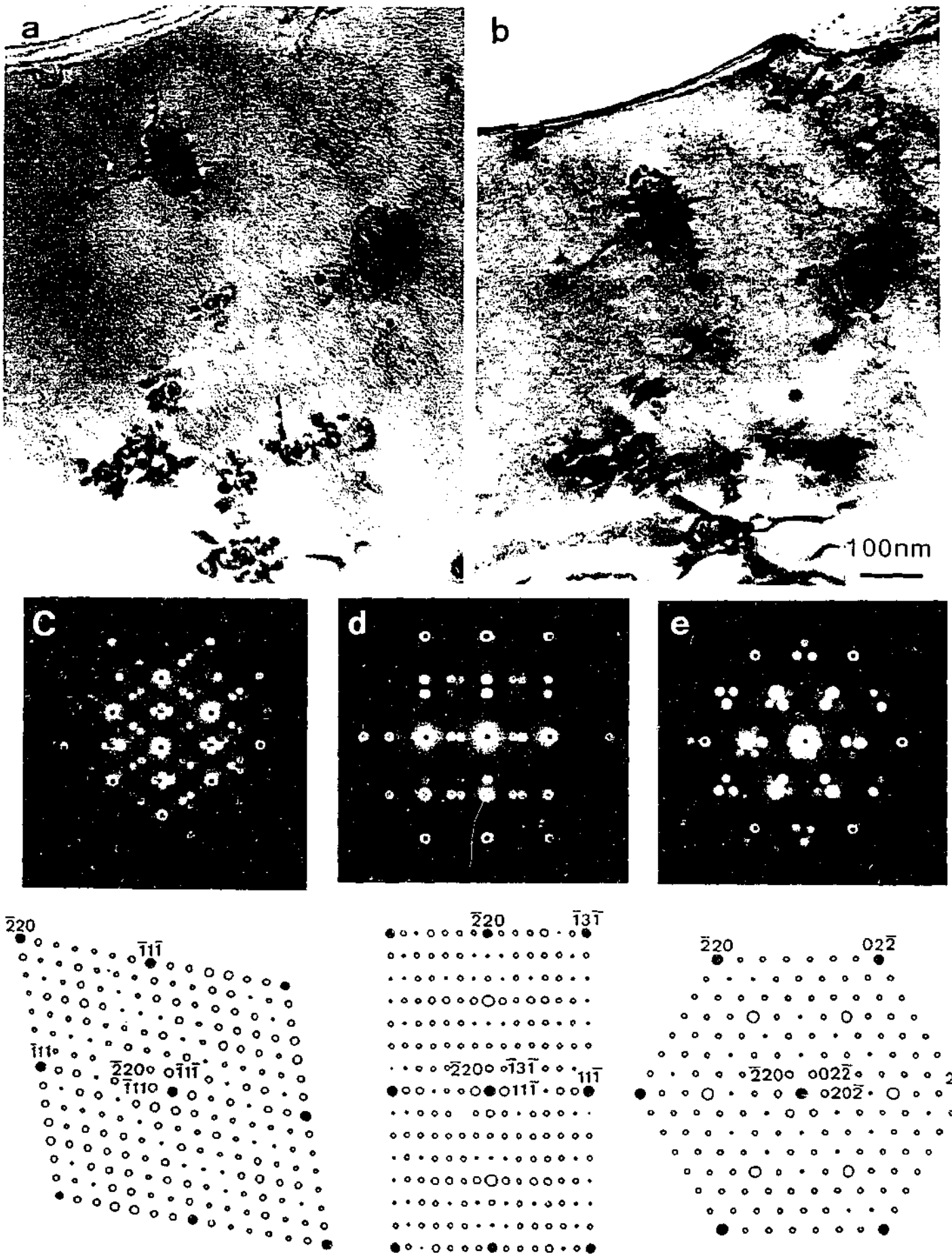

Figure 5.28 BF images recorded parallel to (a) $<110>_\alpha$ and (b) $<112>_\alpha$ directions, showing small spheroidal particles, surrounded by dislocation arrays in the Al-10Mg-0.5Ag alloy aged 72h at 240°C. Electron microdiffraction patterns recorded from the small spheroidal precipitate particles approximately parallel to the (c) $<110>_\alpha$, (d) $<112>_\alpha$ and (e) $<111>_\alpha$ directions.

Figure 5.29 (a) shows a BF image of the microstructure of the specimen aged 72 h at 240°C in an $<110>_\alpha$ orientation. The region contains several coarse-scale, globular particles that are irregularly faceted. SAED patterns recorded from these particles are compared in Figs. 5.29 (b)-(g). The electron beam was approximately parallel to the (b), (e) $<001>_\alpha$; (c), (f) $<110>_\alpha$; and (d), (g) $<112>_\alpha$ directions. Figures 5.29 (b)-(d) were recorded from the particle labelled 1, and could be indexed consistently for the equilibrium β phase, while the SAED patterns recorded from the second particle (labelled 2) contained diffracted spots from the equilibrium β phase, together with diffracted beams arising from a twined substructure within the β phase.

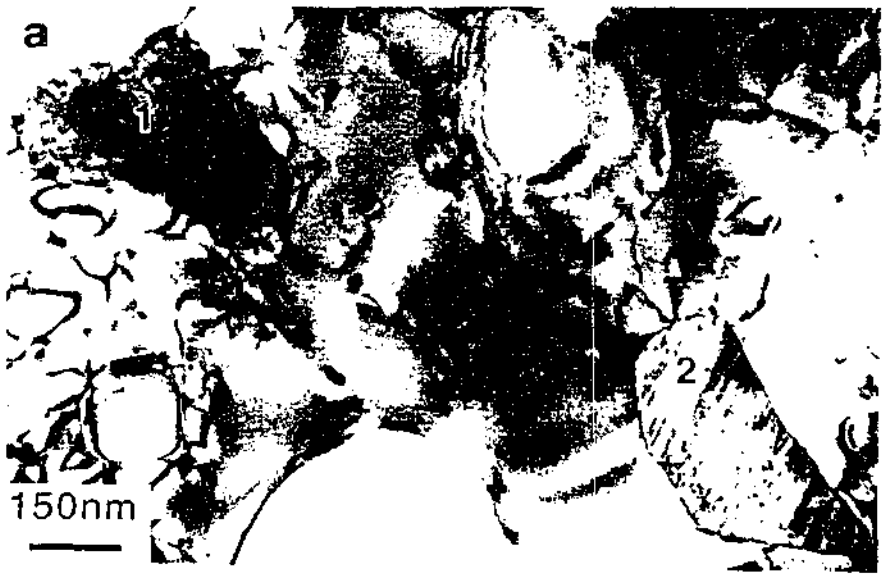

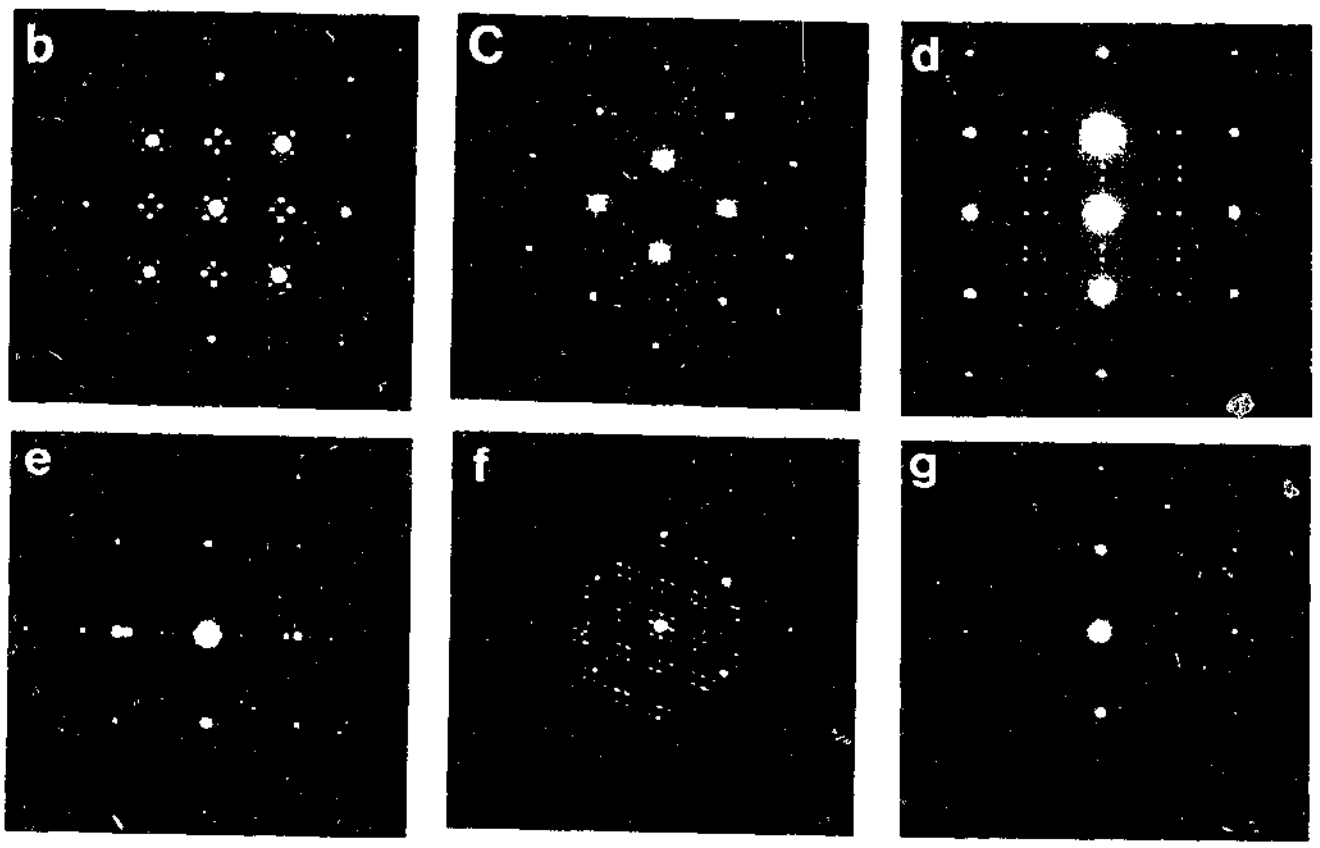

Figure 5.29 (a) BF image showing coarse scale particles within the microstructure of the specimen aged 72 h at 240°C. The SAED patterns were recorded from these particles with the electron beam approximately parallel to the (b), (e) $<001>_\alpha$; (c), (f) $<110>_\alpha$; and (d), (g) $<112>_\alpha$ directions.

Figure 5.20 Continued.

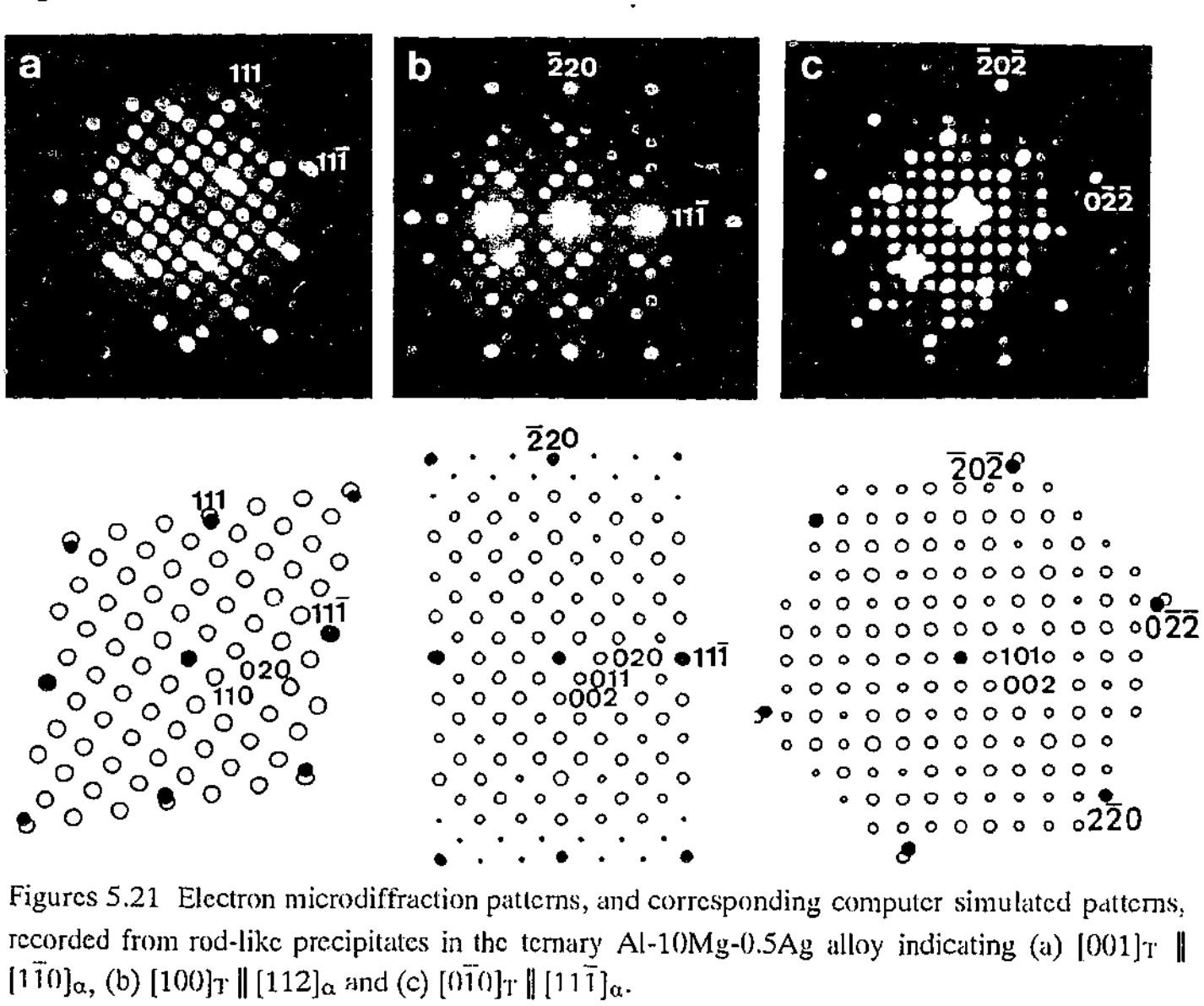

Figures 5.21 Electron microdiffraction patterns, and corresponding computer simulated patterns, recorded from rod-like precipitates in the ternary Al-10Mg-0.5Ag alloy indicating (a) $[001]_T \parallel [1\bar{1}0]_\alpha$, (b) $[100]_T \parallel [112]_\alpha$ and (c) $[0\bar{1}0]_T \parallel [11\bar{1}]_\alpha$.

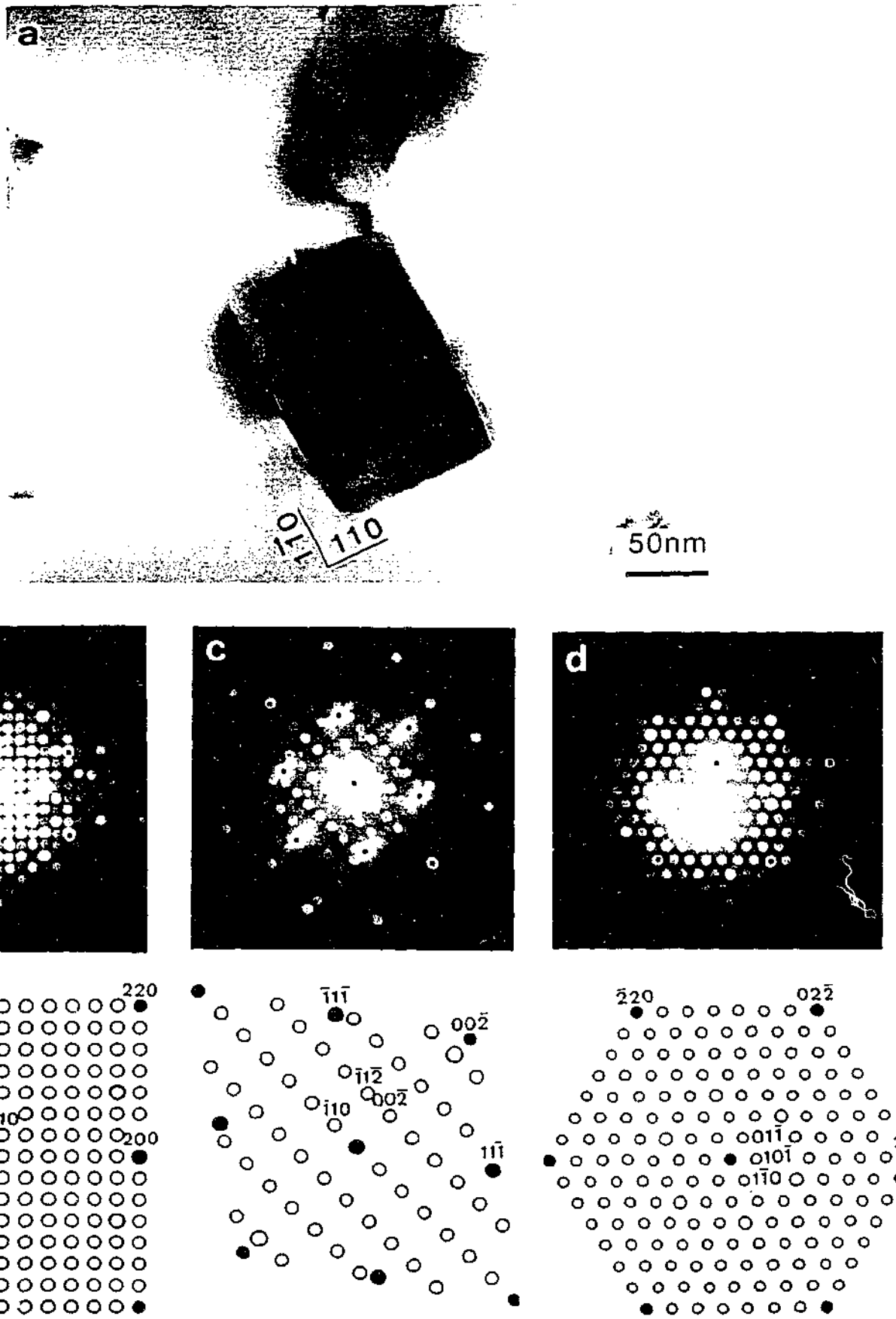

Figure 5.25 TEM micrograph (a) showing the morphology of a third form of precipitate particle in Al-10Mg-0.5Ag alloy. The electron beam was approximately parallel to the $<001>_\alpha$ direction. Electron microdiffraction patterns from such a particle and corresponding schematic solutions based on the body-centred cubic structure of T phases. Patterns were recorded parallel to (b) [001], (c) [110] and (d) [111] zone axes.

A lattice fringe image of a single coarse globular particle recorded with the electron beam parallel to a $<110>_\alpha$ direction is shown in Figure 5.30 (a). Such substructure was a common feature of almost every precipitate, suggesting that twinning may be intimately involved in the nucleation and growth of this precipitate phase. Primary twinning leads to a rotation of about 70°, secondary twinning to an additional rotation of around 70°, and so on. The inter plan spacing between each atomic plan is approximately 1.6 nm along to the $<1\bar{1}1>_\alpha$ and $<\bar{1}\bar{1}1>_\alpha$ directions, which is consistent with the d-spacing of the $\{111\}_\beta$ planes of the equilibrium β phase. This indicates that the traces of the twin variants are consistent with twinning on the {111} planes of the f.c.c. structure. Internal multiple twinning of the globular precipitates by reflection across a {111} plane leads to extra reflection spots in the SAED patterns, as shown in Figure 5.30 (b), and this is related to the primary precipitate by an approximately 70° rotation about the <110> orientation in the twin plane. Multiple twinning is most likely to occur on both twin planes, and the primary twins each of the two twin systems will be related to each other by twice the rotation angle.

From the recorded SAED patterns, an orientation relationship between the β phase and twin structures can be deduced in the form of $(1\bar{1}1)_\beta \parallel (1\bar{1}1)_t$ and $[011]_\beta \parallel [0\bar{1}\bar{1}]_t$. The computer simulated selected area diffraction pattern generated using the proposed orientation relationship is shown in Figure 5.30 (c). This simulated electron diffraction pattern agrees well with the observed electron diffraction pattern.

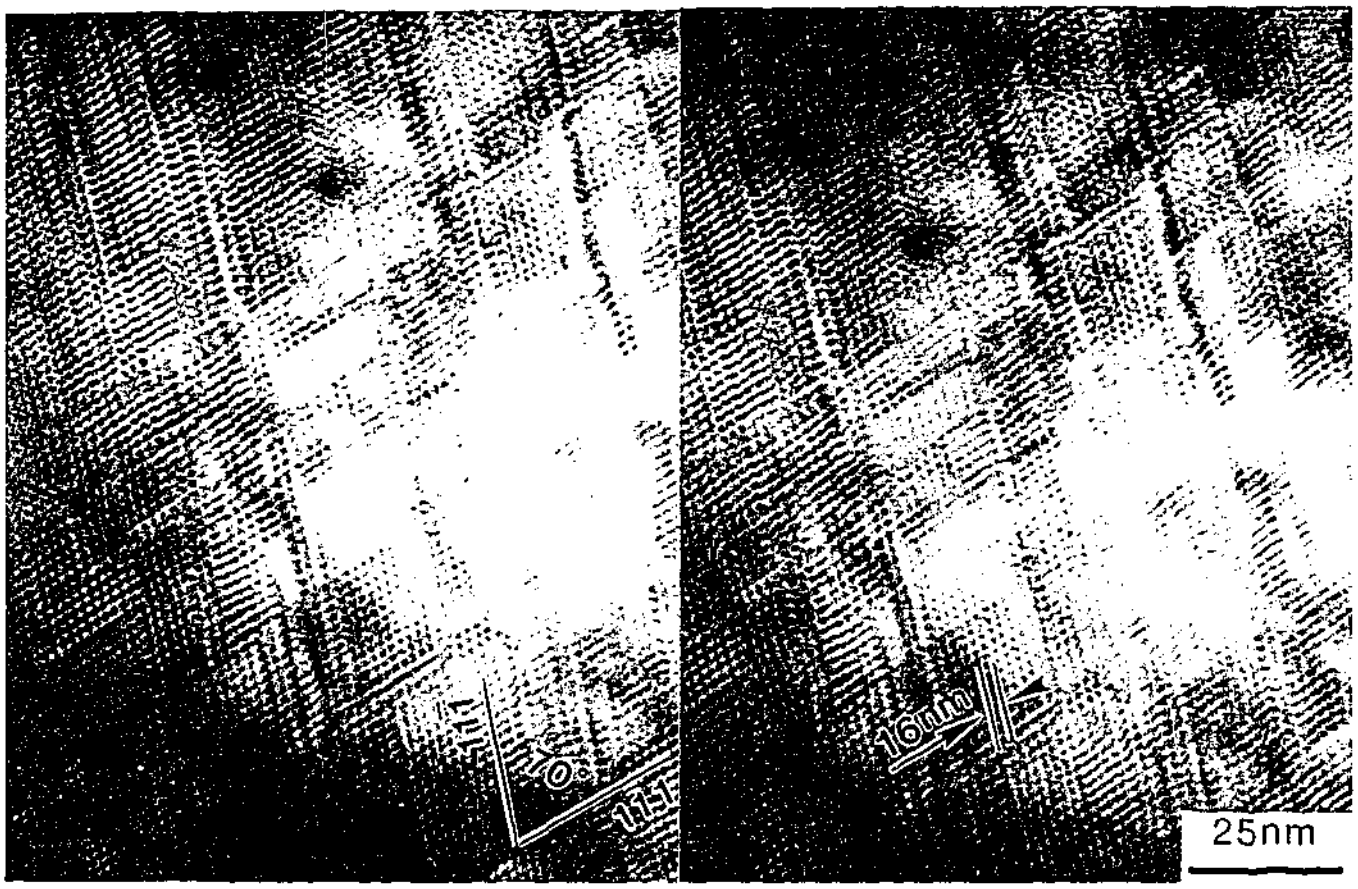

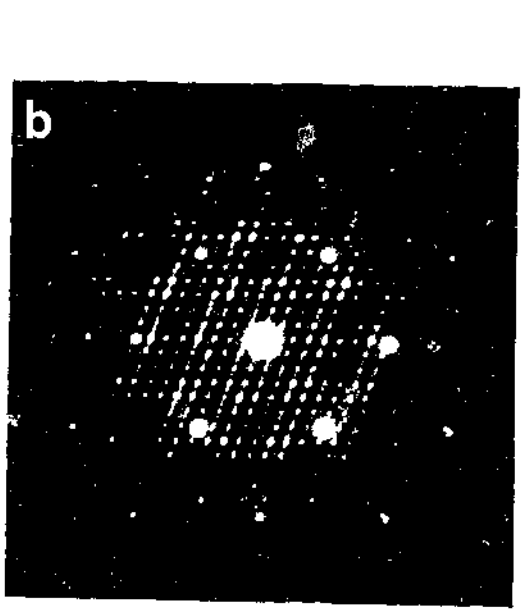

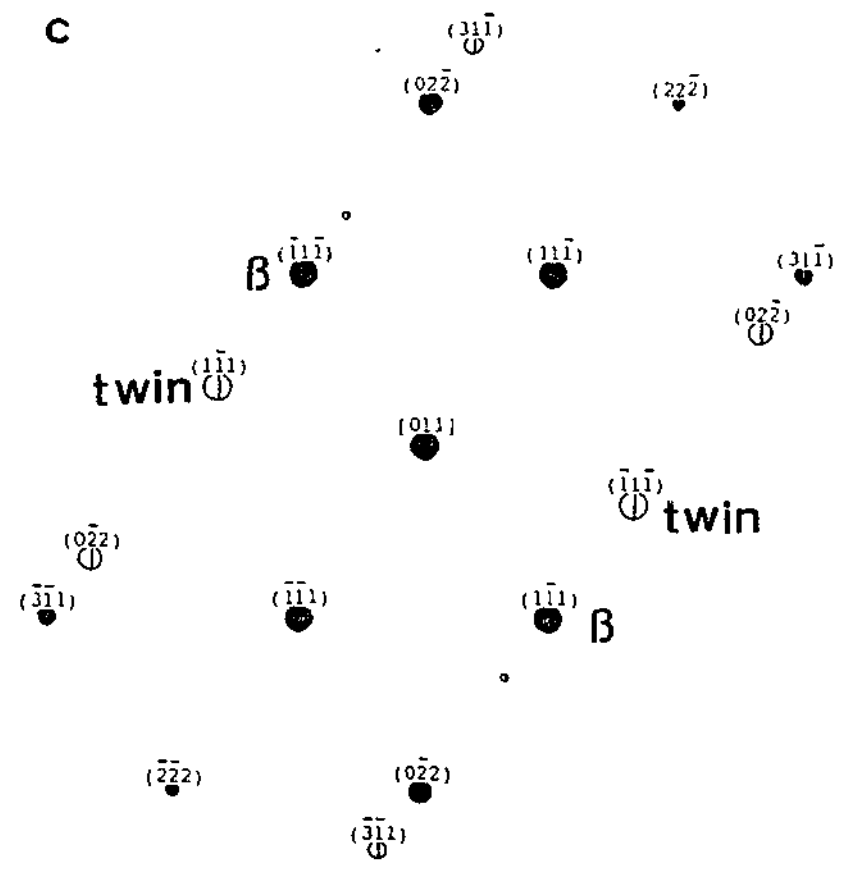

Figure 5.30 (a) a lattice fringe image of a single coarse globular particle oriented with an $<011>_\alpha$ direction parallel to the electron beam direction, (b) a SAED pattern recorded from such a particle exhibiting extra diffracted spots and (c) the corresponding computer simulated diffraction pattern showing the orientation relationship between the β phase and twin structure.

5.3 Discussion

5.3.1 The β' and β Phases in Binary Al-Mg Alloy

As mentioned earlier in Chapter 2, the intermediate β' phase forming in binary Al-8.5% Mg alloys has been reported to form as plate-shaped particles parallel to $(100)_\alpha$, $(111)_\alpha$, $(210)_\alpha$ and $(310)_\alpha$ planes in specimens aged at 150°C, and rod-like particles elongated parallel to $[100]_\alpha$, $[110]_\alpha$, $[120]_\alpha$ and $[111]_\alpha$ directions in specimens aged at 200°C (Matsuura and Koda 1965, Mondolfo 1976). In addition, two forms of morphologies of the equilibrium β phase have been observed in an Al-10% Mg alloy (Bernole et al. 1969). One is a blocky morphology observed in an alloy aged 96 h at 200°C, and the other is globular form detected when the alloy was aged 0.5 h at 300°C (Bernole et al. 1969). Plate- and lath-shaped particles were also reported when Al-10% Mg alloy was aged 2 h at 300°C (Bernole 1974).

The present microstructural observations for Al-10Mg alloy aged at 240°C have revealed that the predominant precipitates in the aged microstructures (e.g. 5 h at 240°C) are generally coarse-scale, and sparsely distributed, and have an irregular blocky shape. However, both plate- and lath-shaped precipitate particles have also been observed in the early stages of ageing (e.g. 0.5 h at 240°C), as shown in Fig. 5.1. Although crystallographic analyses for these plate- and lath-shaped precipitate particles have not been carried out due to difficulties to obtain electron diffraction patterns from those individual particles, the precipitate morphologies observed by TEM in specimens aged at 240°C are generally consistent with the results previously reported.

Although detailed identification of these precipitate particles by the electron diffraction technique has been limited in this current research due to difficulties of sample preparation, it is generally accepted that the intermediate β' and equilibrium β phases are formed during isothermal ageing of binary Al-Mg alloys. Although nucleation of the intermediate β' and equilibrium β phases are time dependence at ageing temperatures, the metastable β' phase is formed at 150°C and 200°C, while the stable β phase is formed above 200°C. From a limited number of electron diffraction patterns collected in the present work it appeared that the crystal structure and lattice parameters of the intermediate β' phase were consistent with results previously reported, i.e. a hexagonal structure with lattice parameters of a = 1.002 nm, c = 1.636 nm, and semi-coherent with the aluminium matrix (Bernole et al. 1969, Bernole 1974, Mondolfo 1976).

As for the orientation relationship between the intermediate β' and aluminium matrix phases, the present electron diffraction results, Fig. 5.9 (d), showed that the $<11\bar{2}6>_{\beta'}$ and $<112>_\alpha$ zone axes were approximately parallel. However, the previous studies reported that orientation relationships have the certain form, i.e. $(0001)_{\beta'} \parallel (001)_\alpha$ and $[21\bar{3}0]_{\beta'} \parallel [110]_\alpha$ (Bernole et al. 1969), and $(0001)_{\beta'} \parallel (001)_\alpha$ and $[01\bar{1}0]_{\beta'} \parallel [110]_\alpha$ (Bernole 1974), which are not consistent with

the present research. The reason for this difference still remains unclear, but the reported orientation relationships were associated with plate-like β' particles (Bernole et al. 1969, Bernole 1974), and not the irregularly-shaped or lath-like particles observed in the present work. In addition, the present ageing temperature (240°C) was significantly higher than the temperature range of previous studies, and this may change the nature and crystallography of the precipitation reaction.

A limited number of electron diffraction patterns has been recorded from precipitate particles, which were subsequently identified as the equilibrium β (Al_3Mg_2) phase. These patterns could be indexed consistently for a f.c.c., with a lattice parameter of a = 2.82 nm, which is consistent with the results previously reported for the β phase (Perlitz 1944, Samson 1965, Bernole et al. 1969).

As for the orientation relationship between the β phase and aluminium matrix, the present study has been indicated that the precipitate β phase generally dose not share the low symmetry index axes of the aluminium matrix except for two examples, such as $<110>_\beta \parallel <110>_\alpha$ and $<110>_\beta \nparallel <112>_\alpha$, as shown in Figs. 5.9 (c) and (e) respectively. This result is readily different from the orientation relationships previously reported, i.e. $[001]_\beta \parallel [001]_\alpha$ and $[110]_\beta \parallel [100]_\alpha$ in the Al-10% Mg alloy aged at 200°C and 300°C (Bernole et al. 1969), and $(111)_\beta \parallel (001)_\alpha$ and $[110]_\beta \parallel [010]_\alpha$ (Bernole 1974).

The nucleation of the β phase (Al_3Mg_2) has been studied by a number of researchers (Bernole et al. 1969, Bernole 1974, Bouchear et al. 1996, Bhargava et al. 1998). They have suggested from TEM observations that the β phase is preferentially formed either at the interphase boundary between the intermediate β' and matrix phases, or at matrix grain boundaries or on dislocations within the matrix. This clearly implies that the intermediate β' particles nucleate first from the supersaturated matrix solid solution, and then provide in turn nucleation sites for the formation of the equilibrium β particles. This evidence of almost exclusively heterogeneous nucleation of the equilibrium particles suggests that homogeneous nucleation of the β phase is energetically quite difficult in the aluminium matrix. This perhaps explains the low number density and coarse scale of the equilibrium precipitate particles, and these microstructural parameters in turn account qualitatively for the lack of a significant strengthening response during ageing of the binary alloys.

Irregular, equiaxed particles of equilibrium β phase have previously been observed in an Al-9% Mg alloy aged 5 h at 250°C, repeatedly forming preferentially at the interface between the intermediate β' particles and the aluminium matrix, although no direct evidence was provided to support phase identification (Bouchear et al. 1996). In the present work, the blocky particles of β phase were associated with irregularly-shaped particles of an unidentified phase in which were

also associated with lath-like intermediate β' particles, as shown in Figs. 5.4. In addition, there was also evidence that the blocky β particles were attached to the unidentified irregularly-shaped particles, as presented in Figs. 5.8. These evidence mentioned above were supported by the limited electron diffraction patterns recorded from individual precipitate particles. However, the detailed orientation relationships between these unidentified, β' and β phases, as well as the orientation relationships with respect to the aluminium matrix have not been identified.

5.3.2 The Quasicrystalline Phase

Introduction

A quasicrystalline phase with icosahedral structure was first discovered in a rapidly solidified Al-14 at% Mn alloy (Shechtman et al. 1984). This new phase does not easily fall into the categories of either crystalline or glassy phases. Diffraction patterns show sharp intensity maxima and their arrangement reveals an icosahedral point group symmetry, which is incompatible with translation symmetry. Unique to this new class of structures, the diffraction patterns show five-, three- and two-fold axes of rotational symmetry conforming to point group m35 (Bendersky and Kaufman 1986). The arrangement of the diffraction maxima in selected area electron diffraction (SAED) patterns, which can be interpreted to represent projected sections through the three-dimensional reciprocal lattice, is not regularly periodic. The diffraction spots are arranged in a quasiperiodic fashion, with the distance ratios between adjacent pairs of reflections in a given systematic row being given by τ^n, where the irrational number τ is equal to $(1+\sqrt{5})/2 = 1.618$, and $n = 1, 2, 3$ ($\tau^1 = 1.618$, $\tau^2 = 2.618$).

A range of icosahedral quasicrystalline phases has been identified in several aluminium alloy systems, especially those based on combinations involving the transition metals. In most cases these metastable phase have been produced by non-equilibrium processing, usually involving rapid quenching techniques (Shechtman et al. 1984, Tsai et al. 1987). Such phases are much less common as the product of solid state transformations. A stable ternary compound design at T_2 (Al_6CuLi_3) (Hardy and Silcock 1955) has been observed in Al-Cu-Li alloys, and has been shown to exhibit an icosahedral structure when the alloy has been produced by either conventional casting with low solidification rates (formed as dendrites) or subjected to isothermal ageing treatments of the supersaturated solid solution (formed as precipitates) (Sainfort et al. 1985). This icosahedral quasicrystalline compound exhibits unusual thermal stability, which is uncharacteristic of most rapidly solidified Al alloy systems. The T_2 phase generally nucleates at grain boundaries from melt during casting, and is then replaced by a crystalline phase during prolonged annealing. No significant contributions to mechanical strength from the icosahedral T_2 particles would be expected.

The major importance of this discovery was that the quasicrystalline phase was observed in Al-Cu-Li alloy compositions, which lie within the range of commercial importance, e.g. 2090 type alloys, and that this phase was produced during a conventional ingot metallurgy process for an Al-2.1Li-2.1Cu-1Mg (wt%) alloy (Sainfort and Dubost 1987) and an Al-9Li-1Cu-0.05Zr (at%) alloy (Cassada and Shiflet 1986). However, it is to be emphasised that the icosahedral T_2 phase is still apparently the product of a solidification reaction. In contrast, the current research has established that, in Al-10Mg-0.5Ag alloy, an icosahedral quasicrystalline phase may arise in a fine scale, uniform distributions of faceted particles as the product of a solid state transformation during a conventional isothermal ageing process. The uniform nucleation of such precipitate particles promotes a significant strengthening response (Chapter 4), although the icosahedral particles are replaced by a metastable crystalline phase prior to reaching maximum hardness.

It should be noted that the formation of the icosahedral quasicrystalline particles in Al-Mg-Ag alloys during isothermal ageing heat treatments is perhaps one of the first observation of a quasicrystalline phase forming as the product of a solid state reaction during a conventional processing treatment. Upon this unique and first observation, it is thus very important to discuss the structure of this precipitate phase in detail. Detailed characterisation for uniform nucleation of such precipitate particles based on the results from electron microdiffraction will be discussed in the next section.

Identification

As confirmed earlier in the separate SAED patterns recorded from arrays of coarser (Fig. 5.11 (a)-(c)) and finer (Fig. 5.11 (d)-(f)) scale precipitate particles in the different regions of a grain, the crystal structure of these different forms of precipitate particle appeared to be the same. A series of microbeam electron diffraction patterns recorded from relatively large scale, diamond-shaped particles was established the detailed tilting angle among icosahedral symmetry including the aluminium matrix orientations, as listed in Table 5.1.

As indicated in Table 5.1, there is tilt angle of 63° between five-fold rotational symmetry. This angle is almost similar to that of $[110]_\alpha$ matrix axes. The misorientation between the precipitate five-fold axis and the matrix $<110>_\alpha$ axis was experimentally obtained during a large angle tilting, and was approximately 2° - 4° tilted away from the $<110>_\alpha$ matrix zone axis towards to the matrix $<002>_\alpha$ direction. Three-fold rotational symmetry in the precipitate pattern in a $<111>_\alpha$ orientation is truly parallel orientation, as confirmed in Figs. 5.16 (a)-(c). The angle of tilt required to move from the axis of five-fold symmetry to that of three-fold symmetry was approximately 37°. Two-fold rotational symmetry of the precipitate pattern is detectable in the $<112>_\alpha$ orientation, when the specimen is tilted approximately 21° from the $<111>_\alpha$ to near $<112>_\alpha$ zone axis. These results from systematic tilting experiments entirely confirmed that tilt angles among major rotational symmetry axes are consistent with the result previously reported

(Shechtman et al. 1984).

It is well established (Shechtman et al. 1984) that selected area electron diffraction (SAED) patterns recorded from icosahedral quasicrystalline phases display three-fold and five-fold rotational symmetry with the golden ratio $\tau = (1+\sqrt{5})/2$ (the characteristic number of icosahedral quasiperiodicity) and two-fold rotational symmetry with a non-uniform scaling factor. To examine whether the observed microbeam electron diffraction patterns in the present research were consistent with this requirement, careful measurements of the electron diffraction patterns were carried out. The distances of diffracted spots between the transmitted spot and the first reflection spot from the precipitate phase, between the transmitted spot and the second reflection spot from the precipitate phase, and between the transmitted spot and the third reflection spot from the precipitate phase (corresponding to the $(220)_\alpha$ spot) in the three-fold rotational symmetry patterns (e.g. Fig. 5.15 (c) and Fig. 5.16 (c)) in the negative films are approximately 4.4±0.1 mm, 7.0±0.1 mm and 11.3±0.1 mm, respectively, which are closely corresponded to the golden ratio, τ = 1.618 (7.0/4.4=1.591) and the square of the golden ratio, τ^2 = 2.618 (11.3/4.4=2.568). The ratios obtained from the measurements of the negative films are also consistent with the five-fold rotational symmetry patterns of the precipitate phase (e.g. Fig. 5.15 (b) and Fig. 5.17 (c)).

It has been pointed out that a quasicrystalline phase can be characterised by a quasilattice constant a_R (Elser and Henley 1985), which corresponds to the edge length of the rhombohedra (either prolate or oblate) which must be packed quasi-periodically to form three-dimensional Penrose tiling. Since the three-dimensional Penrose tiling structure can be generated by projections from a six-dimensional simple-cubic lattice, the cubic lattice constant a_c and the value of a_R are related (Henley and Elser 1986), and this relationship may be expressed in the form $a_c = \sqrt{(4+8/\sqrt{5})}a_R$.

From the presently observed microdiffraction patterns, the quasilattice constant a_R of icosahedral phase may be estimated (Mackay 1987) from an expression of the form $a_R = \tau^3 d_{i5}/2$, where τ is the golden mean, and d_{i5} represents the spacing of planes perpendicular to the five-fold axis giving rise to the most intense diffracted beams. Careful measurements for the d_{i5} value in the present 5-fold electron microdiffraction patterns gave a value of a_R = 0.505±0.01 nm. The lattice parameter a_c of the corresponding crystalline cubic approximant may be derived from an equation of the form $a_c = \sqrt{(4+8/\sqrt{5})}a_R$, and is thus calculated to have a value of 1.390±0.028 nm. This is in good agreement with the lattice parameter of the crystalline T phase (a = 1.416 nm) (Bergman et al. 1957).

It is to be recognised that crystals with an apparent five-fold axis of symmetry may also occur as a result of multiple twinning, and not as a result of true icosahedral symmetry (Pauling

1985). The faces of a regular icosahedron may be generated by the $\{111\}_\alpha$ planes of an appropriate assembly of twenty twin-related crystals, which have a tetrahedral form defined by facets parallel to $\{111\}_\alpha$. If a cubic crystal is given a slight rhombohedral distortion (α = 92.88 degrees), then the angle between the $\{111\}_\alpha$ planes is equal to 72 degrees and the an assembly of $\{111\}_\alpha$ tetrahedra may be assembled in twin-related orientations to construct an icosahedron. Therefore, it has been proposed that icosahedral and decahedral quasicrystals are the result of icosatwin and decatwin assemblies formed from cubic crystals (Pauling 1987). While it is now known (Shechtman et al. 1984, Sainfort et al. 1985) that this is not a universal explanation for apparent quasicrystalline structures of icosahedral symmetry, it cannot be eliminated as a potential explanation for the present observations. Apparent five-fold symmetry, resulting from multiple twinning, has been observed, for example, in heavily microtwinned particles of the T_2 phase formed in Al-2.5Li-1.2Cu-0.7Mg-0.1Zr alloys (wt%) (Ball and Lloyd 1985) as a result of grain boundary precipitate particles formed by overaged at 325°C after solution treated and water quenched. In the present research, although electron microdiffraction patterns recorded from a large scale, faceted precipitate particle exhibited the uniformly sharp and strong intensity maxima as the evidence of the icosahedral structure, it is difficult to distinguish between true icosahedral structure and twinned-related structure in those obtained electron diffraction patterns.

An attempt was made to determine whether these precipitate particles were truly of icosahedral structure or multiply-twinned crystals using high resolution transmission electron microscopy (HRTEM). However, the attempt was largely unsuccessful due to difficulties associated with producing suitably clean and thin specimens of appropriate orientations. Very limited experimental observations suggested no evidence of defect microstructures within the particles. However, these observations cannot be regarded as conclusive. A further attempt to evaluate the structure of the precipitate particles using convergent beam electron diffraction (CBED) was also unsuccessful because of the scale and thickness of the precipitate particles.

As a summary of the section of identification, the experimental tilt angle recorded between the major symmetry axes of the precipitate phase was consistent with those results previously reported for an icosahedral phase in rapidly solidified Al-Mn alloys (Shechtman et al. 1984). In addition, careful measurements of d-spacings in the observed microbeam electron diffraction patterns exhibiting five-fold, three-fold and two-fold axes revealed that they are equivalent to those reported for a phase of icosahedral symmetry by Shechtman et al. (1984). Considerations of the quasilattice constant revealed that the icosahedral structure has a close relationship with the crystalline T phase. It has also been recognised (Bergman et al. 1957, Henley and Elser 1986) that the prototype crystalline T phase, $(Al,Ag)_{49}Mg_{32}$, may be described in terms of assemblies of polyhedra dominated by close-packed icosahedral coordination shells. It is thus perhaps not so surprising that an icosahedral phase that appears initially coherent with the aluminium matrix phase should have an opportunity to form as a precursor to the crystalline T phase in this alloy

system. These consideration above and direct evidence from TEM observation suggest that the homogeneously distributed, fine scale of precipitate particles formed during the isothermal ageing heat treatment process has the icosahedral structure of a quasicrystalline phase.

Orientation Relationship

Several orientation relationships have been reported between an icosahedral quasicrystalline phase and a crystalline phase with which it has contact. These relationships have been observed in a range of different alloy systems and in materials produced by a range of different processing techniques. Most commonly, they have been from samples in which the quasicrystalline phase has been produced by non-equilibrium processing (rapid solidification) and then surrounded by a crystalline phase during subsequent cooling. The reported orientation relationships can be classified into four major distinguishable groups.

In the group designated type A, the orientation relationship is such that a two-fold axis of the icosahedral phase is parallel to a four-fold axis ($<001>_\alpha$) of aluminium solid solution phase, while a three-fold axis of the icosahedral phase is simultaneously parallel to a three-fold axis $<111>_\alpha$. This relationship requires that a five-fold axis of the icosahedral phase is parallel to the $<1\tau0>_\alpha$ zone axis, where τ is the golden mean. This orientation relationship has been observed in rapidly solidified Al-Mn-Cr-Si alloys (Guo et al. 1991), in rapidly solidified Ti-V-Si and Ti-Cr-Si alloys (Zhang and Kelton 1991), in rapidly solidified Al-Mn-Si alloys (Fung and Zhou 1986) and in rapidly solidified Al-V-Fe and Al-Mo-Fe alloys (Zhang et al. 1993). It may be summarised in the form: i2 $\parallel <001>_\alpha$, i3 $\parallel <111>_\alpha$ and i5 $\parallel <1\tau0>_\alpha$.

Orientation relationships of type B can be expressed as follows: i5 $\parallel <305>_\alpha$, i3 $\parallel <013>_\alpha$ and i2 $\parallel <001>_\alpha$. This orientation relationship has been observed in samples of Al-based alloys containing transition metals, which have been annealed at 400°C for 100 h after having been produced by the melt spinning technique (Zhang and Loretto 1991). The type B is different nucleation of icosahedral particles compared to one in the type A because the icosahedral particles of the type A are produced as the liquid-solid transformation products, however, the icosahedral particles of the type B are produced through the solid-solid phase transformation products.

A third form of an orientation relationship (type C) that has been observed between icosahedral and crystalline phases is that in which there are five-fold axes parallel to the $[110]_c$, $[101]_c$, $[113]_c$ and $[311]_c$ axes of adjacent cubic phase. A three-fold axis is parallel to $[111]_c$, and a two-fold axis is parallel to one of the $<001>_c$ cube axes. This relationship has been observed in the Al-Li-Cu-Mg alloys produced by the conventional ingot metallurgy route, in which the alloys were solution treated at 540°C, then water quenched and subsequently annealed at 400°C (Loiseau and Lapasset 1987).

A last form of an orientation relationship (type D) that has been observed in strip-cast Al-Mn-Si alloys with the cooling rate for the range of 300°C/s to 700°C/s, and subsequently heated at 400°C for typical ~18 min. (Hansen et al. 1989). The obtained form of the orientation relationship is as follow:

i5 ‖ $<110>_\alpha$ and $<113>_\alpha$.

i3 ‖ $<111>_\alpha$, $<123>_\alpha$, $<115>_\alpha$, $<234>_\alpha$ and $<113>_\alpha$.

i2 ‖ $<110>_\alpha$, $<111>_\alpha$, $<112>_\alpha$, $<114>_\alpha$, $<115>_\alpha$, $<125>_\alpha$ and $<225>_\alpha$.

A newly identified icosahedral structure of a quasicrystalline phase has been observed in the Al-10Mg-0.5Ag alloy aged 0.5 h at 240°C after solution treated and water quenched in the present research. This quasicrystalline phase as a product of solid-solid phase transformation during the conventional isothermal ageing process shares a certain orientation relationship with respect to the aluminium matrix, and they are induced from the series of recorded microbeam electron diffraction patterns. The orientation relationships between the icosahedral quasicrystalline and matrix phases are as follow i5 ‖ $[011]_\alpha$, and i3 ‖ $[111]_\alpha$. These two superimposed axes between the icosahedral and aluminium matrix phases are exactly parallel to each other. However, the following orientation relationships between icosahedral and aluminium matrix phases have been summarised below, but they have very small misorientation between two phases.

i5 ~‖ $[110]_\alpha$, i5 ~‖ $[11\bar{3}]_\alpha$

i3 ~‖ $[117]_\alpha$, i3 ~‖ $[31\bar{2}]_\alpha$

i2 ~‖ $[112]_\alpha$, i2 ~‖ $[11\bar{1}]_\alpha$, i2 ~‖ $[10\bar{1}]_\alpha$

As for comparison the orientation relationship between the present observation and type A; i2 ‖ $<001>_\alpha$, i3 ‖ $<111>_\alpha$ and i5 ‖ $<1\tau0>_\alpha$, although a three-fold axis of the icosahedral phase is simultaneously parallel to a three-fold axis $<111>_\alpha$, which is consistent with the currently established orientation relationship, a two-fold axis of the icosahedral phase is not parallel to a four-fold axis of aluminium in the present research. In addition, orientation relationships of type B are also not compatible with the newly established orientation relationship in the current research because a five-fold axis of the icosahedral phase is not simultaneously parallel to a $<305>_\alpha$ axis in this research. Furthermore, even the producing process of the quasicrystalline phase in the observed orientation relationship; type C is almost equivalent to the present research, orientation relationship (type C) is also not consistent with the present observation because the two-fold axis of the icosahedral phase is not parallel to one of the $<001>_\alpha$ cube axes in the present research. Thus the orientation relationships established in the present research are not compatible with these orientation relationships, described as types A, B and C. However, the similar type of the orientation relationship compared to the current study has been found to be the type D.

The Relationship Between Morphology and Orientation Relationship

The microstructure of quasicrystalline particles observed in this research, as shown in Figure 5.11, revealed that the regions close to the grain boundaries contained evidence of a precipitate-free zone (PFZ) and coarse-scale, faceted precipitate particles adjacent to that zone, that while the particles became coarser (60-80 nm) approaching the grain boundary precipitate-free zones. The coarser distribution adjacent to the PFZ presumably reflects a lower nucleation rate in these regions, perhaps arising from a combination of a depleted solute and a reduced vacancy concentration. On the other hand, within the core of the grains, a uniform distribution of much finer-scale (typically 20 nm), faceted precipitate particles was observed, suggesting that such precipitate particles were nucleated homogeneously from the supersaturated solid solution of the aluminium matrix during the isothermal ageing treatment. The refined scale of these precipitate particles implies a high nucleation rate. These unique features of microstructures are implied that quasicrystalline particles nucleate from the supersaturated solid solution during the conventional isothermal aging heat treatment, and these are significantly different from quasicrystalline particles observed in samples produced by rapid solidification processing.

It is worthwhile to note that the series of detailed microstructural observations reveal clearly the morphology of precipitate particles. The dominant particles of the icosahedral quasicrystalline phase exhibit the regular diamond shape in the $<110>_\alpha$ orientation and one of square outline in the $<001>_\alpha$ orientation. The traces of the projected edges of the precipitate particles in the $<001>_\alpha$ orientation are parallel to the traces of $\{110\}_\alpha$ planes of the aluminium matrix. Further careful examinations of a regular diamond shape in the $<110>_\alpha$ orientation reveal that there were, in fact, two distinguishable shapes within the particle array defined by two different angles of approximately 70° and 80°. When these particles were observed in the $<001>_\alpha$ orientation, there were also two apparent forms; One shape is almost rectangular or square in section and the other is not well-faceted square-shaped particle. From these microstructural observations of the precipitate particles over a range of different orientations, it is deduced that they have the form of rhombohedra.

Certain orientation relationships result the requirement to have a coherent interface with minimum interfacial energy. When the icosahedral quasicrystalline precipitate particles form from a supersaturated solid solution during the conventional isothermal ageing, it appears to share an orientation relationship with the aluminium matrix phase. This is clearly demonstrated by the observed microstructures and electron microdiffraction patterns, shown in Figures. 5.15, 5.16 and 5.17. The morphology of both the diamond- and square-shaped particles in sections in the $<110>_\alpha$ and the $<001>_\alpha$, orientations, respectively may be accounted for reasonably using considerations of symmetry analysis proposed by Cahn and Kalonji (1982). The precipitate shapes are determined by the intersection point group analysis based on symmetry elements common to precipitates and matrix structures in their observed orientation relationships.

The orientation relationship between the icosahedral quasicrystalline and the matrix phases were described in the result section, 5.2.2, and the superimposed axes between them were shown in Figure 5.18. The three-fold rotational symmetry of the icosahedral phase is parallel to the three-fold axis of the matrix $<111>_\alpha$ orientation and the five-fold rotational symmetry of the icosahedral phase is parallel to the two-fold axis of the matrix $<101>_\alpha$ orientation. Most prominently, common symmetry elements from these parallel axes are $\bar{3}$ which is coincident in precipitates and the matrix crystals, thus an intersection point group symmetry is defined as $\bar{3}$. Consideration of the crystal forms for the intersection point group symmetry of $\bar{3}$ is performed, then the crystal forms compatible with this point group include a rhombohedron, which is consistent with the observed precipitate shape. Since the point group of the matrix phase $m\bar{3}m$ contains 48 order symmetry elements and the intersection point group $\bar{3}$ contains 6. The index of the intersection point group with respect to the point group of the matrix phase is 8 (48/6). Therefore, symmetry permits 8 crystallographic variants of the precipitate particles in a given matrix orientation.

5.3.3 The Metastable T Phase

Williams (1972) investigated the aluminium-rich corner of the Al-Mg-Ag phase diagram, which is shown in Figure 2.5, and established the possible phases present when the alloys were aged at 200°C, which is listed in Table 2.1. He concluded that the T phase would be the stable phase over the range of 1.03 - 10.50 Mg and 0.30 - 5.50 Ag compositions (William 1972). It is seen that the experimental alloys in this study, Al-5Mg-0.5Ag and Al-10Mg-0.5Ag, when aged at 200°C lie in the (α + T) phase field according to the phase diagram of Williams (1972). On this basis, it might be expected that the T phase would be the equilibrium phase in the present alloys. However, the present TEM observations of the Al-10Mg-0.5Ag alloys aged at 240°C revealed that the T phase was, in fact, a metastable intermediate phase. In samples aged for more than 10 h at 240°C, the rod-like particles of the T phase shown in Figure 5.20 were completely replaced by coarse particles of the β phase (Al_3Mg_2) which was thus observed to be the equilibrium phase.

The precipitate phases in an Al-5Mg-0.5Ag (wt%) alloy aged at 200°C have previously been examined using the bulk X-ray diffraction technique (Auld 1967). In this earlier work, the T phase was identified as the major strengthening constituent present at peak hardness and assumed to be the equilibrium phase. The orientation relationship proposed between the T and matrix phases was of the form: $(100)_T \parallel (112)_\alpha$ and $[001]_T \parallel [1\bar{1}0]_\alpha$. This orientation relationship is, however, incompatible with the results obtained from the current experiments.

In the present work, two different forms of the metastable T phase have been identified in

an Al-10Mg-0.5Ag alloy aged at 240°C, each with a different orientation relationship with matrix α. The predominant morphology of precipitate T particles in aged Al-10Mg-0.5Ag alloy was that of fine-scale, uniformly dispersed rod-like shapes, while the number density of newly-discovered rectangular plate-shaped T phase particles was significantly lower. The reason why they have different morphologies of the T phase is still remain unclear, and the different popularity of the T particles is also could not fully explained in this research. However, the rod-like particles may have low mismatch at the interface between the T and matrix phases rather than that of rectangular-shaped particles.

The form of intermediate strengthening precipitate phases in precipitation hardened alloys is an important consideration because it has been demonstrated that the shape and orientation of the strengthening particles are important factors in determining the strength increment that arises from such particles (Nie et al. 1998). In the present case, the morphology of the $<110>_\alpha$ rod-like precipitates of T phase could be accounted for successfully using the symmetry analysis reviewed by Cahn and Kalonji (1982).

According to this analysis, the precipitate shape is determined by the intersection point group defined by symmetry elements common to the precipitate and the matrix structure in the observed orientation relationship. For the precipitate T phase, formed as rods of square section parallel to $<110>_\alpha$, the orientation relationship was such that; $(010)_T \parallel (11\bar{1})_\alpha$ and $[001]_T \parallel [1\bar{1}0]_\alpha$. The stereographic projection of Fig. 5.22 shows that the four-fold axis $[100]_T$ is parallel to the two-fold axis $[110]_\alpha$, and the intersection point group is thus defined as 2/m, with the common two-fold axis parallel to the rod axis. Special crystal forms compatible with point group 2/m include pinacoids both parallel and normal to the two-fold axis, and the observed shape is consistent with a form bound by such pairs of parallel surfaces. Since the point group of the f.c.c. aluminium matrix phase, $m\bar{3}m$, is of order 48 and the intersection point group is of order 4, the index of the intersection point group with respect to the point group of the matrix phase is 12 (48/4). Symmetry thus permits 12 crystallographic variants of the precipitate phase in a given matrix grain, which is entirely consistent with rod-like forms growing parallel to the $<110>_\alpha$, axes.

5.3.4 The Stable β Phase in Ternary Alloy

As shown in Fig. 5.26, a mixture of coarse-scale, globular particles and smaller spheroidal precipitate particles was commonly observed in over-aged samples of the Al-10Mg-0.5Ag alloy (typically 72 h at 240°C). Both forms of particle were identified as having the f.c.c. structure of β phase (Al_3Mg_2) (lattice parameter, a = 2.824 nm) based on evidence from microbeam electron diffraction patterns from individual particles. Previous reports have indicated that the equilibrium

β phase is generally observed only in binary Al-Mg alloys and there has been no prior evidence of equilibrium β phase forming in Ag-containing Al-Mg alloys (Auld 1967, William 1982). These particles could be the products of transformation from the metastable rod-like T particles, but based on the present TEM observations the formation mechanism is not clear. The β particles may equally nucleate independently following dissolution of T phase.

Although the crystal structure and lattice parameter of the metastable T phase (b.c.c.) are not the same compared with those of the equilibrium β phase (f.c.c.), there is evidence of structural and chemical similarities between the T and β phases identified in the aged samples in the Al-10Mg-0.5Ag alloy. Firstly, lattice parameter of the β phase (a = 2.824 nm) is approximately twice larger than that of the T phase (a = 1.41 nm). Secondly, the ratio of constitute elements between Al : Mg in the compounds of the β phase (Al_3Mg_2) and T phase ($(Al,Ag)_{49}Mg_{32}$) is the approximately same of 1 : ~1.50. These similarities would be implied to transform from the T phase to β phase during the isothermal ageing process in the Al-10Mg-0.5Ag alloy.

In the current study, the smaller spheroidal particles were observed in the over-aged sample, and were identified as the equilibrium β phase. An orientation relationship between the β phase and matrix α phase was identified to be of the form; $(100)_\beta \parallel (100)_\alpha$ and $[001]_\beta \parallel [001]_\alpha$. It should be noted that this orientation relationship has not been reported previously in binary Al-Mg alloy, e.g. in Al-10Mg alloy aged at 200°C and 300°C; $(111)_\beta \parallel (001)_\alpha$ and $[1\bar{1}0]_\beta \parallel [010]_\alpha$ (Bernole et al. 1969) and $[001]_\beta \parallel [001]_\alpha$ and $[110]_\beta \parallel [100]_\alpha$ (Bernole 1974).

It is interesting to note that the coarse β phase particles were invariably multiply-twinned, which is again an observation that has not previously been reported in alloys of the Al-Mg-Ag system. Such twinning is a common feature of solid state precipitates of diamond cubic structure in Al-Ge (Douin, Dahmen and Westmacott 1991) and Al-Si (Kobayashi and Hogan 1979) alloys in particles of (diamond) f.c.c. structure forming directly from the liquid or vapour states. It is commonly interpreted as arising from the need for the particles to minimise surface and volume free energy by maintaining close-packed planes parallel to planer facets on an approximately spheroidal form.

It also should be noted that two forms of the equilibrium β phase were observed in the over-aged samples in ternary Al-10Mg-0.5Ag alloy, and it may be that the coarse globular particles are derived from the rod-like T phase particles, while the finer spheroidal particles are nucleated independently and homogeneously.

5.3.5 Precipitation Hardening Response and Precipitation Sequences

Figure 5.31 compares the hardness curves of the Al-10Mg and Al-10Mg-0.5Ag alloys aged

isothermally at 240°C. There is apparently little or no precipitation hardening response in the binary alloy for a period of 1-2 h, after which the hardness rises modestly to a maximum of ~100 VHN following 5 h isothermal ageing at 240°C. According to the characterisation work presented in this chapter, this hardening response is attributable initially to an array of coarse-scale, sparsely distributed plate- and lath-like precipitate particles, that have been identified as the metastable β' phase. With ageing up to 5 h, the microstructure contained an increased volume fraction of coarse-scale precipitate particles, which were identified at maximum hardness to comprise a mixture of the metastable β' and stable β phases. With further longer term ageing up to 72 h, which corresponded to a well over-aged condition, the microstructure exhibited very coarse scale precipitate particles of what was not identified in detail but presumed to be equilibrium β phase.

In the case of the ternary Ag-modified alloy, the precipitation hardening response was stimulated and accelerated compared to that of the Ag-free binary alloy during the early stages of the ageing process. The hardness had, for example, increased beyond the maximum hardness of the binary alloy within just 0.5 h. This accelerated hardness increment was found to be attributable to a fine scale (typically 50 nm), uniform distribution of faceted precipitate particles, identified as being quasicrystalline and having the icosahedral structure. The hardness continued to increase to a maximum of ~120VHN after ~2 h at 240°C and, at maximum hardness, it was observed that the metastable icosahedral phase was replaced by uniformly distributed, finer-scale rod-like particles, identified as metastable T phase. With prolonged ageing time, the hardness decreased gradually and during over-ageing the T phase particles were replaced by a bimodal distribution of the equilibrium β phase (Al_3Mg_2). This distribution corresponded coarse-scale (~500 nm), globular particles together with fine-scale (~100 nm), spaisely distributed spheroidal particles.

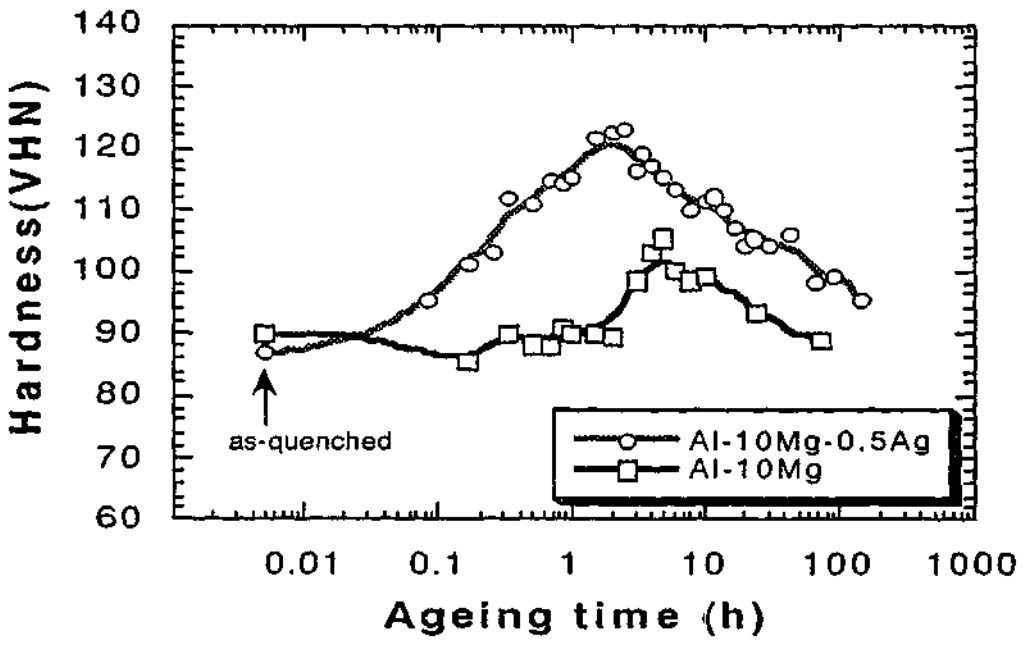

Figure 5.31 Comparison of the age-hardening curves for Al-10Mg and Al-10Mg-0.5Ag alloys aged at 240°C.

According to early work on Al-5Mg-0.5Ag alloy, using the bulk X-ray diffraction technique (Auld 1967), the early stages of the precipitation hardening response was attributed to the formation of GP zones, while the maximum hardness was associated with formation of what was described as equilibrium T phase. More recently, Cousland and Tate (1986) described maximum hardness as being associated with a metastable T' phase, while the equilibrium T phase was suggested to form in the later stages of the ageing process. However, in the present work, each precipitate phase has been identified using direct observations by TEM and electron microdiffraction recorded from individual particles and there was no evidence of the formation of GP zones or a metastable T' phase. While there have been suggestions that the T phase is an equilibrium phase in such systems, the present characterisation of over-aged samples has revealed that the T phase is metastable and that the equilibrium phase in the present Al-10Mg(-0.5Ag) alloys aged at 240°C is the β phase (Al_3Mg_2).

As a result of the present characterisation of precipitate microstructures in both binary and ternary alloys the precipitation sequences during the isothermal ageing process at 240°C, may be summarised as follows:

Al-10Mg alloy :

Supersaturated α solid solution (S.S.S.) -----> supersaturated metastable α solid solution + metastable β' phase -----> stable β phase + equilibrium α phase.

Al-10Mg-0.5Ag alloy :

S.S.S. -----> metastable icosahedral quasicrystalline phase +
metastable α solid solution -----> metastable T phase +
metastable α solid solution -----> stable β phase + equilibrium α phase.

The ternary Al-10Mg-0.5Ag alloy, aged to near maximum hardness (2 h) at 240°C, contained a fine-scale, uniform distribution of rod-like precipitate particles identified as metastable T phase, while the binary alloy, given a similar ageing treatment, showed microstructures contain sparsely distributed β' particles. It is thus clearly demonstrated that trace additions of Ag to binary Al-Mg alloys modify the identity of the primary precipitation strengthening phases, and the precipitate distributions.

As presented evidence in BF micrographs including electron microdiffraction patterns, the metastable icosahedral quasicrystalline precipitates are replaced by crystalline metastable T phase during isothermal ageing for periods from 1 to 2 h at 240°C. This transition will be discussed in more detail in Chapter 6.

5.4 Conclusions

Detailed characterisation of the precipitate phases and precipitate microstructures in supersaturated Al-10Mg(-0.5Ag) (wt%) alloys subjected to isothermal ageing treatments have been carried out using a combination of TEM and electron diffraction, and the following conclusions have been obtained:

(1) In the early stages of isothermal ageing at 240°C, a relatively low density of plate- and lath-like precipitate particles was formed in binary Al-10Mg alloy. The maximum hardness was associated with a distribution of coarse-scale, equiaxed particles of equilibrium β phase, lath-like particles of metastable β' phase and a small volume fraction of irregularly-shaped particles of an as yet unidentified phase.

(2) The precipitation sequence in the binary Al-10Mg alloy, solution treated 1 h at 500°C, water quenched and aged at 240°C, may be summarised as follows:

Supersaturated α solid solution (S.S.S.) -----> supersaturated metastable α solid solution + metastable β' phase -----> stable β phase + equilibrium α phase.

(3) A metastable icosahedral quasicrystalline phase has been observed for the first time in the Al-10Mg-0.5Ag alloy aged 0.5 n at 240°C. Uniformly dispersed, fine-scale particles of the icosahedral are formed from supersaturated solid solution (α-Al phase) via a solid-state transformation reaction. The morphology of these particles, confirmed by both direct TEM observations and intersection point group symmetry analysis, is rhombohedral.

(4) The orientation relationship between the icosahedral quasicrystalline (i-phase) and the matrix (α -phase) phases has been identified as i5 ∥ $<011>_\alpha$ and i3 ∥ $<111>_\alpha$. This new icosahedral phase appeared to preserve the same orientation relationship reported previously by Hansen et al. (1989) for Al-Fe-Si alloy.

(5) The icosahedral quasicrystalline precipitate phase contained all three principal elements in the alloy, with the Ag content apparently significantly lower than the Mg content.

(6) Rod-like precipitate particles with a rod axes parallel to $<110>_\alpha$ directions were the predominant dispersed phase in the ternary Al-10Mg-0.5Ag alloy aged 2 h at 240°C, and were thus associated with the maximum hardness condition. Microbeam electron diffraction patterns recorded from the $<110>_\alpha$ rod-like precipitate particle could be indexed for the body-centred cubic structure of the T phase (lattice parameter a = 1.416 nm). The orientation relationship between T phase and matrix α was of the form $(010)_T \parallel (11\bar{1})_\alpha$ and $[001]_T \parallel [1\bar{1}0]_\alpha$. Qualitative microanalysis suggested that the metastable crystalline T phase was a ternary compound that

contained all three elements Al, Mg and Ag. The icosahedral quasicrystalline phase was observed to be replaced by metastable crystalline T phase after the alloy is aged 2 h at 240°C, and the rod-like precipitates appeared to be the main strengthening constitute in the Al-10Mg-0.5Ag alloy aged at 240°C.

(7) A small number density of precipitate particles with a rectangular shape were also observed in the Al-10Mg-0.5Ag alloy aged 2 h at 240°C. These precipitate particles were identified as T phase (lattice parameter a = 1.416 nm), with an orientation relationship of the form: $(100)_T \parallel (100)_\alpha$ and $[001]_T \parallel [001]_\alpha$.

(8) Coarse-scale, globular particles were commonly observed in over-aged samples of the Al-10Mg-0.5Ag alloy aged (72 h at 240°C). These coarse globular particles were identified by electron microdiffraction to have the face-centred cubic structure of equilibrium β phase (Al_3Mg_2) (lattice parameter a = 2.824 nm). The orientation relationship between the β phase and α matrix was such that: $(100)_\beta \parallel (100)_\alpha$ and $[001]_\beta \parallel [001]_\alpha$. This orientation relationship differs from that reported previously for the β phase formed in binary Al-Mg alloys . The coarse-scale, globular particles β phase were invariably multiply-twinned when observed in the Al-10Mg-0.5Ag alloys aged 72 h at 240°C.

(9) The precipitation sequence in the Al-10Mg-0.5Ag alloy, solution treated 1 h at 500°C, water quenched and aged at 240°C may be summarised as follows:

S.S.S. -----> metastable icosahedral quasicrystalline phase +
metastable α solid solution -----> metastable T phase +
metastable α solid solution -----> stable β phase + equilibrium α phase.

(10) The present observations confirm that microalloying additions of Ag to the alloy of Al-Mg system promote a change in the identity of the primary strengthening precipitate phase. This phase may lead to significantly improved mechanical properties. It is clear the presence of Ag stabilises both quasicrystalline and crystalline forms of the T phase in sequence during isothermal decomposition of supersaturated Al-Mg-Ag solid solution. However, the precise role of Ag in facilitating the precipitation of the T phase remains to be understood.

Chapter 6

Isothermal Ageing Processes in Al-10Mg(-0.5Ag) Alloys

6.1 Introduction

It is well established that the precipitation hardening response of an alloy is controlled mainly by the shape, size, distribution and properties of the precipitate particles distributed within the continuos matrix phase. The precipitate distribution is in tern controlled by processing conditions, including the time and temperature of solution treatment, severity of quench and the time and temperature of the ageing treatment. The latter are important because the decomposition of the supersaturated solid solution is invariably diffusion-controlled. For example, if the ageing temperature is relatively low, then typically the level of supersaturation will be increased, increasing the driving force for precipitation. However, at lower temperatures, the diffusion rates will inevitably be lower and may ultimately control the rates of nucleation and growth of the precipitate phase, requiring longer ageing times to achieve maximum hardness. In addition, it is important to recognise that different ageing temperatures may give rise to different forms and orientations of a particular precipitate phase and/or to different precipitation sequences. Such changes may have a significant influence on the mechanical properties of the alloys.

Those results presented in the previous Chapter 5, were focused on the base alloys, binary Al-10Mg and ternary Al-10Mg-0.5Ag, aged at a single relatively high temperature of 240°C in order to accelerate the precipitation processes. However, it is to be recognised that this is likely to promote relatively coarse distributions of the precipitate phases and thus sacrifice potential increases in strength and hardness. While it facilitates identification of the precipitate phases, it is to be recognised that the sizes, distributions, morphologies and crystallographic parameters, such as crystal structures, lattice parameters and orientation relationships with respect to the aluminium matrix, of the precipitate particles in the aged binary and ternary alloys are characteristic of this ageing temperature alone (Chapter 5). There remains a need to examine the microstructural changes occurring at different ageing temperatures in order to fully understand the precipitation sequences in the these experimental alloys and their influence on mechanical properties.

As described in Chapter 2 (Section 2.3.3), the precipitation sequences in the Al-12% Mg alloys have been investigated (Nebti et al. 1995) indirectly using the DSC technique. The following precipitation sequence during direct heating of solution treated and quenched samples (10 °C/min) has, in summary, been proposed:

supersaturated α (430°C) ------> GP zones (0°C) ------> β'' phase (45°C) ------> dissolution of (GP zones + β'' phase, 45°C - 100°C) ------> β' phase (100°C) ------> β phase (250°C) ------> dissolution of (β' + β phases, 250°C - 420°C)

In addition to these results, it has been established that the GP zone solvus temperature for a binary Al-10% Mg alloy was measured and the temperature is approximately 56°C, according to a

published version of the Al-Mg equilibrium diagram to which the GP zone metastable boundary has been added (Lorimer 1978). This diagram has been shown in Fig. 2.4 in Chapter 2. This phase diagram also suggests that the GP zone solvus temperature increases with increasing solute Mg content. According to these results, it is possible to predict that, if an Al-10Mg alloy were aged at room temperature for an extended exposed time , it may not be possible to observe GP zones. These GP zones would ultimately be replaced by the β'' phase (Al_3Mg, the ordered cubic $L1_2$ structure). However, GP zones and the β'' phase would be unlikely to be formed if the Al-10Mg alloy were aged at 90°C, and it would be likely that only the metastable β' phase (Al_3Mg_2, a = 1.002 nm, c = 1.636 nm) would be observed as a precursor to the equilibrium β phase.

There has been little attention paid to the precipitation hardening behaviour in ternary Al-Mg-Ag alloys aged at relatively low ageing temperatures, and it was thus considered important to extend the present work to examine the effects of trace additions of Ag on the precipitate microstructures of the Al-Mg alloys aged at lower temperatures. It is the purpose of the present Chapter to report the observations of microstructural changes in binary Al-10Mg and ternary Al-10Mg-0.5Ag alloys (wt%) aged at room temperature (natural ageing: T4) and at 90°C. Following these results, selected observations on microstructural evolution in samples artificially aged at the conventional ageing temperatures of 200°C and 240°C will be presented. These results will be closely compared with those obtained at 240°C and reported in detail in Chapter 5. The result of Chapter 5 will be used as the basis for comparison.

6.2 Experimental Results

6.2.1 Microstructural Characterisation

Natural Ageing

Figures 6.1 (a)-(f) present the microstructures of Al-10Mg(-0.5Ag) alloys solution treated 1 h at 500°C, water quenched and aged 6 months at room temperature (natural ageing: T4). The electron beam is approximately parallel to (a), (d) $<001>_\alpha$; (b), (e) $<110>_\alpha$ and (c), (f) $<112>_\alpha$ directions, respectively. The TEM micrographs for the Ag-free alloy, Figs. 6.1(a)-(c), reveal no evidence of nucleation of precipitate particles, even after the specimens have been aged for 6 months, and suggest only a dislocation structure which is similar to that in the as-quenched microstructure described in Chapter 4 (e.g. Fig. 4.5 and Fig. 4.6). Corresponding selected area electron diffraction (SAED) patterns, which were recorded from the local areas shown in these BF images, contain only diffracted beams from the aluminium matrix, and there is no evidence of diffraction spots or diffuse diffracted intensity that might suggest decomposition of the supersaturated α solid solution. It thus appeared that the as-quenched microstructure remained relatively stable at ambient temperature (20°C) for periods up to 6 months.

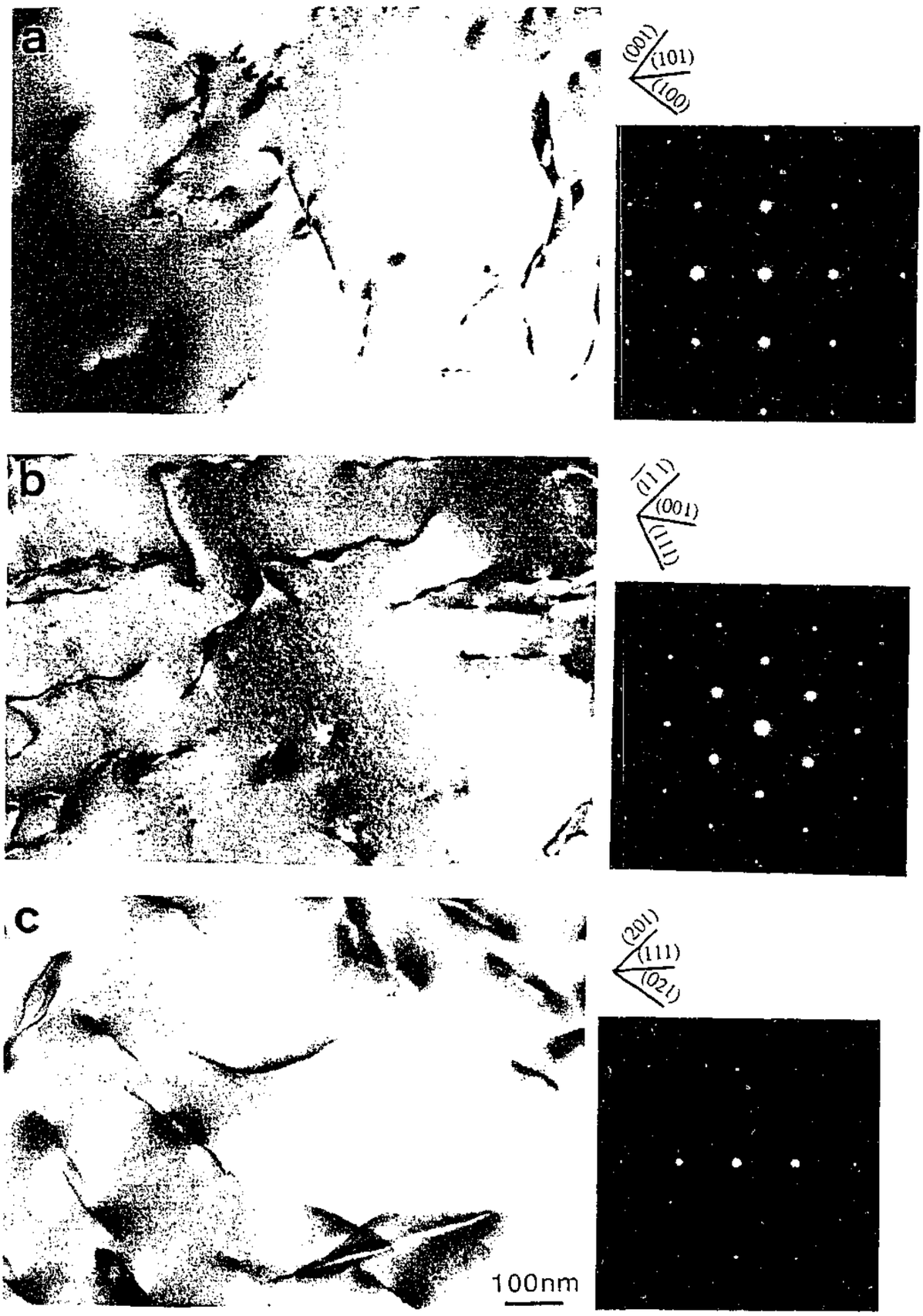

Figure 6.1 Microstructures of (a)-(c) binary Al-10Mg and (d)-(f) ternary Al-10Mg-0.5Ag alloys aged 6 months at room temperature (20°C). The electron beam was approximately parallel to (a), (d) $<001>_\alpha$; (b), (c) $<110>_\alpha$; and (c), (f) $<112>_\alpha$ directions.

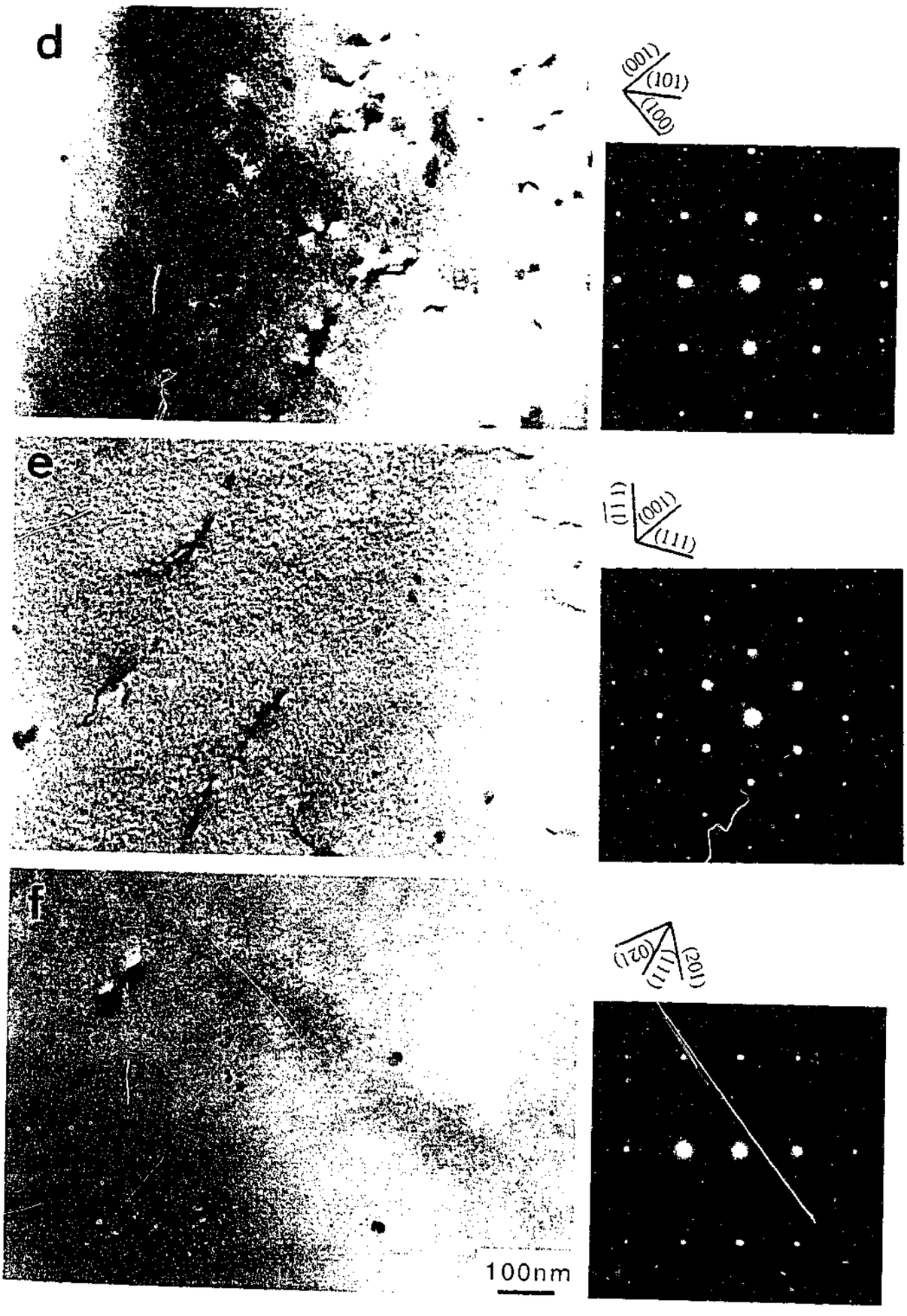

Figures 6.1 Continued.

The microstructures of the solution treated and quenched Ag-containing alloy, Figs. 6.1 (d)-(f), also exhibited no detectable evidence of decomposition during the initial 6 months of ageing at room temperature (20°C), and the corresponding SAED patterns contained no extra diffraction spots or diffuse scattered intensity raising from a second phase. The microstructure retained similar to that of the as-quenched alloy, as described in Chapter 4 (e.g. Fig. 4.9 and Fig. 4.10).

Figures 6.2 (a)-(f) show the microstructures of Al-10Mg(-0.5Ag) alloys aged for 12 months at room temperature (natural ageing: T4). The electron beam was approximately parallel to (a), (d) $<001>_\alpha$; (b), (e) $<110>_\alpha$ and (c), (f) $<112>_\alpha$ orientations, respectively. The TEM micrographs for the binary alloy, Figs. 6.2 (a)-(c), still provide no evidence for the presence of precipitate particles, and these microstructures appeared to be similar to those of samples aged 6 months at 20°C. The corresponding SAED patterns, which were recorded with a relatively long exposure time to impose prospects of detecting intensity maxima of low intensity, again showed only diffracted beams from the aluminium matrix, and those were no extra reflections or diffused scattered intensity of significance in any of the zone axis patterns parallel to $<001>_\alpha$, $<110>_\alpha$ and $<112>_\alpha$.

Similarly, the microstructures of the Ag-containing ternary alloy, Figs. 6.2 (d)-(f), also contained no detectable precipitate particles and, although each SAED pattern was recorded with longer exposure time, these patterns contained no evidence of extra diffraction spots or diffuse streaking from a second phase in the $<001>_\alpha$, $<110>_\alpha$ and $<112>_\alpha$ orientations. The observations from these BF images and SAED patterns suggest that the supersaturated solid solution in Al-Mg alloy is quite thermally stable at low temperatures (20°C), even when trace additions of Ag are added to the binary Al-10Mg alloy.

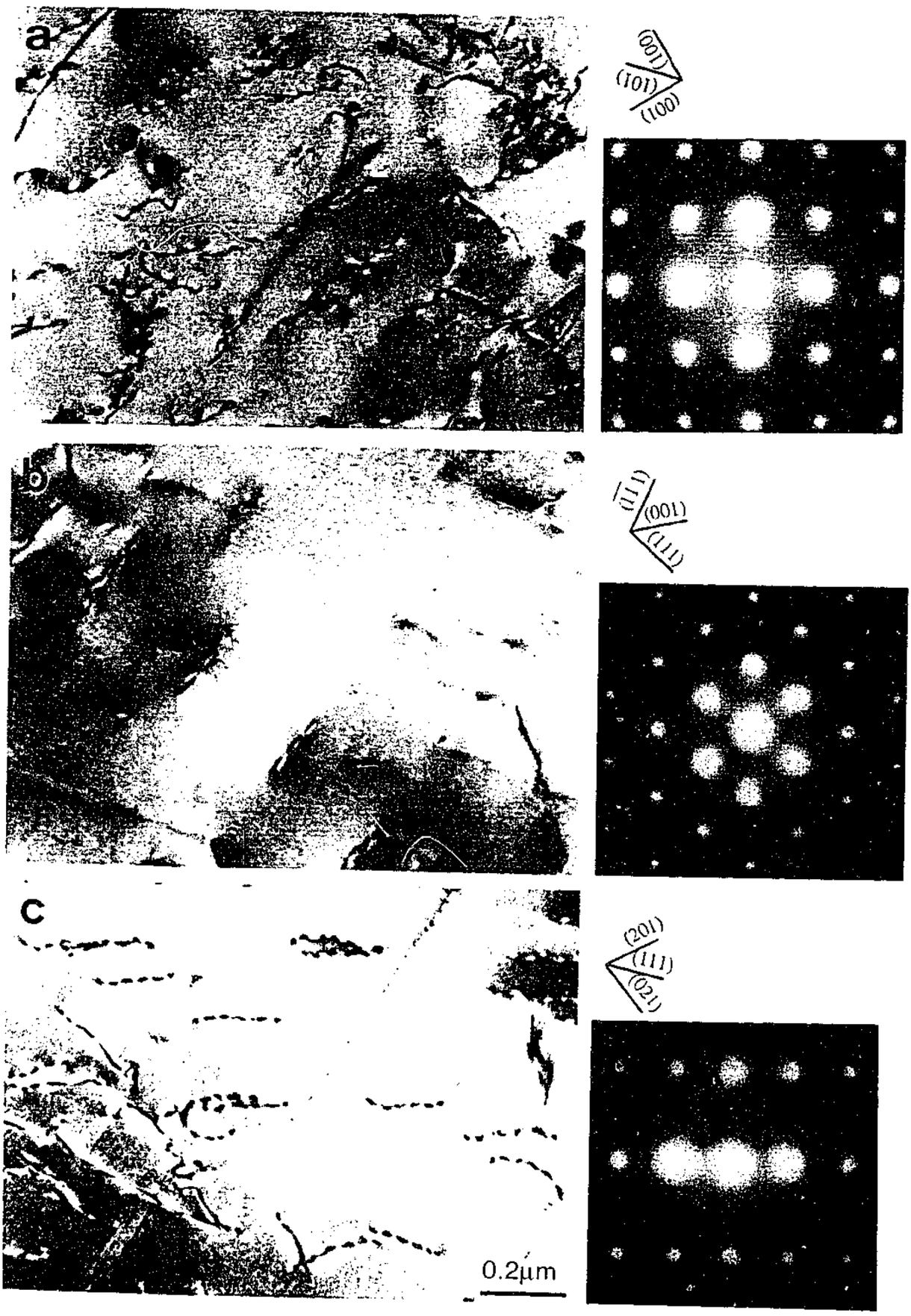

Figure 6.2 Microstructures of (a)-(c) binary Al-10Mg and (d)-(f) ternary Al-10Mg-0.5Ag alloys aged 12 months at room temperature (20°C). The electron beam was approximately parallel to (a), (d) $<001>_\alpha$; (b), (c) $<110>_\alpha$ and (c), (f) $<112>_\alpha$ directions.

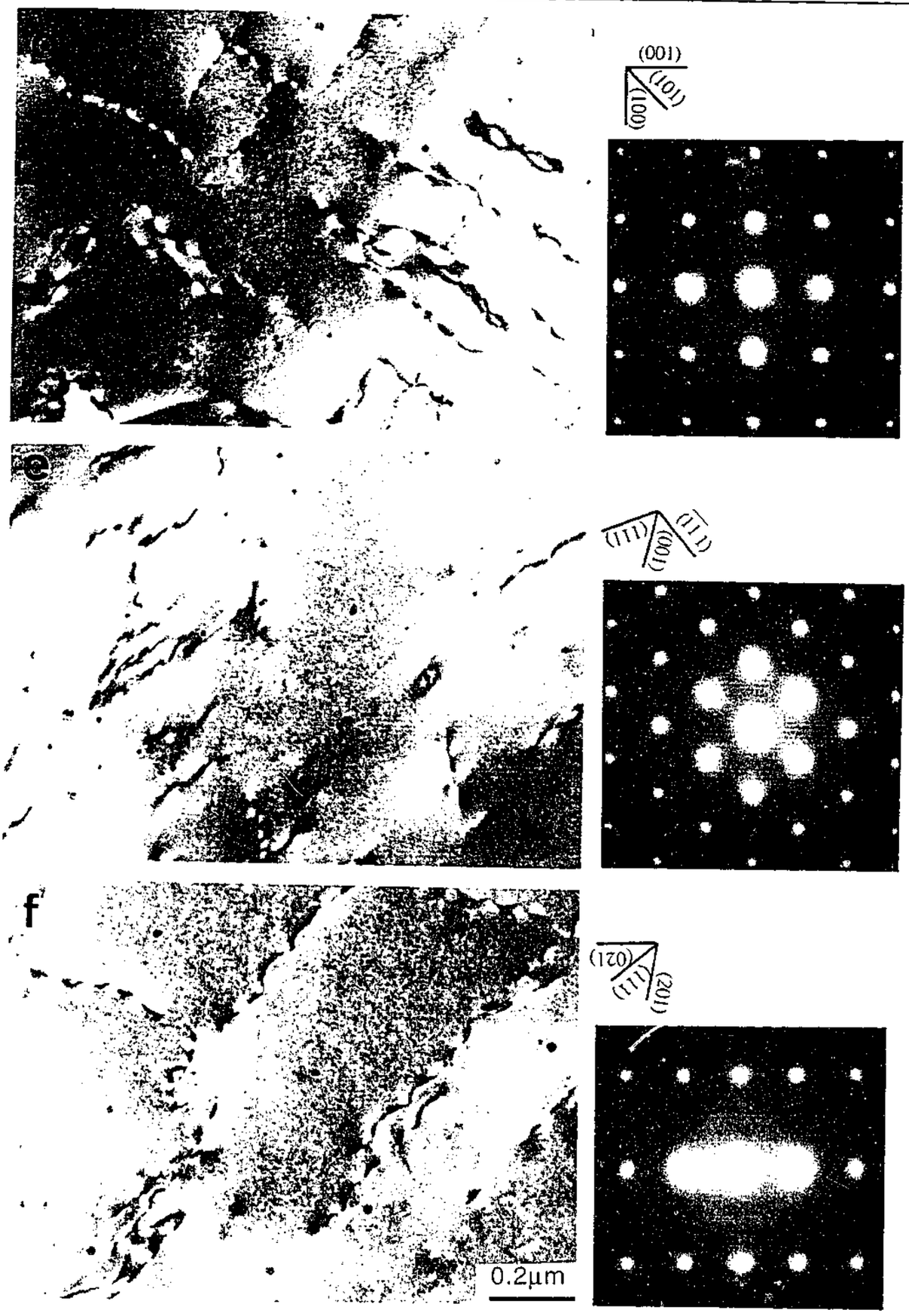

Figure 6.2 Continued.

Figures 6.3 (a)-(f) present bright field (BF) images of the microstructures in Al-10Mg(-0.5Ag) alloys solution treated 1 h at 500°C, water quenched and aged 16 months at room temperature (20°C). The electron beam was approximately parallel to (a), (d) $<001>_\alpha$; (b), (e) $<110>_\alpha$ and (c), (f) $<112>_\alpha$ directions. The microstructures of the binary alloy, Figs. 6.3 (a)-(c), show no evidence of precipitate particles in these different orientations, suggesting that the decomposition process from the supersaturated solid solution is very slow at this low temperature. The microstructures retain a significant dislocation content at this stage of the ageing, and it is worthy of note that the apparent dislocation density in the binary alloy was consistently much higher than in the Ag-containing alloy for periods of natural ageing up to 16 months. Although detailed analyses of the dislocation contents have not been conducted, these results from TEM observations are consistent with those presented in the Section 4.4 of Chapter 4. Corresponding SAED patterns from the microstructures of the binary alloy showed only diffracted beams from the aluminium matrix in each orientation.

In contrast, the microstructures of the corresponding Ag-modified alloy, Figs. 6.3 (d)-(f), exhibited very fine-scale, spheroidal precipitate particles, which were uniformly dispersed and showed uniform contrast throughout the α-Al matrix. These microstructures generally contained dislocations as well, but the number of defects was apparently less than in samples aged 6 or 12 months at room temperature, c.f. Figs. 6.1 and 6.2, respectively. Electron diffraction patterns for corresponding zone axes indicated that these uniformly-distributed fine scale precipitate particles have an ordered cubic $L1_2$ type crystal structure, with a lattice parameter of a = 0.408 nm. The additional weak reflections in the recorded SAED patterns imply that the orientation relationship between the $L1_2$ structure and the α-matrix phase was of the form: $(100)_{L1_2} \parallel (100)_\alpha$, $[001]_{L1_2} \parallel [001]_\alpha$. Schematic patterns corresponding to these SAED patterns were simulated using the atomic positions equivalent to the $AuCu_3$ structure type (Villars and Calvert 1985), i.e., (0, 0, 0), (0, 0.5, 0.5), (0.5, 0, 0.5) and (0.5, 0.5, 0), and were found to be in excellent agreement with the observed SAED patterns in each orientation (Figs. 6.3 (d)-(f)). It should be noted that the precipitate phase, having the ordered cubic $L1_2$ structure has a structure fully consistent with the metastable β'' phase, that has been reported previously in the Al-Mg system (Kumada et al. 1970, and Nebti et al. 1995) and has a composition of Al_3Mg (Kumada et al. 1970, and Nebti et al. 1995).

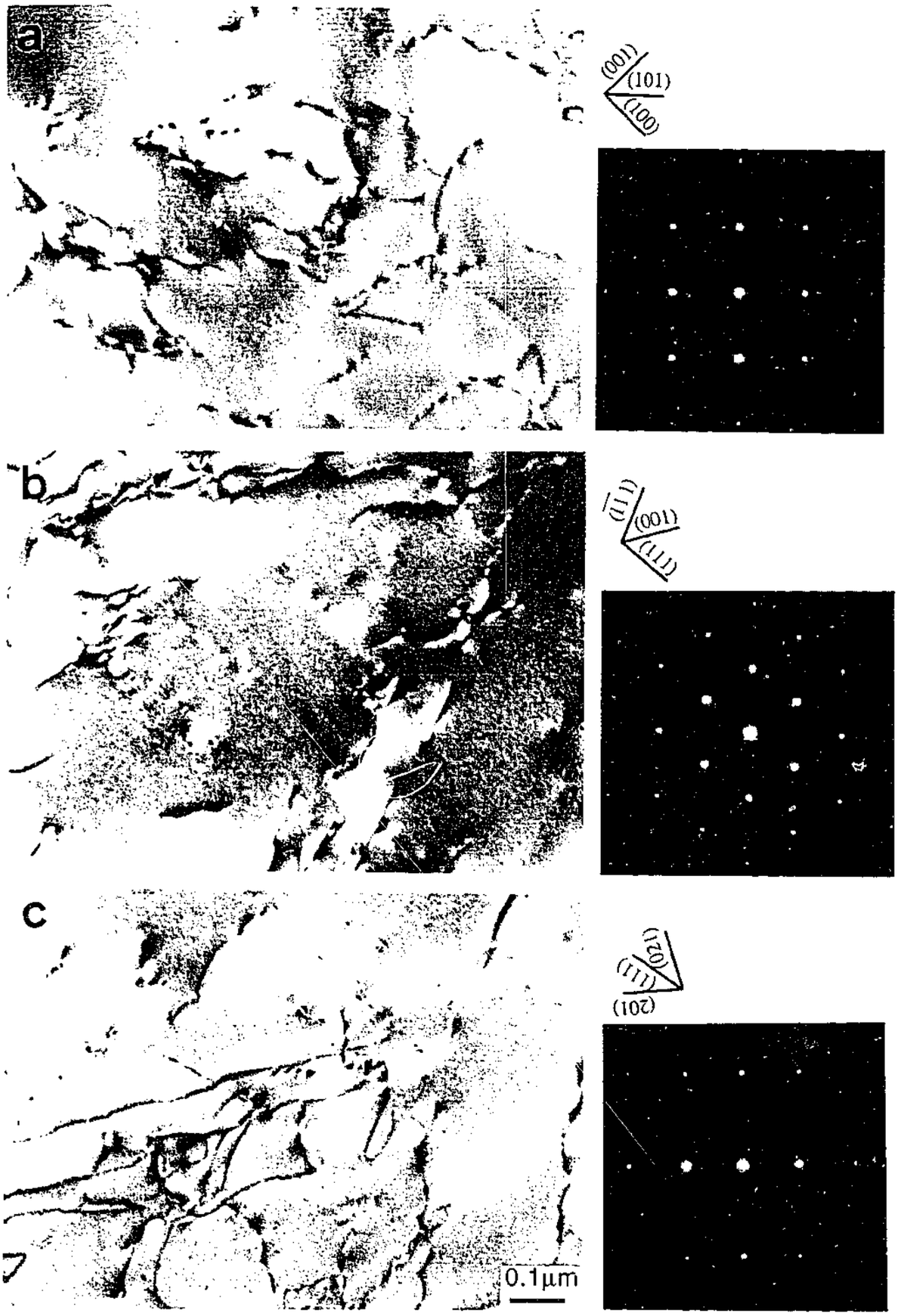

Figure 6.3 Microstructures of (a)-(c) binary Al-10Mg and (d)-(f) ternary Al-10Mg-0.5Ag alloys, aged 16 months at room temperature (20°C). The electron beam was approximately parallel to (a), (d) $<001>_\alpha$; (b), (c) $<110>_\alpha$; and (c), (f) $<112>_\alpha$ directions.

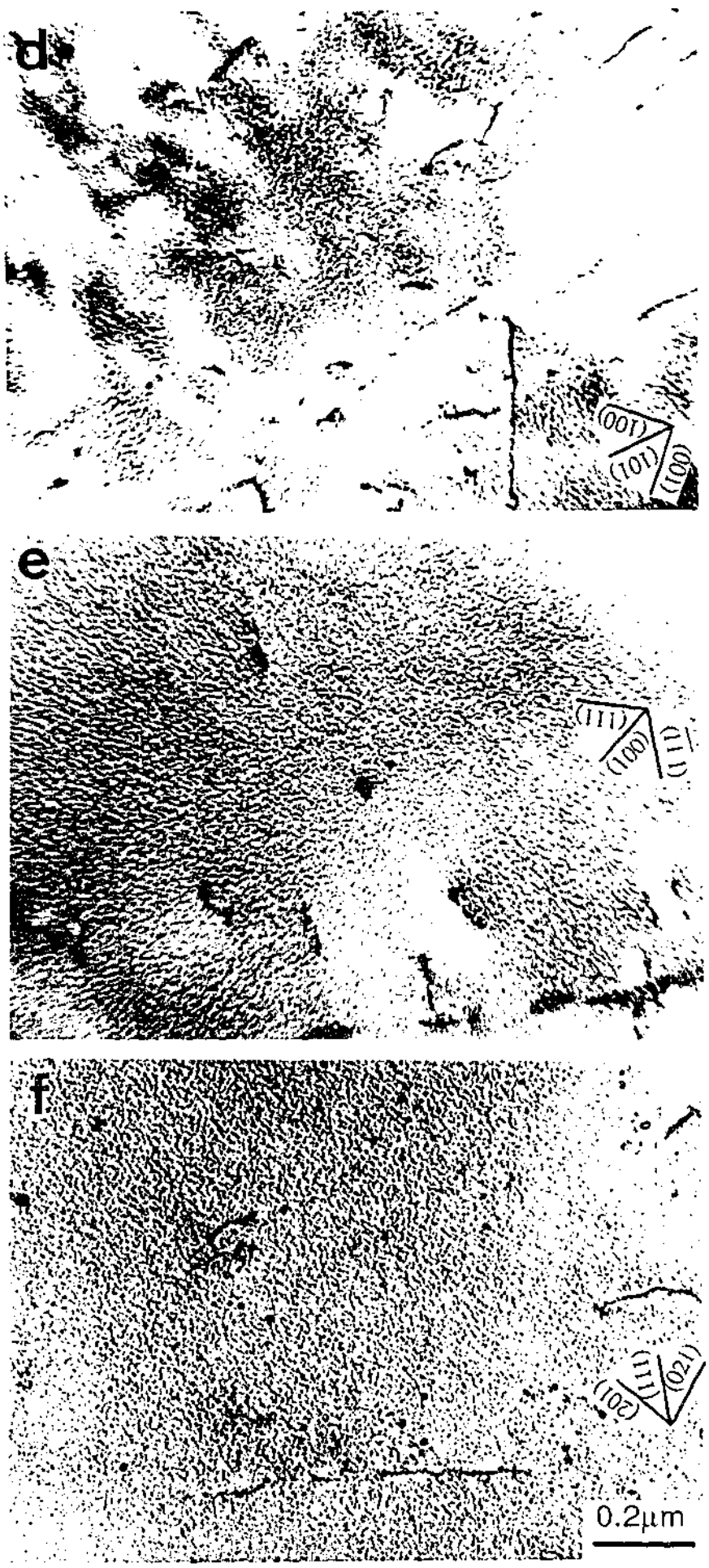

Figures 6.3 Continued.

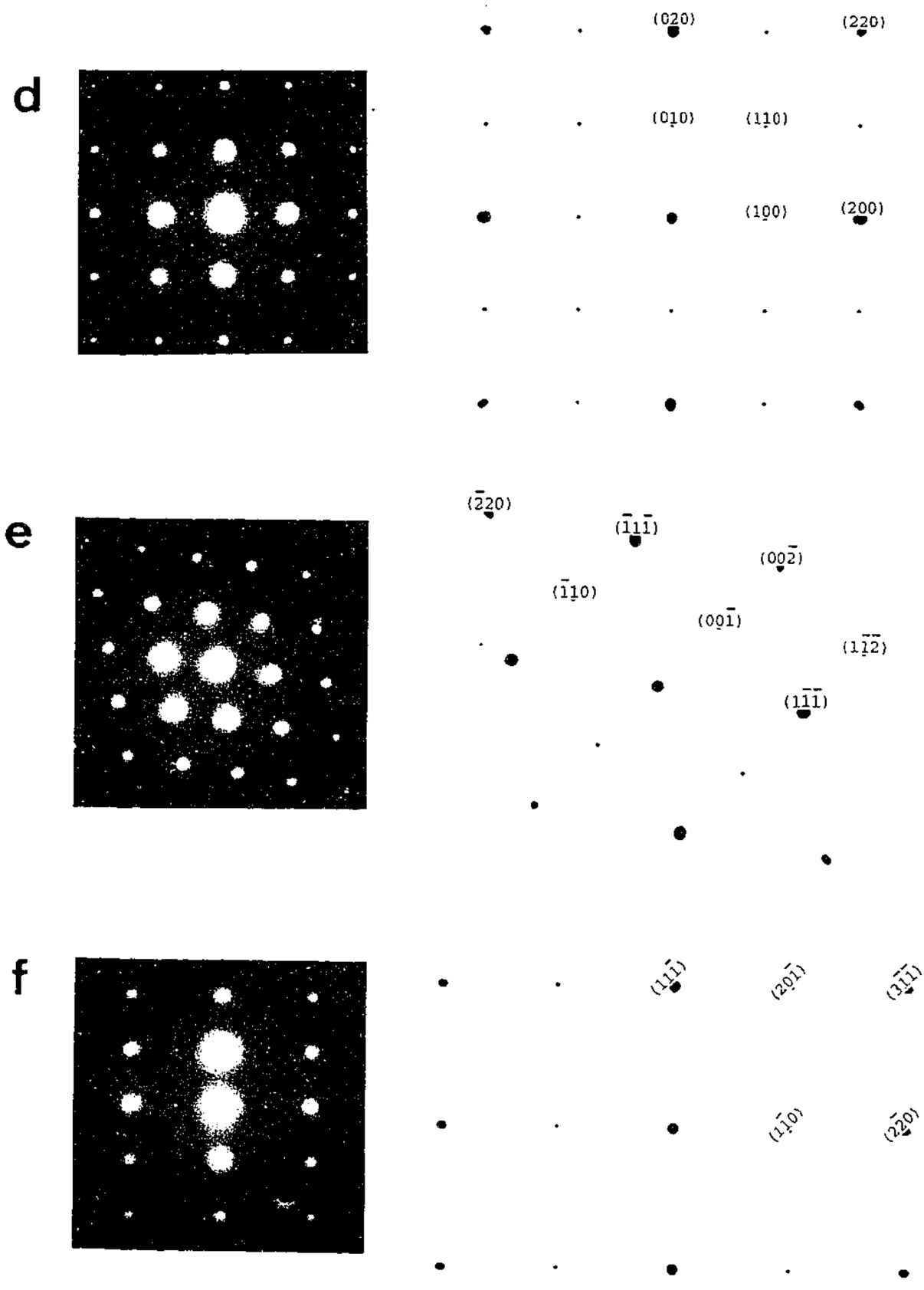

Figures 6.3 Continued.

The technique of weak beam centred dark field (WBCDF) imaging is one that permits a higher resolution image of microstructural features surrounded by an elastic strain field than conventional bright-field (BF) or CDF images (Williams and Carter 1996). In order to establish the morphology of the finely-distributed precipitate particles in the Al-10Mg-0.5Ag alloy aged 16 months at 20°C, both CDF and WBCDF images were thus recorded, together with BF images. Figures 6.4 (a)-(h) present TEM micrographs of a series of BF, CDF and WBCDF images in the Ag-containing alloy naturally aged for 16 months. The electron beam for Figs. 6.4 (a)-(d) and Figs. 6.4 (e)-(h) were approximately parallel to $<001>_\alpha$ and $<110>_\alpha$ directions, respectively. The WBCDF images of the aged microstructures, Figs. 6.4 (c) and (g), were taken using the diffraction condition of (-g, 3g) using g = $(200)_\alpha$ and $(111)_\alpha$ for the $<001>_\alpha$ and $<110>_\alpha$ images respectively.

The microstructures revealed in the BF images of Figs. 6.4 (a) and (e), recorded parallel to $<001>_\alpha$ and $<110>_\alpha$ directions respectively, contain fine-scale precipitate particles; however, the detailed precipitate forms and the particle distributions are not clear due to inadequate resolution and the presence of strain contrast. Conventional CDF images, Figs. 6.4 (b) and (f), confirm the presence of a fine-scale second phase, but offer little more detail. In comparison, the WBCDF images of Figs. 6.4 (c) and (g), corresponding to the BF images of Figs. 6.4 (d) and (h), reveal a uniform distribution of very-fine scale precipitate particles that are spheroidal in form.

Figures 6.5 (a)-(c) present the microstructure of the Ag-containing ternary alloy following a further period of ageing up to 28 months at room temperature (20°C). The electron beam was approximately parallel to (a) $<001>_\alpha$, (b) $<110>_\alpha$ and (c) $<112>_\alpha$ directions, respectively. The microstructure in these BF images comprises a fine-scale distribution of spheroidal precipitate particles which are uniformly dispersed in the aluminium matrix phase. A very few number of line dislocations was still observed at this stage of the ageing process. Electron diffraction patterns recorded from corresponding the microstructures indicated the $L1_2$ type of an ordered structure, and these SAED patterns were the same as one in the sample naturally aged for 16 months. This result from SAED patterns implies that the $L1_2$ type of an ordered structure formed during the natural ageing has not been transformed to another phases during 12 months of natural ageing at 20°C.

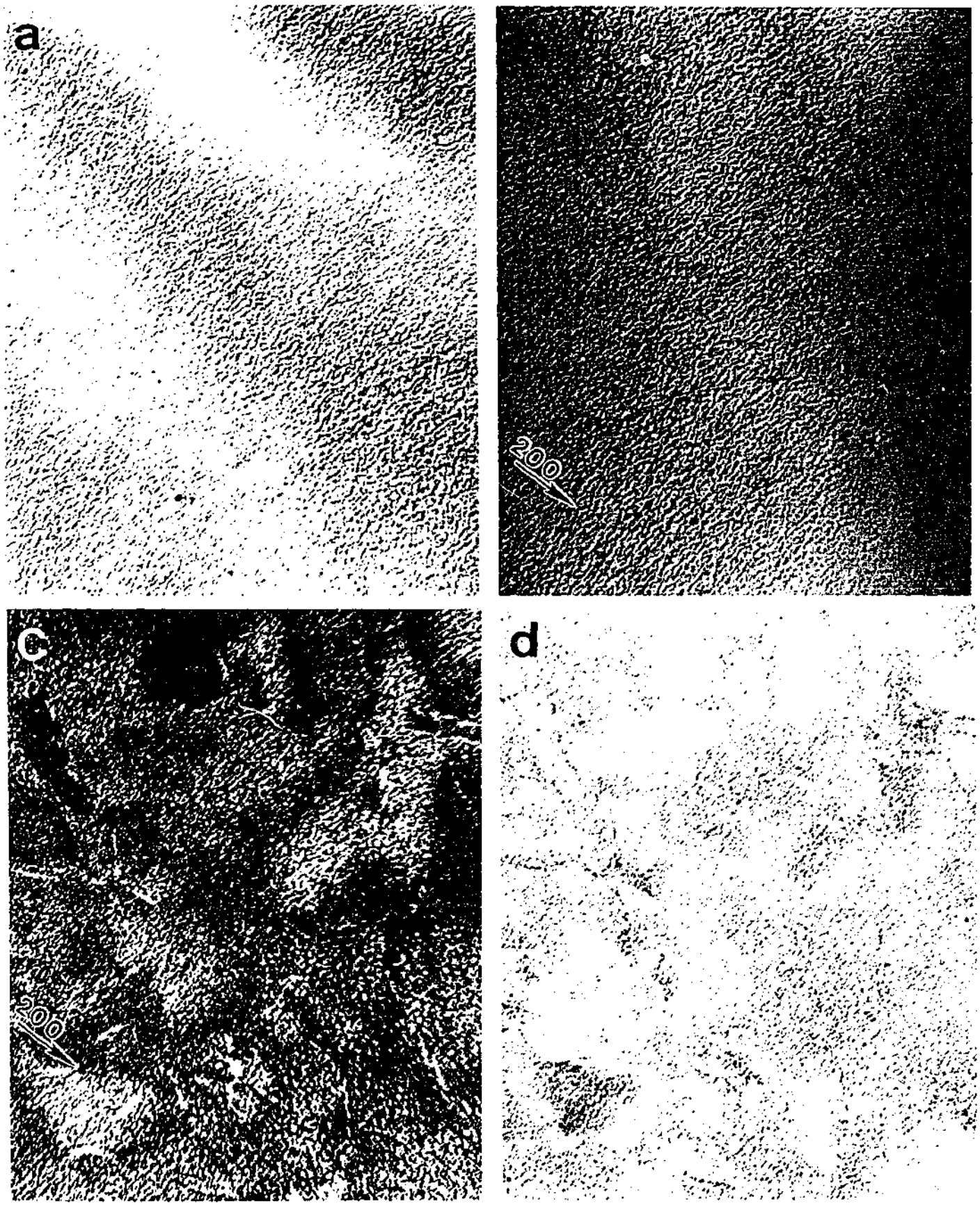

Figure 6.4 Electron micrographs of the Al-10Mg-0.5Ag alloy aged 16 months at 20°C.
(a) BF image, $\mathbf{B} = \langle 001 \rangle_\alpha$; (b) CDF image, $\mathbf{B} = \langle 001 \rangle_\alpha$;
(c) WBCDF image, $\mathbf{B} = \langle 001 \rangle_\alpha$, (-g,3g) $\mathbf{g} = \langle 200 \rangle_\alpha$; (d) BF image, $\mathbf{B} = \langle 001 \rangle_\alpha$; $\mathbf{g} = \langle 200 \rangle_\alpha$,
(e) BF image, $\mathbf{B} = \langle 110 \rangle_\alpha$; (f) CDF image, $\mathbf{B} = \langle 110 \rangle_\alpha$;
(g)WBCDF image, $\mathbf{B} = \langle 110 \rangle_\alpha$, (-g,3g) $\mathbf{g} = \langle 111 \rangle_\alpha$; (h) BF image, $\mathbf{B} = \langle 001 \rangle_\alpha$; $\mathbf{g} = \langle 111 \rangle_\alpha$.

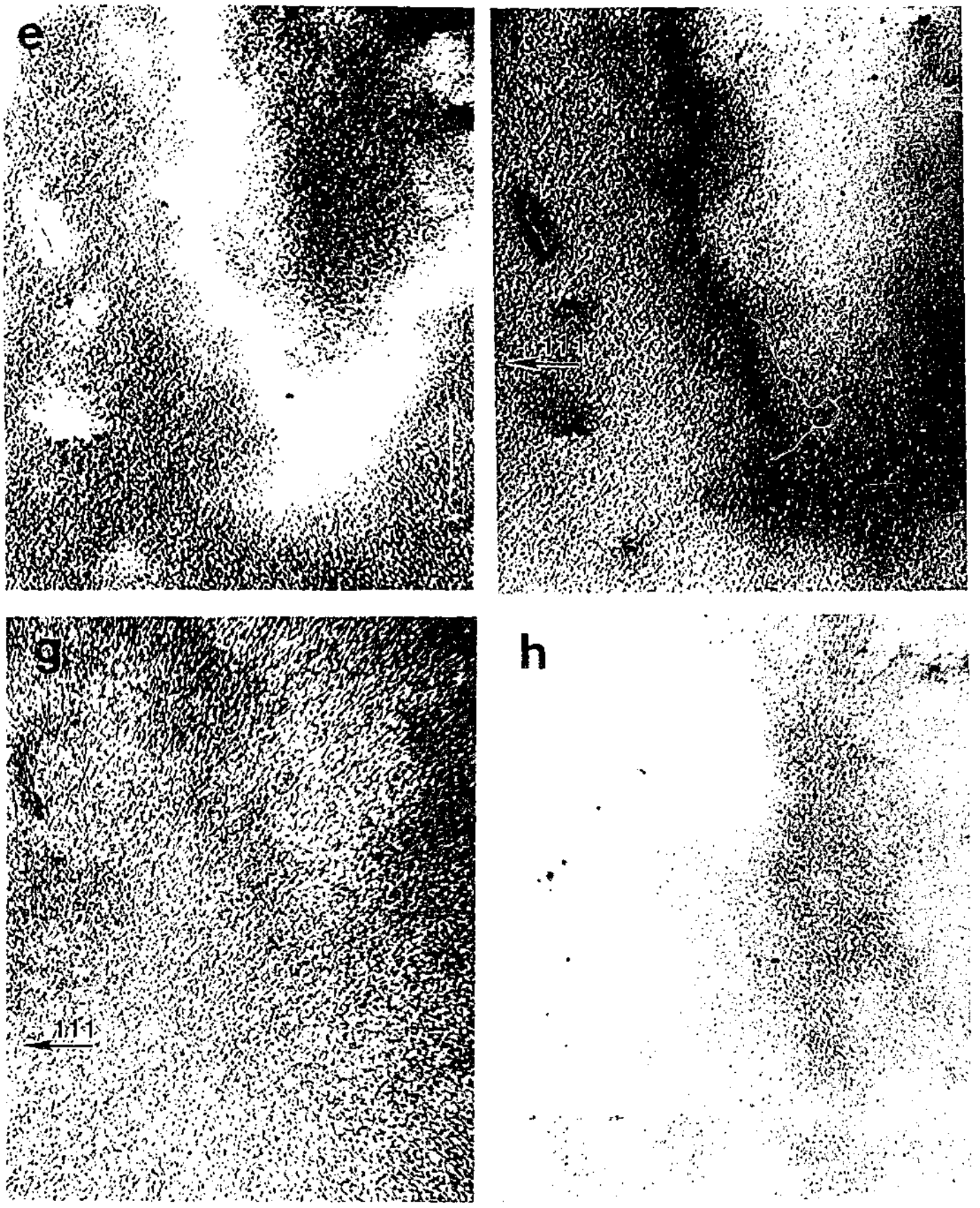

Figure 6.4 Continued

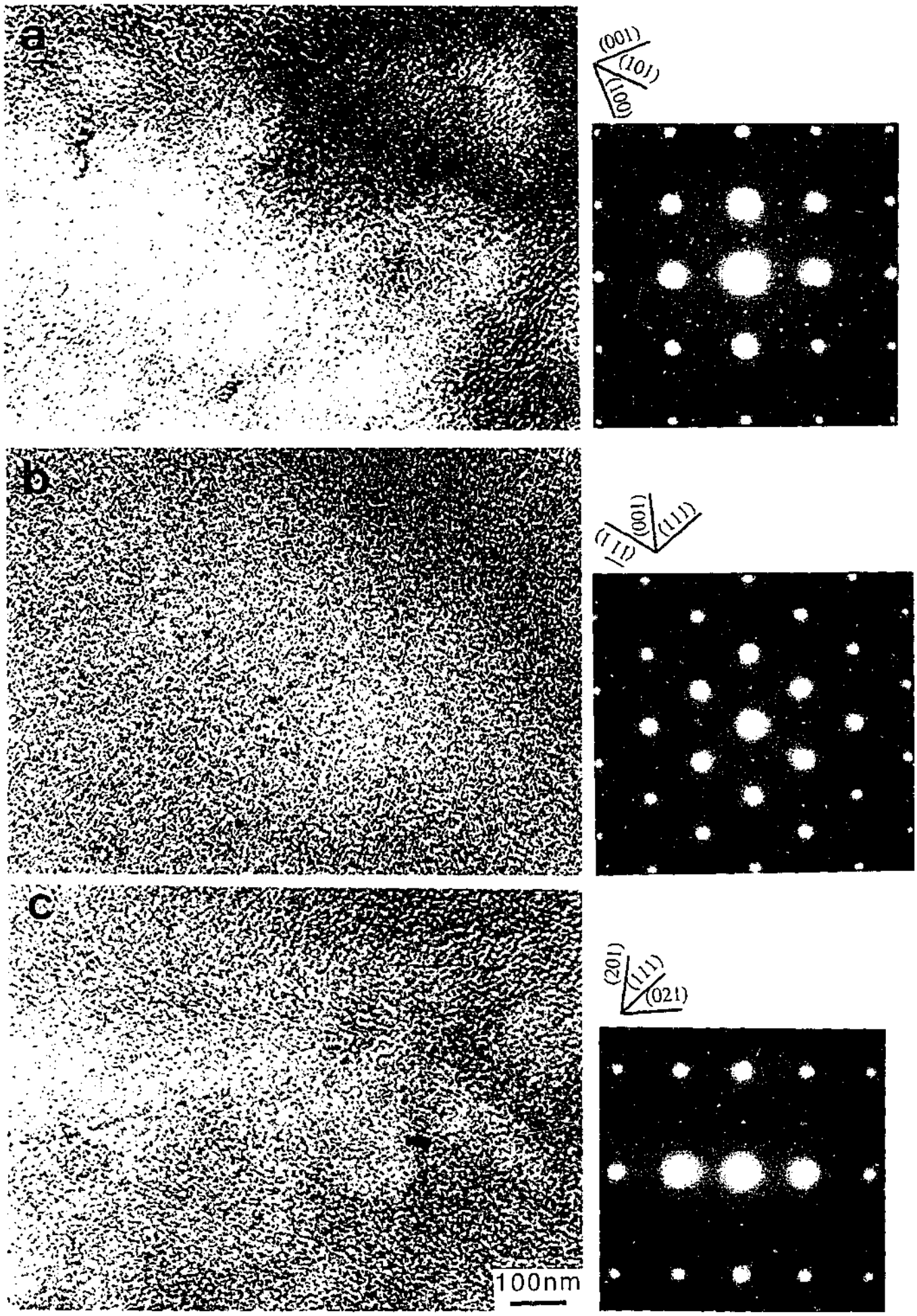

Figure 6.5 BF images of the ternary Al-10Mg-0.5Ag alloy aged 28 months at room temperature (20°C), showing finer-scale, uniform distributions of ordered precipitate particles. The electron beam is approximately parallel to (a) $<001>_\alpha$, (b) $<110>_\alpha$ and (c) $<112>_\alpha$ directions.

Ageing at 90°C

According to the available binary Al-Mg phase diagram (Murray 1990), and direct observations (Lorimer 1978) of the decomposition process in Al-Mg alloys, an ageing temperature of 90°C is above the metastable solvus curves for both GP (Mg rich) zones and β'' phase (Al_3Mg, the ordered cubic $L1_2$ structure) in an Al-10%Mg alloy. On this basis, microstructures containing β' phase (Al_3Mg_2, a = 1.002 nm, c = 1.636 nm) would be expected following ageing at this temperature. However, despite a number of existing reports, the potential morphologies and distributions of β' phase are still poorly understood, principally because most previous studies have used indirect analytical techniques, such as measurements of electrical resistivity and DSC (Panseri et al. 1963, Osamura and Ogura 1984). In this section of the experimental results, an attempt is thus made to characterise the microstructures of binary Al-10Mg and ternary Al-10Mg-0.5Ag alloys aged at 90°C by TEM.

The microstructures of binary Al-10Mg and ternary Al-10Mg-0.5Ag alloys aged 7 days at 90°C are compared in Figures 6.6 (a)-(f); the electron beam is approximately parallel to (a), (d) $<001>_\alpha$; (b), (e) $<110>_\alpha$ and (c), (f) $<112>_\alpha$ directions. The BF images of the binary alloy, Figs. 6.6 (a)-(c), show that no obvious evidence of precipitate particles in any of the orientations. However, there remains a dislocation substructure comprising. The corresponding SAED zone axis patterns also indicate no detectable evidence of diffraction from a precipitate phase or phases.

In contrast to the very fine scale, uniformly distributed spheroidal particles of precipitate β'' phase that were observed in the ternary alloy following prolonged natural ageing (20°C), Figs. 6.5, the microstructures of the Ag-containing alloy aged at 90°C, Fig. 6.6 (d)-(f), contained no detectable evidence of a precipitate phase and appeared similar to the as-quenched microstructures. However, it was noticeable that the dislocation density appeared to be substantially reduced in the specimen aged at 90°C.

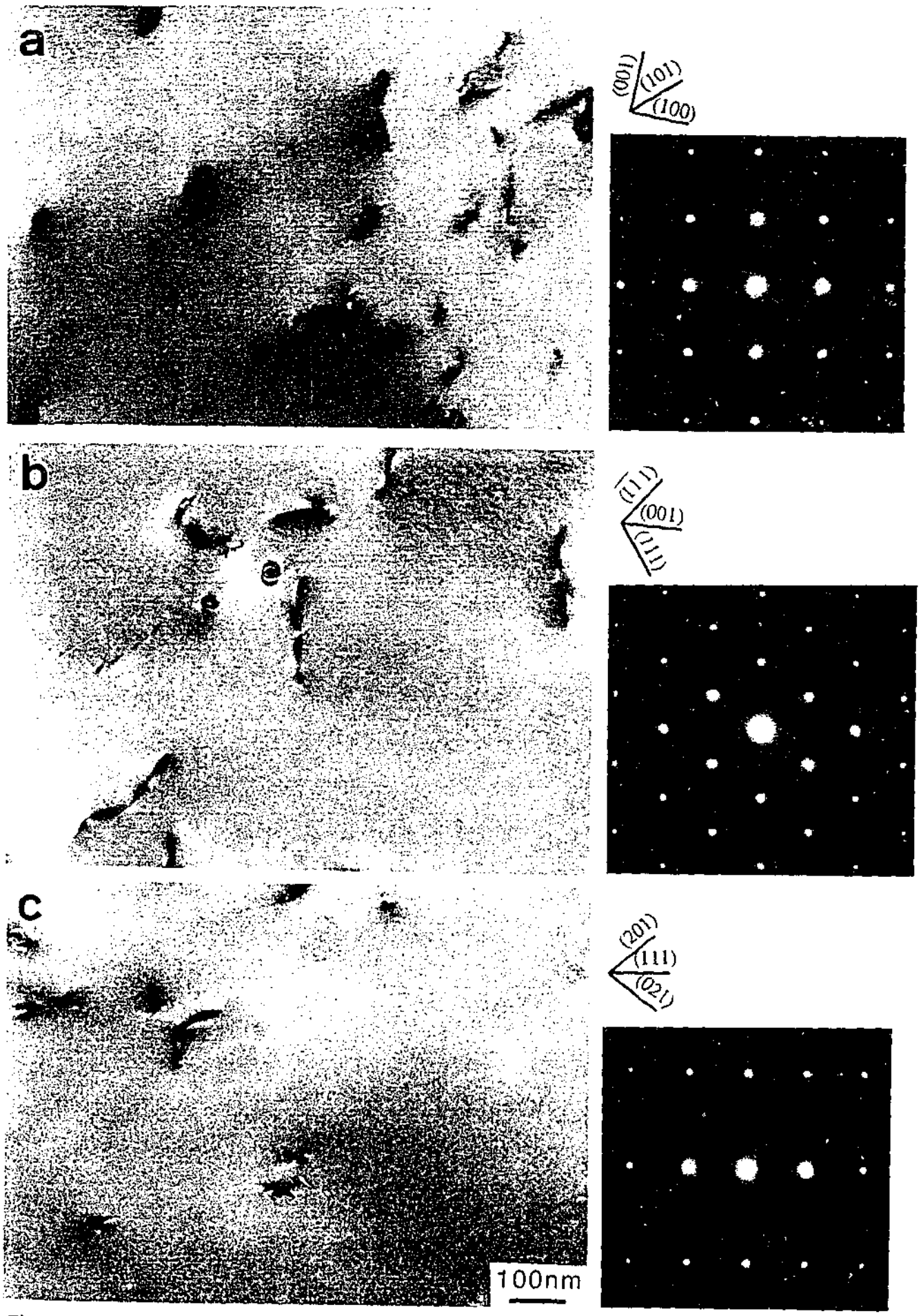

Figure 6.6 BF images of (a)-(c) binary Al-10Mg and (d)-(e) ternary Al-10Mg-0.5Ag alloys aged 7 days at 90°C showing no evidence of precipitation in either alloy after this ageing treatment. The electron beam is approximately parallel to (a), (d) $<001>_\alpha$; (b), (e) $<110>_\alpha$ and (c), (f) $<112>_\alpha$ directions.

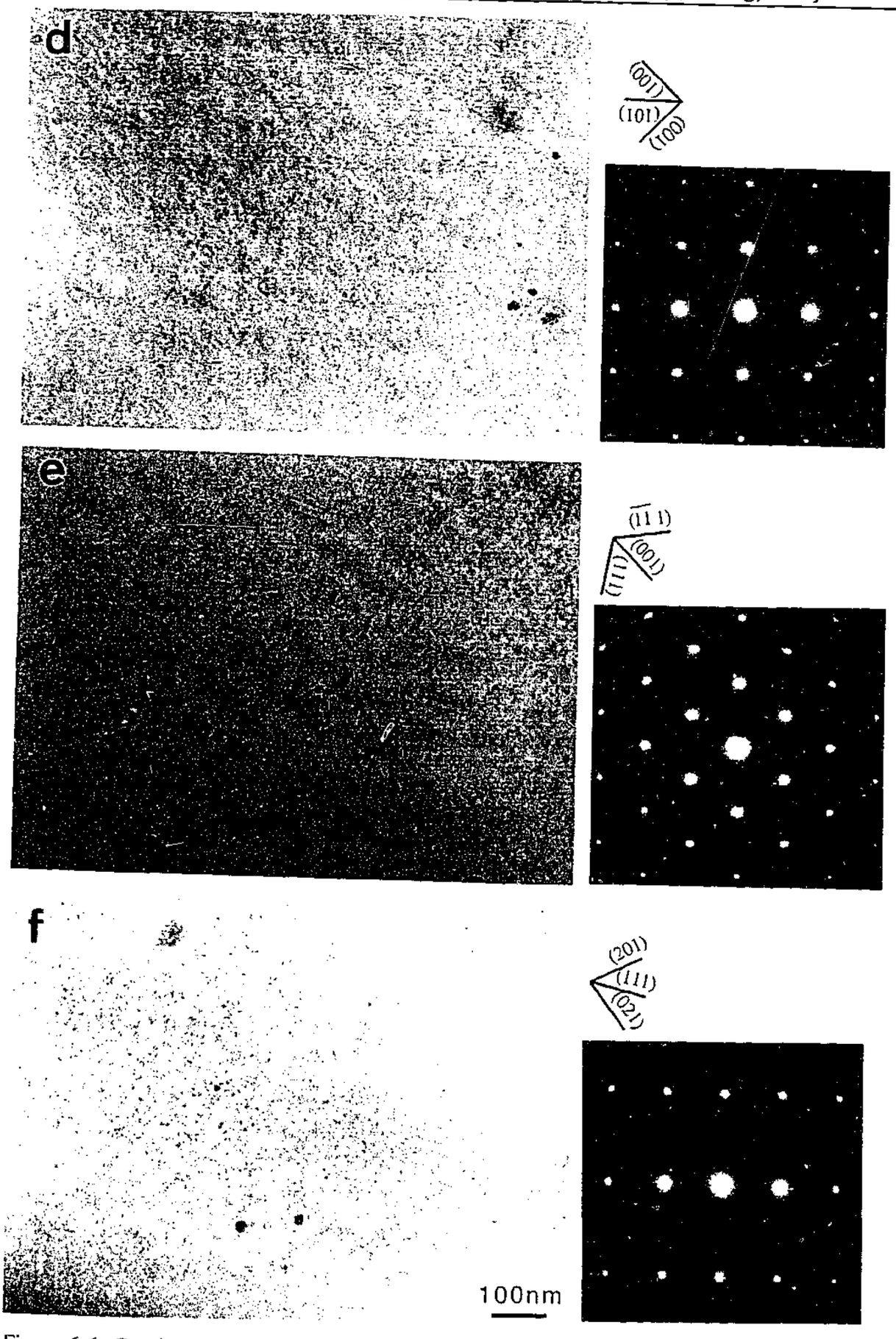

Figure 6.6 Continued.

Bright-field TEM images of Al-10Mg(-0.5Ag) alloys aged 30 days at 90°C are presented in Figures 6.7 (a)-(f); the electron beam is approximately parallel to (a), (d) $<001>_\alpha$; (b), (e) $<110>_\alpha$ and (c), (f) $<112>_\alpha$ directions. The microstructure of the binary alloy, Figs. 6.7 (a)-(c), contained a few discrete precipitate particles that were sparsely distributed in the aluminium matrix, and generally associated with dislocations or surrounded by strain contrast. These particles appeared plate-like and formed parallel to $\{001\}_\alpha$. However, the volume fraction of precipitate phase was too low to give rise to detectable diffraction patterns using conventional SAED. An attempt was made to obtain electron microdiffraction patterns from those individual particles. However, any useful information was not able to obtain in the diffraction patterns due to heavily etched precipitate particles during electropolishing of samples.

In contrast, in the Ag-modified alloy aged 30 days at 90°C, Figs. 6.7 (d)-(f), the microstructure contained a much higher volume fraction of precipitate particles compared to both the ternary alloy aged 7 days at 90°C (Figs. 6.6 (d)-(f)) and the Ag-free alloy aged 30 days at 90°C (Figs. 6.7 (a)-(c)). These particles appeared plate-like and formed parallel to $\{001\}_\alpha$ and were typically surrounded by intense strain contrast. Although the number density of precipitate particles in the Ag-modified alloy appeared to be much higher than in the Ag-free alloy, recorded SAED patterns again showed no evidence of diffraction from precipitate phase. An attempt was made to obtain electron microdiffraction patterns from these individual particles. However, these particles were heavily etched during TEM specimen preparation by electropolishing, so that identification of these precipitate particles was not able to be carried out.

It proved interesting to observe the microstructural changes accompanying isothermal ageing during further prolonged ageing at 90°C (e.g. 45 and 60 days). Bright field TEM micrographs of Al-10Mg(-0.5Ag) alloys aged 45 days at 90°C are shown in Figures 6.8 (a), (b); the electron beam is approximately parallel to (a), (b) $<001>_\alpha$ direction. The microstructure of the binary alloy, Figs. 6.8 (a), contained a very small number density of precipitate particles, which appeared to be a plate-like form with parallel to the $\{100\}_\alpha$ planes. In comparison to the microstructure of binary alloy aged 30 days at 90°C (Figs. 6.7 (a)-(c)), the size of plate-like form became larger as increased ageing time to 45 days (e.g. ~100 nm (Figs. 5.7 (a)) to ~500 nm (Figs. 5.8 (a))), but the microstructure contained similar dislocation structures.

The ternary alloy aged 45 days at 90°C, Figs. 6.8 (b) contained sparsely-distributed plate-like precipitate particles that were aligned approximately parallel to the $\{100\}_\alpha$ planes. It was not possible to identify these plate-like precipitate particles in either the binary or the ternary alloys, because it proved difficult to prepare thin foil samples in which the precipitate particles were preferentially etched from the foil during the TEM sample preparation process. In addition, the SAED patterns recorded again showed no any evidence of crystallographic information from the precipitate particles, due principally to the small volume fraction of precipitate phase.

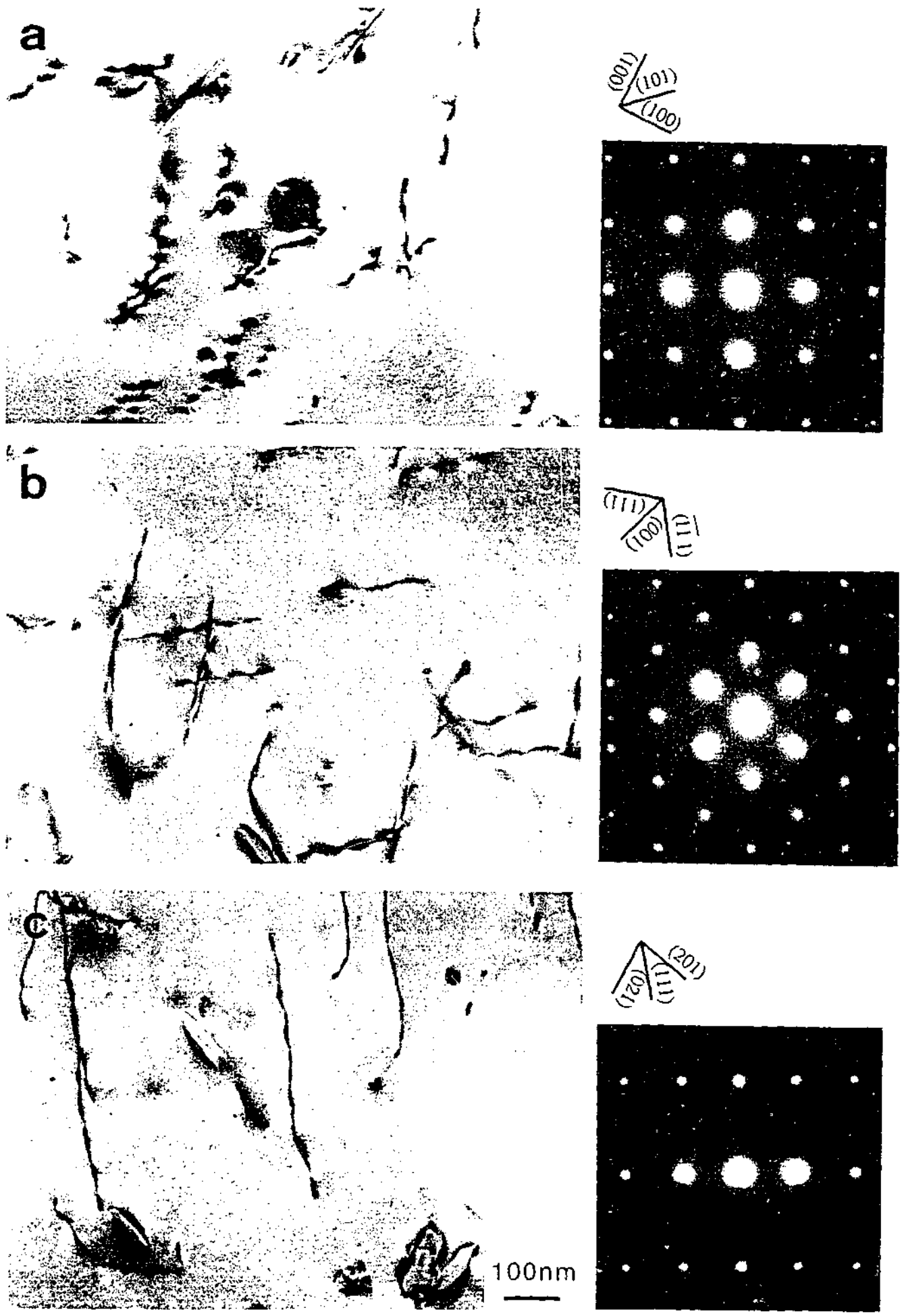

Figure 6.7 Microstructures of (a)-(c) binary Al-10Mg and (d)-(f) ternary Al-10Mg-0.5Ag alloys aged 30 days at 90°C. The electron beam is approximately parallel to (a), (d) $<001>_\alpha$, (b), (c) $<110>_\alpha$ and (c), (f) $<112>_\alpha$ directions.

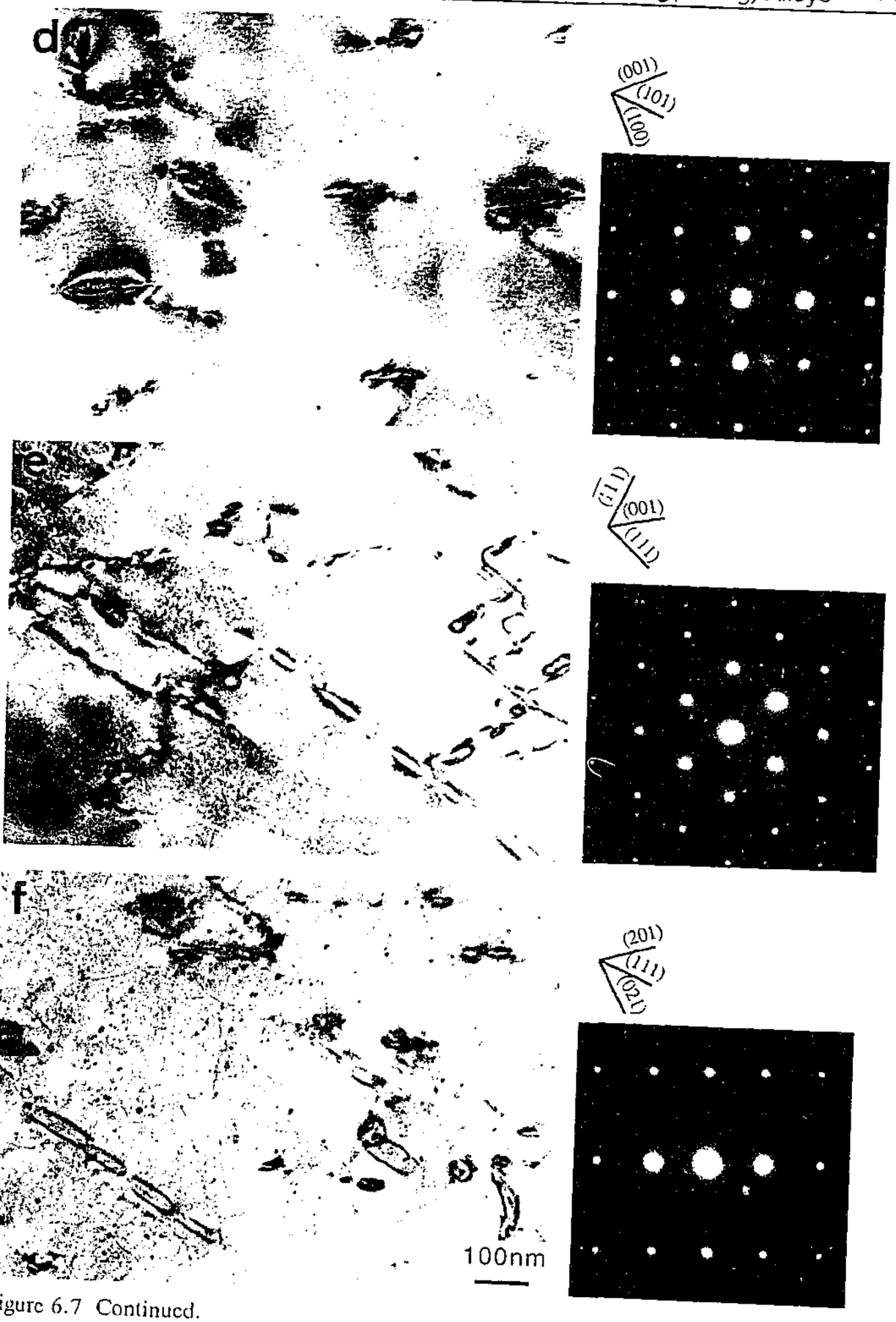

Figure 6.7 Continued.

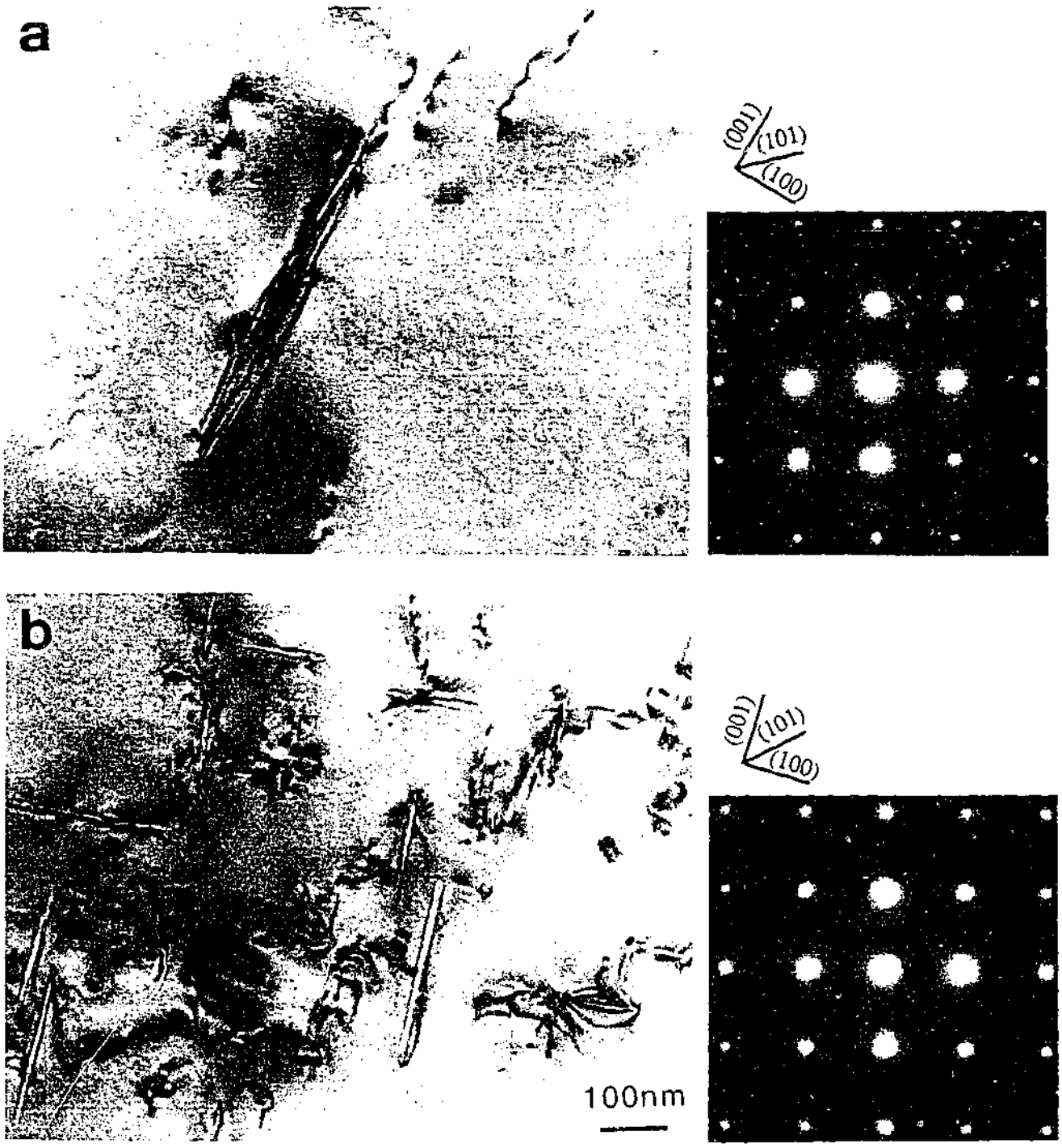

Figure 6.8 TEM micrographs of (a) Al-10Mg and (b) Al-10Mg-0.5Ag alloys aged 45 days at 90°C. The electron beam is approximately parallel to (a), (b) $<001>_\alpha$ direction.

Bright-field TEM images of Al-10Mg(-0.5Ag) alloys aged 60 days at 90°C are presented in Figures 6.9 (a)-(d); the electron beam is approximately parallel to (a), (c) $<001>_\alpha$ and (b), (d) $<110>_\alpha$ directions. When the ageing time was increased from 45 to 60 days, the microstructure of the binary alloy, Fig. 6.9 (a), was changed significantly and now contained coarse scale, plate-like precipitate particles, together with a relatively fine-scale distribution of cuboidal precipitate particles. In $<001>_\alpha$ orientations, Figs. 6.9 (a), there were two variants of edge-on plate-like shapes, which were orthogonal and parallel to the electron beam, and the third variant, which was inclined to the electron beam. It was thus interpreted that these plate-like precipitate particles have

a habit plane of $\{100\}_\alpha$. It is to be noted that the microstructure contained a relatively high dislocation density, with individual dislocations associated with the precipitate particles, especially with the $\{100\}_\alpha$ plate-shaped precipitates. The microstructure of the binary alloy observed in the $<110>_\alpha$ orientation, Fig. 6.9 (b), contained only one variant of edge-on plate-like particles in this orientation, confirming that plate-like precipitate particles have a habit plane of the $\{100\}_\alpha$. The finer scale precipitate particles, which appeared cuboidal in the $<001>_\alpha$ orientation, were also observed to have a diamond-shaped in the $<110>_\alpha$ orientation.

A finer scale and more uniform distribution of plate-like precipitate particles was observed in the Ag-modified alloys given a similar heat treatment of 60 days at 90°C, Figs. 6.9 (c) and (d). These plate-like particles were parallel to $\{100\}_\alpha$ planes, and similar in appearance and form to the plate-like particles observed in the microstructure of the binary alloy, Figs. 6.9 (a) and (b). Interestingly, there was no evidence of the finer-scale spherical particles in the ternary alloy. It has already been explained that it was extremely difficult to obtain quality thin foils of these samples by the electro-polishing technique, and it similarly proved difficult to retain precipitate particles in thin foils prepared by ion milling. There was again a tendency for the precipitate phase to be preferentially ion etched, and identification work using electron diffraction techniques has been proved very difficult.

It has been pointed out above that preparation of thin foil samples for TEM observations was extremely difficult due to the formation of oxidation films on the surface of samples and preferentially etching of precipitate particles, especially for the $\{100\}_\alpha$ plate-like, during sample preparation by the electro-polishing process. There were many chemical solutions that had been tried to use for the sample preparation. It implied that the $\{100\}_\alpha$ precipitate particles observed in both binary and ternary alloys aged 60 days at 90°C, which were heavily etched by chemical solutions, may contain a relatively higher amount of Mg rather than Ag because it has been generally known that Mg is an active element with oxygen compared to that of Ag.

Successful, but a limited microbeam electron diffraction pattern recorded from the $\{100\}_\alpha$ plate-like is presented in Figures 6.9 (e). The electron microdiffraction pattern, Figs. 6.9 (e), showed a similar diffraction pattern observed in binary Al-10Mg alloy aged 5 h at 240°C, as previously shown in Figs 5.6 (a), and was successfully indexed for a $[11\bar{2}6]_{\text{hexagonal}}$ direction of a metastable β' phase. A limited number of microbeam electron diffraction patterns recorded from the $\{100\}_\alpha$ plate-like particles thus identified the β' phase having a hexagonal structure with the lattice parameters of a = 1.002 nm, c = 1.636 nm that are consistent with the simulated pattern and results previously reported (Bernole et al. 1969, Bernole 1974, Mondolfo 1976). The identification work for the diamond-shaped precipitate particles using electron microdiffraction was not well successful due to difficulties of thin foils preparation, so that detailed microstructural characterisation still remain unclear.

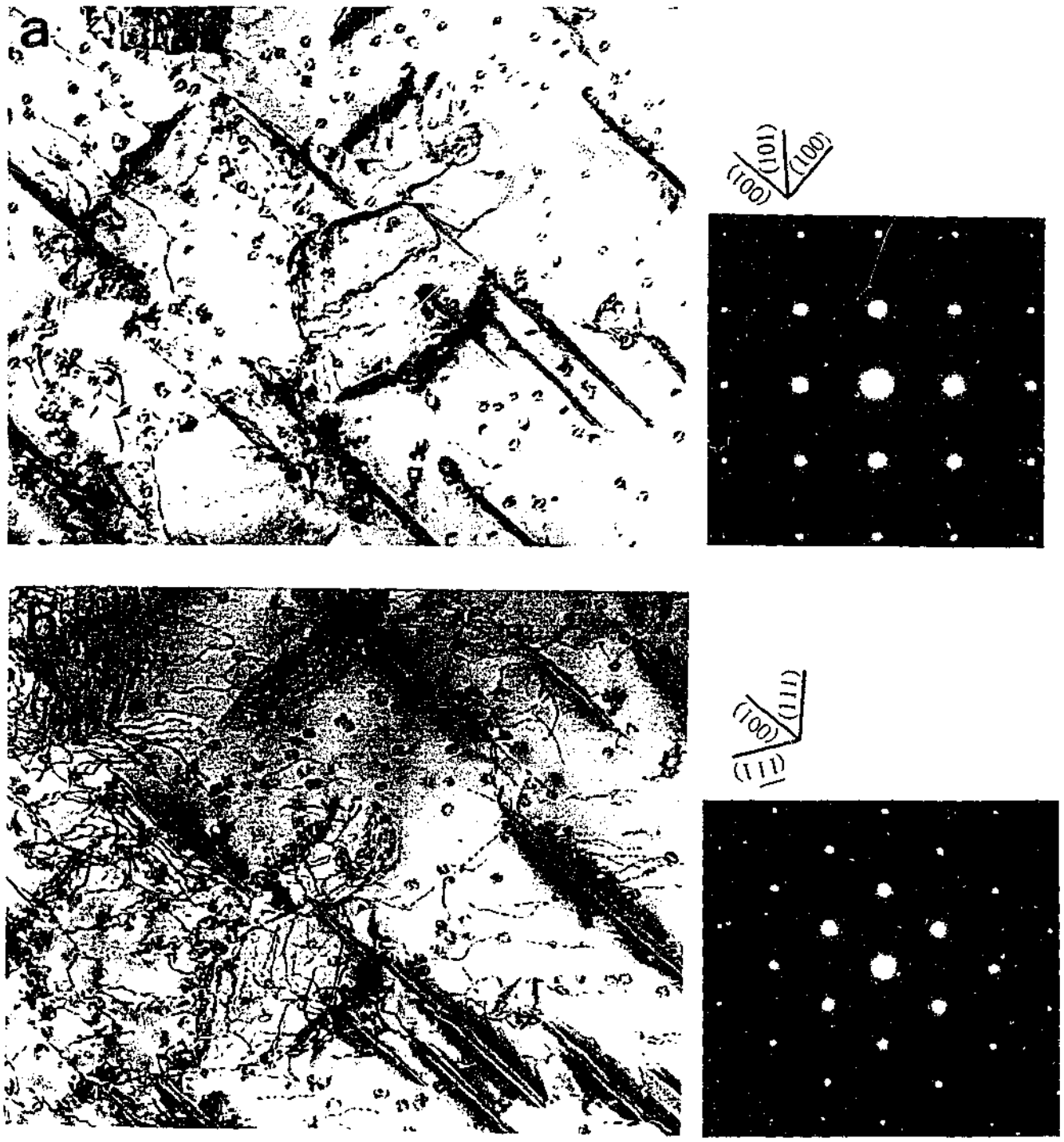

Figure 6.9 Bright field TEM micrographs of (a), (b) Al-10Mg and (c), (d) Al-10Mg-0.5Ag alloys aged 60 days at 90°C. The electron beam is approximately parallel to (a), (c) $<001>_\alpha$ and (b), (d) $<110>_\alpha$ directions. A microbeam electron diffraction pattern recorded from the plate-like particle showing (e) hexagonal structure.

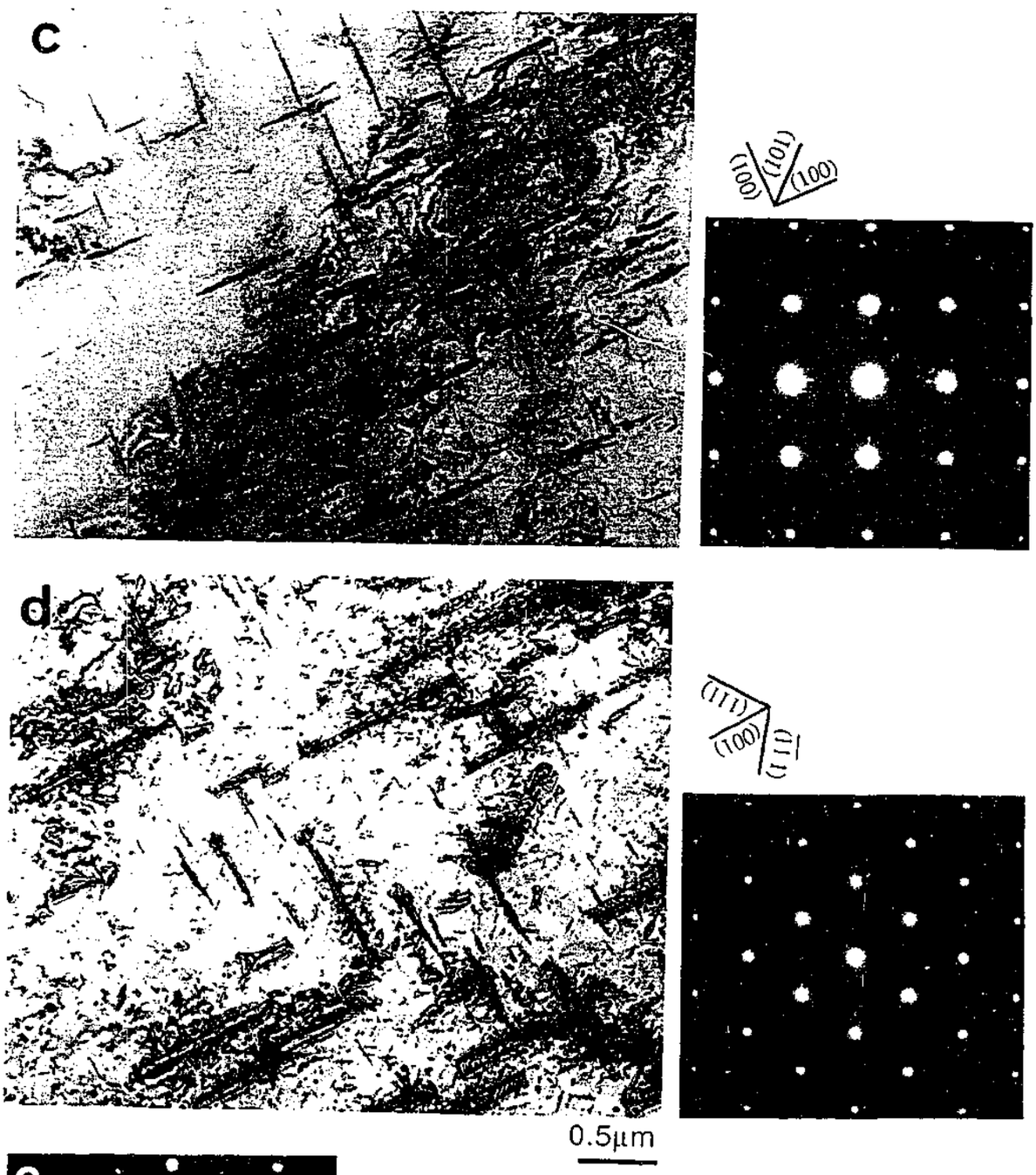

Figure 6.9 Continued.

Ageing at 200°C

In this sub-section, the microstructural changes in the binary Al-10Mg and ternary Al-10Mg-0.5Ag alloys aged from 1 h to 10 h at 200°C are characterised. These heat treatments correspond to under ageing conditions, according to the ageing curves (Fig. 4.2) presented in Chapter 4. Only limited TEM work was conducted on this range of samples due to the stated difficulties of preparing thin foils for TEM observation.

A series of BF images and corresponding SAED patterns, obtained from the Al-10Mg alloy aged at 200°C for periods of 1 h, 2 h and 4 h, is shown in Figures 6.10 (a), (b) and (c), respectively. The electron beam is approximately parallel to a $<001>_\alpha$ zone axis in each. Based on both the previous literature (Lorimer 1978) and on the characterisation of microstructures in samples aged at 90°C, it was expected that the $\{001\}_\alpha$ plate-like precipitate particles were the most likely consistent of the microstructure of the specimens aged at 200°C. The specimens, were thus, preferentially examined in $<001>_\alpha$ orientations.

Figure 6.10 (a) suggests that the microstructure contains no detectable precipitate particles after 1 h at 200°C, with only a residual dislocation substructure to be observed in the aluminium matrix. When the ageing time was increased to 2 h, Fig. 6.10 (b), the microstructure contained a small number density of few precipitate particles, primarily nucleated in association with dislocations. These precipitate particles appeared to be a plate-like form with $\{100\}_\alpha$ habit planes. Further increase in the ageing time to 4 h at 200°C, Fig. 6.10 (c), produced a coarse-scale, sparsely-distributed array of plate-like particles that are again typically associated with or generating dislocations. These plate-like precipitate particles again have an approximately $\{001\}_\alpha$ habit plane. In addition, this microstructure also contained a small number density of coarse cuboidal particles. It is interesting to note that, the finer-scale cuboidal precipitates, that were typical of specimens aged at 90°C, were not observed in the specimens aged at 200°C.

All of the SAED patterns corresponding to the BF images exhibited that no diffraction evidence, such as extra reflection spots and streaking from the precipitate phase(s), was observed. Detailed crystallographic analyses by electron diffraction technique including SAED were failed due to the heavily oxidised and etched precipitate particles in the obtained thin foils.

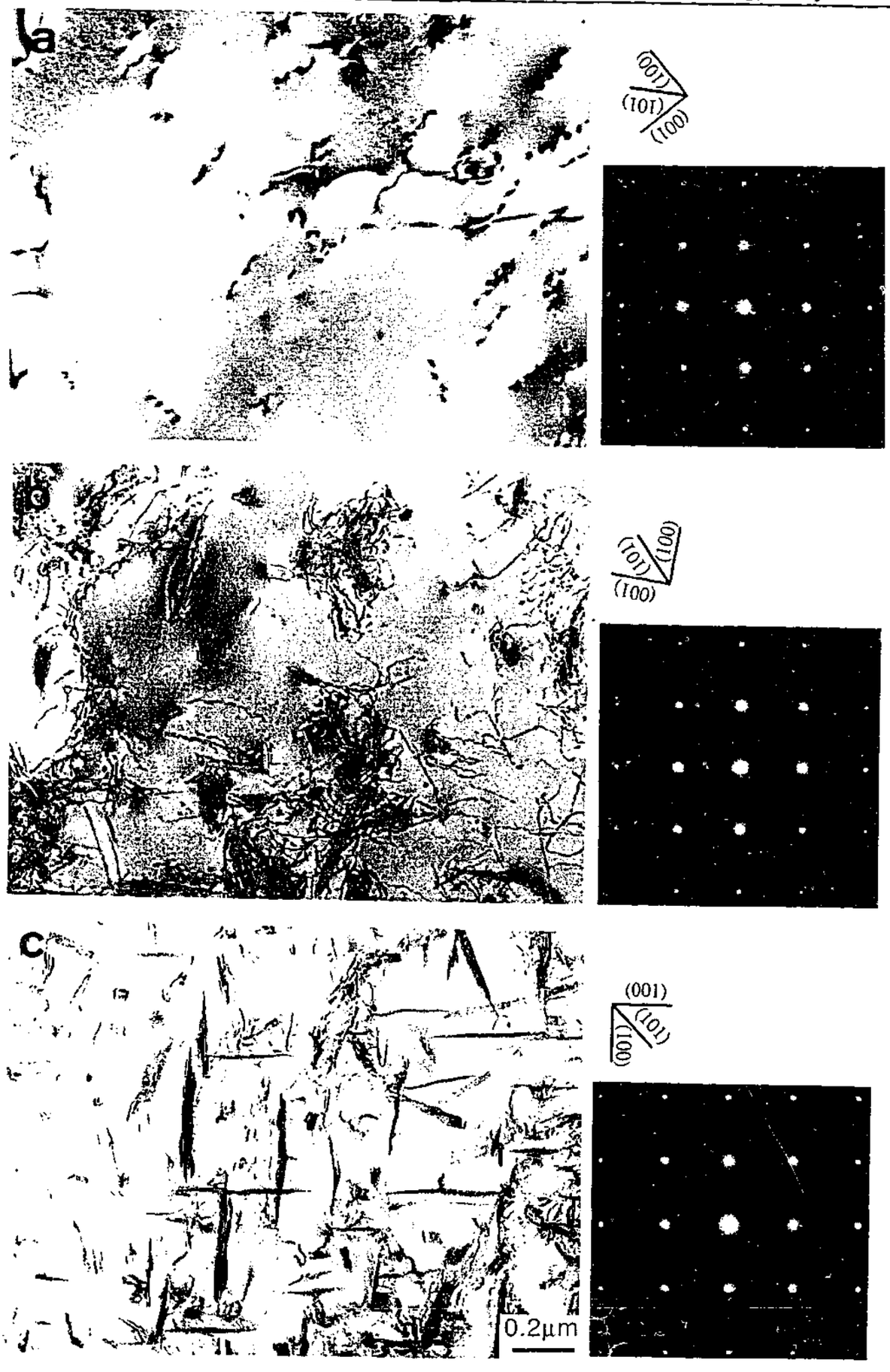

Figure 6.10 TEM micrographs of Al-10Mg alloy aged (a) 1 h, (b) 2 h and (c) 4 h at 200°C; the electron beam is approximately parallel to an $<001>_{\alpha}$ direction in each.

A series of BF images and the corresponding SAED patterns, obtained from specimens of the Al-10Mg-0.5Ag alloy aged at 200°C for periods of 4 h and 6 h, is shown in Figures 6.11 (a) and (b), respectively. The electron beam is approximately parallel to the $<110>_{\alpha}$ zone axis. These heat treatments correspond to under ageing conditions, according to the ageing curves (Fig. 4.2) presented in Chapter 4. Based on the characterisations of microstructures aged at 240°C and described in the previous Chapter 5, the specimens were preferentially oriented parallel to $<110>_{\alpha}$ zone axes for observation.

The very fine scale, uniformly distributed spherical shape of precipitate particles can be seen in the BF image, Figs. 6.11 (a). Based on comparison of the SAED patterns presented earlier, Figs. 5.12, in the section of 5.2.2 in Chapter 5, the corresponding SAED pattern presented in Figs. 5.11 (a) is consistent with the pattern previously presented (Figs. 5.12). This implies that small spherical precipitate particles may have an icosahedral structure. When the ageing time is increased to 6 h from 4 h, Figs. 6.11 (b), the microstructure shows a predominantly fine scale, uniformly distributed, faceted diamond-shaped precipitate particles together with a minor fraction of coarse scale precipitate particles that were not observed in the early stages of ageing at 240°C. Although detailed crystallographic analyses for the precipitate particles by electron diffraction technique were limited, recorded SAED patterns corresponding the same area of the BF image were approximately same. It thus suggest that fine scale, uniformly distributed precipitate particles are to be having the icosahedral structure. A microbeam electron diffraction pattern, Figs. 6.11 (c), recorded from the single coarse scale precipitate particle (Figs. 6.11 (a)) is indexed for a $[11\bar{2}6]$ direction of a hexagonal structure, and suggests to be a metastable β' phase.

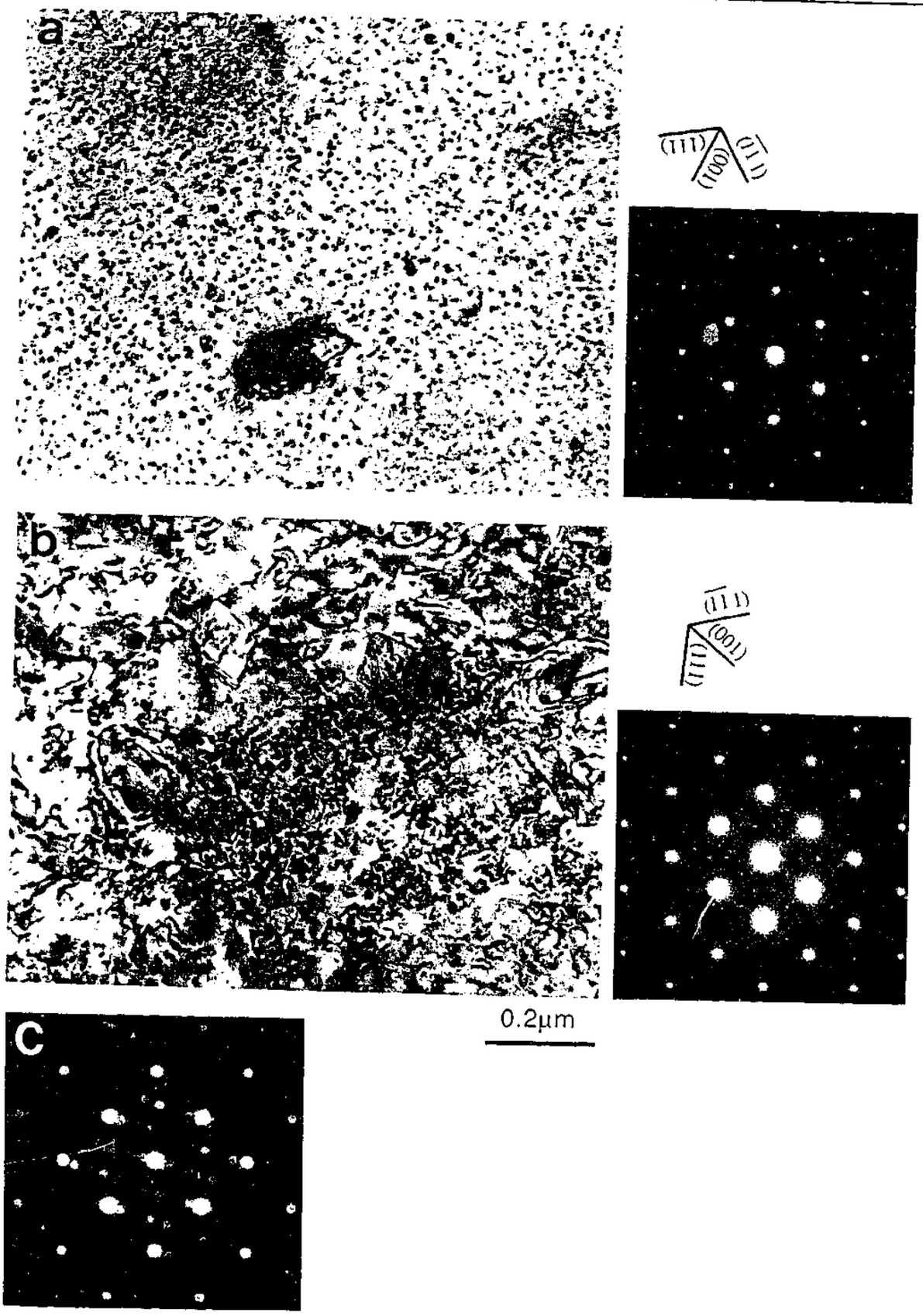

Figure 6.11 TEM micrographs of Al-10Mg-0.5Ag alloys aged (a) 4 h and (b) 6 h at 200°C. The electron beam is approximately parallel to an $<110>_{\alpha}$ direction in each case.

Ageing at 240°C

It is important to understand the microstructural evolution in the Al-10Mg-0.5Ag alloy aged for periods of 10 min. to 40 min. at 240°C, because this corresponds to the requirement of increasing hardness that leads to the maximum hardness, as shown the age-hardening curve in Fig. 4.3. Such observations these potentially provide a basis for a correlation between microstructure and hardness, and thus form the basis of this following sub-section.

As an example, TEM micrographs of a specimen of Al-10Mg-0.5Ag alloy aged 10 min. at 240°C are presented in Figure 6.12. The electron beam is approximately parallel to (a) $<001>_\alpha$, (b) $<110>_\alpha$ and (c) $<112>_\alpha$ directions, respectively. The series of the BF images, Figs. 6.12 (a)-(c), shows a microstructure containing fine-scale, equiaxed precipitate particles uniformly distributed within the grains in all three orientations. The microstructure also contained line dislocation structures. As increasing ageing time from 10 min. to 40 min., in a specimen of Al-10Mg-0.5Ag alloy aged at 240°C, the morphology and the distributions of precipitate particles were approximately the same, but the number density of precipitate particles has been increased and size of particles became larger. The SAED patterns recorded from the same area in the BF images contain precipitate patterns of weak intensity, but sufficient clarity to suggest that the precipitate particles have a limited number of forms and that the precipitate phase has a well-defined orientation relationship with respect to the aluminium matrix. It is noted that diffracted spots from the precipitate particles were approximately similar to the recorded SAED patterns in the sample aged 0.5 h at 240°C, as presented in Figs. 5.11 (a)-(f). It thus implies that these precipitate particles are to be having the icosahedral quasicrystalline structure based on comparisons between obtained SAED patterns and the one presented (Fig.5.11) in the Chapter 5. A microbeam electron diffraction patterns were not successfully obtained from a single faceted precipitate particle due to their fine-scale precipitate particles.

In samples of ternary alloy aged 2 h at 240°C, which corresponded approximately to the peak hardness condition, the microstructure contained a higher density distribution of precipitate particles, which included a mixture of rod-like, square- and diamond-shaped particles, presented previously in Fig. 5.20 in Chapter 5. It has previously been established that the square-section precipitates are rod-like particles of T phase observed parallel to the rod-axis, while the rod-like particles with rod-axes parallel to $<110>_\alpha$ directions represent the other variants of the b.c.c. T phase. The diamond-shaped or rhombohedral particles have previously been identified as having the icosahedral structure.

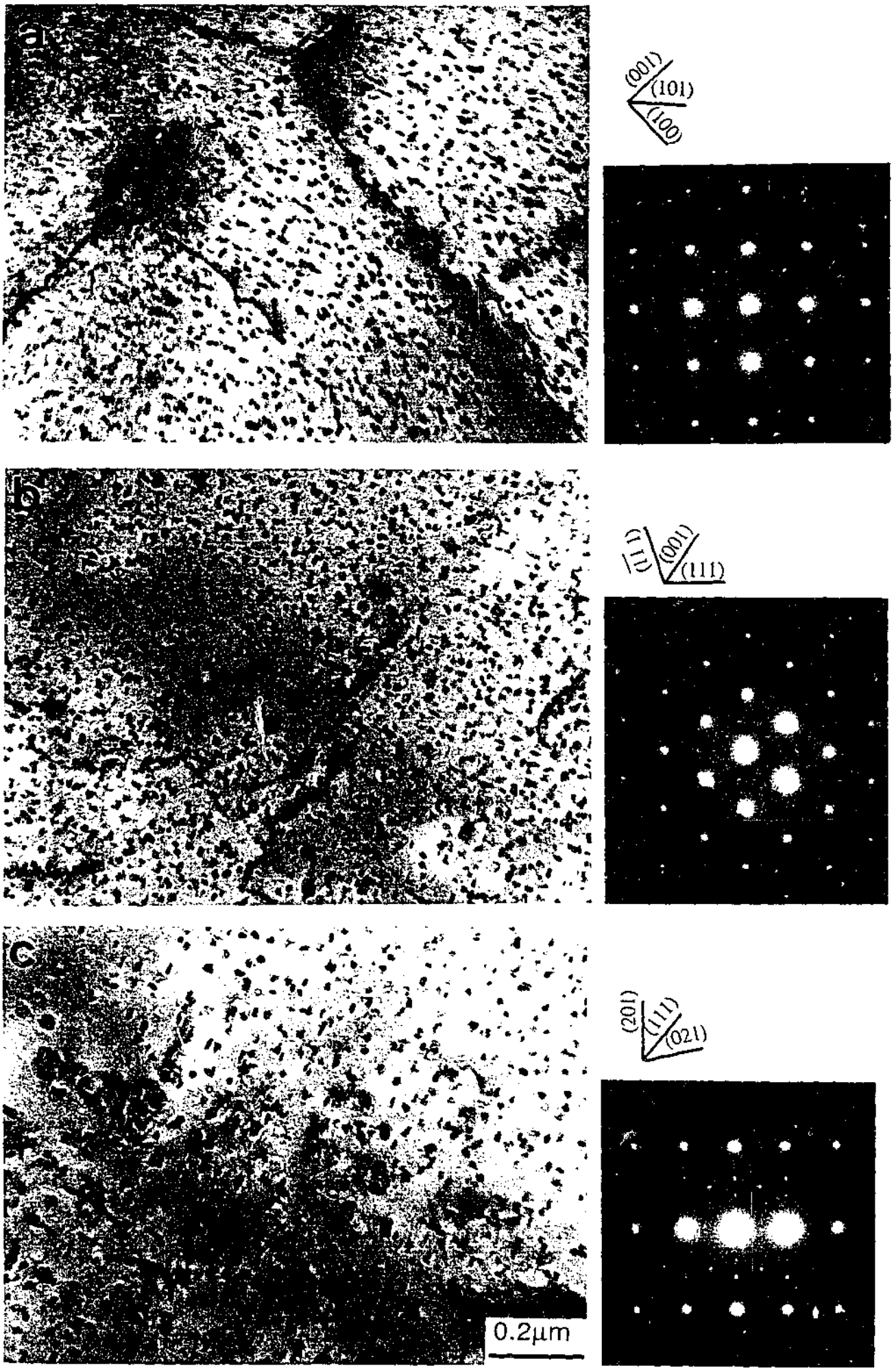

Figure 6.12 TEM micrographs of Al-10Mg-0.5Ag alloy aged 10 min. at 240°C. The electron beam is approximately parallel to (a) $<001>_\alpha$, (b) $<110>_\alpha$ and (c) $<112>_\alpha$ directions.

After the samples were aged 5 h at 240°C, which corresponds to slightly beyond the maximum hardness condition, the BF images showed a higher volume fraction of dispersed precipitate phases which comprised a mixture of a coarse-scale, rod-like particles and blocky particles, as shown in Figures 6.13 (a)-(c). The corresponding SAED patterns exhibited increased diffracted intensity from these precipitate phase, but the essential pattern symmetry remained similar to that observed in Fig. 6.12, suggesting that the identity of the precipitate phase remained the same but that the volume fraction of precipitate particles had increased.

With further increase of ageing time up to 24 h at 240°C, corresponding to a well over-aged condition, the microstructure contained a high volume fraction of coarse-scale, globular precipitate particles, together with a secondary distribution of fine-scale spheroidal precipitates, as shown in Figures 6.14 (a)-(c). Although no detailed crystallographic information was obtained from these precipitate particles, previously established identification of similar particles in Chapter 5 would suggest that such particles are the equilibrium β phase.

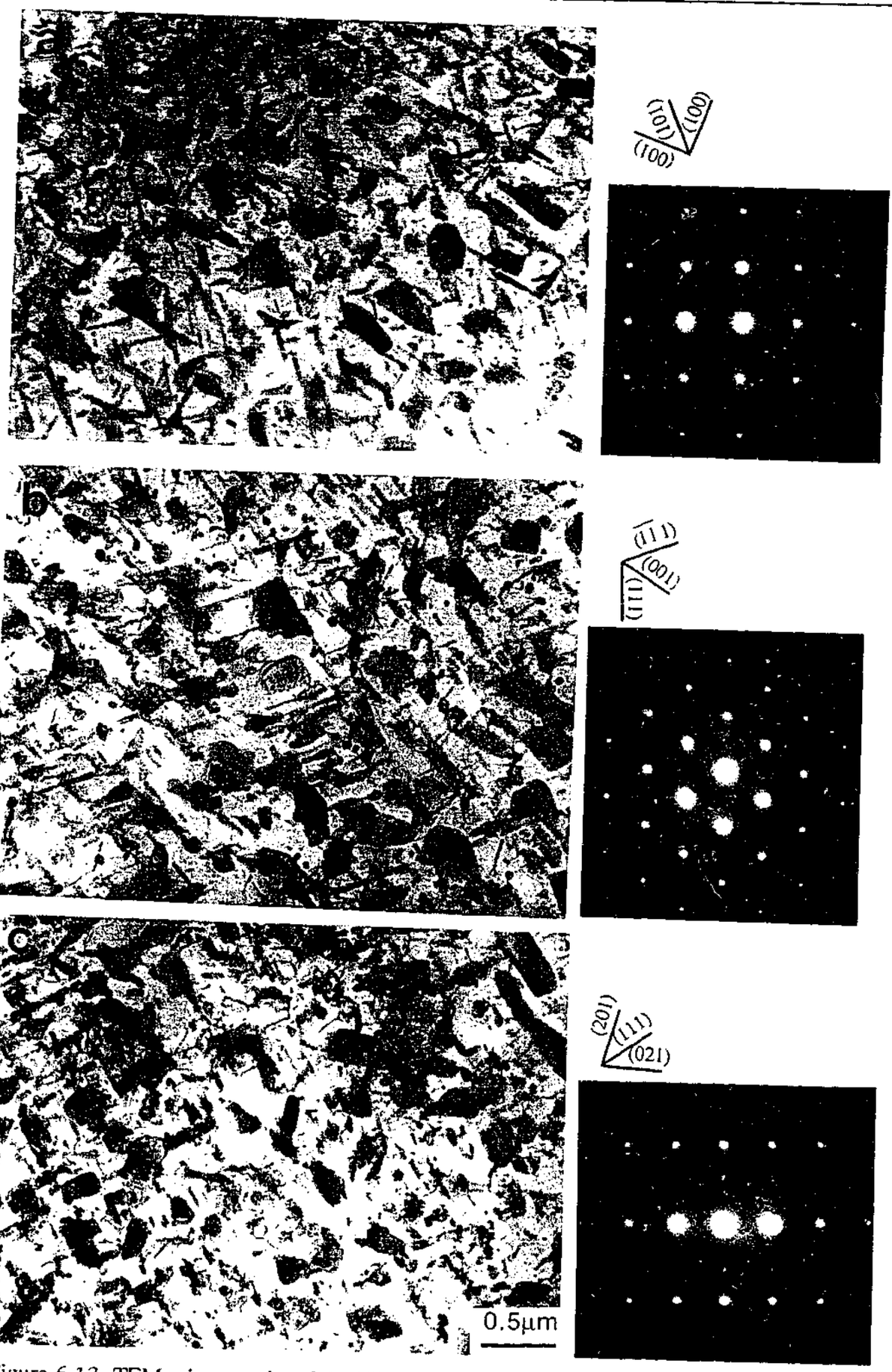

Figure 6.13 TEM micrographs of Al-10Mg-0.5Ag alloys aged 5 h at 240°C. The electron beam is approximately parallel to (a) $<001>_\alpha$, (b) $<110>_\alpha$ and (c) $<112>_\alpha$ directions.

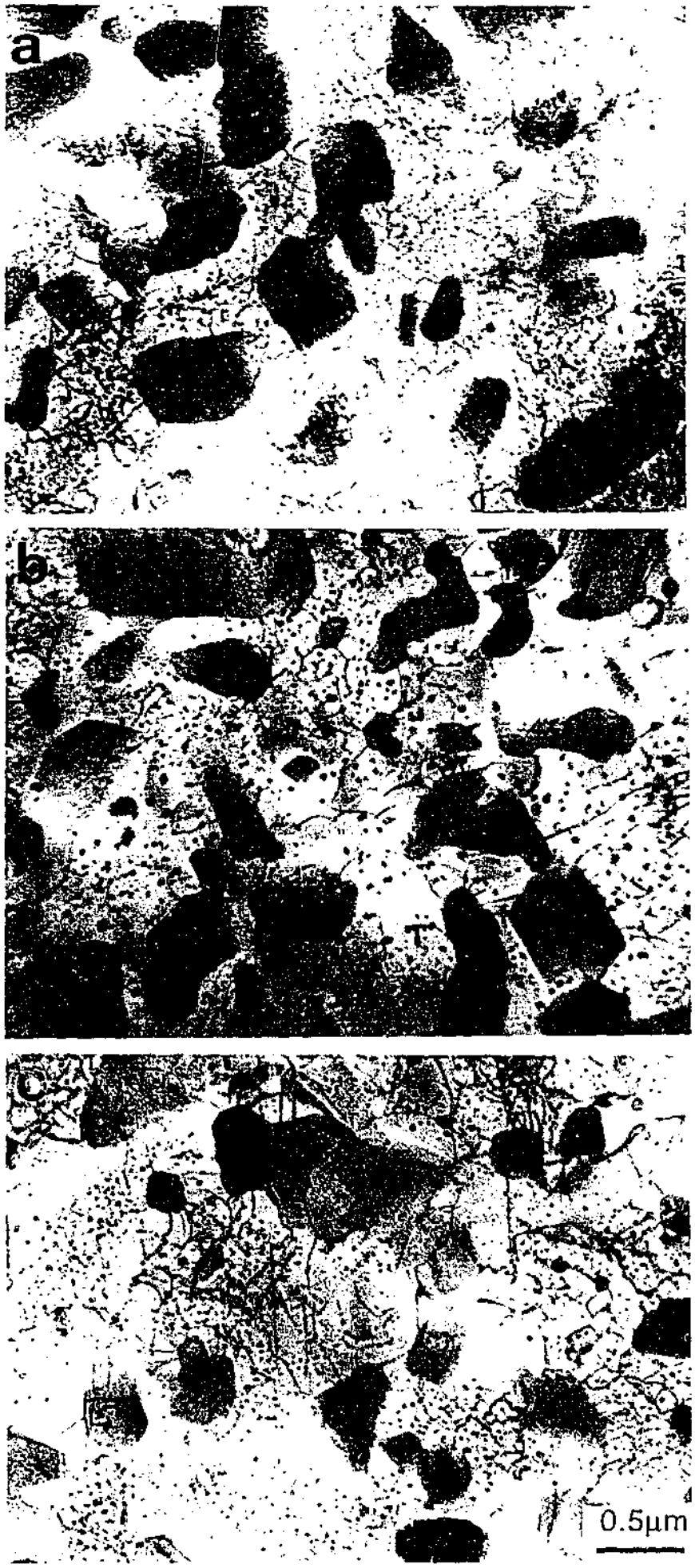

Figure 6.14 Microstructures comprising a mixture of coarse, globular and fine, spheroidal precipitate particles in Al-10Mg-0.5Ag alloy aged 24 h at 240°C. The electron beam is approximately parallel to (a) <001>α , (b) <110>α and (c) <112>α directions.

6.3 Discussion

6.3.1. Effects of Ageing Temperature on Precipitation Sequences

Natural Ageing

The results of microstructural observations on specimens of binary Al-10Mg and Ag-containing ternary alloys aged at room temperature (20°C), arising from TEM images shown in Figs. 6.1 to 6.5, clearly suggest that the supersaturated solid solution of the binary alloy is significantly more stable thermodynamically than the ternary Al-10Mg-0.5Ag alloy under similar conditions. What has been described as a modulated structure, giving rise to superlattice electron diffraction, has previously been observed in the quenched Al-10Mg alloys aged 550 h at room temperature, and this microstructure developed into GP zones (153 months) having the ordered $L1_2$ type crystal structure (Sato et al. 1982). The present natural ageing treatments of the binary alloy were not a sufficient duration to confirm these observations. In the present case, there was no evidence of decomposition of binary supersaturated solid solution for periods up to 16 months at room temperature (20°C).

While it was observed that fine-scale, uniformly-distributed, spherical precipitate particles were uniformly nucleated within the aluminium matrix in the Al-10Mg-0.5Ag alloy aged only 16 months at room temperature (20°C), as shown in Figs. 6.3 (d)-(f), there was no sign of a similar decomposition process in the binary alloy, as shown in Figs. 6.3 (a)-(c). Based on evidence from SAED patterns, fine-scale, uniformly-distributed, spherical precipitate particles observed in the ternary Al-10Mg-0.5Ag alloy aged from 16 months at room temperature were identified to be the ordered $L1_2$ type structure with a lattice parameter of a = 0.408 nm. The additional precipitate reflections in the recorded SAED patterns define that the orientation relationship between the $L1_2$ structure and the α-matrix phase was of the form: $(100)_{L1_2} \parallel (100)_\alpha$, $[001]_{L1_2} \parallel [001]_\alpha$. It should be noted that the precipitate phase identified to be having the ordered $L1_2$ structure is considered as the β'' phase (Al_3Mg, the ordered cubic $L1_2$ structure) based on both present electron diffraction evidence and results reported previously (Kumada et al. 1970, Sato et al. 1982, Nebti et al. 1995, Starink and Zahra 1997).

Similar electron diffraction patterns, which have the $L1_2$ type superlattice Al_3Mg phase, was also observed in liquid-quenched Al-21.2Mg and 26.2Mg alloys (at %) aged at 100°C for 20 and 40 min. (Kumada et al. 1970). Although the lattice parameter of this superlattice structure was not reported, this previously reported ordered $L1_2$ type superlattice structure in liquid-quenched binary alloys might be the same as one observed in the present experimental ternary Al-10Mg-0.5Ag alloy. These observations clearly suggested that the trace additions of Ag to the binary Al-10Mg alloy do effect on not only the nucleation of the $L1_2$ structure in the ternary alloys, but also promotion of the formation of the $L1_2$ structure in the ternary alloys.

On significant effect of trace additions of Ag to the binary alloy was thus a significant acceleration of the decomposition process of the supersaturated solid solution even during natural ageing. It should be noted that the ordered β'' phase identified in the ternary alloy aged at room temperature (20°C) has not been transformed to another phases even the specimen were aged for up to 28 months at room temperature (20°C). These microstructural comparisons between binary and ternary alloys aged naturally at room temperature apparently suggest that trace additions of Ag to the binary Al-10Mg alloy stimulate and promote nucleation of the ordered $L1_2$ phases significantly because the time to achieve the formation of the $L1_2$ structure in ternary alloys is significantly shorter than that of in binary alloys that had been reported previously (Sato et al. 1982).

Ageing at 90°C

When the ageing temperature was increased from 20°C to 90°C, microstructures in the binary alloys significantly changed. Microstructural evolutions were as follow; in samples aged 7 days at 90°C, no evidence from precipitate particles was detected, but with increasing ageing time to 30 days microstructures contained low number density of plate-like particles which are aligned parallel to $\{100\}_\alpha$ planes. As manner of precipitate growth by ageing periods of 45 days at 90°C, these plate-like $\{100\}_\alpha$ precipitates became coarsen. Further prolonged periods of ageing at 90°C (60 days), microstructure changed to contain a mixture of plate-like $\{100\}_\alpha$ and diamond-shaped precipitate particles which was not observed in the samples in the natural ageing condition. As mentioned earlier, identification work for these individual particles by electron diffraction was failed due to preferentially etched precipitate particles. Based on limited evidence from recorded electron diffraction patterns including both reported literature previously and one of the features of precipitate morphologies that have been observed in the binary Al-10Mg alloy aged at 90°C, it is assumed that the plate-like precipitate particles are to be the β' phase (Al_3Mg_2, a = 1.002 nm, c = 1.636 nm), and identification of these diamond-shaped particles is still remain unclear.

Similarly, microstructures in the ternary Al-10Mg-0.5Ag alloys significantly altered when the ageing temperature was increased from 20°C to 90°C. Fine-scale, uniformly-distributed, spherical β'' particles, that were observed in the Al-10Mg-0.5Ag alloy aged 16 months at room temperature (20°C), were not detectable in samples aged 7 days at 90°C. This microstructural observations may be suggested that the dissolution temperatures of the β'' phases (Al_3Mg, the ordered cubic $L1_2$ structure) was less than 90°C, and this is consistent with the result reported previously that the β'' phase is formed at 45°C, and dissolution temperatures of this phase are between 45°C and 100°C (Nebti et al. 1995).

With increasing ageing time to 30 days, microstructures in both binary and ternary alloys contained plate-like precipitate particles that are parallel to $\{100\}_\alpha$ planes. There precipitate particles in ternary alloy were much finer than one in binary alloy, suggesting that effects of trace

additions of Ag may have refinement of the precipitate particle. Further increasing ageing time up to 60 days, number density of plate-like $\{100\}_\alpha$ particles increased in both binary and ternary alloys. Similar to the previous approach to understand the phases of precipitate particles was made on assumption that, based on both reported literature previously and one of the features of precipitate morphologies that observed in ternary alloy, the $\{100\}_\alpha$ plate-like precipitate particles are identified to be the β' phase (Al_3Mg_2, a = 1.002 nm, c = 1.636 nm). It should be noted that diamond-shaped precipitate particles, which were observed in binary alloy aged 60 days at 90°C, were not observed in the ternary alloy under the same ageing condition.

Ageing at 200°C and 240°C

However, the ageing temperature was increased to 200°C, only the plate-like and square-shaped precipitate particles were observed in binary alloy. Although detailed crystallographic analyses by electron diffraction technique including SAED were failed due to the heavily oxidised precipitate particles, the previously reported literature and established existing phases in the section of 5.2.1 in Chapter 5 may suggest that the $\{100\}_\alpha$ plate-like particles are to be the β' phase and the square-shaped particles are to be either β' and β phases. It should be noted that, when the ageing time was further increase up to ~16 h at 200°C, which is corresponded toward to the maximum hardness (Fig. 4.2), producing of thin foils for TEM observations was extremely difficult due to increasing rates of oxidation. One of reasons for this kind of phenomena would be that, when volume fractions of precipitate particles that containing Mg are increased with increasing ageing time, preferential oxidation sites are also increased.

These plate-like β' precipitate particles with parallel planes of $\{100\}_\alpha$ were generally associated with dislocations or typically surrounded by intense strain contrast, and this is consistent with the results previously reported (Matsuura and Koda 1965, Bernole et al. 1969). This implies that nucleation of these particles appears to be energetically difficult.

As for the ternary Al-10Mg-0.5Ag alloy, when the ageing temperature was increased to 200°C, spherical precipitate particles were apparently observed as the predominant phase, together with only few plate-like β' precipitate particles which were major precipitates when specimens were aged at 90°C under ageing condition. At the ageing temperature of 240°C, however, no plate-like β' precipitate particles were detectable, and only the fine-scale, uniform distributions of the faceted precipitate particles were nucleated in the aluminium matrix during this ageing condition, suggesting that the dissolves temperature of the plate-like β' phase in the ternary alloy is approximately 200°C. As presented in Figs. 5.20, fine-scale, uniform distributions of the faceted precipitate particles were replaced by fine distributions of rod-like T precipitate particles near the peak hardness condition. In the over ageing condition (aged at 240°C), as presented in Figs. 6.14, the microstructures contained coarse globular particles. Based on established precipitate phase in Chapter 5, these coarse-scale globular particles were identified to be

metastable β' and/or stable β phases.

According to these microstructural observations comparing between binary and ternary alloys clearly demonstrate that trace additions of Ag to binary Al-10Mg alloy significantly change nature of microstructures, such as size, distribution and morphology of precipitate particles that are important factors to contribute the strength of alloys. It also suggests that the icosahedral phase is formed at relatively higher ageing temperatures (> 200°C) for the ternary alloys, suggesting that trace additions of Ag to binary alloys are necessary to have an effect of stabilisation of the formation of the icosahedral phase at higher temperature. These effects by the trace additions of Ag are attributable to increase strength of alloys, presented ageing curves in Chapter 4. These observations thus are well consistent with the results of the age-hardening curves presented in Chapter 4.

6.4 Conclusions

In this Chapter, the observations of microstructural changes in binary Al-10Mg and ternary Al-10Mg-0.5Ag alloys (wt %) aged at room temperature (natural ageing), 90°C, 200°C and 240°C, have been undertaken, and following conclusions are obtained;

(1) The fine-scale and uniformly distributed spheroidal precipitate particle were formed in the ternary Al-10Mg-0.5Ag alloy during the natural ageing process of periods of 16 months, while no precipitate particles were observed in the binary Al-10Mg alloy under the same ageing conditions.

(2) These fine scale, spheroidal precipitate particles observed in the ternary Al-10Mg-0.5Ag alloy were identified as the β'' phase which has the ordered $L1_2$ structure with the lattice parameter of a = 0.408 nm. The orientation relationship between the $L1_2$ (β'') phase and the aluminium matrix was of the form: $(100)_{L1_2} \| (100)_\alpha$, $[001]_{L1_2} \| [001]_\alpha$.

(3) The spheroidal precipitate particles having the ordered $L1_2$ structure in the Ag-modified alloys were unstable when the specimen were aged at 90°C.

(4) No evidence of GP zones was recorded in SAED patterns in both binary and ternary alloys during the natural ageing process with periods up to 16 months for binary alloy and up to 28 months for ternary alloy.

(5) The plate-like precipitate particles were formed in binary alloys aged from 30 days at 90°C. The plate-like particles had habit planes of $\{100\}_\alpha$, and were identified as the β' phase which is

consistent with the metastable β' phase (Al_3Mg_2, a = 1.002 nm, c = 1.636 nm) in Al-Mg alloys.

(6) Fine-scale, uniform distributions of the faceted precipitate particles were nucleated in the Al matrix as the dominant precipitate particle in ternary alloy aged from 4 h at 200°C. These particles were identified to be icosahedral phase while no icosahedral phase was observed in the Ag-free alloys when samples were aged at 200°C.

(7) Present TEM observations may be summarised as the following precipitation sequences during the isothermal ageing process at different ageing temperatures;

Ageing at room temperature:

Binary alloy: supersaturated α solid solution ------> α phase.

Ternary alloy: supersaturated α solid solution ------> metastable α phase + β'' phase

Ageing at 90°C:

Binary alloy: supersaturated α solid solution ------> metastable α phase + β' phase

------> metastable α phase + β' phase + unidentified phase

Ternary alloy: supersaturated α solid solution ------> metastable α phase + β' phase

Ageing at 200°C:

Binary alloy: supersaturated α solid solution ------> metastable α phase + β' phase

------> metastable α phase + β' phase + β phases

Ternary alloy: supersaturated α solid solution ------> metastable α phase +

β' phase + icosahedral phase

Chapter 7

Conclusions

7.1 Conclusions

The present investigation has involved the examination of the age-hardening response in both Al-5Mg and Al-10Mg alloys (wt %), with and without trace additions of 0.5Ag (wt %). The aim was to explore whether these alloys exhibit significant potential for precipitation hardening. The work was stimulated initially by the practical need for low density, high strength aluminium alloys in the 5000 series. The age-hardening response of these experimental alloys was monitored by measurements of their bulk Vickers hardness as a function of isothermal ageing temperature and time. Transmission electron microscopy, combined with electron diffraction and EDXS techniques, was employed to characterise both the precipitate microstructures and the precipitate phases within these alloys. In particular, the as-quenched and aged microstructures of ternary Al-10Mg alloy, with and without microalloying additions of 0.5Ag, were more the focus of detailed characterisation using transmission electron microscopy.

Hardness measurements for the aged binary alloys indicated little or no age-hardening response in Al-5Mg alloy aged at 200°C, but an increase of solute Mg stimulated a modest precipitation hardening response in Al-10Mg alloy aged at 160°C, 200°C and 240°C. In contrast, trace additions of Ag to Al-5Mg alloy promoted a significant age-hardening response, and to Al-10Mg alloy accelerated significantly the age-hardening response and substantially increased the maximum hardness achievable. For example, in the Al-10Mg-0.5Ag alloy, maximum hardness values of ~150VHN, 140VHN and 120VHN could be achieved by ageing at 160°C, 200°C and 240°C respectively, while maximum hardness values of ~119VHN, ~112VHN and ~105VHN were achieved by ageing at 160°C, 200°C and 240°C respectively, in the binary Al-10Mg alloy.

It is well known that cold work carried out post solution treatment and prior to ageing of aluminium alloys may promote an enhanced age-hardening response in certain alloy systems. The present experiments were designed to establish whether this phenomenon was to be detected in the experimental ternary Al-10Mg-0.5Ag alloy. The observations confirmed a significant effect of cold work on the age-hardening response in the ternary Al-10Mg-0.5Ag alloys, both the maximum hardness was significantly enhanced and the rate of the age-hardening response was moderately accelerated. These existed results suggest significant potential for further enhancing the strength and hardness of the Ag-modified alloys through appropriate thermomechanical treatments, involving a stage of low temperature deformation prior to ageing.

Based on qualitative evidence from defect analyses of as-quenched microstructures of an Al-10Mg alloy with and without 0.5Ag, the number density of dislocations in the as-quenched condition in the binary Al-10Mg alloy was approaching twice that in the ternary Al-10Mg-0.5Ag alloy, i.e. $5.1\pm0.2\times10^9$ cm^{-2} for the binary Al-10Mg alloy and $2.8\pm0.1\times10^9$ cm^{-2} for the ternary Al-10Mg-0.5Ag alloy. These differences in defect density may account for the small but significant differences in the hardness values of the two alloys in the as-quenched state, i.e. ~90VHN (±3VHN) for the binary Al-10Mg alloy and ~85VHN (±3VHN) for the ternary Al-10Mg-0.5Ag alloy. The Vergers vectors of representative dislocations in samples of both the Al-10Mg and Al-10Mg-0.5Ag alloys in the as-quenched condition were also determined, but no significant difference in the identity of the dislocations was detectable for all those examined. The dislocations were universally perfect dislocations with Burgers vectors of the type a/2<110>. In summary, while there appeared potential for microalloying additions of Ag to effect the dislocation density observed in as-quenched Al-10Mg alloy, there was no evidence that Ag modified the identity of those dislocations.

Characterisation of the precipitate microstructures in the Al-10Mg(-0.5Ag) alloys aged naturally at room temperature (20°C) revealed a fine-scale, uniform distribution of spheroidal precipitate particles formed in the ternary alloys after a period of 16 months, while no precipitate particles were detectable in the binary alloy under the same ageing conditions. These fine-scale, spheroidal precipitate particles were identified as the β'' phase, which has an ordered $L1_2$ structure (Al_3Mg, lattice parameter a = 0.408 nm). The orientation relationship between the β'' phase and the aluminium matrix phase was of the form $(100)\beta'' \parallel (100)_\alpha$, $[001]\beta'' \parallel [001]_\alpha$. The spheroidal precipitate particles of ordered $L1_2$ structure in the Ag-modified alloys were unstable when the specimens were aged at 90°C. No evidence from GP zones was detected in either the binary and ternary alloys during natural ageing for periods of up to 16 months and 28 months, respectively.

When the ageing temperature was increased to 90°C, plate-like precipitate particles were initially nucleated from supersaturated solid solution, followed by cuboidal precipitate particles in the later stage of decomposition processes in the binary Al-10Mg alloy. These plate-like particles

were typically ~100 nm x 5 nm in dimension and had habit planes of $\{100\}_\alpha$, and were identified as the metastable β' phase (Al_3Mg_2, a = 1.002 nm, c = 1.636 nm). The cuboidal particles were still remained unclear. In contrast, only plate-like β' particles were observed in the Ag-containing alloy exposed to similar ageing conditions.

When the alloys were aged at 200°C, the dominant precipitate phase in the binary Al-10Mg alloy took the form of $\{100\}_\alpha$ plate-like particles of β' phase, while the major precipitate phase in the Ag-modified alloy was icosahedral phase distributed uniformly as fine-scale (~20 nm) particle and accompanied by a small volume fraction of β' phase.

Detailed characterisation of the precipitate microstructures and precipitate phases in Al-10Mg(-0.5Ag) alloys aged at 240°C revealed that, in the early stages of ageing, a low number density of plate- and lath-like precipitate particles of β' phase was formed in the Al-10Mg alloy. Maximum hardness was associated with a mixture of coarse-scale, blocky β particles, lath-like β' particles and a small volume fraction of unidentified, irregularly-shaped precipitate particles. These latter precipitate particles appeared not to share an orientation relationship with the aluminium matrix phase.

In comparison, the aged microstructures at 240°C were significantly changed by microalloying additions of Ag. Fine-scale, uniformly dispersed diamond-shaped precipitate particles were observed in the Al-10Mg-0.5Ag alloy aged just 0.5 h at 240°C, in the very under-aged condition. These particles have been identified as having an icosahedral quasicrystalline structure, despite being formed from supersaturated solid solution (the α-Al phase) by a solid-state reaction during isothermal ageing. The quasicrystalline icosahedral precipitate phase contained all three principal elements, with the Ag content apparently significantly lower than the Mg content. The quasicrystalline particles were rhombohedral in shape, which was confirmed by a combination of direct TEM observations and analysis based on intersection point group symmetry. The orientation relationship between the icosahedral quasicrystalline and the aluminium matrix phases was determined to be such that i5 $\parallel$ $<011>_\alpha$ and i3 $\parallel$ $<111>_\alpha$. This newly-observed icosahedral phase thus appeared to preserve the same orientation relationship as that reported previously by Hansen et al. (1989) for Al-Fe-Si alloy. The present microstructural observations confirm that microalloying additions of Ag, to an alloy of the Al-Mg system, promote a change in the identity of the primary strengthening precipitate phase. It is noteworthy that the presence of this quasicrystalline was attributable to significant increase in the mechanical properties during the early stages of the decomposition process.

With increasing ageing time (2 h) at 240°C, a fine-scale, uniform distribution of rod-like precipitate particles, with a rod axis parallel to $<110>_\alpha$ directions, was observed in the ternary Al-10Mg-0.5Ag alloy. An optimum distribution of these particles was associated with the maximum

hardness condition. Microbeam electron diffraction patterns recorded from individual $<110>_\alpha$ rod-like precipitate particles could be indexed for the body-centred cubic structure of the T phase ($Mg_{32}(Al,Ag)_{49}$, lattice parameter a = 1.416 nm), and the orientation relationship with respect to the α - Al matrix phase was of the form $(010)_T \parallel (11\bar{1})_\alpha$ and $[001]_T \parallel [1\bar{1}0]_\alpha$. The rod-like precipitates were the primary strengthening phase in the Al-10Mg-0.5Ag alloy aged at 240°C. Qualitative microanalysis by EDXS suggested that the crystalline T phase observed here was a ternary compound that contained all three elements Al, Mg and Ag. In addition, a small number density of elongated particles with a rectangular profile was observed in the Al-10Mg-0.5Ag alloy aged 2 h at 240°C. These precipitate particles were also identified as the T phase, but the orientation relationship was of the form: $(100)_T \parallel (100)_\alpha$ and $[001]_T \parallel [001]_\alpha$.

Coarse-scale, globular precipitate particles were commonly observed in over-aged samples of the Al-10Mg-0.5Ag alloy (e.g. aged 72 h at 240°C). These coarse globular particles could be consistently indexed for the face-centred cubic structure of the β phase (Al_3Mg_2, lattice parameter a = 2.824 nm) that is the equilibrium precipitate phase in the binary Al-Mg alloy. The orientation relationship between the β phase and α -Al matrix phase was such that; $(100)_\beta \parallel (100)_\alpha$ and $[001]_\beta \parallel [001]_\alpha$. This orientation relationship, established on the basis of evidence from electron diffraction patterns in this current project, has not been reported previously. The coarse-scale globular particles were generally observed to be multiply twinned which observed in the Al-10Mg-0.5Ag alloy aged 72 h at 240°C.

Based on the detailed characterisation of precipitate particles using TEM, combined with electron diffraction and EDXS techniques, the precipitation sequences in supersaturated Al-10Mg(-0.5Ag) alloys aged at different temperatures may be summarised as follows;

Ageing at room temperature:

Binary alloy: supersaturated α solid solution ------> stable α phase.

Ternary alloy: supersaturated α solid solution ------> metastable α phase + β'' phase.

Ageing at 90°C:

Binary alloy: supersaturated α solid solution ------> metastable α phase + β' phase
------> metastable α phase + β' phase + unidentified phase.

Ternary alloy: supersaturated α solid solution ------> metastable α phase + β' phase.

Ageing at 200°C:

Binary alloy: supersaturated α solid solution ------> metastable α phase + β' phase
------> metastable α phase + β' phase + β phases.

Ternary alloy: supersaturated α solid solution ------> metastable α phase +
β' phase + icosahedral phase.

Ageing at 240°C:

Binary alloy: Supersaturated α solid solution -----> supersaturated metastable α solid solution + metastable β' phase -----> stable β phase + equilibrium α phase.

Ternary alloy: Supersaturated α solid solution -----> metastable icosahedral quasicrystalline phase + metastable α solid solution -----> metastable T phase + metastable α solid solution -----> stable β phase + equilibrium α phase.

As stated already earlier in this Chapter, the present observations confirm that microalloying additions of Ag to alloys of Al-Mg system commonly promote a change in the identity of the primary strengthening precipitate phase, and often an associated improvement in the mechanical properties. However, the precise role of Ag in facilitating the precipitation of the metastable strengthening icosahedral and T phases remains to be understood.

The quasicrystalline icosahedral phase identified in the present research was replaced by the metastable crystalline T phase when the Al-10Mg-0.5Ag alloy was aged 2 h at 240°C, and the T phase was the primary strengthening phase in the maximum hardness condition. However, the precise mechanism for the phase transformation from quasicrystalline icosahedral phase to crystalline T phase still remains unclear. Furthermore, this metastable T phase was replaced by the equilibrium β phase when the Al-10Mg-0.5Ag alloy was aged for 24 h at 240°C, into what corresponded to an over-aged condition. Again, however, the mechanism of phase transformation remains unclear. It is important to point out, from the point of view of the understanding of these phase transformation mechanisms, that the icosahedral quasicrystalline phase is closely related to the crystalline T phase in terms of atomic co-ordinates (Bergman et al. 1957), while the lattice parameter of the metastable T phase is just half that of the equilibrium β phase (Bergman et al. 1957, Samson 1965). It is thus clear that this sequence of these phases are closely related in terms of atomic arrangements and structure.

References

Auld, J.H. (1968)
X-ray Investigation of Ageing in an Aluminium-5% Magnesium Alloy with Small Silver Additions, Acta Metall., **16**, 97-101.

Auld, J.H. and Cousland, S. Mck. (1976)
The Metastable T' phase in Al-Zn-Mg and Al-Ag-Mg Alloys, Metal Science, **10**, 445-448.

Ashby, M.F. and Brown, L.M. (1963)
Diffraction Contrast from Spherically Symmetrical Coherency Strains, Philosophical Magazine, **8**, 1083-1103.

Baba, Y. (1972)
Effect of Small Amounts of Additional Elements on Ageing Characteristics of Al-9 at% Mg Alloy, Transaction of Journal of Japan Institute of Metals, **13**, 76-81.

Bailey, J.E. and Hirsch, P.B. (1960)
The Dislocation Distribution, Flow Stress, and Stored Energy in Cold-Worked Polycrystalline Silver, Philo. Mag., **5** , 485-497.

Ball, M.D. and Lloyd, D.J (1985)
Particles Apparently Exhibiting Five-Fold Symmetry in Al-Li-Cu-Mg Alloys, Scripta Metall., **19**, 1065-1068.

Bergman, G., Waugh, J.L.T. and Pauling, L. (1957)
The Crystal Structure of the Metallic Phase $Mg_{32}(Al,Ag)_{49}$, Acta Crystallogr., **10**, 254-258.

Bernole, M., Raynal, J. and Graf, R. (1969)
Structure et Orientation des Precipites Apparaissant par Revenu Appes Trempe Dans un Alliage Aluminium-Magnesium a 10% de Magnesium, J. Microscopie, **8**, 831-840.

Bernole, P.M., Graf, R. and Guyot, P. (1973)
Etude au microscope electronique et aux rayons X de la preprecipitation dans un alliage Al-10% Mg vielli a la temperature ambiante, Philo. Mag. A, **28**, 771-782.

Bernole, M. (1974)
Doctorate Thesis, Faculty of Science, University of Rouen.

Bouchear, M., Hamana, D. and Laoui, T. (1996)
GP zones and precipitate morphology in aged Al-Mg alloy,
Philo. Mag. A, **73**, 1733-1740.

Boudilli, E.K., Denanot, M.F. and Dauger, A. (1977)
Decomposition A 20°C Des solutions Solides Sursatures D'Aluminium-Magnesium,
Scripita Metall., **11**, 543-548.

Boyapati, K. and Polmear, I.J. (1979)
Fatigue-Microstructure Relationships in Some Aged Aluminium Alloys,
Fatigue of Engineering Materials and Structures, **2**, 23-33.

Burger, G.B., Gupta, A.K., Jeffrey, P.W. and Lloyd, D.J. (1995)
Microstructural Control of Aluminum Sheet Used in Automotive Applications,
Materials Characterisation, **35**, 23-39.

Caraher, S. K., Polmear, I. J. and Ringer, S. P. (1998)
Effects of Cu and Ag on Precipitation in Al-4Zn-3Mg (wt%), Pro. 6th Inter. Conf. Aluminum Alloys (ICAA-6) Vol. 2, Eds. by T. Sato, S. Kumai, T. Kobayashi and Y. Murakami, The Japan Institute of Light Metals, 739-744.

Caraher, S. K., Hono, K., Polmear, I. J. and Ringer, S. P. (1998)
Unpublished research.

Cassada, W.A. and Shiflet, G.J. (1986)
Formation of an Icosahedral Phase by Solid-State Reaction,
Phys. Rev. Lett., **56**, 2276-2279.

Cassada, W.A., Shiflet, G.J. and Poon, S.J. (1987)
Quasicrystalline Grain Boundary Precipitates in Aluminium Alloys through Solid-Solid Transformations, Journal of Microscopy, **146**, 323-335.

Chandra, S. and Suryanarayana, C. (1988)
Quasicrystalline-to-Crystalline Transformation in Rapidly Solidified $Mg_{32}(Al,Ag)_{49}$,
Philo. Mag. B, **58**, 185-202.

Chester, R.J. and Polmear, I.J. (1983)
Precipitation in Al-Cu-Mg-Ag Alloys, The Metallurgy of Light Alloys, Inst. of Metals, London, 78-81.

Chopra, H. D., Muddle, B. C. and Polmear, I. J. (1996)
The Structure on Primary Strengthening Precipitates in an Al-1.5wt% Cu-4.0wt% Mg-0.5wt% Ag Alloy, Philo. Mag. Lett., **73**, 351-357.

Cordier, H. and Detert, K. (1961)
Untersuchungen uber Entmischungsvorgange bei tiefen Temperaturen in einer Aluminiumlegierung mit 10 Gew.-%Mg, Z. Metallkde., **52**, 321-328.

Cooper, M. and Robinson, K. (1966)
The Crystal Structure of the Ternary Alloy Alpha-(AlMnSi),
Acta Crystallogr., **20**, 614-617.

Cottereau, B., Itoh, G. and Kanno, M. (1989)
Effect of Cold-Working on the Ageing Behavior of an Al-8% Mg Alloy,
J. Japan Institute of Metals, **53**, 157-163.

Cousland, S. Mck. and Tate, G.R. (1986)
Structural Changes Associated with Solid-State Reactions in Al-Ag-Mg Alloys,
J. Appl. Cryst., **19**, 174-180.

Dauger, A, Denanot, M.F. and Caisso, J. (1973)
Observation des effets de diffraction electronique dus auz zones de Guinier-Preston de l'aluminium-argent, l'aluminium-zinc et l'aluminium-magnesium,
Phys. Stat. Sol. (a), **15**, 161-167.

Dieter, G. E., (1988)
Mechanical Metallurgy, Second Edition, McGraw-Hill, 143.

Doyama, M. (1966)
A Relationship Between the Vacancy-Impurity Binding Energy and the Heat of Solution in Aluminum, Phys. Lett., **21**, 395-396.

Edington, J.W. (1976)
Practical Electron Microscopy in Materials Science, Vol.3, 107, Macmillan, London.

Eikum, A. and Thomas, G. (1964)
Precipitation and Dislocation Nucleation in Quenched-Aged Al-Mg Alloys, Acta Metall., **12**, 537-545.

Elser, V. and Henley, C.L. (1985)
Crystal and Quasicrystal Structures in Al-Mn-Si Alloys, Phys. Rev. Lett., **55**, 2883-2886.

Embury, J.D. and Nicholson, R.B. (1963)
Dislocation Sources in an Aluminium Alloy, Acta Metall., **11**, 347-354.

Embury, J.D. and Nicholson, R.B. (1965)
The Nucleation of Precipitates: The System Al-Zn-Mg, Acta Metall., **13**, 403-417.

Entwistle, K. M. and Perry, A. J. (1966)
The Effect of Binding between Indium Atoms and Vacancies on the Kinetics of Zone Growth in Aluminium-4 wt.-% Copper Alloys, J. Inst. Metals, **94**, 24-30.

Fei, W.D. and Kang, S.B. (1996)
A Study on the Precipitates in T4 Treated Al-Mg Alloys, Scripta Materials, **34**, 357-362.

Feller-Kniepmeier, M., Detert, K. and Thomas, L. (1964)
Elektronenmikroskopische Untersuchungen uber Ausscheidungsvorgange in Aluminium-Magnesium-Legierungen, Z. Metallkde., **55**, 83-87.

Frank, F.C. and Kasper, J.S. (1959)
Complex Alloy Structures Regarded as Sphere Packings, Acta Crystallogr., **11**, 184-190.

Gao, X., Nie, J. F. and Muddle, B. C. (1999)
Heterogeneous Nucleation of Precipitate Phase θ' in Microalloyed Al-Cu Based Alloys, Pro. Int. Con. on Solid-Solid Phase Transformations 99 (JIMIC-3), Edited by M. Koiwa, K. Otsuka and T. Miyazaki, The Japan Institute of Metals, Japan, 225-228.

Gault, C., Dauger, A. and Boch, P. (1980)
Decomposition of Aluminium-Magnesium Solid Solutions Studied by Ultrasonic Measurements of Elastic Properties and Electron Microscopy, Acta Metall., **28**, 51-60.

Guinier, A. (1938)
Structure of Age Hardened Aluminium-Cupper Alloys, Nature, **142**, 569-570.

Hansen, N. (1977)
The Effect of Grain Size and Strain on the Tensile Flow Stress of Aluminium at Room Temperature, Acta Metall., **25**, 863-869.

Hardy, H.K. (1951-52)
The Ageing Characteristics of Ternary Aluminium-Copper Alloys with Cadmium, Indium, or Tin, J. Inst. Metals, **80**, 483-492.

Hardy, H.K. (1954-55)
Aluminium-Copper-Cadmium Sheet Alloys, J. Inst. Metals, **83**, 337-346.

Hardy, H.K. (1955-56)
Trace-Element Effects in Some Precipitation-Hardening Aluminium Alloys, J. Inst. Metals, **84**, 429-439.

Hardy, H.K. and Silcock, J.M. (1955-56)
The Phase Sections at 500°C and 350°C of Aluminium-Rich Aluminium-Copper-Lithium Alloys, J. Inst. Metals, **84**, 423-428.

Henley, C.L. and Elser, V. (1986)
Quasicrystal Structure of $Mg_{32}(Al,Ag)_{49}$, Philo. Mag. B, **53**, L59-L66.

Hirsch, J. and Lücke, K. (1988)
Mechanism of Deformation and Development of Rolling Textures in Polycrystalline F.C.C. Metals-I. Description of Rolling Texture Development in Homogeneous CuZn Alloys, Acta Metall., **36**, 2863-2882.

Hono, K., Sano, N., Babu, S. S., Okano, R. and Sakurai, T. (1993)
Atom Probe Study of the Precipitation Process in Al-Cu-Mg-Ag Alloys, Acta Metall. Mater., **41**, 829-838.

Huang, B.-P., and Zheng, Z.-Q. (1998)
Independent and Combined Roles of Trace Mg and Ag Additions in Properties Precipitation Process and Precipitation Kinetics of Al-Cu-Li-(Mg)-(Ag)-Zr-Ti Alloys, Acta. Mater., **46**, 4381-4393.

Inoue, A., Nakano, K., Masumoto, T. and Chen, H.S. (1989)
New Icosahedral $Al_{60}Mg_{38}X_2$ and $Al_{50}Mg_{48}X_2$ Alloys Prepared by Rapid Solidification, Mater. Trans., JIM, **30**, 200-203.

Ito, T., Matsuura, K. and Watanabe, K. (1969a)
Effect of Different Heat Treatments on the Precipitation Phenomena of an Al-6 wt% Mg Alloy Containing 0.5 wt% Ag, J. Japan Institute of Metals, **33**, 1227-1232.

Ito, T., Furuya, T., Matsuura, K. and Watanabe, K. (1969b)
The Solid Solubility of the α -Phase in an Al-Mg Alloy Containing 0.5 wt% Ag and the Ageing Phenomena, J. Japan Institute of Metals, **33**, 1232-27-1238.

Ito, T., Furuya, T., Matsuura, K. and Watanabe, K. (1971)
The Solid Solubility of the α Phase and the Ageing Phenomena in an Al-Mg Alloy Containing 0.5 wt% Ag, Transactions J. Japan Institute of Metals, **12**, 379-385.

Kanno, M., Suzuki, H. and Kanoh, O. (1979)
Energy Dispersive X-ray Spectroscopy on So-Called Sn-Rich Precipitates in Al-Cu Alloy containing a small amount of Sn, J. Japan Inst. Light Metals, **29**, 223-226.

Kanno, M., Suzuki, H. and Kanoh, O. (1980)
The Precipitation of θ' Phase in an Al-4% Cu-0.06% In Alloy,
J. Japan Inst. Metals, **44**, 1139-1145.

Kobayashi, K. and Hogan, L.M. (1979)
Five Fold Twinned Silicon Crystals Growth in an Al-16wt.%Si Melt,
Philo. Mag. A, **40**, 399-407.

Kelly, A. and Nicholson, R.B. (1963)
Precipitation hardening, Progress in Materials Science, **10**, 149-392.

Kelly, P.M., Jostsons, A., Blake, R.G. and Napier, J.G. (1975)
The Determination of Foil Thickness by Scanning Transmission Electron Microscopy,
Phys. Stat. Sol. (a), **31**, 771-780.

Kievits, F.J. and Zuithoff, A.J. (1964)
The Ageing Characteristics of Aluminium-Magnesium Alloys Containing Silver and Cadmium, J. Inst. Metals, **93**, 517-519.

Knowles, K. M. and Stobbs, W. M. (1988)
The Structure of {111} Age-Hardening Precipitates in Al-Cu-Mg-Ag Alloys,
Acta Crys., **B44**, 207-227.

Kojima, Y., Takahashi, T., Kubo, M. and Morinaga, T. (1981)
Decrease of Ductility in Al-10 Pct Mg Alloys During Long-Term Natural Ageing, Met. Trans., **12A**, 1113-1117.

Kuhlmann-Wilsdorf, D. (1958)
On the Origin of Dislocations, Philo. Mag., **3**, 125-139.

Kumada, K., Sumitomo, Y., Nenno, S. and Yamamoto, M. (1970)
Formation of $L1_2$ Type Superlattice Al_3Mg in Liquid-Quenched Al-Mg Alloys, J. Japan Institute of Metals, **34**, 1062-1099.

Laves, F. and Moeller, K. (1938)
Contribution to the Knowledge of the System Aluminium-Magnesium, Z. Metallkde., **30**, 232-235.

Lee, Y.-S., Muddle, B.C. and Polmear, I.J. (1995)
High Strength Al-Cu-Mg-Ag Alloys with Controlled Li Additions, Proceedings of the 2nd Pacific Rim International Conference on Advanced Materials and Processing Edited by K.S. Shin, J.K. Yoon and S.J. Kim, The Korean Institute of Metals, 2221-2228.

Lorimer, G.W. (1978)
Precipitation in Aluminium Alloys, in Precipitation Process in Solid, Editors by K.C. Russell and H.I. Aaronson, TMS-AIME, Warrendale PA, 87-119.

Mackay, A.L. (1986)
A Bibliography of Quasicrystals, International Journal of Rapid Solidification, **2**, S1-S31.

Matsuura, K. and Koda, S. (1965)
Precipitation and Generation of Dislocations in an Al-Mg Alloy, J. Physical Society of Japan, **20**, 251-263.

Mizutani, U., Takeuchi, T. and Fukunaga, T. (1993)
Formation of Quasicrystals and Approximant Crystals by Mechanical Alloying in Mg-Al-Zn Alloy System, Mater. Trans., JIM, **34**, 102-108.

Mondolfo, L.F. (1976)
Al-Mg system in Aluminum Alloys: Structure and Properties, 1st edition, Butterworths, London, 312.

Muddle, B.C. and Polmear, I.J. (1989)
The Precipitate Phase Ω in Al-Cu-Mg-Ag Alloys, Acta Metall., **37**, 777-789.

Murayama, M. and Hono, K. (1998)
Three Dimensional Atom Probe Analysis of Pre-Precipitate Clustering in an Al-Cu-Mg-Ag Alloy, Scripta Mater., **38**, 1315-1319.

Murray, J.L. (1988)
Binary Alloy Phase Diagrams Second Editions Vol. 1, Editor-in-Chief T.B. Massalski, ASM International, 170.

Nebti, S., Hamana, D. and Cizeron, G. (1995)
Calorimetric Study of Pre-Precipitation and Precipitation in Al-Mg Alloy, Acta Metall. Mater., **43**, 3583-3588.

Nie, J.F., Muddle, B.C. and Polmear, I.J. (1996)
The Effect of Precipitate Shape and Orientation on Dispersion Strengthening in High Strength Aluminium Alloys, Materials Science Forum, **217-222**, 1257-1262.

Nie, J. F., Aaronson, H. I. and Muddle, B. C. (1999)
The Role of Microalloying Elements in the Formation of Precipitate Plates in Aluminium Alloys, Pro. Int. Con. on Solid-Solid Phase Transformations 99 (JIMIC-3), Edited by M. Koiwa, K. Otsuka and T. Miyazaki, The Japan Institute of Metals, Japan, 157-160.

Nozato, R. and Ishihara, S. (1980)
Calorimetric Study of Precipitation Process in Al-Mg Alloys, Transactions of Japan Institute of Metals, **21**, 580-588.

Nuyten, J. B. M. (1967)
Quenched Structures and Precipitation in Al-Cu Alloys with and without trace-Additions of Cd, Acta Met., **15**, 1765-1770.

Osamura, K. and Ogura, T. (1984)
Metastable Phases in the Early Stage of Precipitation in Al-Mg Alloys, Metall. Trans., **15A**, 835-842.

Panseri, C., Federighi, T. and Ceresara, S. (1963)
On the Precipitation Process in Al-Mg Alloys, Transactions of the Metallurgical Society of AIME, **227**, 1122-1126.

Parker, B. A. (1972)
The Effect of Certain Trace Element Additions on the Ageing Behaviour of an Aluminium-4wt% Zinc-3wt% Magnesium Alloy, J. Australian Institute Metals, **17**, 31-38.

Perlitz, H. (1944)
Crystal Structure of β-Aluminium-Magnesium Alloy, Nature, **154**, 606.

Perry, A. J. and Entwistle, K. M. (1968)
The Binding free Energy Between Vacancies and Solute Atoms in Aluminium, J. Inst. Metals, **96**, 344-349.

Perryman, E.C.W. and Brook, G.B. (1950-51)
Mechanism of Precipitation in Aluminium-Magnesium Alloys, J. Inst. Metals, **79**, 19-34.

Pollard, W.A. (1964-65)
Long-Term Ageing Behaviour of Aluminium-10% Magnesium Casting Alloys, J. Inst. Metals, **93**, 339-346.

Polmear, I. J. (1960)
The Ageing Characteristics of Complex Al-Zn-Mg Alloys: Distinctive Effects of Cu and Ag on the Ageing Mechanism, J. Inst. Metals, **89**, 51-59.

Polmear, I.J. and Sargant, K.R. (1963)
Enhanced Age-hardening in Aluminium-Magnesium Alloys, Nature, **200**, 669-670.

Polmear, I.J. (1964)
The Effects of Small Additions of Silver on the Ageing of Some Aluminum Alloys, Transactions of the Metallurgical Society of AIME, **230**, 1331-1339.

Polmear, I.J. (1968)
The Influence of Small Additions of Silver on the Structure and Properties of Aged Aluminum Alloys, Journal of Metals, **20**, 44-51.

Polmear, I. J. (1972)
The Development and Commercial Evaluation of Aluminium-Zinc-Magnesium Alloys Containing Small Additions of Silver, J. Australian Institute of Metals, **17**, 1-17.

Polmear, I.J. (1987)
Role of Trace Elements in Aged Aluminium-Alloys,
Materials Science Forum, **13/14**, 195-214.

Polmear, I. J. (1995)
Private Communication.

Polmear, I. J. (1995)
Light Alloys: Metallurgy of the Light Metals, Third Edition, Arnold, London.

Porter, D.A. and Easterling, K.E. (1987)
Phase Transformation in Metals and Alloys, Van Nostrand Reinhold, UK, 291-302.

Preston, G. D. (1938)
Structure of Age-hardened Aluminium-Cupper Alloys, Nature, **142**, 570.

Ramachandrarao, P. and Sastry, G.V.S. (1985)
A Basis for the Synthesis of Quasicrystals, Pramana J. Phys., **25**, L225-L230.

Ratchev, P., Verlinden, B., De Smet, P. and Van Houtte, P. (1994)
S Phase Precipitation in Al-4 WT.% Mg-1 WT.% Cu Alloy,
Scripta Materialia, **30**, 599-604.

Ratchev, P., Verlinden, B., De Smet, P. and Van Houtte, P. (1998)
Effect of Cooling Rate and Predeformation on the Precipitation Hardening of an Al-4.2% Mg-0.6% Cu Alloy, Scripta Materialia, **38**, 1195-1201.

Raynal, J.M. and Roth, M. (1975)
Neutron Small-Angle Scattering Aged in Al-Mg Alloys, J. Appl. Cryst., **8**, 535-537.

Reiderer, K. (1936)
Das System Aluminium-Magnesium-Zink, Z. Metallkde., **28**, 312-317.

Ringer, S. P., Hono, K. and Sakurai, T. (1995)
The Effect of Trace Additions of Sn on Precipitation in Al-Cu Alloy: An Atom Probe Field Ion Microscopy Study, Metall. Mater. Trans., **26A**, 2207-2217.

Ringer, S.P., Hono, K., Polmear, I.J. and Sakurai, T. (1996)
Nucleation of Precipitates in Aged Al-Cu-Mg(-Ag) Alloys with High Cu:Mg Ratios, Acta. Mater. Metall., **44**, 1883-1898.

Ringer, S.P., Polmear, I.J. and Sakurai, T. (1996)
Effect of Additions of Si and Ag to Ternary Al-Cu-Mg Alloys in the α+S Phase Field, Materials Science and Engineering A**217/218**, 273-276.

Ringer, S. P., Quan, G. C. and Sakurai, T. (1998)
Microstructural Evolution in High Strength Microalloyed Aluminium Alloys, Materials Science and Engineering, **A250**, 120-125.

Roth, M. and Raynal, J.M. (1974)
Small-Angle Neutron Scattering by Guinier-Preston Zones in Al-Mg Alloys, J. Appl. Cryst., **7**, 219-221.

Samson, A. (1965)
The crystal structure of the phase β Mg_2Al_3, Acta Cryst., **19**, 401-413.

Sato, T., Kojima, Y. and Takahashi, T. (1982)
Modulated Structures and GP zones in Al-Mg Alloys, Met. Trans., **13A**, 1373-1378.

Sato, T., Takahashi, T., Iizumi, M. and Doi, K. (1984)
Ageing Phenomena in Al-10% Mg Alloy at Room Temperature, J. Japan Institute of Light Metals, **34**, 110-114.

Sato, T. and Kamio, A. (1991)
High Resolution Electron Microscopy of Phase Decomposition Microstructures in Aluminium-Based Alloys, Materials Science and Engineering, **A146**, 161-180.

Sainfort, P., Dubost, B. and Dubus, A. (1985)
Quasicrystalline Precipitation from Solid Solutions of the Al-Li-Cu-Mg System, C.R. Acad., Paris, t. 301, serie2, **10**, 689-692.

Sainfort, P. and Dubost, B. (1987)
Coprecipitation Hardening in Al-Li-Cu-Mg Alloys, Journal de Physique C3-**47**, 407-413.

Saulnier, A. and Mirand, P. (1960)
Quelques applications recentes de l'examen direct de coupes metalliques minces dans le microscope electronique, Mem. Sci. Rev. Met., **2**, 91-95.

Shechtman, D., Blech, I., Gratias, D. and Cahn, J.W. (1984)
Metallic Phase with Long-Range Orientational Order and No Translational Symmetry, Phys. Rev. Lett., **53**, 1951-1953.

Silcock, J. M., Heal, T. J. and Hardy, H. K. (1955-56)
The Structural Ageing Characteristics of Ternary Aluminium-Copper Alloys with Cadmium, Indium, or Tin, J. Inst. Metals, **84**, 23-31.

Starink, M.J. and Zahra, A.-M. (1997)
Low-Temperature Decomposition of Al-Mg Alloys: Guinier-Preston Zones and L12 Ordered Precipitates, Philo. Mag. A, **76**, 701-714.

Suzuki, H., Kanno, M. and Kitayama, T. (1978)
The ununiformity in precipitates-density in high magnesium Al-Mg alloy sheets, J. Japan Institute of Light Metals, **28**, 292-299.

Takahashi, T., Kojima, Y. and Okaniwa, S. (1978)
Effect of Ag Addition on the Age-hardening in Al-10% Mg Alloys, J. Japan Institute of Metals, **42**, 396-402.

Takahashi, T. and Sato, T. (1986)
Formation of a Modulated Structure and an Ordered Structure in Concentrated Al-10% and 14% Mg Alloys, J. Japan Institute of Metals, **50**, 133-140.

Tsai, A-.P., Inoue, A. and Masumoto, T. (1987)
A Stable Quasicrystal in Al-Cu-Fe System, Japanese J. Appl. Phys., **26**, L1505-1507.

Tsai, A.P., Tsurui, T., Memezawa, A., Aoki, K., Inoue, A. and Masumoto, T. (1993)
Formation of Quasicrystals through Peritectoid Reactions from a Non-Equilibrium Cubic Phase Prepared by Mechanical Alloying, Philo. Mag. Lett., **67**, 393-398.

Trehan, Y.N. (1969)
On the Structure of βAl-Mg, Indian J. Pure Appl. Phys., **7**, 209-210.

Van Nuyten, J. B. M. (1967)
Quenched Structures and Precipitation in Al-Cu Alloys with and without Trace Additions of Cd, Acta Metall., **15**, 1765-1770.

Vietz, J.T. and Polmear, I.J. (1966)
The Influence of Small Additions of Silver on the Ageing of Aluminium Alloys: Observations on Al-Cu-Mg Alloys, J. Inst. Metals, **94**, 410-419.

Vietz, J. T., Sargant, K. R. and Polmear, I. J. (1963-64)
The Influence of Small Additions of Silver on the Ageing of Aluminium Alloys: Further Observations on Al-Zn-Mg Alloys, J. Inst. Metals, **92**, 327-333.

Wheeler, M.J., Blankenburgs, G. and Staddon, R.W. (1965)
Evidence for a Ternary Phase in the Aluminium-Magnesium-Silver System, Nature, **207**, 746-747.

Williams, B.E. (1972)
The Aluminium-Rich Corner of the Al-Mg-Ag Phase diagram, J. Australian Institute of Metals, **17**, 171-174.

Williams, D.B. (1987)
Practical Analytical Electron Microscopy in Materials Science, 2nd Edition, Weinheim, Basel, Electron Optics Pub. Co.

Williams, D.B. and Carter, C.B. (1996)
Transmission Electron Microscopy - A Textbook for Materials Science, Chapter 25, Plenum Press, New York.

Yukawa, H., Murata, Y., Morinaga, M., Takahashi, Y. and Yoshida, H. (1995)
Heterogenous Distributions of Magnesium Atoms Near the Precipitate in Al-Mg Based Alloys, Acta Metall. Mater., **43**, 681-688.

Publications

M. KUBOTA, J.F. NIE, B.C. MUDDLE and I.J. POLMEAR,
The Precipitation Hardening Response in Al-Mg(-Ag) Alloys,
Materials Research '96, Institute of Metals and Materials Australasia (IMMA),
Brisbane, AUSTRALIA, 9-12 July, 1996, vol.1, pp.17-20.

M. Kubota, J.F. Nie and B.C. Muddle,
Characterisation of Precipitate Phases in Aged Al-Mg(-Ag) Alloys,
The 15th Australian Conference for Electron Microscopy (ACEM-15),
Tasmania, AUSTRALIA, 1-6 February, 1998, pp.123.

M. KUBOTA, J.F. NIE and B.C. MUDDLE,
Characterisation of Precipitate Phases in Aged Al-Mg(-Ag) Alloys,
Workshop on Phase Transformation in Engineering Materials,
Melbourne, AUSTRALIA, 9-10 February, 1998, pp.33.

M. KUBOTA, J.F. NIE and B C. MUDDLE,
Enhanced Precipitation Hardening in Al-Mg(-Ag) Alloys,
The 6th International Conference on Aluminum Alloys (ICAA-6),
Toyohashi, JAPAN, 5-10 July, 1998, pp.763-768.

M. Kubota, J.F. Nie and B.C. Muddle,
Characterisation of Quasicrystalline and Crystalline Forms of the T Phase in Isothermally Aged Al-Mg-Ag Alloys,
Solid-Solid Phase Transformation (JIMIS-3),
Kyoto, JAPAN, 24-28 May, 1999, pp.1349-1352.